Reduction-oxidation cycling of metal oxides for hydrogen production

Author:
Sim, Andrew Gregory

Publication Date:
2010

DOI:
https://doi.org/10.26190/unsworks/22950

Reduction-Oxidation Cycling of Metal Oxides For Hydrogen Production

A Thesis

by

Andrew G. Sim

B.Sci. (Nanotechnology)

Submitted to the University of New South Wales in Partial Fulfillment of the Requirements for the Degree of

Doctor of Philosophy in **Chemical Engineering**

School of Chemical Engineering

The University of New South Wales

Australia

April 2010

ABSTRACT

A process for the production of clean hydrogen from methane based upon the sequential reduction and oxidation of metal oxides has been studied. The original process, based on iron oxide, suffers from significant disadvantages including deactivation by sintering and coke deposition. Improvement of the iron based system and identification and development of alternative metal oxides for hydrogen production has formed the basis of this study.

The literature review outlines current methods for hydrogen production, followed by a review of the Steam-Iron Process as an improved and simpler method for clean hydrogen production. Thermodynamic assessment shows Fe_3O_4/FeO/Fe, WO_3/WO_2/W and SnO_2/SnO/Sn to be the most prospective systems for the Steam-Metal Process.

Experimental testing showed that Fe and W based systems were suitable for hydrogen production, but Sn based systems were unsuitable due to poor reducibility using methane. Attention was then focused on the addition of CeO_2/ZrO_2 promoters to Fe and W based systems in order to improve reactivity and prevent catalyst deactivation. CeO_2/ZrO_2 promoted Fe_2O_3 showed improved redox reactivity and increased stability, with formation of FeO. This aided in mitigation of sintering and introduced the possibility of prevention of coking, as catalysed by methane decomposition over fully reduced Fe metal.

Although WO_3 was found to be a suitable oxide, complete reduction to tungsten metal resulted in the formation of tungsten carbide and contamination of hydrogen produced. The formation of 31mol% [CeO_2/ZrO_2] / 69 mol% WO_3 showed stabilised reduction using methane, allowing for redox cycling of the WO_3-WO_2 couple and preventing complete reduction to W metal. The use of the doped metal oxide showed the best performance of all the metal oxides tested, with clean hydrogen production over multiple redox cycles and high metal oxide stability.

Further kinetic studies of both the reduction and oxidation reactions show reduction is chemical reaction controlled process ($WO_3/WO_{2.9} \rightarrow WO_2$) with an apparent activation energy of 142 ± 3 kJ/mol. Oxidation is also fitted to a chemically controlled process, with a reaction rate expression derived as:

$$r_{H_2} = [0.064 + (F \times 0.00038)] \cdot e^{(-108750/8.314 \times T)} \cdot [P_{H_2O}]^{0.75}$$

The apparent activation energy for oxidation was calculated as 109 ± 1 kJ/mol.

ACKNOWLEDGEMENTS

I would like to thank the following people, whom without I could not have completed this undertaking.

Firstly, I would very much like to thank Professor David Trimm for his guidance and support throughout the course of my research, which kept me motivated and provided much needed encouragement. I was able to learn a great deal from his depth of knowledge and invaluable insight.

I would like to thank to Professor Noel Cant, for his interest and advice, along with many insightful discussions and in helping me in general with my research.

I would like to thank Dr Andrew Smith, who started me off on this project and provided guidance at the beginning.

I would like to thank the technical staff, including our Laboratory Manager John Starling and Geoffrey Vaughan, for all their assistance and support with my research. I would also like to thank Dr Yun Lei, for her much needed help and patience.

Finally I would like to extend my sincerest thanks to my family and friends, for their unwavering support and belief in me, which gave me the motivation to see this through to the end.

TABLE OF CONTENTS

LIST OF FIGURES

LIST OF TABLES

INTRODUCTION

1.1 Introduction

The Steam-Iron Process is a redox process by which clean hydrogen can be produced:

$Fe_3O_4 + 4CH_4 \rightarrow 3Fe + 4CO + 8H_2$ $\Delta H°_{298}$ = +488 kJ/mol **1.1**

$3Fe + 4H_2O \rightarrow Fe_3O_4 + 4H_2$ $\Delta H°_{298}$ = -76 kJ/mol **1.2**

This process can be enhanced via addition of promoters or supporting oxides.

Current industrial methods for hydrogen production include methane steam reforming (**Equation 1.3**) and methane partial oxidation (**Equation 1.4**):

$CH_4 + H_2O \rightarrow CO + 3H_2$ $\Delta H°_{298}$ = +206 kJ/mol **1.3**

$\frac{1}{2}O_2 + CH_4 \rightarrow CO + 2H_2$ $\Delta H°_{298}$ = -38 kJ/mol **1.4**

These processes are designed for large scale industrial hydrogen production, requiring cost effective generation of expensive steam (methane steam reforming) or pure oxygen separated from air (methane partial oxidation). Hydrogen produced via these processes also requires energy intensive separation and purification from carbon oxides, such that it is suitable for use in hydrogen fuel cells.

The Steam-Iron Process is a means for decentralised small to medium scale clean hydrogen production in a two-step process. It has the potential for utilising cheaper materials and minimising distribution costs. Whilst current metal oxides used in this process perform well, various alternatives are sought in the interest of more efficient and effective clean hydrogen production.

This thesis is focused toward identifying potential metal oxides which are suited to the Steam-Metal Process. Low temperature methane reduction and clean hydrogen production from water oxidation are the primary focus, along with an investigation of promoter addition to enhance the redox process.

The literature review (**Chapter 2**) outlines current methods for hydrogen production and the potential shortcomings of these methods. The Steam-Iron Process is one method of hydrogen production that may address these shortcomings. Whilst the most widely utilised system for the Steam-Iron Process is iron oxide (Fe_3O_4), clean hydrogen production is impeded by catalyst deactivation through both sintering of reduced Fe metal and carbon formation stemming from use of carbon based reductants. Identification of alternative metal oxide systems that may fulfill a similar function to that of iron oxide without deactivation under similar circumstances are tentatively identified.

Based on thermodynamic assessment (**Chapter 3**) and information obtained from the literature review, potential metal oxides were assessed. A range of reactions using methane as a reductant and water as an oxidant over these metal oxide systems were analysed to develop experimental conditions best suited to achieving clean hydrogen production. It is sought to limit potential deactivation of selected metal oxides via addition of promoters to reduce sintering, stabilise metal oxide reduction, and limit carbon formation.

Chapter 4 outlines the experimental conditions employed for the redox system using a fixed bed reactor. The details of experimental method, catalyst preparation methods, catalyst testing and catalyst characterisation are all outlined in this chapter.

The reactivity of iron oxide (Fe_2O_3) was analysed with and without addition of CeO_2 and CeO_2/ZrO_2 as promoters (**Chapter 5**). Potential stabilisation of intermediate iron oxide (FeO) over multiple redox cycles resulting from addition of CeO_2/ZrO_2 is found.

Addition of this promoter also leads to increased reactivity for both reduction and oxidation cycles.

Chapter 6 outlines the addition of CeO_2/ZrO_2 promoters to SnO_2. This proves to be an unsuitable system for the Steam-Metal Process, due to the poor reducibility of both unpromoted and CeO_2/ZrO_2 promoted SnO_2 by methane.

Study of the CeO_2/ZrO_2 promoted WO_3 system shows that, stabilisation of the metal oxide during methane reduction at specific promoter concentration is achieved (**Chapter 7**). By limiting complete reduction to form W metal, reproducible clean hydrogen production over numerous cycles is possible, with minimised catalyst deactivation. Detailed kinetic analysis identifies the reaction process for both reduction and oxidation (**Chapter 8**). Subsequently, greater understanding of the kinetic controlling mechanisms enables optimisation of experimental conditions.

More detailed presentation of gas concentration calculations are outlined in **Appendix I**.

LITERATURE REVIEW

2.1 Introduction

The environmental impact of fossil fuel usage has resulted in damaging environmental effects, of which the most well known is global warming [1, 2]. The use of non-renewable carbon-based energy sources must be limited and eventually phased out, or we run the risk of irreparable damage to our ecosystem. At this time, only ~25% of energy consumption is based on carbon-free or 'green' energy. Despite the need to stem emissions, there exists an ever increasing demand for energy, and new energy solutions must be found which can overcome this problem. Investment made toward research and development in alternative clean fuels must compete with established technologies to be equally if not more cost effective. Taking this factor into consideration, the transition toward clean energy must be gradual, utilising current infrastructure and resources, such that it may remain competitive and relevant to today's economy.

Hydrogen is at the forefront of alternative fuels research as the prime candidate for replacing conventional fossil fuels provided methods can be found to generate hydrogen cheaply and efficiently. The gas can be generated from a broad range of methods, utilising any number of resources. The most heavily employed methods today involve extracting hydrogen from hydrocarbons including methane and longer chain fossil fuels. It is also possible to extract hydrogen from water using such methods as electrolysis but this is a highly inefficient process, coupled with a high energy cost for extraction. The studies described in this thesis are focused on one means of generating hydrogen.

2.2 Background

Hydrogen is a source of clean burning fuel, releasing heat and yielding water as a by-product from combustion, providing an ideal energy carrier.

$$2H_2 + O_2 \rightarrow 2H_2O \qquad \textbf{2.1}$$

In the long term, solar-based water decomposition to produce hydrogen is highly attractive for carbon-free hydrogen.

$$H_2O \rightarrow H_2 + \tfrac{1}{2}O_2 \qquad \textbf{2.2}$$

The feasibility of this route was first considered in the early 1970's by Wentorff and Hannerman [3], with high levels of interest generated and a number of papers published soon thereafter [4-10]. This is a highly endothermic reaction with temperatures of up to 4300K (4027°C) required for the reaction to proceed, as demonstrated by thermodynamic calculations. Whilst water splitting is achievable at lower temperatures, at ≥2500K (~2200°C) only ~25% conversion is achievable [11]. At high temperature, re-radiation losses become more predominant, resulting in process efficiency reaching a maximum before declining as temperature is systematically increased [12]. High temperature separation of H_2 and O_2 is difficult due to recombination of the products at even moderate temperatures, and the H_2 and O_2 mixture possessing a low limit of flammability [13].

Thermal water decomposition is highly inefficient and is made more difficult by these excessively high temperatures. In the short term hydrogen production from fossil fuels allows for the realisation of a hydrogen based economy, by more efficient utilisation of readily available resources and without implementing significant changes to current infrastructure [14]. In addition, hydrogen production at a central site offers the possibility of sequestration of greenhouse gases also produced in the conversion.

To this point, demand for hydrogen has been primarily as feedstock for use in various syntheses reactions, as well as for hydrotreatment in industrial processes. The shift in use of hydrogen as an energy carrier has led to a substantial increase in demand [15, 16]. Hydrogen production in the immediate future will depend on hydrocarbons as feedstock for economic reasons, utilising abundant reserves of natural gas. Hydrogen production from clean and/or renewable resources cannot be economically competitive for a number of years, requiring a great deal more research before the technology is mature. Current methods for hydrogen generation are designed for large scale industrial processes, due to the necessity for generating either large amounts of expensive steam (methane steam reforming) or generating clean oxygen separated from air (methane partial oxidation). When considering centralised hydrogen production, there is a high cost involved with building the necessary infrastructure for large scale transmission and utilisation combined with safety issues associated with hydrogen compression and transportation.

In the short term, hydrogen from hydrocarbons on a small to medium scale is the most viable option. This will allow for on-site and decentralised hydrogen production which can help to reduce distribution costs and potentially utilise cheaper materials and reactants. The Steam-Iron Process has significant potential to fulfill these needs, with the possibility for small scale hydrogen production from methane, as well as producing clean hydrogen without additional hydrogen purification steps. This process involves cyclic redox of metal oxides using methane and water to produce hydrogen in a two-step process.

$$Fe_3O_4 + 4CH_4 \rightarrow 3Fe + 4CO + 8H_2 \quad \textbf{2.3}$$

$$3Fe + 4H_2O \rightarrow Fe_3O_4 + 4H_2 \quad \textbf{2.4}$$

.

This review will introduce current methods of hydrogen generation from methane. This is followed by an assessment of the Steam-Iron Process in its current form, identification of potential metal oxides that are potentially suited for this process, as well as developments in metal oxide promotion to improve performance and limit deactivation.

2.3 Hydrogen from Methane

2.3.1 Steam Reforming

Steam reforming is currently the most widely utilised process at an industrial scale for the production of syngas. This process was first industrially implemented as early as the late 1800's for the purpose of producing syngas for both Fischer-Tropsch synthesis reactions and for the synthesis of liquid fuels [17]. The status of steam methane reforming as a mature technology makes it the most industrially important reaction for hydrogen production, with 90% of hydrogen production currently derived from steam reforming [18, 19]. A large number of carbon-based fuel sources are suitable feedstock in the steam reforming cycle but methane derived from natural gas is the most commonly used - due not only to its abundance, but also to the reduced coking produced by this lighter hydrocarbon, in comparison to other hydrocarbon types [20].

The endothermic steam methane reforming (SMR) reaction is favoured by high temperatures (700-950ºC) with low pressures, due to volume expansion of the system resulting from an increase in number of moles of gas from reactants to products. The high temperature water gas shift (HTS) and low temperature water gas shift (LTS) reaction follow the steam reforming reaction, and both are used to either alter the ratio of CO to H_2 ratio when producing syngas, or to produce more hydrogen whilst minimising the amount of CO in the product gas [16]. The reverse methanation reaction occurs spontaneously alongside the steam reforming reaction, resulting in excess production of CO_2 gas [21]:

SMR (700ºC-950ºC)

$$CH_4 + H_2O \rightarrow CO + 3H_2 \qquad \Delta H^\circ_{298} = +206 \text{ kJ/mol} \qquad \textbf{2.5}$$

HTS (350ºC-500ºC)

$$CO + H_2O \rightarrow CO_2 + H_2 \qquad \Delta H^\circ_{298} = -41 \text{ kJ/mol} \qquad \textbf{2.6}$$

LTS (200ºC)

$CO + H_2O \rightarrow CO_2 + H_2$ $\Delta H°_{298}$ = -41 kJ/mol **2.7**

Reverse Methanation

$CH_4 + 2H_2O \rightarrow CO_2 + 4H_2$ $\Delta H°_{298}$ = +165 kJ/mol **2.8**

In the final step, pressure swing adsorption (PSA) is used for removal of CO and CO_2 to produce clean hydrogen gas. Actual operating temperatures of steam reforming are largely dependant upon maximising the desired product gas. To maximise the amount of hydrogen in the product gas stream, the exothermic WGS reaction is operated at lower temperatures, favouring high conversion of CO to form greater amounts of H_2. Favourable catalysts for the steam reforming reaction include $Ni/MgAl_2O_4$ and $Ni/CaAl_2O_4$. Stoichiometric ratios of H_2O/CH_4 cannot be used due to carbon formation below a critical ratio and increasing carbon formation with temperature [22]. Therefore, the ratio of H_2O/CH_4 lies somewhere between 2-5, with the excess steam in the feedgas limiting carbon formation by gasification of adsorbed carbon (**Equation 2.9-2.10**):

$H_2O + C \rightarrow CO + H_2$ **2.9**

$2H_2O + C \rightarrow 2H_2 + CO_2$ **2.10**

Higher ratios of steam favours production of hydrogen, resulting from a shift in the thermodynamic equilibrium toward the reactants. However, at low temperatures and low activity the catalyst is prone to deactivation by oxidation with this higher ratio of steam. The steam reforming catalyst is only active in the metallic state and once it is oxidised, the oxide form must be reduced to retain activity. This is especially the case when using nickel catalysts. At lower temperatures there is limited activity and insufficient conversion of methane, which results in low levels of reducing H_2 with high levels of oxidizing H_2O.

2.3.2 Dry Reforming

Dry reforming does not require generation of expensive heated H_2O, unlike steam reforming, utilising cheap and widely available CO_2. The dry reforming reaction uses methane which is reacted with CO_2 gas in the presence of a catalyst, producing CO and H_2 in a ratio of 1:1 [22].

$$CO_2 + CH_4 \rightarrow 2CO + 2H_2 \qquad \Delta H°_{298} = +247 \text{ kJ/mol} \qquad \textbf{2.11}$$

This reaction is accompanied by the reverse water-gas shift reaction (RWGS), resulting in production of excess amounts of CO:

$$CO_2 + H_2 \rightarrow CO + H_2O \qquad \Delta H°_{298} = +41 \text{ kJ/mol} \qquad \textbf{2.12}$$

Rhodium and ruthenium noble metal catalysts demonstrate high activity for the dry reforming reaction, with no observed carbon formation [23]. Whilst nickel catalysts traditionally used in the steam reforming reaction are also active for the dry reforming reaction, rapid deactivation via carbon deposition is observed. There is a marked decrease in the rate of reforming observed for the dry reforming reaction in comparison to steam reforming. This could be explained by the increased ratio of CO formed, resulting in higher levels of coking from the Boudouard reaction (**Equation 2.13**) and more rapid catalyst deactivation [23].

$$2CO \rightarrow C + CO_2 \qquad \Delta H°_{298} = -172 \text{ kJ/mol} \qquad \textbf{2.13}$$

Addition of TiO_x demonstrates an increased activation barrier for the CO dissociation reaction, inhibiting carbon formation by blockage of active sites at which carbon deposition may occur. MgO is also used to react with Ni to form a solid solution, aiding in prevention of carbon dissolution into the nickel crystal [24]. Ceria has demonstrated unique properties in being able to oxidise carbon species to regenerate the catalyst and

prevent deactivation even at low temperatures [25]. Ceria as a catalyst has proven highly effective [26], and ceria as a promoter has demonstrated not only increased catalytic stability, but also enhanced prevention of catalyst coking by the removal of adsorbed carbon species [27, 28].

2.3.3 Partial Oxidation / Oxyreforming

Partial oxidation can proceed by both catalytic and non-catalytic means but the high temperature requirement for the non-catalytic partial oxidation and the tendency for carbon formation have shifted focus toward catalytic methods. On the outset, partial oxidation looks to be more energy efficient than reforming processes, being slightly exothermic, unlike the highly endothermic steam reforming process [29]. Methane is reacted with pure oxygen to produce H_2 and CO in a ratio of 2:1.

$$\tfrac{1}{2}O_2 + CH_4 \rightarrow CO + 2H_2 \qquad \Delta H^\circ_{298} = -38 \text{ kJ/mol} \qquad \textbf{2.14}$$

This process requires a supply of pure oxygen which, when produced by air separation units, can account for up to 40% of expenditure in the partial oxidation plant. In contrast, steam reforming has been shown to be far more economical and efficient, resulting in a period of disinterest in partial oxidation research for a number of years. More recently, the increasing demand for fuel and syngas has led to renewed research into this field.

Research initially conducted by Prettre et al. [30] demonstrated that despite the exothermic nature of the reaction, high temperatures of >850°C were required to obtain a substantial yield of H_2. Reactor temperatures are generally in the range of ~1300K (1027°C) to prevent carbon deposition, with very short contact times between catalyst and reactants. Products of the reaction include not only H_2 and CO, but also CO_2 and H_2O in smaller amounts. Product selectivity is difficult to control, and whilst H_2 and CO are desired, complete oxidation of CH_4 results in the production of CO_2 and H_2O, thus the need for high temperatures to better control selectivity for CO [31]. Stoichiometric ratios

favour high selectivity of syngas in a ratio of 2:1 but a decrease in reactant ratio tends toward total combustion of reactants, producing both carbon dioxide and water, whilst an increase in ratio results in lower methane conversion. In the instance of complete oxidation, further reactions become of importance, including steam reforming and the water gas shift reaction. Introduction of H_2O to the partial oxidation reaction results in greater conversion of methane as well as mitigating formation of surface carbon species [15]. At higher pressures, complete oxidation tends to be favoured, resulting in production of carbon dioxide and water, rather than carbon monoxide and hydrogen [29].

In order to produce pure hydrogen from partial oxidation, methanation of the product is used to re-form CH_4 and H_2O, such that all carbon monoxide is removed to prevent contamination of fuel cells and catalysts [32].

Noble metal catalysts demonstrate high affinity for the partial oxidation reaction by increasing product selectivity and providing better resistance to catalyst deactivation by coking [33, 34]. Addition of rare earth oxides limits carbon formation, where it was found that high conversion of CH_4 to synthesis gas is possible with minimal contact time, mitigating the formation of carbonaceous species [35, 36]. The short contact time with the catalyst not only produces decreased coking effects in comparison to reforming reactions, but also limits the effects of catalyst sintering. Despite their appeal, use of noble and rare earth metal catalysts is generally cost prohibited in industrial scale catalysis. The general consensus is that cheaper nickel supported catalysts are most active for production of syngas [29, 37-41].

2.3.4 Autothermal Reforming

Autothermal reforming combines both steam reforming and non-catalytic partial oxidation to create a more efficient process. Utilisation of heat from the exothermic partial oxidation reaction is used in the subsequent steam reforming reaction for the generation of syngas and/or hydrogen. The process was developed in the 1950's by

Haldor Topsoe as a self contained process for conversion of hydrocarbons to syngas/hydrogen within a single reactor [42].

The autothermal reactor consists of a feed preheat sector, reactor and a gas separation unit. The feed introduced into the reformer is generally a mixture of $CH_4 + H_2O$ and $CH_4 + O_2$ where, at the top of the reactor, methane is initially combusted using O_2 in a partial oxidation reaction for the production of CO, H_2O and heat using temperatures in excess of 2000K (~1700°C). Further down the reactor, CO and H_2 are combined with steam in a reforming reaction for production of hydrogen and/or syngas in precise ratios, with temperatures of around ~1500K (~1200°C) [43].

Combustion zone:

$$CH_4 + \tfrac{3}{2}O_2 \rightarrow CO + 2H_2O \qquad \Delta H°_{298} = -520 \text{ kJ/mol} \qquad \textbf{2.15}$$

Catalytic zone:

$$CH_4 + H_2O \rightarrow CO + 3H_2 \qquad \Delta H°_{298} = -206 \text{ kJ/mol} \qquad \textbf{2.16}$$

$$CO + H_2O \rightarrow CO_2 + H_2 \qquad \Delta H°_{298} = -41 \text{ kJ/mol} \qquad \textbf{2.17}$$

The advantage of autothermal reforming is the requirement for less O_2 of lower purity, which is one of the biggest expenditures in the partial oxidation reaction. The reaction is able to proceed at lower temperature than the partial oxidation reaction alone, reducing process cost. Whilst there is less flexibility in feedstock availability for autothermal reforming when compared to partial oxidation, the range of available feedstock still exceeds that of steam reforming.

Catalysts used in the steam reforming reaction have also demonstrated high affinity for autothermal reforming, with noble metal and suitably supported nickel catalysts retaining high activity for the latter process [43-45]. However, Ni catalysts are prone to oxidation due to the presence of oxygen and steps must be taken to avoid this. The lower selectivity of feedstock requires autothermal reforming catalysts are able to process ‘dirtier’ and are less susceptible to carbon deposition [46].

2.3.5 Catalytic Decomposition

Carbon monoxide and dioxide emissions are an undesirable by-product of the reforming and partial oxidation processes for hydrogen production. Sequestration of CO_2 is an option, but product gas still requires stringent processes for removal of carbon monoxide prior to its use in hydrogen fuel cell applications. Catalytic decomposition of methane is a method for eliminating carbon oxide emissions completely [47]. This process can proceed by either catalytic or non-catalytic means, with the prospect of producing carbon that is easily separated from hydrogen [48].

$$CH_4 \rightarrow C + 2H_2 \qquad \Delta H^\circ_{298} = +75.6 \text{ kJ/mol} \qquad \textbf{2.18}$$

Non-catalytic decomposition of methane requires high temperatures, with direct decomposition requiring temperatures upward of 1800K (~1500°C). This process is ultimately impeded by formation of carbon deposits on the interior of the reactor, eventually leading to overheating by reactor blockage. Potential catalysts have been found for this reaction, notably by Muradov et al., who are focused toward producing CO-free hydrogen [48, 49]. Transition metal catalysts such as Fe and Ni have demonstrated high affinity for the methane decomposition reaction [50, 51]. Despite higher catalytic activity observed at higher temperature, the resultant increase in carbon deposition facilitates rapid catalyst deactivation. Therefore, effective and efficient removal of surface carbon is required for improved catalyst performance and sustained hydrogen production. By controlling the type of carbon produced at the surface, stable catalyst activity is observed over a longer period of time [52, 53], and this can be controlled by use of various catalyst supports. Formation of filamentous carbon is less harmful than encapsulating carbon, which is known to block active sites and results in catalyst deactivation. It is also possible to catalyse formation of carbon nanotubes and/or nanofibres on Ni based catalysts, which are a useful by-product that can be later separated [54, 55]. Use of appropriate support materials such as SiO_2 and Nb_2O_5 can also retard catalyst deactivation [56, 57].

Some amount of CO and CO_2 formation will result from the use of metal oxide catalysts due to oxidation of deposited carbon by the oxide support [58]. The amount of CO_2 produced by the decomposition reaction was observed to be far less than CO_2 produced during the process of steam reforming. For limiting or eliminating CO_2 based emissions, catalytic methane decomposition is the most effective means of generating hydrogen from hydrocarbons [48]. However, this process is not sustainable, largely due to the aforementioned reason of catalyst deactivation.

In an effort to overcome this problem of carbon deposition associated with transition metal oxide catalysts, carbon based catalysts are another option which has been investigated [59]. Activation energy for this reaction is slightly higher when using active carbon catalysts compared to metal oxides. The rate of carbon formation during this reaction is high and frequent purging of the catalyst is a significant factor to retaining catalytic activity over a number of cycles, resulting in carbon oxide emissions which arise during the gasification and/or oxidation process [48, 60]. With the specific formation of carbon black at the surface of catalytically active carbons, rather than using gasification or oxidation for removal of carbon, a fluidized bed mechanism can be used for circulating active carbon particles, alleviating the effects of carbon buildup and blockage of active sites [61].

2.3.6 Catalyst Deactivation

A challenge faced with hydrogen generated from methane is the formation of unwanted carbon deposits, resulting in catalyst deactivation. Ni catalysts have high activity for industrial processing of methane, but they tend to promote much higher levels of coke formation [62]. Different manufacturers use various additives to promote coke gasification. The main reactions contributing to formation of coke include [22]:

$$CH_4 \rightarrow C + 2H_2 \qquad \Delta H^\circ_{298} = +75 \text{ kJ/mol} \qquad \textbf{2.19}$$

$2CO \rightarrow C + CO_2$ $\Delta H°_{298}$ = -172 kJ/mol **2.20**

$CO + H_2 \rightarrow C + H_2O$ $\Delta H°_{298}$ = -131 kJ/mol **2.21**

$C_nH_m \rightarrow (CH_2)_n$ (gum) **2.22**

$C_nH_m \rightarrow olefins \rightarrow coke$ **2.23**

Carbon can be formed as 'gum' carbon (**Equation 2.22**), pyrolytic carbon/coke (**Equation 2.23**) and whisker carbon (**Equation 2.19-2.21**). Gum formation is favoured at lower temperatures, resulting from adsorbed long chain hydrocarbons being converted to a polymer film which deposits itself upon the catalyst surface causing deactivation. Formation of pyrolytic coke is promoted at high temperatures by the pyrolysis of long chain hydrocarbons. This results in the deposition of coke at the surface and eventual encapsulation of the catalyst to cause deactivation. Whisker carbon is the predominant form of carbon resulting in catalyst deactivation. This is initiated by dissolution of adsorbed surface carbon into the substrate, which nucleates as a whisker and diffuses through the particle destroying the catalyst structure. These carbon fibres then precipitate out at the surface, resulting in lifting of catalyst particles from the surface. Whilst this does not affect catalyst activity to a significant degree, the lifting of particles does results in eventual reactor blockage due to the breaking up of the catalyst.

Another form of carbon formed at the catalyst surface is graphitic carbon. This is produced by decomposition of CO and/or CH_4, allowing for the nucleation of carbon at the energetically favourable step sites and surface defects. Graphene can form and propagate out from this step to form graphene islands and block active sites by surface coverage.

Smaller particle size has been observed to retard carbon formation [63]. In addition, smaller particle size impedes the migration of dissolved carbon through the substrate for the formation of whisker carbon. Sintering has a promoting effect upon sample coking, given that larger particle sizes and larger pore sizes from sintering allow for easier carbon diffusion through the catalyst. A catalyst support aids in maintaining dispersion of the catalytically active phase and increases stability of the catalyst, and generally acts to retard catalyst deactivation.

The addition of promoters can also act as an effective aid in this regard. This is achieved by enhancing adsorption of reactants and increasing rate of reaction, whilst decreasing the rate of methane decomposition, thereby preventing carbon formation. Besides increasing catalytic surface area and retarding deactivation, promoters can also actively participate in the reaction process, such as by increasing dissociation of H_2O at oxide sites to expedite the reaction process. Use of high oxygen capacity supports can aid in preventing buildup of coke at the surface by oxidizing adsorbed carbon.

2.3.7 Summary

Current methods for hydrogen production stem primarily from methane. Such methods include steam methane reforming, dry methane reforming, methane partial oxidation, methane autothermal reforming and methane catalytic decomposition. These processes are suited toward large scale industrial production of hydrogen due to generation of large amounts of expensive steam for methane steam reforming, or generation of pure oxygen for methane partial oxidation, these being the most widely employed processes for hydrogen production today. The hydrogen produced via these processes must also be separated from carbon oxides and undergo stringent purification.

Use of Ni catalysts in methane based hydrogen production processes is highly favoured, but also tends to promote high levels of coking. Catalyst deactivation results from carbon formation, with various types of carbon formed which may act to block active sites or facilitate structural degradation of the catalyst over time. The limitations of current hydrogen production technologies include hydrogen separation and storage combined with the economic limitations of large scale hydrogen production and transportation. In light of these issues, the Steam-Iron Process has been identified as a potential means of fulfilling hydrogen production needs on a smaller scale, allowing for hydrogen to be stored in a relatively innocuous form and generated cleanly from steam at lower temperatures.

2.4 Steam-Iron Process

2.4.1 History

The first successful implementation of the Steam-Iron Process on a commercial scale was demonstrated by Lane as early as 1903 [64]. Approximately 10 years later, Messerschmitt introduced an improved design which was subsequently implemented due to reduced operating cost [65]. The basic process involved the reduction of iron oxide to form iron by passing over a reducing gas generated by steam gasification of coke, followed by re-oxidation using steam for the production of hydrogen. The process is able to be repeated indefinitely provided complete re-oxidation can be achieved and metal oxide deactivation does not occur.

$$Fe_3O_4 + 4CO / H_2 \rightarrow 3Fe + 4CO_2 / H_2O \qquad \textbf{2.24}$$

$$3Fe + 4H_2O \rightarrow Fe_3O_4 + 4H_2 \qquad \textbf{2.25}$$

Whilst **Equation 2.24** and **Equation 2.25** above depict reduction of magnetite to iron metal and subsequent re-oxidation to form magnetite, there are numerous possible oxidation states of iron oxide:

$3Fe_2O_3$ (hematite) → $2Fe_3O_4$ (magnetite) → 6FeO (wustite) → 6Fe (iron)

Reduction of Fe_2O_3 by CO or H_2 does not yield FeO due to its thermodynamic instability, where below approximately 570ºC the formation of FeO is not formed [66, 67]. The reduction pathway proceeds from $3Fe_2O_3 \rightarrow 2Fe_3O_4$, followed by $2Fe_3O_4 \rightarrow 6Fe$. At higher temperatures, the reduction of Fe_2O_3 shifts to allow reduction of $2Fe_3O_4 \rightarrow 6FeO$, followed by reduction of $6FeO \rightarrow 6Fe$ [68]. Re-oxidation of Fe_3O_4 by water to form Fe_2O_3 is thermodynamically unfavourable.

It was not until 1976 that the process was further developed by Tarman *et al.* [69-71], utilising gasified coal as a reductant. The problem with utilising gasified coal products is the high level of sulphur impurities present in coke along with carbon deposition from carbon monoxide decomposition [72]. With repeated cycling, accumulation of these impurities contaminates the hydrogen product, as well as causing deactivation of the iron oxide.

The Steam-Iron Process has been well documented as a method for hydrogen production and as a means for storage of hydrogen generated by other processes, in the form of syngas (CO + H_2) [73-79]. This process has a distinct advantage over current processes for hydrogen production, including steam reforming and partial oxidation, as it facilitates pure hydrogen production in a two step process, independent upon purity of the reducing gas. Syngas used in the Steam-Iron Process is derived from coal, biomass and steam reforming and/or partial oxidation of methane.

The use of methane is a relatively recent introduction to the Steam-Iron Process, which allows for the intermediate step of generating syngas from methane as a reductant to be eliminated. Methane is a much cleaner burning fuel than coal derived products, leading to decreased greenhouse gas emissions, with potential production of useful synthesis gas [80]. The introduction of methane in the Steam-Iron Process was initially proposed by Steinfeld et. al. [68, 81], with further in depth investigation of reduction of modified iron oxide using methane undertaken by Takenaka et. al. [82-84].

$$Fe_3O_4 + 4CH_4 \rightarrow 3Fe + 4CO + 8H_2O \qquad \textbf{2.26}$$

More recently, Hacker *et al.* have proposed the implementation of a reformer sponge iron cycle (RESC) in the Steam-Iron Process [73, 74, 85-87]. This method improves on previous SIR designs by better circulation of iron catalyst to prevent sintering and better cycling of the catalyst, with use of cheaper sponge iron. In addition, combining the Steam-Iron Process together with reforming allows for utilisation of a much wider range

of feedstock, and the production of high quality syngas to be used for the reduction reaction [85-87]. This in turn gives better reduction of the iron oxide and by doing so, increases catalyst lifetime and efficiency significantly. Product gases from the reduction reaction can be recycled, enabling CO and CO_2 produced to be re-fed to the reformer, reducing emissions.

2.4.2 Promotion of the Steam-Iron Process

Improvements to the Steam-Iron Process can be made by mitigation of sintering to increase metal oxide stability and prevent deactivation and by improving kinetic activity. Process temperatures are limited due to sintering at higher temperature, yet kinetic activity is directly proportional to temperature. Therefore, it is necessary to add promoters that may increase kinetic activity at lower temperature and/or to maintain metal oxide stability at higher temperature in order to mitigate sintering.

Kodama et. al. reported on the reduction of metal ferrites, with metals comprising Mg, Mn, Ni, Zn and In [88]. In-FeO_x showed the highest activity and selectivity for the reduction reaction, with high levels of H_2 production from water oxidation as compared to magnetite alone. Ni-FeO_x supported on ZrO_2 showed high selectivity for CO production from methane reduction, with clean hydrogen production in the oxidation reaction [89].

Takenaka et. al. have performed an extensive study of the addition of a wide range of metal and metal oxide promoters to iron oxide [79, 82]. Reports indicate that noble metals, specifically Rh and Ir, markedly enhance redox activity but these metals are unable to prevent sintering. The addition of other metal elements including Mo, Cr, Al, Zr, Ga, V and Ti prevent iron oxide sintering over numerous cycles. This resulted in maintaining catalytic surface area approximately 10 times higher than unmodified iron oxide with repeated cycling, whilst achieving reduction temperatures as low as 770K (500°C) [90]. It was concluded that the addition of both Rh to enhance reactivity and

another metal support such as Mo was necessary to improve the process [91]. Further investigation found that Cu and Ni could also increase redox activity of iron oxide but enhanced sintering of iron oxide was observed [83, 84, 92]. Co-addition of Cr in these systems is necessary to maintain metal oxide dispersion and mitigate sintering. Cu, Ni and Rh are present in the metallic form, whereas, Cr forms an oxide. Park et. al. also reported Cu to both enhance reduction kinetics and to decrease reduction temperature, whilst preventing iron carbide and graphite formation during methane reduction [93].

Addition of rare earth oxides such as ceria can enhance the redox reaction due to high oxygen storage capacity coupled with the ability to rapidly donate and release oxygen from the lattice. The promoting effect of ceria upon iron oxide for methane oxidation has been reported by Kang and Wang [94], along with reports by Huang et. al. attesting to the positive effect of ceria addition upon CO oxidation [95]. Addition of ceria shows high activity and increased stability of iron oxide over numerous cycles [96], with addition of zirconia further enhancing these effects [97, 98]. The presence of ceria as a promoter is known to participate in removal of adsorbed surface carbon as a result of oxidation by lattice oxygen species of ceria [99]. Use of zirconia enhanced ceria has shown favourably to increase catalytic activity whilst limiting the degree of carbon deposition at the catalyst surface, more so than ceria alone [98].

Addition of supporting oxides such as Al_2O_3, TiO_2, ZrO_2 and SiO_2 are used for mitigation of sintering at high temperature. Addition of ZrO_2 can maintain iron oxide stability at temperatures as high as 1600ºC, as observed from thermochemical decomposition of ZrO_2 supported iron oxide in a hydrogen production cycle [100, 101]. Interestingly, it has been reported by Kodama et. al. that the addition of SiO_2 as a support showed selective formation of C_2 hydrocarbons from methane oxidation [102].

2.4.3 Thermodynamic and Kinetic Studies of the Steam-Iron Process

By initial assessment of thermodynamics for both the reduction and oxidation of various metal oxides in the Steam-Iron Process, reaction products and metal oxide formation can be predicted based upon reaction conditions. A more detailed study of redox thermodynamics is presented later in **Chapter 4**. Plotting change in change in Gibbs Free Energy as a function of temperature can predict the thermodynamic likelihood of the reaction proceeding [103, 104].

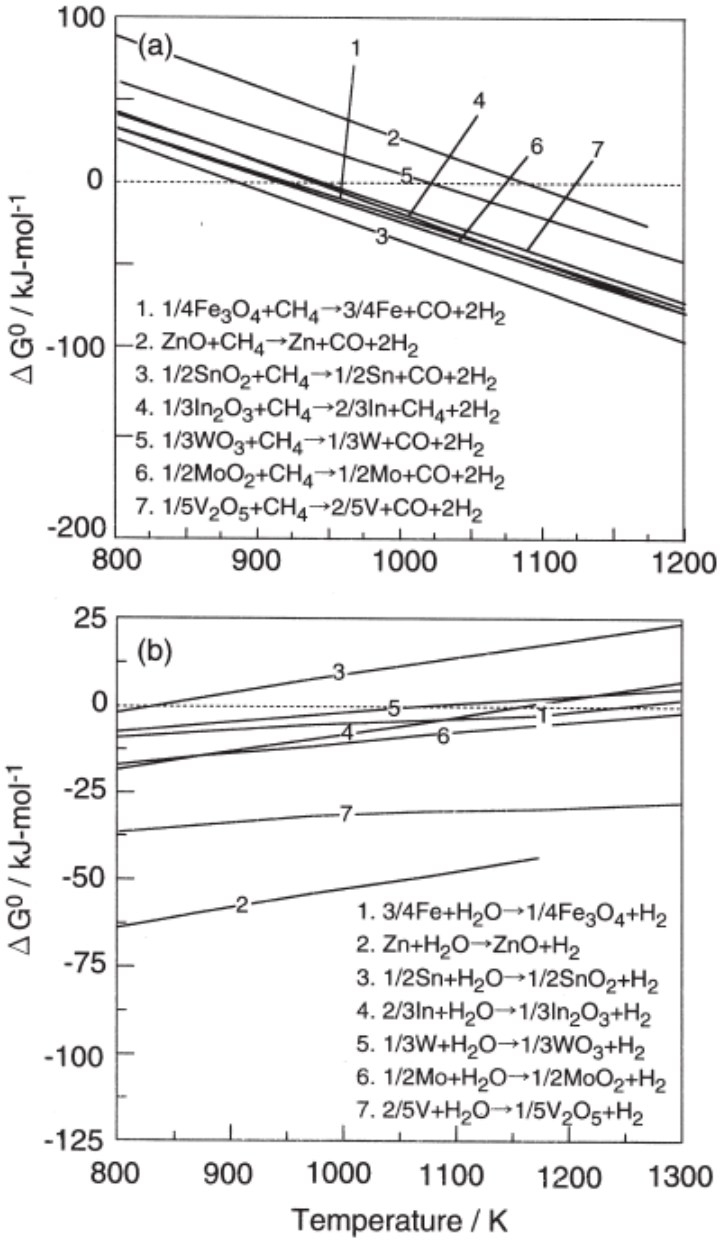

Figure 2.1 Variations in ΔG° for the reactions (a) $1/yM_xO_y+CH_4 \rightarrow CO+2H_2+x/yM$ and (b) $x/yM+H_2O \rightarrow H_2+1/yM_xO_y$ with temperature for the metal oxide, redox pair candidates [105]

Thermodynamics of iron oxide reduction by carbon based reductants predicts both carbon formation by methane decomposition at high temperature and also iron carbide formation, with the possibility of CO decomposition from the product gas [106]. Careful management of the incoming gas stream and temperature control is necessary to favour iron oxide formation and exclusion of unwanted products. Xin et. al. present equilibrium composition data calculated based on minimisation of Gibbs Free Energy, which indicates high methane to iron oxide ratios favours both partial oxidation and carbon formation following complete reduction to metallic iron, whilst maximising the ratio of iron oxide to methane tends incomplete reduction and formation of lower iron oxidation states [107].

A Baur-Glaessner plot based upon CO + H_2 reduction of iron oxide also suggests formation of different oxidation states of iron is largely dependent on both temperature and H_2/CO ratio [73], with the formation of FeO as an intermediate state in the reduction of Fe_3O_4 to Fe bypassed completely at lower temperature. A thermodynamic study of the RESC conducted by Hacker et. al. suggests that a reduction temperature of 800ºC is the upper limit for this process, with further increasing temperature showing negligible change in conversion efficiency [108]. Theoretically, up to 75% conversion of hydrocarbon reductants can be achieved.

Thermodynamics of oxidation by water is relatively easily examined, with the possible formation of only H_2 from H_2O. **Figure 2.1** shows the high temperature reduction reaction to be the rate limiting step of the Steam-Iron Process, with the oxidation reaction favoured at lower temperatures for most metal oxides examined. However, despite being thermodynamically favourable, the oxidation process is often kinetically limited and proceeds too slowly at very low temperatures.

The kinetics of iron oxide reduction have been studied extensively via the method of hydrogen temperature programmed reduction (TPR) [66, 67, 109, 110]. These results reflect predicted thermodynamics, with reduction of Fe_2O_3 at lower temperature

proceeding in a two-step process from Fe_2O_3 to Fe_3O_4 followed by Fe_3O_4 to Fe. The formation of FeO is not observed except at high temperature [68]. There exists a large degree of discrepancy between reported values for apparent activation energy of iron oxide reduction, as well as the specific mechanism governing the reduction process. Some reports indicate that random nucleation according to the Avrami-Erofeyev model to be the governing kinetic model, whilst others suggest the reaction is phase boundary controlled. The particle size and reaction conditions such as flow rate and ramping rate play a large part in governing reduction kinetics. The kinetics of the reduction of promoted iron oxide has also been examined for $Ce_{0.5}Zr_{0.5}O_2$ promoted Fe_2O_3 by Galvita et. al. [111]. Formation of Ni and Cu based ferrites show greater reaction rate upon reduction [112].

In comparison to reduction kinetics, detailed reports of oxidation kinetics of iron oxide are limited. Analysis of the oxidation of Fe_2O_3 undertaken by Herguido et. al. shows application of the Johnson–Mehl–Avrami–Kolmogorov (JMAK) model, based on a random nucleation method, adequately describes oxidation kinetics [113]. Steam partial pressure and temperature are determined to be independent of oxidation reaction rate. Oxidation kinetics of molten reduced iron oxide (FeO) following thermochemical decomposition of Fe_2O_3 at high temperature is governed by diffusion, following rapid oxidation of the particle surface [114]. Kim et. al. report oxidation of Mn and Zn modified ferrites are also controlled by diffusion processes in a first order reaction [112]. Higher reaction rate and lower temperature oxidation are observed, compared to oxidation of unpromoted iron oxide.

2.4.4 Suitable Alternative Metal/Metal Oxide Systems

A number of papers assessing the feasibility of a wide range of metals to be used for the Steam-Iron Process has been published [115-118]. Testing of metal oxide systems for the Steam-Iron Process reveals that low reduction temperature is often coupled with limited hydrogen yield upon subsequent oxidation with water. The reverse is also true, in that for

metals which demonstrate favourable hydrogen generation at lower temperature from water oxidation also show a temperature of reduction that is prohibitively high. Therefore, by thermodynamic assessment, a wide range of metals have been eliminated on the basis of either temperature of reduction or limited hydrogen yield. Subsequently, metal oxides which have been identified as potential Steam-Iron Process candidates from thermodynamic analysis include Fe_3O_4, ZnO, SnO_2, In_2O_3, WO_3, CeO_2, MoO_2, V_2O_5, Nb_2O_5 and GeO_2. A number of these identified metal oxides have been experimentally tested in a Steam-Iron type process.

Zn/ZnO

Following iron oxide, zinc oxide has been the most extensively investigated, with a large amount of work undertaken by Steinfeld et. al. in relating to zinc oxide for use in hydrogen production via a redox cycle [119-121]. The interest in zinc oxide stems primarily from the possibility for relatively low temperature thermochemical decomposition of ZnO to Zn, thereby eliminating the presence of carbon in the redox cycle. Use of methane as a reducing agent further reduces reduction temperature as reported by Steinfeld et. al. [121-125].

$$ZnO + CH_4 \rightarrow Zn + CO + 2H_2 \qquad \textbf{2.27}$$

$$Zn + H_2O \rightarrow ZnO + H_2 \qquad \textbf{2.28}$$

Thermodynamic analysis suggests that use of a solar reactor combined with flow of methane gas will enable yields of up to 90% Zn from ZnO to be achieved [126]. Due to the low melting point of metallic zinc and the high temperature of reduction, the formation of gaseous zinc is a possibility, requiring quenching for the condensation of liquid zinc. This is to prevent both recombination of Zn and O_2, as well as to allow for zinc to be separated from gaseous CO and H_2 before it can be oxidised by steam. The

quenching of zinc represents a high energy loss, given that the heat from this reaction is wasted and unable to be recycled for the lower temperature oxidation reaction. Limited research has demonstrated the possibility for oxidation of zinc to form hydrogen from water by bubbling of steam through a solution of molten metal [127].

The rate limiting step of the reaction process is the diffusion of products through the zinc oxide film formed at the surface of the zinc particles. Synthesis of ZnO nanoparticles has demonstrated increased reaction rates and complete reduction of ZnO to Zn as well as oxidation of Zn to ZnO due to the high surface to volume ratio of these particles and faster diffusion through the surface film [121]. Addition of previous metals such as Rh and Pt have shown to increase water re-oxidation reaction rates by up to 600 times compared to the negligible rate of hydrogen production observed for re-oxidation of unpromoted ZnO [128]. In any reaction process in which the final zinc product ultimately undergoes melting, the addition of promoters may prove useless, given that - after one cycle - the promoters will inevitably precipitate out from solution.

SnO_2/SnO_x

Similarly to zinc oxide, investigation of tin oxide is focused toward a carbon free thermochemical cycle, wherein tin oxide is thermally decomposed before being re-oxidised by water to produce hydrogen [129, 130]. Oxidation of reduced tin oxide and/or tin metal with water shows high reactivity for hydrogen production [130-132]. Thermodynamic calculations demonstrate the feasibility of methane use for reduction of SnO_2, proceeding at temperatures >1000ºC [133].

$$SnO_2 + (2-x)CH_4 \rightarrow SnO_x + (2-x)CO + 2(2-x)H_2 \qquad \textbf{2.29}$$

$$SnO_x + (2-x)H_2O \rightarrow SnO_2 + (2-x)H_2 \qquad \textbf{2.30}$$

Despite favourable thermodynamics of the above reaction, reduction of SnO_2 alone by methane shows limited activity, with removal of only weakly bonded surface oxygen species and no observable reduction of lattice SnO_2 oxygen in the bulk. Subsequent re-oxidation by water yields negligible hydrogen, and it is necessary to achieve complete reduction of bulk oxygen species. Addition of Fe and/or Cr to SnO_2 to create a composite oxide shows high activity for methane oxidation and increased resistance to thermal sintering [134-136]. Addition of alkali earth metals to create tin based oxides doped with Bi has shown the capability for selective oxidation of methane to produce C_2 hydrocarbons [137]. Kodama et. al. also show the addition of Fe_3O_4 and SiO_2 to SnO_2 to have a similar effect when reducing using methane with a co-feed of water [138].

For deep reduction of SnO_2 by methane, the addition of promoters is required. The low temperature melting point of unpromoted Sn metal is also a limiting factor in this system, making addition of support oxides to maintain SnO_x stability a necessity.

In_2O_3/In

A significant amount of work has been compiled by Otsuka et. al. regarding hydrogen production by redox of indium oxide [139-142]. Whilst this initial work focused primarily upon reduction of indium oxide via H_2, C and CO, later work included reduction of indium oxide by methane for the CO_2 free production of hydrogen [143]. Addition of promoters to results in higher hydrogen yield upon re-oxidation by water, whilst showing efficient reduction [144-146].

$$In_2O_3 + 3CH_4 \rightarrow 2In + 3CO + 6H_2 \qquad \textbf{2.31}$$

$$2In + 3H_2O \rightarrow In_2O_3 + 3H_2 \qquad \textbf{2.32}$$

The bulk of this work was performed over two decades ago, with only recent studies to determine the suitability of methane used in the reduction process. A primary reason for this is likely to be the low melting point of indium metal, which results in extensive sintering or complete melting of the catalyst following reduction, with evaporation of indium at high temperature remaining a problem. Over numerous cycles catalyst functionality would rapidly decline and, from an economic standpoint, the requirement for constant catalyst regeneration coupled with the high cost of indium is a significant drawback to this process.

WO_3/WO_x

Kodama et. al. have reported testing of WO_3/W in a Steam-Iron type process, whereby, WO_3 was reduced by methane with high selectivity for CO and H_2 formation [105, 147, 148]. Addition of ZrO_2 improved process reactivity for both reduction and oxidation, due to formation of smaller more well dispersed particles of WO_3 on ZrO_2. This study demonstrated the possibility of partial reduction to form WO_2, and re-oxidation of WO_2 by water to WO_3 [147]. Complete reduction of unpromoted WO_3 to W formed WC, which was subsequently unable to be re-oxidised to WO_3 [148].

$$WO_3 + CH_4 \rightarrow WO_2 + CO + 2H_2 \quad \textbf{2.33}$$

$$WO_3 + 3CH_4 \rightarrow W + 3CO + 6H_2 \quad \textbf{2.34}$$

$$WO_2 + 2CH_4 \rightarrow W + 2CO + 4H_2 \quad \textbf{2.35}$$

$$W + 2H_2O \rightarrow WO_2 + 2H_2 \quad \textbf{2.36}$$

$$WO_2 + H_2O \rightarrow WO_3 + H_2 \quad \textbf{2.37}$$

$$W + 3H_2O \rightarrow WO_3 + 3H_2 \quad \textbf{2.38}$$

WO_3/WO_x is a promising candidate for hydrogen production in a Steam-Iron type process, with methane reduction temperatures comparable to iron oxide. The high molecular weight of W may prove to be a limitation in hydrogen production, given the low oxygen to metal ratio as compared to other such candidates as iron oxide.

CeO_2/Ce_2O_3

Ceria (CeO_2) as a catalyst demonstrates unique oxygen storage properties, which can be attributed to an ability to retain its lattice structure, following reduction and removal of lattice oxygen to form oxygen lattice vacancies [149, 150]. This enables faster reduction and oxidation, making this an ideal choice to use in redox reactions for the storage and release of oxygen. A significant amount of work has been published by Trovarelli *et al.* pertaining to the catalytic properties of ceria [25, 99, 149-152].

From the early 1980's, a series of papers published by Otsuka et. al. identified a number of potential metal oxides for hydrogen production via a redox cycle, with ceria showing favourable reactivity for further investigation [115, 144, 153-155]. The unique properties of ceria as a catalyst, such as its high affinity for the oxidation of hydrocarbon species, led to use of methane for the low temperature reduction of ceria in the production of syngas [155-157].

$$2CeO_2 + CH_4 \rightarrow Ce_2O_3 + CO + 2H_2 \qquad \textbf{2.39}$$

$$Ce_2O_3 + H_2O \rightarrow 2CeO_2 + H_2 \qquad \textbf{2.40}$$

It has been demonstrated, that, despite sintering of ceria over a number of reduction/oxidation cycles and subsequent reduction in surface area, the reaction rate is observed to remain constant over time. Thus, it is suggested that the active sites may not be uniformly distributed across the surface, and that the reduction rate is not wholly

dependant upon available surface area [149]. Following reduction and oxidation of the ceria-zirconia solid solution over a number of cycles, the reduction temperature is actually observed to decrease by almost 200°C, a remarkable trait in contrast to expected behaviour [158].

Use of promoters for enhancing the catalytic properties of ceria have been investigated, with the addition of rare earth and noble metals demonstrating increased catalytic activity for the reduction-oxidation process, allowing for reduction of ceria at lower temperatures [144, 159]. The addition of zirconia to ceria particularly enhances the unique properties of ceria, dependant upon the final composition, be it a mixed oxide of separated ZrO_2 and CeO_2 phases or a solid solution. Introduction of ZrO_2 has shown to significantly enhance the catalytic properties of ceria by both increasing oxygen storage capacity (OSC) as well as decreasing temperature of reduction [25]. Comparison between formation of a mixed oxide and a solid solution demonstrates that, although a mixed oxide composition does act to increase the OSC, the effect of solid solution formation upon OSC is at least twice that of the same mixed oxide [160]. A number of papers have been published on the catalytic properties of Ce-ZrO_2 mixed oxide and its application in oxidation reactions [160-163]. Ceria-zirconia solid solution has also exhibited high affinity for the catalytic decomposition of methane as a reducing agent in the reduction reaction, proceeding at low temperature [164, 165].

Additional Metal/Metal Oxide Systems

Investigation of other systems include a prior study of germanium oxide [166], in which impure hydrogen and carbon monoxide derived from gasified coal or syngas was purified by reduction of GeO_2 and subsequent re-oxidation with water. Al_2O_3 was used as a support material, and addition of Ni and Cu enhanced yield of hydrogen from water re-oxidation. Use of magnesium oxide in a solar driven Steam-Iron type process required temperatures in excess of 1700ºC for carbon reduction of MgO and 1900ºC for methane

reduction of MgO [167]. Despite reasonably low water oxidation temperatures of 350ºC, the excessive temperature of reduction is prohibitively high for this system.

2.4.5 Deactivation Studies

Deactivation of iron oxide in the Steam-Iron Process occurs by either sintering, resulting in decreasing redox activity with repeated cycles, or carbon deposition from the use of carbon based reductants.

Mitigation of sintering effects can be achieved by addition of support oxides to maintain dispersion and stability. Additionally, by increasing reactivity the process is accelerated, limiting high temperature exposure of the system and enabling repetition of a greater number of cycles in the same amount of time. The primary cause for deactivation of iron oxide in the Steam-Iron Process has been identified by Kersten et. al. to be the result of sintering effects [168]. The degree of sintering is directly proportional to the relative conversion of iron oxide. By limiting total conversion it is possible to limit sintering but limited conversion will also limit hydrogen production capacity.
Other methods to mitigate sintering include addition of metal oxides. For promoter addition to be effective in prevention of sintering, it is necessary to limit interaction effects with iron oxide. Galvita et. al. have reported the addition of CeO_2 and La_2O_3 to Fe_2O_3 formed solid solutions during redox cycling, resulting in both lower oxygen storage capacity and deactivation by sintering [169]. Addition of $Ce_{0.5}Zr_{0.5}O_2$ to Fe_2O_3 is maintained as two separate phases in a mixed oxide configuration, giving much better resistance to deactivation. Further addition of Mo played a role in preventing contact between iron oxide particles and enabling stable hydrogen production over 100 redox cycles.

Thermodynamic assessment conducted by Baxter et. al. illustrate the tendency for both carbon deposition and iron carbide formation from methane at the high operating temperature necessary for reduction of iron oxide by methane [106]. Assessment of

equilibrium composition of iron oxide and methane at various temperatures shows the importance of iron oxide to methane ratio upon subsequent reaction products [107]. At higher iron oxide to methane ratio, it is possible to limit carbon formation but reduction of iron oxide is also limited, requiring higher temperatures to proceed. With higher ratio of methane to iron oxide, complete reduction is observed and there is high selectivity for partial oxidation to form CO and H_2 products, but the likelihood of carbon formation is increased.

$CH_4 \rightarrow C + 2H_2$	ΔH^o = +74.8 kJ/mol	**2.41**
$CH_4(ad) \rightarrow CH_3(ad) + H(ad)$	ΔH^o = +438.6 kJ/mol	**2.42**
$CH_3(ad) \rightarrow CH_2(ad) + H(ad)$		**2.43**
$CH_2(ad) \rightarrow CH(ad) + H(ad)$		**2.44**
$CH(ad) \rightarrow C(ad) + H(ad)$		**2.45**
$2H(ad) \rightarrow H_2(g)$		**2.46**
$C(ad) \rightarrow C(dissolved)$		**2.47**

Equation 2.41 shows methane decomposition to be a moderately endothermic reaction but calculations predict methane decomposition to proceed at much lower temperature than has been demonstrated experimentally. Various studies have shown that decomposition of methane does not proceed via a single step, but rather, through sequential decomposition of methane adsorbed at the metal surface [170-172]. The energy required for initial removal of a hydrogen atom from methane is much higher than is required for direct decomposition of methane (**Equation 2.42**). Via this reaction process, methane is sequentially broken down to a form carbon atom adsorbed at the surface of the metal, which can dissolve into the metal to form carbide species (**Equation 2.47**).

Carbon formation from methane during reduction of iron oxide has been demonstrated by Hacker et. al. to be a significant problem of the Steam-Iron Process at temperatures

greater than 800ºC [173]. Carbon deposition from methane decomposition occurs upon complete reduction of iron oxide to the metallic iron form. It is suggested that partial reduction of iron oxide to a lower oxidation state and prevention of iron metal formation is a means of preventing carbon deposition. These findings illustrate the formation of carbon is generally favoured in conditions where oxygen availability is low relative to methane concentration.

Carbon formation from reaction products via the Boudouard Reaction is also considered, due to CO production from methane reduction.

$2CO \rightarrow C + CO_2$ ΔH^o = -172.4 kJ/mol **2.48**

Calculations show that carbon formation via the Boudouard Reaction is favoured at low temperatures, whilst methane decomposition only occurs at high temperature (**Equation 2.48**).

2.4.6 Summary

The Steam-Iron Process favours use of iron oxide due to a number of factors, those of which include oxygen storage capacity, high activity and low temperature reduction. However, problems associated with use of iron oxide, such as deactivation by sintering at higher temperatures and carbon deposition from carbon based reductants must be eliminated. Methods of improving iron oxide activity include addition of metal and/or metal oxide promoters, with addition of support oxides to increase stability over numerous cycles. Addition of precious metals such as Rh and Pt show marked improvement of both reduction and oxidation activity. Supporting metal oxides such as ZrO_2, Al_2O_3 and SiO_2 are able to maintain dispersion of iron oxide particles, preventing sintering with numerous cycles. Promoting oxides such as CeO_2 which possess high oxygen storage capacity maybe also enhance the process by participation in the redox

reaction through donation of oxygen, as well as limit deactivation by possible oxidation of adsorbed carbon species.

Analysis of thermodynamics suggests that careful control of gas compositions and reaction conditions are important to ensure selective formation of product gases and limit carbon and/or iron carbide formation. Coupled with knowledge of reaction kinetics, this enables more calculated determination of optimal experimental parameters based upon controlling redox mechanisms.

This literature investigation reveals the need for further analysis of iron oxide; despite the wide range of literature currently available pertaining to use of iron oxide in the Steam-Iron Process, its favourable characteristics as a candidate for this process still makes it the most appropriate selection. Further analysis of other metal oxides including SnO_2, In_2O_3, WO_3, MoO_2, Nb_2O_5 and V_2O_5 should also be conducted by experimental methods for their potential in the Steam-Iron Process, with their performance possibly matching or exceeding that of iron oxide. Thus the aim of conducting this further investigation is for the identification of novel metal oxide candidates which are equally suitable, if not more so, than metal oxides already found in the literature. Further to this, by control of reaction conditions and detailed analysis of reaction kinetics, a more complete understanding of performance and methods for improving hydrogen production can be gained.

2.5 References

1. H. Oeschger, 'CO_2 and the Greenhouse-Effect - Present Assessment and Perspectives', *Ciba Foundation Symposia* **1993**, 175, 2-22
2. R.A. Houghton and G.M. Woodwell, 'Global Climatic Change', *Scientific American* **1989**, 260(4), 36-44
3. R.H. Wentorf and R.E. Hanneman, 'Thermochemical Hydrogen Generation', *Science* **1974**, 185(4148), 311-319
4. S. Ihara, 'Feasibility of hydrogen production by direct water splitting at high temperature', *International Journal of Hydrogen Energy* **1978**, 3(3), 287-296
5. E.A. Fletcher and R.L. Moen, 'Hydrogen and Oxygen from Water', *Science* **1977**, 197(4308), 1050-1056
6. R.B. Diver and E.A. Fletcher, 'Hydrogen and oxygen from water-II. Some considerations in the reduction of the idea to practice', *Energy* **1979**, 4(6), 1139-1150
7. R.B. Diver and E.A. Fletcher, 'Hydrogen and Oxygen from Water-IV. Control of an Effusional Separator During a Solar Intensity Transient', *Energy* **1980**, 5(12), 1261-1263
8. R.B. Diver and E.A. Fletcher, 'Hydrogen and Oxygen from Water-III. Evaluation of a Hybrid Process', *Energy* **1980**, 5(7), 597-607
9. J.E. Noring, R.B. Diver, and E.A. Fletcher, 'Hydrogen and Oxygen from Water-V. The Roc System', *Energy* **1981**, 6(2), 109-121
10. R.B. Diver, S. Pederson, T. Kappauf, and E.A. Fletcher, 'Hydrogen and Oxygen from Water-VI. Quenching the Effluent from a Solar Furnace', *Energy* **1983**, 8(12), 947-955
11. A. Kogan, 'Direct solar thermal splitting of water and on-site separation of the products - IV. Development of porous ceramic membranes for a solar thermal water-splitting reactor', *International Journal of Hydrogen Energy* **2000**, 25(11), 1043-1050

12. A. Hammache and E. Bilgen, 'Evaluation of thermal efficiency and cost of high temperature solar heat from central receiver systems to use in hydrogen producing thermochemical processes', *International Journal of Hydrogen Energy* **1988**, 13(9), 539-546
13. C. Perkins and A.W. Weimer, 'Likely near-term solar-thermal water splitting technologies', *International Journal of Hydrogen Energy* **2004**, 29(15), 1587-1599
14. G.P. Dinga, 'Hydrogen: The ultimate fuel and energy carrier', *International Journal of Hydrogen Energy* **1989**, 14(11), 777-784
15. M.A. Pena, J.P. Gomez, and J.L.G. Fierro, 'New catalytic routes for syngas and hydrogen production', *Applied Catalysis A - General* **1996**, 144(1-2), 7-57
16. J.N. Armor, 'The multiple roles for catalysis in the production of H_2', *Applied Catalysis A - General* **1999**, 176(2), 159-176
17. P.V. Beurden, '*On the Catalytic Aspects of Steam-Methane Reforming - A Literature Survey*'. 2004, Energy research Centre of the Netherlands. 1–27.
18. K. Nath and D. Das, 'Hydrogen from biomass', *Current Science* **2003**, 85(3), 265-271
19. J.R. Rostrup-Nielsen, 'Syngas in perspective', *Catalysis Today* **2002**, 71(3-4), 243-247
20. P.G. Menon, 'Coke on Catalysts - Harmful, Harmless, Invisible and Beneficial Types', *Journal of Molecular Catalysis* **1990**, 59(2), 207-220
21. G.F. Froment, 'Production of synthesis gas by steam- and CO_2-reforming of natural gas', *Journal of Molecular Catalysis A: Chemical* **2000**, 163(1-2), 147-156
22. J.R. Rostrup-Nielsen, J. Sehested, and J.K. Norskov, 'Hydrogen and synthesis gas by steam- and CO_2 reforming', *Advances in Catalysis* **2002**, 47, 65-139
23. J.R. Rostrup-Nielsen and J.H.B. Hansen, 'CO_2-Reforming of Methane over Transition Metals', *Journal of Catalysis* **1993**, 144(1), 38-49
24. M.C.J. Bradford and M.A. Vannice, 'Catalytic reforming of methane with carbon dioxide over nickel catalysts. 1. Catalyst characterisation and activity', *Applied Catalysis A - General* **1996**, 142(1), 73-96

25. E. Aneggi, M. Boaro, C. De Leitenburg, G. Dolcetti, and A. Trovarelli, 'Insights into the redox properties of ceria-based oxides and their implications in catalysis', *Journal of Alloys and Compounds* **2006**, 408, 1096-1102

26. N. Laosiripojana and S. Assabumrungrat, 'Catalytic dry reforming of methane over high surface area ceria', *Applied Catalysis B - Environmental* **2005**, 60(1-2), 107-116

27. N. Laosiripojana, W. Sutthisripok, and S. Assabumrungrat, 'Synthesis gas production from dry reforming of methane over CeO_2 doped Ni/Al_2O_3: Influence of the doping ceria on the resistance toward carbon formation', *Chemical Engineering Journal* **2005**, 112(1-3), 13-22

28. S.M. Stagg-Williams, F.B. Noronha, G. Fendley, and D.E. Resasco, 'CO_2 reforming of CH_4 over Pt/ZrO_2 catalysts promoted with La and Ce oxides', *Journal of Catalysis* **2000**, 194(2), 240-249

29. A.P.E. York, T.C. Xiao, and M.L.H. Green, 'Brief overview of the partial oxidation of methane to synthesis gas', *Topics in Catalysis* **2003**, 22(3-4), 345-358

30. M. Prettre, C. Eichner, and M. And Perrin, 'Catalytic Oxidation of Methane to Carbon Monoxide and Hydrogen', *Transactions of the Faraday Society* **1946**, 43, 335

31. D.A. Hickman and L.D. Schmidt, 'Production of Syngas by Direct Catalytic-Oxidation of Methane', *Science* **1993**, 259(5093), 343-346

32. W.H. Scholz, 'Processes for industrial production of hydrogen and associated environmental effects', *Gas Separation & Purification* **1993**, 7(3), 131-139

33. P.D.F. Vernon, M.L.H. Green, A.K. Cheetham, and A.T. Ashcroft, 'Partial Oxidation of Methane to Synthesis Gas', *Catalysis Letters* **1990**, 6(2), 181-186

34. D.A. Hickman and L.D. Schmidt, 'Synthesis gas formation by direct oxidation of methane over Pt monoliths', *Journal of Catalysis* **1992**, 138(1), 267-282

35. V.R. Choudhary, A.M. Rajput, and V.H. Rane, 'Low-Temperature Oxidative Conversion of Methane to Synthesis Gas over Co Rare-Earth-Oxide Catalysts', *Catalysis Letters* **1992**, 16(3), 269-272

36. V.R. Choudhary, V.H. Rane, and A.M. Rajput, 'Selective Oxidation of Methane to CO and H_2 over Unreduced NiO-Rare Earth Oxide Catalysts', *Catalysis Letters* **1993**, 22(4), 289-297

37. V.R. Choudhary, A.M. Rajput, and V.H. Rane, 'Low-Temperature Catalytic Selective Partial Oxidation of Methane to CO and H_2 over Ni/Yb_2O_3', *Journal of Physical Chemistry* **1992**, 96(22), 8686-8688

38. Y. Lu, Y. Liu, and S. Shen, 'Design of stable Ni catalysts for partial oxidation of methane to synthesis gas', *Journal of Catalysis* **1998**, 177(2), 386-388

39. E. Ruckenstein and Y.H. Hul, 'Methane partial oxidation over NiO MgO solid solution catalysts', *Applied Catalysis A - General* **1999**, 183(1), 85-92

40. V.A. Tsipouriari, Z. Zhang, and X.E. Verykios, 'Catalytic partial oxidation of methane to synthesis gas over Ni-based catalysts - I. Catalyst performance characteristics', *Journal of Catalysis* **1998**, 179(1), 283-291

41. V.A. Tsipouriari and X.E. Verykios, 'Catalytic partial oxidation of methane to synthesis gas over Ni-based catalysts - II. Transient, FTIR, and XRD measurements', *Journal of Catalysis* **1998**, 179(1), 292-299

42. H.T. A/S, *Hydrocarbon Processing* **1988**, 67(4), 77

43. T.S. Christensen and Primdahl, Ii, 'Improve Syngas Production Using Autothermal Reforming', *Hydrocarbon Processing* **1994**, 73(3), 39-&

44. S. Ayabe, H. Omoto, T. Utaka, R. Kikuchi, K. Sasaki, Y. Teraoka, and K. Eguchi, 'Catalytic autothermal reforming of methane and propane over supported metal catalysts', *Applied Catalysis A - General* **2003**, 241(1-2), 261-269

45. P.K. Cheekatamarla and A.M. Lane, 'Catalytic autothermal reforming of diesel fuel for hydrogen generation in fuel cells - I. Activity tests and sulfur poisoning', *Journal of Power Sources* **2005**, 152(1), 256-263

46. A.F. Ghenciu, 'Review of fuel processing catalysts for hydrogen production in PEM fuel cell systems', *Current Opinion in Solid State & Materials Science* **2002**, 6(5), 389-399

47. N.Z. Muradov, 'How to Produce Hydrogen from Fossil-Fuels without CO_2 Emission', *International Journal of Hydrogen Energy* **1993**, 18(3), 211-215

48. N.Z. Muradov, 'CO_2-free production of hydrogen by catalytic pyrolysis of hydrocarbon fuel', *Energy & Fuels* **1998**, 12(1), 41-48

49. N.Z. Muradov and T.N. Veziroglu, 'From hydrocarbon to hydrogen-carbon to hydrogen economy', *International Journal of Hydrogen Energy* **2005**, 30(3), 225-237

50. T.V. Choudhary, C. Sivadinarayana, C.C. Chusuei, A. Klinghoffer, and D.W. Goodman, 'Hydrogen Production via Catalytic Decomposition of Methane', *Journal of Catalysis* **2001**, 199(1), 9-18

51. N. Shah, D. Panjala, and G.P. Huffman, 'Hydrogen production by catalytic decomposition of methane', *Energy & Fuels* **2001**, 15(6), 1528-1534

52. P. Wang, E. Tanabe, K. Ito, J. Jia, H. Morioka, T. Shishido, and K. Takehira, 'Filamentous carbon prepared by the catalytic pyrolysis of CH_4 on Ni/SiO_2', *Applied Catalysis A - General* **2002**, 231(1-2), 35-44

53. S. Takenaka, M. Serizawa, and K. Otsuka, 'Formation of filamentous carbons over supported Fe catalysts through methane decomposition', *Journal of Catalysis* **2004**, 222(2), 520-531

54. Y.D. Li, J.L. Chen, Y.N. Qin, and L. Chang, 'Simultaneous production of hydrogen and nanocarbon from decomposition of methane on a nickel-based catalyst', *Energy & Fuels* **2000**, 14(6), 1188-1194

55. W.H. Qian, T.A. Liu, Z.W. Wang, F.A. Wei, Z.F. Li, G.H. Luo, and Y.D. Li, 'Production of hydrogen and carbon nanotubes from methane decomposition in a two-stage fluidized bed reactor', *Applied Catalysis A - General* **2004**, 260(2), 223-228

56. T. Zhang and M.D. Amiridis, 'Hydrogen production via the direct cracking of methane over silica-supported nickel catalysts', *Applied Catalysis A - General* **1998**, 167(2), 161-172

57. J. Li, G. Lu, K. Li, and W. Wang, 'Active Nb_2O_5-supported nickel and nickel-copper catalysts for methane decomposition to hydrogen and filamentous carbon', *Journal of Molecular Catalysis A: Chemical* **2004**, 221(1-2), 105-112

58. Y. Li, B.C. Zhang, X.L. Tang, Y.D. Xu, and W.J. Shen, 'Hydrogen production from methane decomposition over Ni/CeO_2 catalysts', *Catalysis Communications* **2006**, 7(6), 380-386

59. N. Muradov, 'Hydrogen via methane decomposition: an application for decarbonization of fossil fuels', *International Journal of Hydrogen Energy* **2001**, 26(11), 1165-1175

60. N. Muradov, F. Smith, and A. T-Raissi, 'Catalytic activity of carbons for methane decomposition reaction', *Catalysis Today* **2005**, 102, 225-233

61. A.M. Dunker, S. Kumar, and P.A. Mulawa, 'Production of hydrogen by thermal decomposition of methane in a fluidized-bed reactor - Effects of catalyst, temperature, and residence time', *International Journal of Hydrogen Energy* **2006**, 31(4), 473-484

62. J.R. Rostrup-Nielsen, 'Catalytic Steam Reforming'. Catalysis: Science and Technology, ed. J.R.A. and M. Boudart. *Springer*, **1984**

63. H.S. Bengaard, J.K. Norskov, J. Sehested, B.S. Clausen, L.P. Nielsen, A.M. Molenbroek, and J.R. Rostrup-Nielsen, 'Steam reforming and graphite formation on Ni catalysts', *Journal of Catalysis* **2002**, 209(2), 365-384

64. H. Lane, Process for the production of hydrogen, U.S. Patent 1,078,686, **1913**

65. A. Messerschmitt, Process for producing hydrogen, U.S. Patent 971,206, **1910**

66. J. Bessières, A. Bessières, and J.J. Heizmann, 'Iron oxide reduction kinetics by hydrogen', *International Journal of Hydrogen Energy* **1980**, 5(6), 585-595

67. O.J. Wimmers, P. Arnoldy, and J.A. Moulijn, 'Determination of the Reduction Mechanism by Temperature-Programmed Reduction: Application to Small Fe_2O_3 Particles', *Journal of Physical Chemistry* **1986**, 90, 1331-1337

68. A. Steinfeld, P. Kuhn, and J. Karni, 'High-temperature solar thermochemistry: Production of iron and synthesis gas by Fe_3O_4-reduction with methane', *Energy* **1993**, 18(3), 239-249

69. P.B. Tarman. 'The status of the steam-iron process for hydrogen production', in *Proceedings of Synthetic Pipeline Gas Symposium* (1976).

70. R. Biljetina and P.B. Tarman, 'Steam-iron process for hydrogen production', *Energy Research Abstracts* **1978**, 3(23),

71. P.B. Tarman, 'Hydrogen by the steam-iron process', *Coal Processing Technology* **1979**, 5, 114-16

72. S. Hurst, 'Production of hydrogen by the steam-iron method', *Journal of the American Oil Chemists' Society* **1939**, 16(2), 29-35

73. V. Hacker, G. Faleschini, H. Fuchs, R. Fankhauser, G. Simader, M. Ghaemi, B. Spreitz, and K. Friedrich, 'Usage of biomass gas for fuel cells by the SIR process', *Journal of Power Sources* **1998**, 71(1-2), 226-230

74. V. Hacker, R. Fankhauser, G. Faleschini, H. Fuchs, K. Friedrich, M. Muhr, and K. Kordesch, 'Hydrogen production by steam-iron process', *Journal of Power Sources* **2000**, 86(1-2), 531-535

75. P. Gupta, L.G. Velazquez-Vargas, and L.S. Fan, 'Syngas redox (SGR) process to produce hydrogen from coal derived syngas', *Energy & Fuels* **2007**, 21(5), 2900-2908

76. C.D. Bohn, C.R. Müller, J.P. Cleeton, A.N. Hayhurst, J.F. Davidson, S.A. Scott, and J.S. Dennis, 'Production of Very Pure Hydrogen with Simultaneous Capture of Carbon Dioxide using the Redox Reactions of Iron Oxides in Packed Beds', *Industrial & Engineering Chemistry Research* **2008**, 47, 7623–7630

77. R. Sime, J. Kuehni, L. D'souza, E. Elizondo, and S. Biollaz, 'The redox process for producing hydrogen from woody biomass', *International Journal of Hydrogen Energy* **2003**, 28(5), 491–498

78. K. Urasaki, N. Tanimoto, T. Hayashi, Y. Sekine, E. Kikuchi, and M. Matsukata, 'Hydrogen production via steam-iron reaction using iron oxide modified with very small amounts of palladium and zirconia', *Applied Catalysis A - General* **2005**, 288(1-2), 143-148

79. K. Otsuka, T. Kaburagi, C. Yamada, and S. Takenaka, 'Chemical storage of hydrogen by modified iron oxides', *Journal of Power Sources* **2003**, 122(2), 111-121

80. R. Alizadeh, E. Jamshidi, and G. Zhang, 'Transformation of methane to synthesis gas over metal oxides without using catalyst', *Journal of Natural Gas Chemistry* **2009**, 18(2), 124-130

81. A. Steinfeld, A. Frei, and P. Kuhn, 'Thermoanalysis of the Combined Fe_3O_4 - Reduction and CH_4-Reforming Processes', *Metallurgical and Materials Transactions B - Process Metallurgy and Materials Processing Science* **1995**, 26(3), 509-515

82. K. Otsuka and S. Takenaka, 'Storage and supply of pure hydrogen mediated by the redox of iron oxides', *Journal of Japan Petroleum Institute* **2004**, 47(6), 377-386

83. S. Takenaka, N. Hanaizumi, V.T.D. Son, and K. Otsuka, 'Production of pure hydrogen from methane mediated by the redox of Ni- and Cr-added iron oxides', *Journal of Catalysis* **2004**, 228(2), 405-416

84. S. Takenaka, V.T.D. Son, and K. Otsuka, 'Storage and supply of pure hydrogen from methane mediated by modified iron oxides', *Energy & Fuels* **2004**, 18(3), 820-829

85. M. Thaler, V. Hacker, M. Anilkumar, J. Albering, J.O. Besenhard, H. Schrottner, and M. Schmied, 'Investigations of cycle behaviour of the contact mass in the RESC process for hydrogen production', *International Journal of Hydrogen Energy* **2006**, 31(14), 2025-2031

86. V. Hacker, 'A novel process for stationary hydrogen production: the reformer sponge iron cycle (RESC)', *Journal of Power Sources* **2003**, 118(1-2), 311-314

87. H. Kindermann, M. Kornberger, J. Hierzer, J.O. Besenhard, and V. Hacker, 'First investigations of structural changes of the contact mass in the RESC process for hydrogen production', *Journal of Power Sources* **2005**, 145(2), 697-701

88. T. Kodama, S. Miura, T. Shimizu, and Y. Kitayama, 'Thermochemical conversion of coal and water to CO and H_2 by a two-step redox cycle of ferrite', *Energy* **1997**, 22(11), 1019-1027

89. T. Kodama, T. Shimizu, T. Satoh, M. Nakata, and K.I. Shimizu, 'Stepwise production of CO-RICH syngas and hydrogen via solar methane reforming by using a Ni(II)-ferrite redox system', *Solar Energy* **2002**, 73(5), 363-374

90. K. Otsuka, C. Yamada, T. Kaburagi, and S. Takenaka, 'Hydrogen storage and production by redox of iron oxide for polymer electrolyte fuel cell vehicles', *International Journal of Hydrogen Energy* **2003**, 28(3), 335-342

91. S. Takenaka, T. Kaburagi, C. Yamada, K. Nomura, and K. Otsuka, 'Storage and supply of hydrogen by means of the redox of the iron oxides modified with Mo and Rh species', *Journal of Catalysis* **2004**, 228(1), 66-74

92. S. Takenaka, K. Nomura, N. Hanaizumi, and K. Otsuka, 'Storage and formation of pure hydrogen mediated by the redox of modified iron oxides', *Applied Catalysis A - General* **2005**, 282(1-2), 333-341

93. K.-S. Kang, C.-H. Kim, W.-C. Cho, K.-K. Bae, S.-W. Woo, and C.-S. Park, 'Reduction characteristics of $CuFe_2O_4$ and Fe_3O_4 by methane; $CuFe_2O_4$ as an oxidant for two-step thermochemical methane reforming', *International Journal of Hydrogen Energy* **2008**, 33(17), 4560-4568

94. Z. Kang and Z.L. Wang, 'Novel Oxides for Cycled Hydrogen Production from Methane and Water using a Temperature Swing', *Advanced Materials* **2003**, 15(6), 521-526

95. H. Bao, X. Chen, J. Fang, Z. Jiang, and W. Huang, 'Structure-activity Relation of Fe_2O_3–CeO_2 Composite Catalysts in CO Oxidation', *Catalysis Letters* **2008**, 125(160-167),

96. E. Lorente, J.A. Peña, and J. Herguido, 'Separation and storage of hydrogen by steam-iron process: Effect of added metals upon hydrogen release and solid stability', *Journal of Power Sources* **2009**, 192 (1), 224–229

97. D.H. Lee, K.S. Cha, Y.S. Lee, K.S. Kang, C.S. Park, and Y.H. Kim, 'Effects of CeO_2 additive on redox characteristics of Fe-based mixed oxide mediums for storage and production of hydrogen', *International Journal of Hydrogen Energy* **2009**, 34(3), 1417-1422

98. V. Galvita and K. Sundmacher, 'Hydrogen production from methane by steam reforming in a periodically operated two-layer catalytic reactor', *Applied Catalysis A - General* **2005**, 289(2), 121-127

99. E. Aneggi, C. De Leitenburg, G. Dolcetti, and A. Trovarelli, 'Promotional effect of rare earths and transition metals in the combustion of diesel soot over CeO_2 and CeO_2-ZrO_2', *Catalysis Today* **2006**, 114(1), 40-47

100. T. Kodama, Y. Nakamuro, and T. Mizuno, 'A two-step thermochemical water splitting by iron-oxide on stabilised zirconia', *Journal of Solar Energy Engineering - Transactions of the ASME* **2006**, 128(1), 3-7

101. N. Gokon, H. Murayama, J. Umeda, T. Hatamachi, and T. Kodama, 'Monoclinic zirconia-supported Fe_3O_4 for the two-step water-splitting thermochemical cycle at high thermal reduction temperatures of 1400–1600ºC ', *International Journal of Hydrogen Energy* **2009**, 34(3), 1208-1217

102. T. Kodama, T. Shimizu, A. Aoki, and Y. Kitayama, 'High-Temperature Conversion of CH_4 to C_2-Hydrocarbons and H_2 Using a Redox System of Metal Oxide', *Energy & Fuels* **1997**, 11, 1257-1263

103. H. Kameyama, K. Yoshida, and D. Kunii, 'A method for screening possible thermochemical decomposition processes for water using δG_0 -T diagrams', *The Chemical Engineering Journal* **1976**, 11(3), 223-229

104. S.L. Marshall and J.G. Blencoe, 'Equilibrium analysis of thermochemical cycles for hydrogen production', *Separation Science and Technology* **2005**, 40(1-3), 483-505

105. T. Kodama, H. Ohtake, S. Matsumoto, A. Aoki, T. Shimizu, and Y. Kitayama, 'Thermochemical methane reforming using a reactive WO_3/W redox system', *Energy* **2000**, 25(5), 411-425

106. K. Svoboda, G. Slowinski, J. Rogut, and D. Baxter, 'Thermodynamic possibilities and constraints for pure hydrogen production by iron based chemical looping process at lower temperatures', *Energy Conversion and Management* **2007**, 48(12), 3063-3073

107. J. Xin, H. Wang, F. He, and Z. Zhang, 'Thermodynamic and Equilibrium Composition Analysis of Using Iron Oxide as an Oxygen Carrier in Nonflame Combustion Technology', *Journal of Natural Gas Chemistry* **2005**, 14, 248–

108. S.D. Fraser, M. Monsberger, and V. Hacker, 'A thermodynamic analysis of the reformer sponge iron cycle', *Journal of Power Sources* **2006**, 161 (1), 420–431

109. A. Pineau, N. Kanari, and I. Gaballah, 'Kinetics of reduction of iron oxides by H_2 Part I: Low temperature reduction of hematite', *Thermochimica Acta* **2006**, 447(1), 89–100

110. A. Pineau, N. Kanari, and I. Gaballah, 'Kinetics of reduction of iron oxides by H_2 Part II. Low temperature reduction of magnetite', *Thermochimica Acta* **2007**, 456(2), 75–88

111. V. Galvita and K. Sundmacher, 'Redox behaviour and reduction mechanism of Fe_2O_3-$CeZrO_2$ as oxygen storage material', *Journal of Materials Science* **2007**, 42(22), 9300-9307

112. K.S. Go, S.R. Son, and S.D. Kim, 'Reaction kinetics of reduction and oxidation of metal oxides for hydrogen production', *International Journal of Hydrogen Energy* **2008**, 33(21), 5986-5995

113. E. Lorente, J.A. Peña, and J. Herguido, 'Kinetic study of the redox process for separating and storing hydrogen: Oxidation stage and ageing of solid', *International Journal of Hydrogen Energy* **2008**, 33(2), 615-626

114. P. Charvin, S. Abanades, G. Flamant, and F. Lemort, 'Two-step water splitting thermochemical cycle based on iron oxide redox pair for solar hydrogen production', *Energy* **2007**, 32(7), 1124-1133

115. K. Otsuka, S. Murakoshi, and A. Morikawa, 'Potential Metal-Oxides for the Production of Hydrogen from Water by a Reduction Oxidation Cycle Using Carbon as a Reductant', *Fuel Processing Technology* **1983**, 7(3), 203-211

116. M. Lundberg, 'Model calculations on some feasible two-step water splitting processes', *International Journal of Hydrogen Energy* **1993**, 18(5), 369-376

117. A. Steinfeld, P. Kuhn, A. Reller, R.P.J. Murray, and Y. Tamauras, 'Solar-Processed Metals as Clean Energy Carriers and Water-Splitters', *Int. J. Hydrogen Energy* **1998**, 23(9), 767–774

118. S. Abanades, P. Charvin, G. Flamant, and P. Neveu, 'Screening of water-splitting thermochemical cycles potentially attractive for hydrogen production by concentrated solar energy', *Energy* **2006**, 31(14), 2805-2822

119. P. Haueter, S. Moeller, R. Palumbo, and A. Steinfeld, 'The production of zinc by thermal dissociation of zinc oxide - Solar chemical reactor design', *Solar Energy* **1999**, 67(1-3), 161-167

120. A. Steinfeld, 'Solar hydrogen production via a two-step water-splitting thermochemical cycle based on Zn/ZnO redox reactions', *International Journal of Hydrogen Energy* **2002**, 27(6), 611-619

121. K. Wegner, H.C. Ly, R.J. Weiss, S.E. Pratsinis, and A. Steinfeld, 'In situ formation and hydrolysis of Zn nanoparticles for H_2 production by the 2-step ZnO/Zn water-splitting thermochemical cycle', *International Journal of Hydrogen Energy* **2006**, 31(1), 55-61

122. A. Steinfeld, A. Frei, P. Kuhn, and D. Wuillemin, 'Solar thermal production of zinc and syngas via combined ZnO-reduction and CH_4-reforming processes', *International Journal of Hydrogen Energy* **1995**, 20(10), 793-804

123. A. Steinfeld, C. Larson, R. Palumbo, and I.M. Foley, 'Thermodynamic analysis of the co-production of zinc and synthesis gas using solar process heat', *Energy* **1996**, 21(3), 205-222

124. S. Kraupl and A. Steinfeld, 'Experimental investigation of a vortex-flow solar chemical reactor for the combined ZnO-reduction and CH_4-reforming', *Journal of Solar Energy Engineering - Transactions of the ASME* **2001**, 123(3), 237-243

125. C. Wieckert and A. Steinfeld, 'Solar thermal reduction of ZnO using CH_4 : ZnO and C : ZnO molar ratios less than 1', *Journal of Solar Energy Engineering - Transactions of the ASME* **2002**, 124(1), 55-62

126. A. Steinfeld, M. Brack, A. Meier, A. Weidenkaff, and D. Wuillemin, 'A solar chemical reactor for co-production of zinc and synthesis gas', *Energy* **1998**, 23(10), 803-814

127. A. Berman and M. Epstein, 'The kinetics of hydrogen production in the oxidation of liquid zinc with water vapor', *International Journal of Hydrogen Energy* **2000**, 25(10), 957-967

128. K.M. Jeong and H.E. Swift, 'Catalytic Water Decomposition Via Novel Bimetallic Systems', *Journal of Catalysis* **1986**, 101(2), 246-252

129. S. Abanades, P. Charvin, F. Lemont, and G. Flamant, 'Novel two-step SnO_2/SnO water-splitting cycle for solar thermochemical production of hydrogen', *International Journal of Hydrogen Energy* **2008**, 33(21), 6021-6030

130. P. Charvin, S. Abanades, F. Lemont, and G. Flamant, 'Experimental Study of SnO_2/SnO/Sn Thermochemical Systems for Solar Production of Hydrogen', *AICHE Journal* **2008**, 54(10), 2759-2767

131. K. Otsuka, S. Murakoshi, and A. Morikawa, 'Hydrogen-Production from Water by Reduced Tin Oxide', *Fuel Processing Technology* **1983**, 7(3), 213-223

132. M. Chambon, S. Abanades, and G. Flamant, 'Kinetic investigation of hydrogen generation from hydrolysis of SnO and Zn solar nanopowders', *International Journal of Hydrogen Energy* **2009**, 34(13), 5326-5336

133. M. Forster, 'Theoretical investigation of the system SnO_x/Sn for the thermochemical storage of solar energy', *Energy* **2004**, 29(5-6), 789-799

134. X. Wang and Y.-C. Xie, 'CH_4 Deep Oxidation on SnO_2-Based Composite Oxides: Novel, Active, and Stable Catalysts', *Chemistry Letters* **2001**, 3, 216-217

135. X. Wang and Y.-C. Xie, 'Total oxidation of CH_4 on Sn-Cr composite oxide catalysts', *Applied Catalysis B - Environmental* **2001**, 35, 85–94

136. X. Wang and Y.-C. Xie, 'Total Oxidation of CH4 on Iron-Promoted Tin Oxide: Novel and Thermally Stable Catalysts', *Reaction Kinetics and Catalysis Letters* **2001**, 72(2), 229-237

137. K. Omata, T. Ehara, I. Kawai, and M. Yamada, 'Methane-water redox reaction on A_2SnO_4 (A = Mg, Ca, Sr, Ba) oxide to produce C_2 hydrocarbons', *Catalysis Letters* **1997**, 45 245-248

138. T. Shimizu, Y. Kitayama, and T. Kodama, 'Thermochemical Conversion of CH_4 to C_2-Hydrocarbons and H_2 over $SnO_2/Fe_3O_4/SiO_2$ in Methane - Water Co-Feed System', *Energy & Fuels* **2001**, 15(2), 463-469

139. K. Otsuka, T. Yasui, and A. Morikawa, 'The Decomposition of Water on the Co-Reduced or H_2-Reduced Indium Oxide', *Bulletin of the Chemical Society of Japan* **1982**, 55(6), 1768-1771

140. K. Otsuka, Y. Takizawa, S. Shibuya, and A. Morikawa, 'Hydrogen-Production from Water by In_2O_3 and K_2CO_3 Using Graphite, Active-Carbon and Biomass as Reductants', *Chemistry Letters* **1981**, 3, 347-350

141. K. Otsuka, Y. Takizawa, and A. Morikawa, 'Hydrogen-Production from Water on Carbon-Reduced Indium Oxide', *Fuel Processing Technology* **1982**, 6(3), 215-223

142. K. Otsuka, T. Yasui, and A. Morikawa, 'Reproducible Hydrogen-Production from Water by Indium Oxide', *Journal of Catalysis* **1981**, 72(2), 392-393

143. K. Otsuka, A. Mito, S. Takenaka, and I. Yamanaka, 'Production of hydrogen from methane without CO_2-emission mediated by indium oxide and iron oxide', *International Journal of Hydrogen Energy* **2001**, 26(3), 191-194

144. K. Otsuka, M. Hatano, and A. Morikawa, 'Carriers and Additives Enhancing the Reduction Oxidation of Cerium Oxide', *Reactivity of Solids* **1985**, 1(1), 87-93

145. K. Otsuka, S. Shibuya, and A. Morikawa, 'Effective Supported-In_2O_3 for the Production of Hydrogen from Water by the Reduction-Oxidation Cycle of In_2O_3', *Chemistry Letters* **1982**, 7, 987-990

146. K. Otsuka, S.I. Shibuya, and A. Morikawa, 'Role of Carriers in the Production of Hydrogen from Water by Reduction Oxidation Cycle of In_2O_3', *Journal of Catalysis* **1983**, 84(2), 308-316

147. T. Kodama, T. Shimizu, T. Satoh, and K.I. Shimizu, 'Stepwise production of CO-rich syngas and hydrogen via methane reforming by a WO_3-redox catalyst', *Energy* **2003**, 28(11), 1055-1068

148. T. Shimizu, K. Shimizu, Y. Kitayama, and T. Kodama, 'Thermochemical methane reforming using WO3 as an oxidant below 1173 K by a solar furnace simulator', *Solar Energy* **2001**, 71(5), 315-324

149. A. Trovarelli, 'Catalytic properties of ceria and CeO_2-containing materials', *Catalysis Reviews* **1996**, 38(4), 439-520

150. A. Trovarelli, C. Deleitenburg, and G. Dolcetti, 'Design better cerium-based oxidation catalysts', *Chemtech* **1997**, 27(6), 32-37

151. A. Trovarelli, C. De Leitenburg, M. Boaro, and G. Dolcetti, 'The utilisation of ceria in industrial catalysis', *Catalysis Today* **1999**, 50(2), 353-367

152. F. Giordano, A. Trovarelli, C. De Leitenburg, and M. Giona, 'A model for the temperature-programmed reduction of low and high surface area ceria', *Journal of Catalysis* **2000**, 193(2), 273-282

153. K. Otsuka, M. Hatano, and A. Morikawa, 'Hydrogen from water by reduced cerium oxide', *Journal of Catalysis* **1983**, 79(2), 493-496

154. K. Otsuka, M. Hatano, and A. Morikawa, 'Decomposition of water by cerium oxide of δ-phase', *Inorganica Chimica Acta* **1985**, 109(3), 193-197

155. K. Otsuka, Y. Wang, E. Sunada, and I. Yamanaka, 'Direct partial oxidation of methane to synthesis gas by cerium oxide', *Journal of Catalysis* **1998**, 175(2), 152-160

156. K. Otsuka, T. Ushiyama, and I. Yamanaka, 'Partial Oxidation of Methane Using the Redox of Cerium Oxide', *Chemistry Letters* **1993**, 9, 1517-1520

157. H.S. Roh, K.W. Jun, S.C. Baek, and S.E. Park, 'Extraordinary catalytic behaviour of CeO_2 in partial oxidation of methane', *Chemistry Letters* **2001**, 10, 1048-1049

158. G. Balducci, P. Fornasiero, R. Dimonte, J. Kaspar, S. Meriani, and M. Graziani, 'An Unusual Promotion of the Redox Behaviour of CeO_2-ZrO_2 Solid-Solutions Upon Sintering at High-Temperatures', *Catalysis Letters* **1995**, 33(1-2), 193-200

159. L. Kundakovic and M. Flytzani-Stephanopoulos, 'Cu- and Ag-modified cerium oxide catalysts for methane oxidation', *Journal of Catalysis* **1998**, 179(1), 203-221

160. C.E. Hori, H. Permana, K.Y.S. Ng, A. Brenner, K. More, K.M. Rahmoeller, and D. Belton, 'Thermal stability of oxygen storage properties in a mixed CeO_2-ZrO_2 system', *Applied Catalysis B - Environmental* **1998**, 16(2), 105-117

161. C. Deleitenburg, A. Trovarelli, F. Zamar, S. Maschio, G. Dolcetti, and J. Llorca, 'A Novel and Simple Route to Catalysts with a High Oxygen Storage Capacity - the Direct Room-Temperature Synthesis of CeO_2-ZrO_2 Solid-Solutions', *Journal of the Chemical Society-Chemical Communications* **1995**, (21), 2181-2182

162. P. Fornasiero, R. Dimonte, G.R. Rao, J. Kaspar, S. Meriani, A. Trovarelli, and M. Graziani, 'Rh-Loaded CeO_2-ZrO_2 Solid-Solutions as Highly Efficient Oxygen Exchangers - Dependence of the Reduction Behaviour and the Oxygen Storage Capacity on the Structural-Properties', *Journal of Catalysis* **1995**, 151(1), 168-177

163. P. Fornasiero, G. Balducci, R. Dimonte, J. Kaspar, V. Sergo, G. Gubitosa, A. Ferrero, and M. Graziani, 'Modification of the redox behaviour of CeO_2 induced by structural doping with ZrO_2', *Journal of Catalysis* **1996**, 164(1), 173-183

164. S. Pengpanich, V. Meeyoo, T. Rirksomboon, and K. Bunyakiat, 'Catalytic oxidation of methane over CeO_2-ZrO_2 mixed oxide solid solution catalysts prepared via urea hydrolysis', *Applied Catalysis A - General* **2002**, 234(1-2), 221-233

165. K. Otsuka, Y. Wang, and M. Nakamura, 'Direct conversion of methane to synthesis gas through gas-solid reaction using CeO_2-ZrO_2 solid solution at moderate temperature', *Applied Catalysis A - General* **1999**, 183(2), 317-324

166. A. Miyamoto, M. Miura, K. Sakamoto, S. Kamitomai, Y. Kosaki, and Y. Murakami, 'Development of Germanium Oxide Media for the Production of Concentrated Hydrogen by the Steam Iron Process', *Industrial & Engineering Chemistry Product Research and Development* **1984**, 23(3), 467-470

167. M.E. Gálvez, A. Frei, G. Albisetti, G. Lunardi, and A. Steinfeld, 'Solar hydrogen production via a two-step thermochemical process based on MgO/Mg redox reactions - Thermodynamic and kinetic analyses', *International Journal of Hydrogen Energy* **2008**, 33(12), 2880-2890

168. M.F. Bleeker, H.J. Veringa, and S.R.A. Kersten, 'Deactivation of iron oxide used in the steam-iron process to produce hydrogen', *Applied Catalysis A - General* **2009**, 357 5–17

169. V. Galvita, T. Hempel, H. Lorenz, L.K. Rihko-Struckmann, and K. Sundmacher, 'Deactivation of modified iron oxide materials in the cyclic water gas shift process for CO-free hydrogen production', *Industrial & Engineering Chemistry Research* **2008**, 47(2), 303-310

170. H.J. Grabke and G. Horz, 'Kinetics and Mechanisms of Gas-Metal Interactions', *Annual Review of Materials Science* **1977**, 7, 155–178

171. G.Q. Zhang and O. Ostrovski, 'Reduction of titania by methane-hydrogen-argon gas mixture', *Metallurgical and Materials Transactions B - Process Metallurgy and Materials Processing Science* **2000**, 31(1), 129-139

172. J. Zhang and O. Ostrovski, 'Iron ore reduction / cementation: Experimental results and kinetic modelling', *Ironmaking and Steelmaking* **2002** 29(1), 15-21

173. V. Hacker, R. Vallant, and M. Thaler, 'Thermogravimetric Investigations of Modified Iron Ore Pellets for Hydrogen Storage and Purification: The First Charge and Discharge Cycle', *Industrial & Engineering Research* **2007**, 46(26), 8993-8999

THERMODYNAMIC ASSESSMENT OF POTENTIAL METAL OXIDES FOR THE STEAM-METAL PROCESS

3.1 Introduction

In determining suitable catalysts to be used for the purpose of hydrogen production in a process analogous to the Steam-Iron Process (hereby referred to as the Steam-Metal Process for all non-iron systems), a number of factors must be considered. The catalyst must be reducible at reasonably low temperature and produce a substantial yield of clean hydrogen upon re-oxidation with water, also at low temperature. Using thermodynamic analysis, it is possible to identify potential metal oxide systems for their suitability in a reduction/re-oxidation cycle for hydrogen production [1]. In addition to identification of potential catalysts for investigation, it is necessary also to seek novel methods by which to improve these catalysts. The prevalent method for creating novel catalysts focuses upon the addition of promoters to enhance catalytic activity and function whilst retarding causes of deactivation.

In this chapter it is sought to address these issues by identifying potential catalysts for investigation via a thermodynamic calculation approach. This is followed by preliminary experimental analysis of chosen promoting species using the technique of temperature programmed reduction (TPR). Occurrence of other possible reactions during the redox process can also be predicted via thermodynamics.

3.2 Catalyst Selection

Testing of a number of metal oxide systems for reactivity in the reduction/water oxidation cycle reveals that oxides which reduce at low temperature produce negligible yield of hydrogen at equilibrium upon re-oxidation. The reverse is also true - that for metals which demonstrate high affinity for hydrogen production in the re-oxidation reaction, the temperature of reduction is considered prohibitively high. This has enabled a wide range of metals to be eliminated on the basis of either temperature of reduction and/or limited hydrogen yield.

The energy intensive and rate limiting step of the Steam-Metal Process is known to be the high temperature reduction from metal oxide to a reduced form. It is sought to minimise this temperature whilst producing a substantial yield of hydrogen gas in the subsequent re-oxidation reaction. Ideally, methane is employed as a reducing agent, reducing the metal oxide at lower temperature than required for thermal decomposition. Possible production of syngas (CO + H_2) as a by-product can be used as feedstock in syntheses such as production of ammonia or methanol. The proposed reaction pathway for the primary reduction reaction is as follows:

$$MO_x + CH_4 \rightarrow MO_{x-1} + CO + 2H_2 \qquad \textbf{3.1}$$

Following reduction, re-oxidation of the reduced metal oxide produces hydrogen gas whilst regenerating the metal oxide, allowing for the cycle to be repeated:

$$MO_{x-1} + H_2O \rightarrow MO_x + H_2 \qquad \textbf{3.2}$$

3.2.1 Thermodynamic Analysis

The likely reaction pathway and temperature of reduction/re-oxidation can be predicted through knowledge of the values for enthalpy (ΔH), entropy (S) and heat capacity (C) for

the reactants and products of the reaction. Thermodynamic analysis is calculated on the basis of minimisation of Gibbs Free Energy, where it is expected that the reaction would proceed spontaneously when $\Delta G^{o} < 0$.

$$\Delta H^{\circ} = \Delta H^{\circ}_{PRODUCTS} - \Delta H^{\circ}_{REACTANTS} \quad \textbf{3.3}$$

$$\Delta S = \int_{T2}^{T1} C \cdot dT \quad \textbf{3.4}$$

$$\Delta G^{\circ} = \Delta H^{\circ} - T\Delta S \quad \textbf{3.5}$$

As temperature is increased, the value of Gibbs free energy decreases, such that the reaction is able to proceed forward spontaneously at a sufficiently high temperature. The nature of temperature programmed reduction (TPR) is such that H_2O produced from the reduction reaction is removed from the reaction zone, resulting in lower pressure of H_2O compared to H_2. This results in a significant decrease in ΔG^{o} with increasing temperature (**Equation 3.6**) [2].

$$\Delta G = \Delta G^{\circ} + RT \log\left(\frac{P_{H_2O}}{P_{H_2}}\right) \quad \textbf{3.6}$$

The equilibrium constant, K, can be determined from ΔG^{o} by the formula:

$$\Delta G^{\circ} = -RT \ln K \quad \textbf{3.7}$$

All subsequent calculations are made assuming standard atmospheric pressure (1 atm), with thermodynamic values obtained from Barin [3]. Values are applied to **Equations 3.3** to **3.5**, taking into account the change of enthalpy and entropy with temperature.

The primary focus of the Steam-Metal Process thus far, has been on the use of iron oxide (magnetite, Fe_3O_4) [4-7]. Magnetite exhibits both relatively low temperatures of reduction and re-oxidation, coupled with low molecular weight of Fe to give high oxygen

to metal ratio. However, the reduction of magnetite by methane is susceptible to the formation of iron carbide [8] and formation of iron metal from reduction is known to catalyse methane decomposition [9], resulting in coke formation and deactivation.

More recently, interest moved toward the development of zinc oxide (ZnO) for this application. This is more due to the low temperature of thermal decomposition for this oxide. However some work has been focused upon the use of methane as a reductant for this process [10-12]. Thermal decomposition of metal oxides using heat alone has the advantage of being a completely carbon free cycle, thereby eliminating issues associated with carbon oxide formation upon methane reduction. However, due to the current limitations of generating such high temperatures as is required for this process, it is necessary to introduce reductants that are able to facilitate reduction at lower temperatures in a step toward a completely carbon free cycle. Zinc metal also possesses a low melting point of 693K (420°C), which results in extensive sintering following the reduction reaction.

From the literature, a great number of other potential candidates for this reaction have been identified which meet the selective criteria [13-16]. The most promising of these candidates include tin oxide (SnO_2) [17-19], indium oxide (In_2O_3) [20-23], molybdenum oxide (MoO_2) [14, 15], tungsten oxide (WO_3/WO_2) [24, 25], and niobium oxide (Nb_2O_5) [13, 14]. Whilst other candidates exist, it is not possible to investigate all potential alternatives in order to find and develop metal oxides that match, if not exceed performance of iron oxide and zinc oxide. Assessment of these chosen candidates is performed by plotting calculated Gibbs Free Energy against temperature for the reduction of each metal oxide with methane. This allows direct comparison of a range of metals, illustrating the temperature of reduction and/or re-oxidation above or below which $\Delta G^o < 0$ [1]. **Equations 3.8** to **3.17** show reduction of various metal oxides by methane, per mole of O_2 removed. **Figure 3.1** illustrates reduction of various metal oxides by CH_4, with change in Gibbs Free Energy against temperature.

$\frac{1}{2}Fe_3O_4 + 2CH_4 \rightarrow \frac{3}{2}Fe + 2CO + 4H_2$ **3.8**

$2Fe_3O_4 + 2CH_4 \rightarrow 6FeO + 2CO + 4H_2$ **3.9**

$\frac{2}{3}WO_3 + 2CH_4 \rightarrow \frac{2}{3}W + 2CO + 4H_2$ **3.10**

$2WO_3 + 2CH_4 \rightarrow 2WO_2 + 2CO + 4H_2$ **3.11**

$SnO_2 + 2CH_4 \rightarrow Sn + 2CO + 4H_2$ **3.12**

$2SnO_2 + 2CH_4 \rightarrow 2SnO + 2CO + 4H_2$ **3.13**

$MoO_2 + 2CH_4 \rightarrow Mo + 2CO + 4H_2$ **3.14**

$\frac{2}{3}In_2O_3 + 2CH_4 \rightarrow \frac{4}{3}In + 2CO + 4H_2$ **3.15**

$2Nb_2O_5 + 2CH_4 \rightarrow 4NbO_2 + 2CO + 4H_2$ **3.16**

$2ZnO + 2CH_4 \rightarrow 2Zn + 2CO + 4H_2$ **3.17**

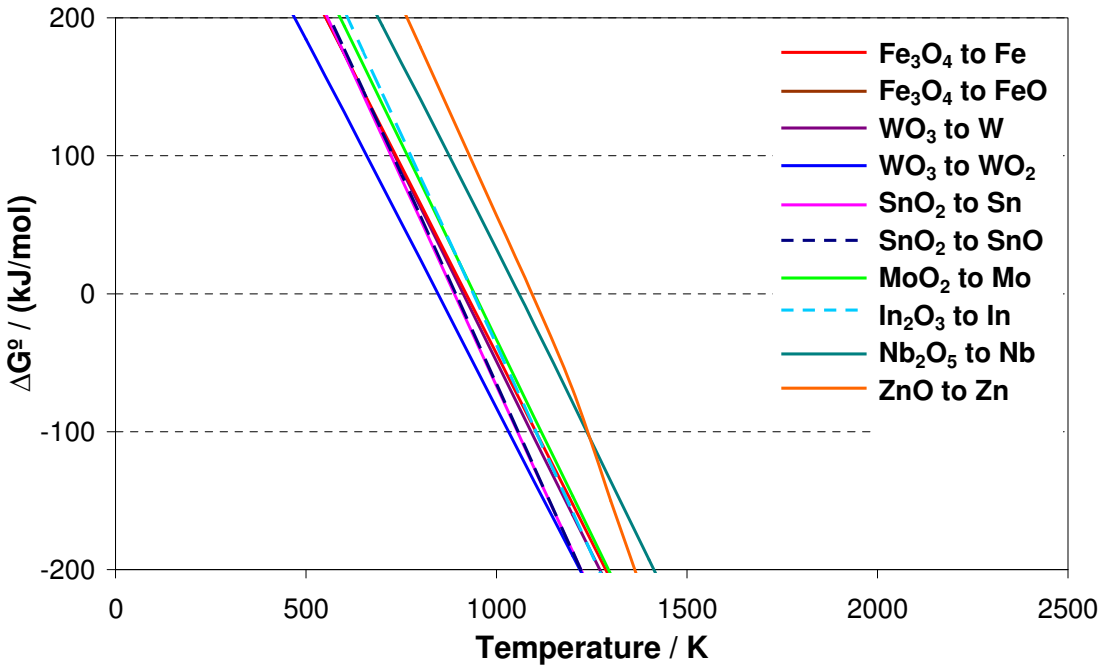

Figure 3.1 Reduction of various metal oxides by CH_4, per mole of O_2 removed. Note that the Gibbs Free Energy of reduction for Fe_3O_4 to FeO falls below -200 kJ/mol

Equations 3.18 to **3.27** show re-oxidation of these reduced metal oxides by H_2O, per mole of O_2 added. These reactions are represented graphically in the form of Gibbs Free Energy against temperature in **Figure 3.2**.

$$\tfrac{3}{2}Fe + 2H_2O \rightarrow \tfrac{1}{2}Fe_3O_4 + 2H_2 \quad \textbf{3.18}$$

$$6FeO + 2H_2O \rightarrow 2Fe_3O_4 + 2H_2 \quad \textbf{3.19}$$

$$\tfrac{2}{3}W + 2H_2O \rightarrow \tfrac{2}{3}WO_3 + 2H_2 \quad \textbf{3.20}$$

$$2WO_2 + 2H_2O \rightarrow 2WO_3 + 2H_2 \quad \textbf{3.21}$$

$$Sn + 2H_2O \rightarrow SnO_2 + 2H_2 \quad \textbf{3.22}$$

$$2SnO + 2H_2O \rightarrow 2SnO_2 + 2H_2 \quad \textbf{3.23}$$

$$Mo + 2H_2O \rightarrow MoO_2 + 2H_2 \quad \textbf{3.24}$$

$$\tfrac{4}{3}In + 2H_2O \rightarrow \tfrac{2}{3}In_2O_3 + 2H_2 \quad \textbf{3.25}$$

$$4NbO_2 + 2H_2O \rightarrow 2Nb_2O_5 + 2H_2 \quad \textbf{3.26}$$

$$2Zn + 2H_2O \rightarrow 2ZnO + 2H_2 \quad \textbf{3.27}$$

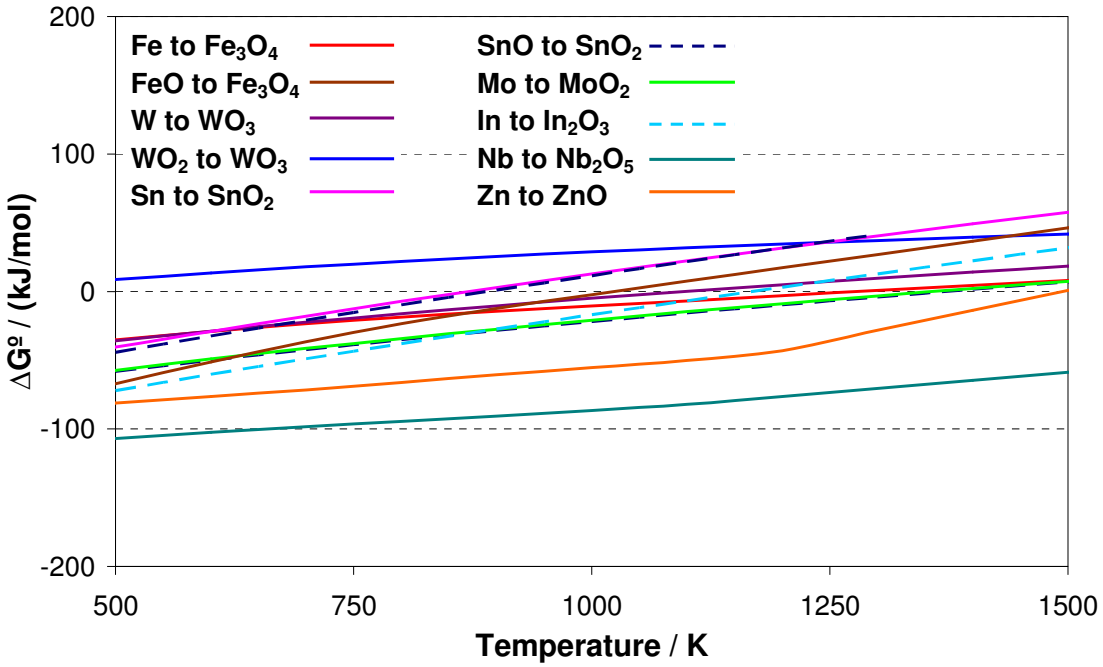

Figure 3.2 Re-oxidation of various reduced metal oxides by H_2O, per mole of O_2 added

Figure 3.1 shows the reduction of SnO_2 to Sn, SnO_2 to SnO and WO_3 to WO_2, at equilibrium, to proceed at temperatures lower than that of Fe_3O_4 reduction. The remaining metal oxides require higher temperature before reduction is favoured. **Figure 3.2** shows re-oxidation of reduced metal oxides to proceed over a range of temperatures. It is noted that, at lower temperature, re-oxidation is more highly favoured for all metal oxides, becoming less favourable with increasing temperature. The metal oxides that are more easily reduced at lower temperature show a limited temperature range for re-oxidation, bar WO_2 to WO_3 re-oxidation, which is seemingly not favoured at temperatures higher than 500K. A shift in Gibbs Free Energy from negative to positive values at higher re-oxidation temperature is observed for all metal oxides. The desire for low temperature re-oxidation would tend to minimise the need to achieve these higher temperatures.

To maximise efficiency of the redox process, it is also necessary to find metal oxide systems of high oxygen storage capacity (OSC). Higher OSC allows for a greater proportion of oxygen to be removed from the metal oxide during reduction, thereby generating a greater amount of hydrogen upon re-oxidation (**Table 3-1**). WO_3 to W shows greatest OSC per mole of metal, followed by MoO_2, SnO_2, In_2O_3, Fe_3O_4, ZnO, WO_3 to WO_2, SnO_2 to SnO, Nb_2O_5 and Fe_3O_4 to FeO. However, when calculated per gram of sample/metal oxide, Fe_3O_4 has the greatest OSC, followed by MoO_2, SnO_2, WO_3, ZnO, In_2O_3, SnO_2 to SnO, with Fe_3O_4 to FeO and WO_3 to WO_2 showing equal H_2 production capacity, and finally Nb_2O_5. The high molecular weight of tungsten metal gives low OSC per gram WO_3. The inhibition of further reduction of Nb_2O_5 beyond NbO_2 also prevents greater OSC. The theoretical hydrogen storage capacity of iron oxide greatly exceeds that of various other metals, highlighting the importance of finding low weight metals to be used for this process.

Table 3-1 Potential H_2 production from H_2O re-oxidation

Eq.	Reaction	H_2 Production		
		mol.H_2/ mol.(sample)[a]	**mol.H_2/ g.(sample)[a]**	**L.H_2/ kg.(sample)[a]**
3.18	$\frac{3}{2}Fe + 2H_2O \rightarrow \frac{1}{2}Fe_3O_4 + 2H_2$	1.33	1.73 x 10^{-2}	384
3.24	$Mo + 2H_2O \rightarrow MoO_2 + 2H_2$	2	1.56 x 10^{-2}	348
3.22	$Sn + 2H_2O \rightarrow SnO_2 + 2H_2$	2	1.33 x 10^{-2}	295
3.20	$\frac{2}{3}W + 2H_2O \rightarrow \frac{2}{3}WO_3 + 2H_2$	3	1.29 x 10^{-2}	288
3.27	$2Zn + 2H_2O \rightarrow 2ZnO + 2H_2$	1	1.23 x 10^{-2}	273
3.25	$\frac{4}{3}In + 2H_2O \rightarrow \frac{2}{3}In_2O_3 + 2H_2$	1.5	0.48 x 10^{-2}	107
3.23	$2SnO + 2H_2O \rightarrow 2SnO_2 + 2H_2$	1	0.84 x 10^{-2}	148
3.19	$6FeO + 2H_2O \rightarrow 2Fe_3O_4 + 2H_2$	0.33	0.43 x 10^{-2}	96
3.21	$2WO_2 + 2H_2O \rightarrow 2WO_3 + 2H_2$	1	0.43 x 10^{-2}	96
3.26	$4NbO_2 + 2H_2O \rightarrow 2Nb_2O_5 + 2H_2$	0.5	0.38 x10^{-2}	84

[a] The sample referred corresponds to the completely oxidised form of metal oxide

These calculations only illustrate theoretical consumption/production of hydrogen, with further experimental evaluation necessary to determine actual degrees of reduction and re-oxidation. This can be quantitatively determined by experimental analysis using temperature programmed reduction.

3.2.2 Experimental Analysis

Temperature programmed reduction (TPR) involves passing a reducing gas across the metal oxide whilst ramping at a constant rate to generate a reduction profile. The information provided by this technique gives not only information regarding the concentration of the reducing gas required for the reduction reaction , but can also provide an insight into the effect upon metal oxide reducibility resulting from introduction of promoter or other metal oxide materials. The presence and identification of different oxidation states can be ascertained, with direct comparison of metal oxide reduction kinetics between various metal oxides made easier by comparing reduction profiles. See following chapter, **Chapter 4** (Experimental Methodology) for details on experimental technique relating to TPR analysis.

H_2 TPR (**Figure 3.3**) shows H_2 consumption during reduction. SnO_2 is completely reduced at the lowest temperature, whilst the reduction temperature of In_2O_3 is comparable to complete reduction of Fe_2O_3. Reduction of WO_3 is known to take place via the following pathway [26. 27]:

$$WO_3 \rightarrow WO_{2.9} \rightarrow WO_2 \rightarrow W$$

This is shown in **Figure 3.3**, with a smaller peak correlating to reduction of WO_3 to $WO_{2.9}$ preceding further reduction to WO_2 followed by WO_2 to W reduction. MoO_3 is reduced to MoO_2, followed by complete reduction of MoO_2 to Mo. Following reduction, both Sn and In were found to have completely melted, due to their low melting points. Nb_2O_5 reduces at much higher temperature, with minimal H_2 consumption.

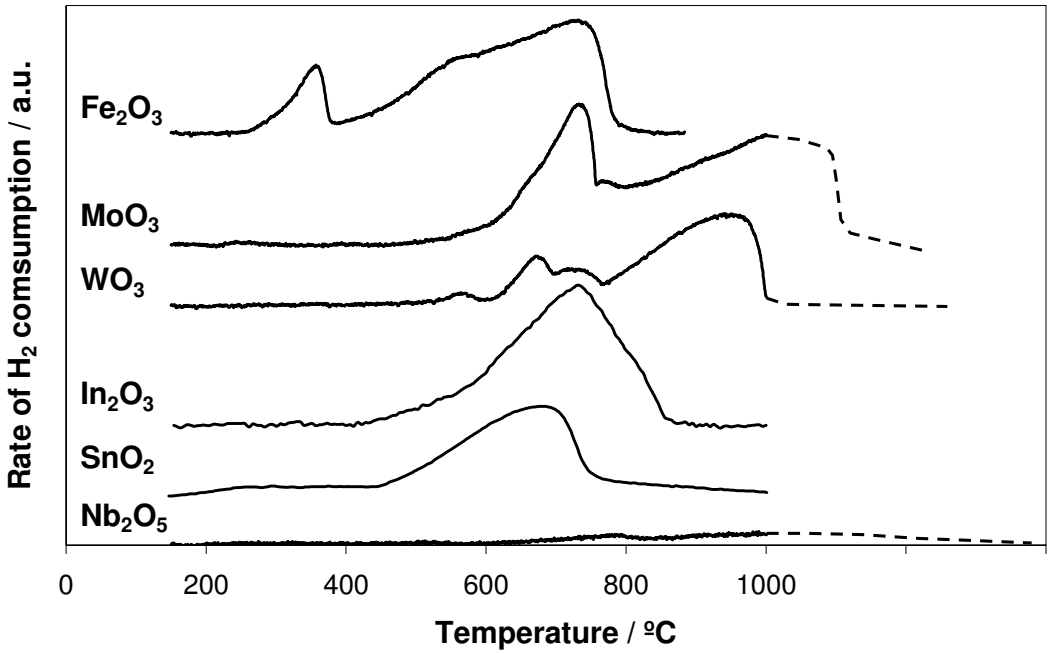

Figure 3.3 5% H_2 TPR of various metal oxides up to 1000°C

TPR gives an approximate determination of OSC for each metal oxide. This study determines that Nb_2O_5 is unsuitable for the Steam-Metal Process, given that the oxide shows minimal H_2 consumption and thus limited OSC, coupled with high temperature reduction. In_2O_3 is also eliminated on the basis of extensive sintering during the redox process coupled with the high cost of using In as a catalyst. MoO_2 is eliminated from further study as reduction of MoO_2 to Mo metal is well known to result carbide formation [28]. A distinct feature of selected metal oxides (SnO_2, Fe_3O_4, WO_3) is the existence of intermediate oxide phases. This has the advantage of mitigating sintering by preventing complete reduction to the metallic form, along with preventing coke or metal carbide formation, which is generally favoured upon complete reduction to the metallic form. Unlike the $WO_3/WO_2/W$ system, complete re-oxidation of MoO_2 to form MoO_3 is thermodynamically limited.

SnO_2 demonstrates a lower temperature of reduction than Fe_3O_4 and high OSC capacity. Despite extensive sintering of Sn upon reduction, there remains scope for further

investigation of SnO_2 as a potential catalyst for the Steam-Metal Process due to the relatively cheap cost of Sn and the possibility for partial reduction of SnO_2 to SnO. It may be possible to find methods for stabilising this intermediate oxide phase, thereby allowing for higher retention of surface area by limiting complete reduction and subsequent melting of Sn metal at low temperature. Furthermore, Sn is relatively cheap which is not prone to carbide formation upon reduction by methane, nor does it catalyse methane decomposition at higher temperature. Methods of mitigating sintering problems following reduction of SnO_2 will be addressed following further study. Experimentally, re-oxidation of SnO by water has shown reasonable hydrogen yield [19, 29]. Re-oxidation of Sn also produces a substantial amount of hydrogen even after melting [17].

Tungsten oxide shows a high level of hydrogen consumption, indicative of high OSC despite higher temperature reduction than Fe_3O_4. Complete reduction of WO_3 to W tends to result in tungsten carbide formation, as addressed later in this study. The possibility for partial reduction of WO_3 to WO_2, which can be re-oxidised by water at low temperature to form WO_3 and hydrogen, has a distinct advantage in both limiting sintering effects, as well as preventing carbide formation.

Whilst Fe_3O_4 metal oxide has been well studied for the Steam-Metal Process and possesses both high OSC coupled with low temperature reduction, there are issues as previously outlined, including sintering and carbon deposition during reduction, resulting in catalyst deactivation. These will be addressed later in this study. Of the various metal oxides assessed for use in a Steam-Metal type process, WO_3 and SnO_2 have been selected for further study, along with a more in depth investigation of Fe_3O_4.

3.3 Thermodynamic Assessment of Chosen Oxides

3.3.1 Possible reactions during Steam-Metal Process

The possible occurrence of side reactions and the formation of intermediates and other products can be predicted by application of **Equations 3.3** to **3.5** and **Equation 3.7**. Reduction may result in formation of CO_2 and H_2O, rather than the preferred products of CO and H_2. Comparison between reaction processes and calculation of formation of other products shows partial oxidation of CH_4 to form CO and H_2 tends to be favoured at higher methane concentration, with a ratio of one mole of methane required per oxygen atom removed. At lower concentration of methane, complete oxidation of CH_4 to form CO_2 and H_2O is more likely, with a ratio of one mole of methane necessary for removal of four oxygen atoms. Plots of Gibbs Free Energy as a function of temperature for all potential reactions and products during reduction of the various metal oxides are presented below (**Figure 3.4** - **Figure 3.9**). All equations and calculations are calculated per mole O_2 removed.

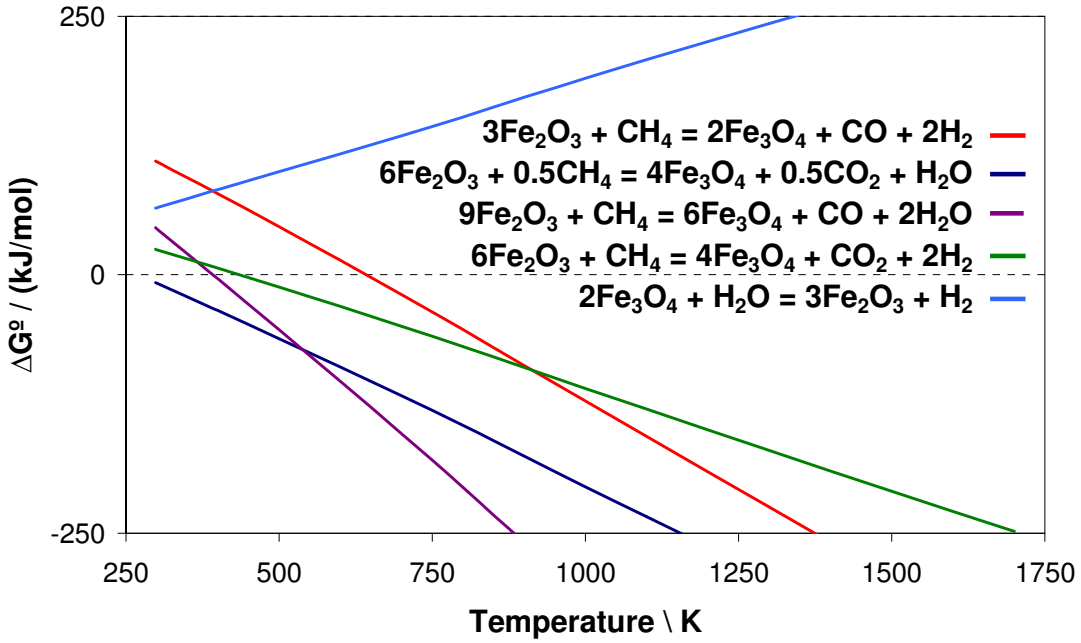

Figure 3.4 Reduction of Fe_2O_3 by CH_4 and re-oxidation of Fe_3O_4 by H_2O

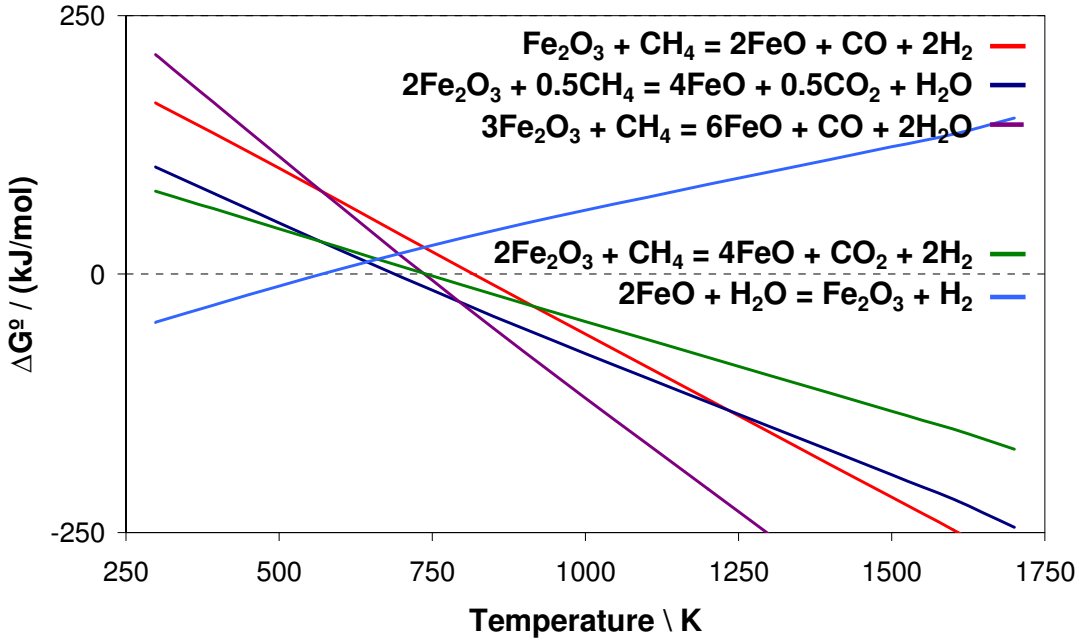

Figure 3.5 Reduction of Fe_2O_3 by CH_4 and re-oxidation of FeO by H_2O

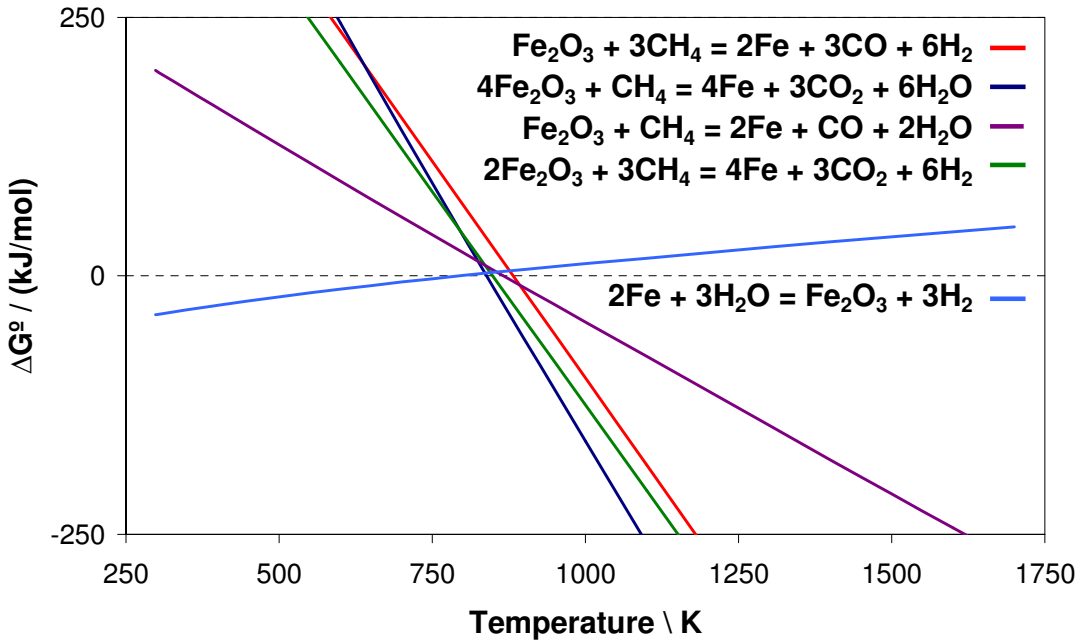

Figure 3.6 Reduction of Fe_2O_3 by CH_4 and re-oxidation of Fe by H_2O

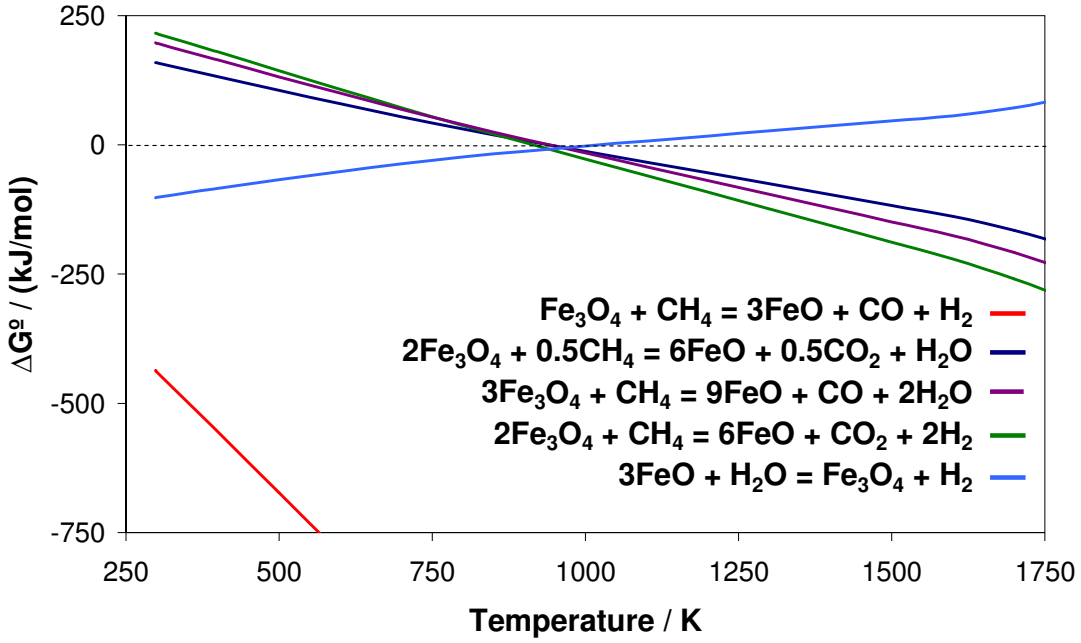

Figure 3.7 Reduction of Fe_3O_4 by CH_4 and re-oxidation of FeO by H_2O

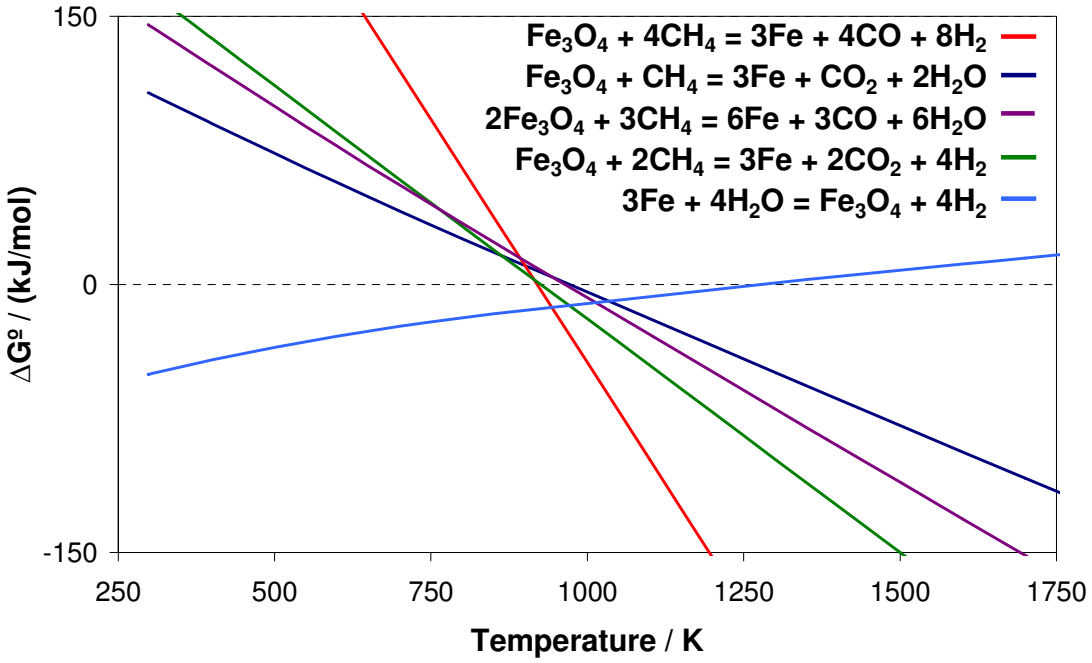

Figure 3.8 Reduction of Fe_3O_4 by CH_4 and re-oxidation of Fe by H_2O

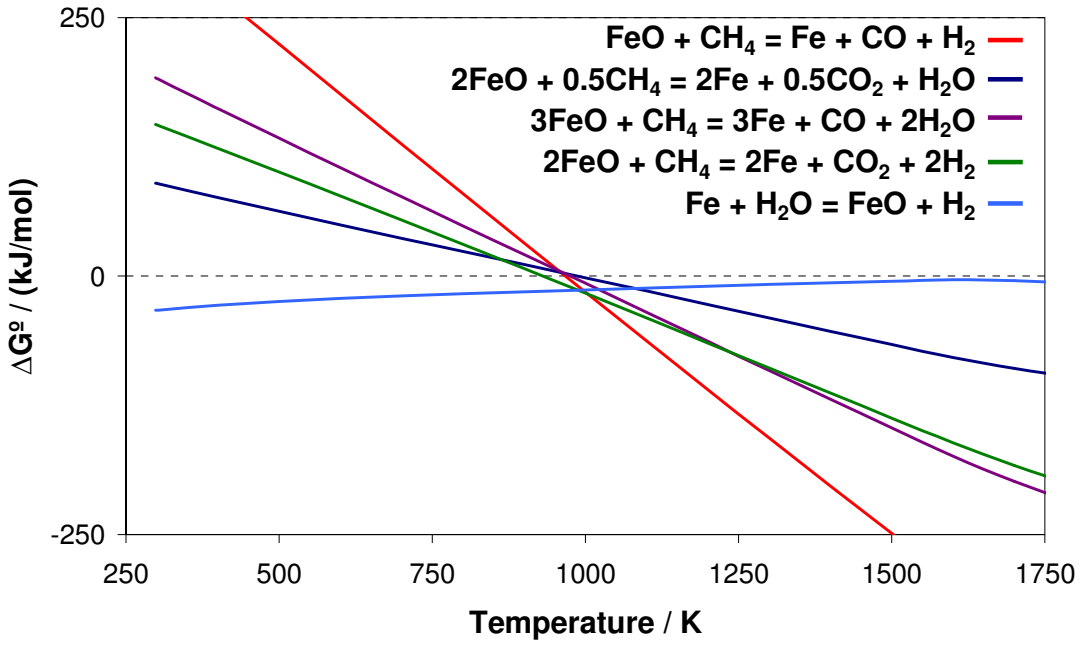

Figure 3.9 Reduction of FeO by CH_4 and re-oxidation of Fe by H_2O

Reduction of Fe_2O_3 is known to follow the pathway Fe_2O_3 to Fe_3O_4 to FeO to Fe [30]. This is also observed through thermodynamic calculations (**Figure 3.4** - **Figure 3.9**). Initial reduction of Fe_2O_3 to Fe_3O_4 shows CO_2 and H_2O to be the favoured products at lower temperature, $6Fe_2O_3 + ½CH_4 \rightarrow 4Fe_3O_4 + ½CO_2 + H_2O$, (**Figure 3.4** - **Figure 3.6**). Re-oxidation of Fe_3O_4 to re-form Fe_2O_3 is unachievable, with Fe_3O_4 the highest possible oxidation state upon re-oxidation with H_2O (**Figure 3.4**). Reduction of Fe_3O_4 to FeO to form CO + H_2 is the predominant reaction (**Figure 3.7**), followed by slight favourability for reduction of FeO to Fe forming CO + H_2 formation at higher temperature (**Figure 3.9**). Whilst FeO exists as an intermediate oxidation phase, this is also known to be metastable at high temperatures and it is not expected that complete reduction of Fe_3O_4 to FeO will occur prior to FeO to Fe reduction [30].

To further assess the thermodynamic probability of over-reduction to form CO_2 and/or H_2O, the subsequent reduction of each metal oxide by the CO and H_2 products is also considered (**Figure 3.10** - **Figure 3.12**).

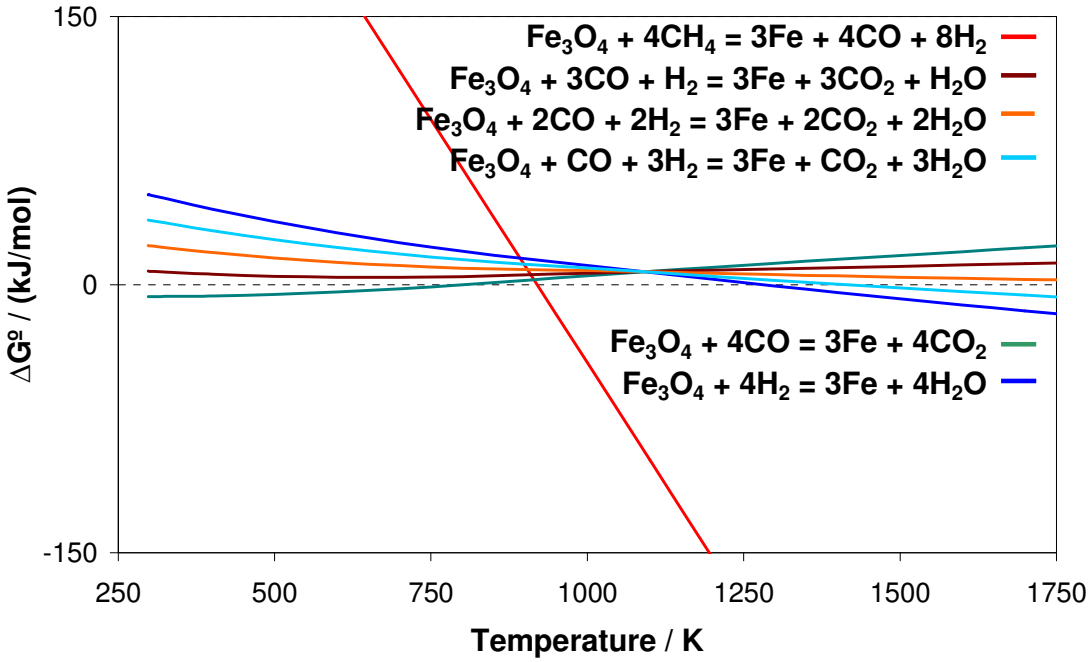

Figure 3.10 Over-reduction of Fe_3O_4/Fe to from CO_2 and H_2O

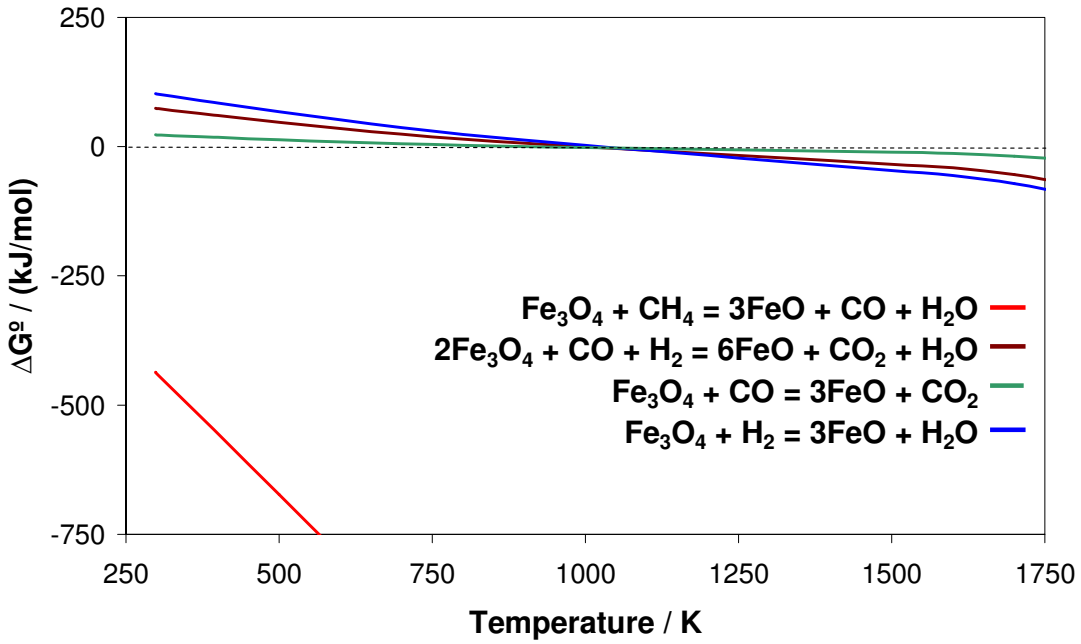

Figure 3.11 Over-reduction of Fe_3O_4/FeO to form CO_2 and H_2O

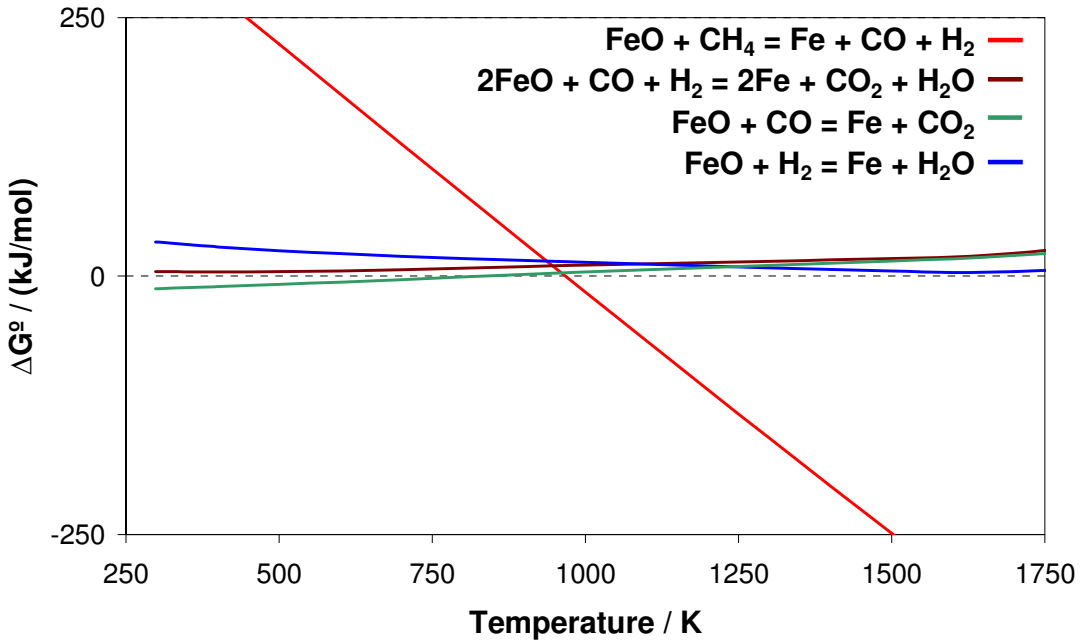

Figure 3.12 Over-reduction of FeO/Fe to form CO_2 and H_2O

Based upon these graphs (**Figure 3.10** - **Figure 3.12**)., all forms of iron oxide show low affinity for further reduction by CO + H_2 resulting in formation of CO_2 and H_2O, in contrast to the thermodynamic favourability of desired reaction producing CO + H_2 from reduction by CH_4. All lines corresponding to further reduction by CO and H_2 show minimal favourability based upon negative values of Gibbs Free Energy over a large temperature range.

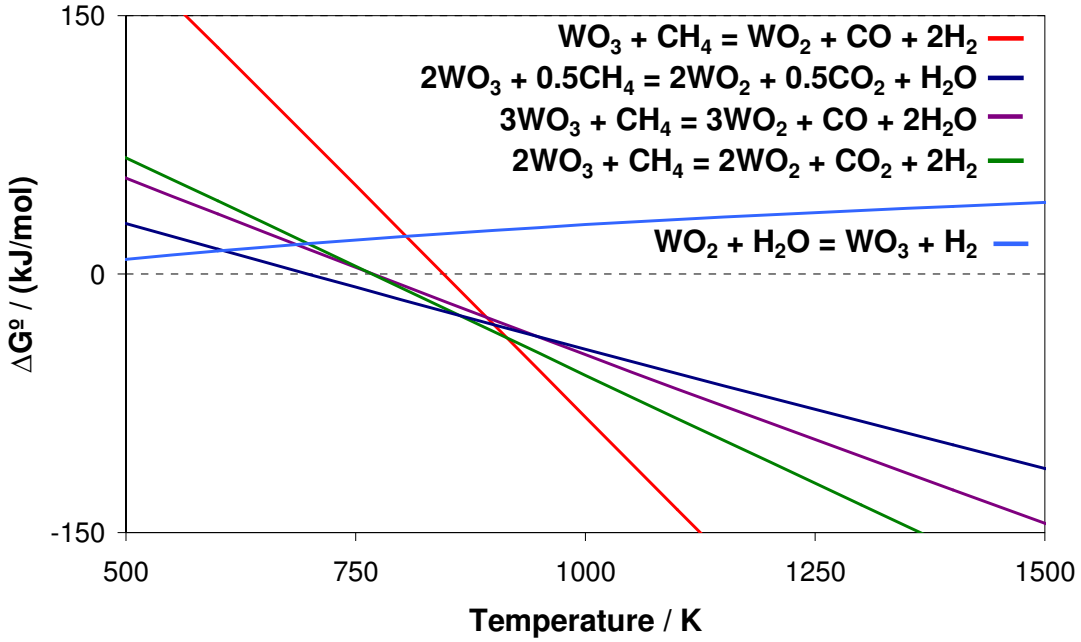

Figure 3.13 Reduction of WO_3 by CH_4 and re-oxidation of WO_2 by H_2O

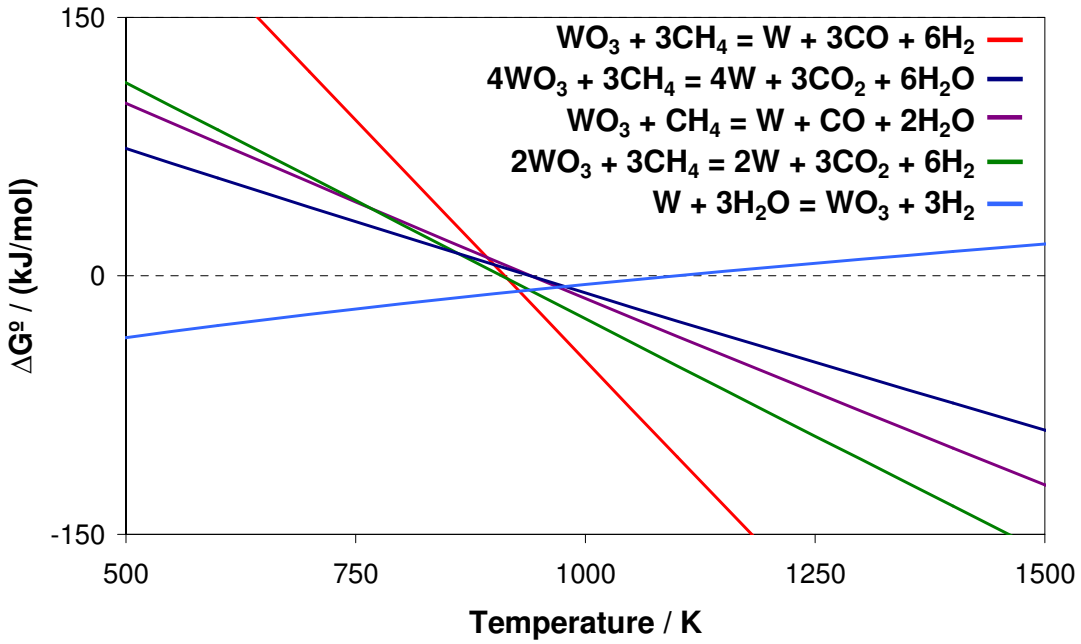

Figure 3.14 Reduction of WO_3 by CH_4 and re-oxidation of W by H_2O

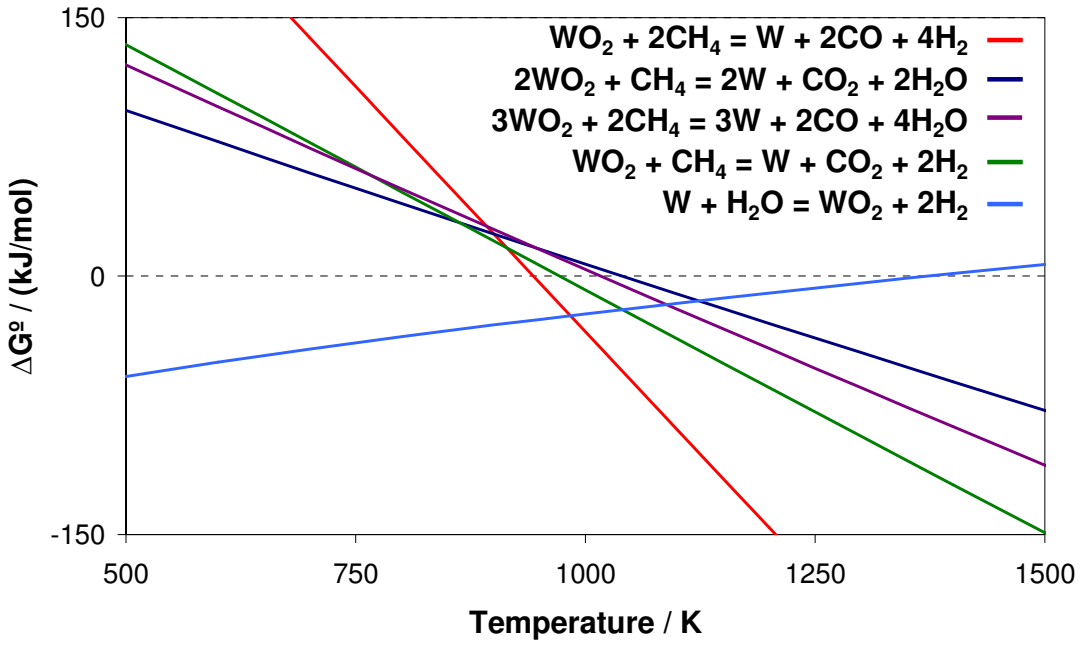

Figure 3.15 Reduction of WO_2 by CH_4 and re-oxidation of W by H_2O

Reduction of WO_3 to WO_2 shows preference for CO + H_2 production only at higher temperature, with re-oxidation unfavourable except at much lower temperatures (**Figure 3.13**, **Figure 3.14**). Despite this, re-oxidation of W to WO_3 is shown to proceed at moderate temperature (**Figure 3.14**), <1100K, therefore WO_3 is worth investigating. Thermodynamic data indicates a two-step reduction in which initial reduction of WO_3 to WO_2 is followed by WO_2 to W reduction. Formation of CO + H_2 upon WO_2 to W reduction is shown to be favourable over a wider range of temperatures (**Figure 3.15**), with re-oxidation by H_2O to form WO_2 and possibly WO_3 also favourable.

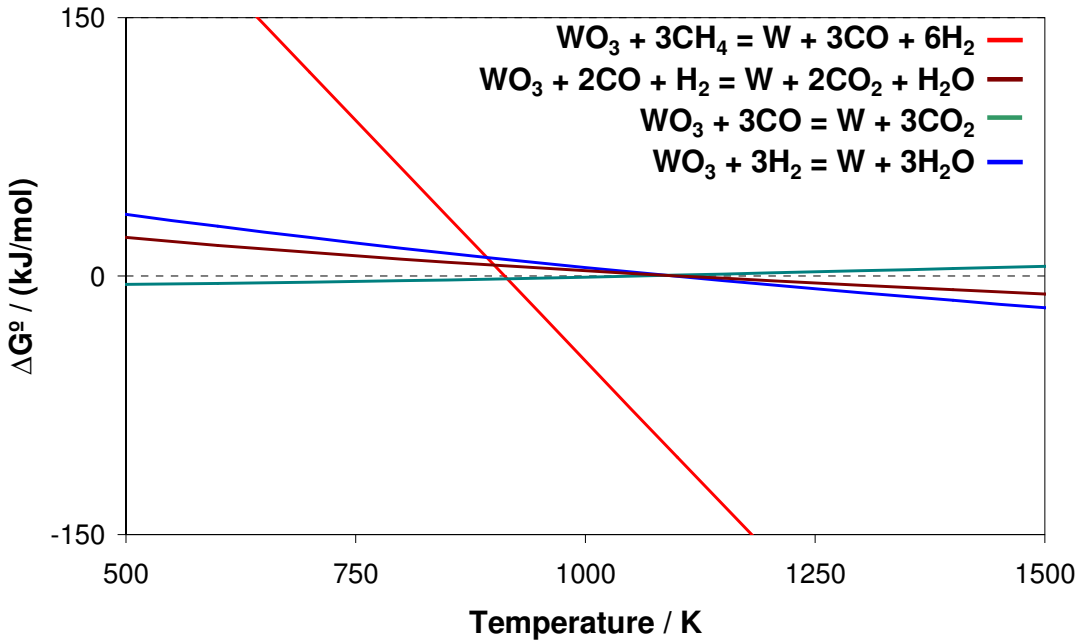

Figure 3.16 Over-reduction of WO_3/W to form CO_2 and H_2O

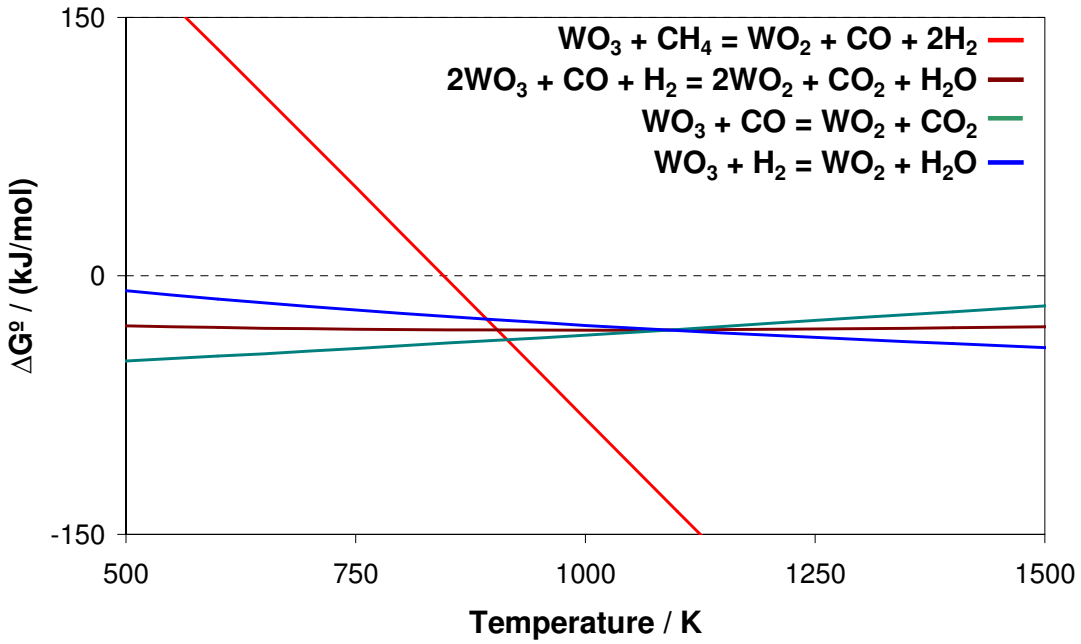

Figure 3.17 Over-reduction of WO_3/WO_2 to form CO_2 and H_2O

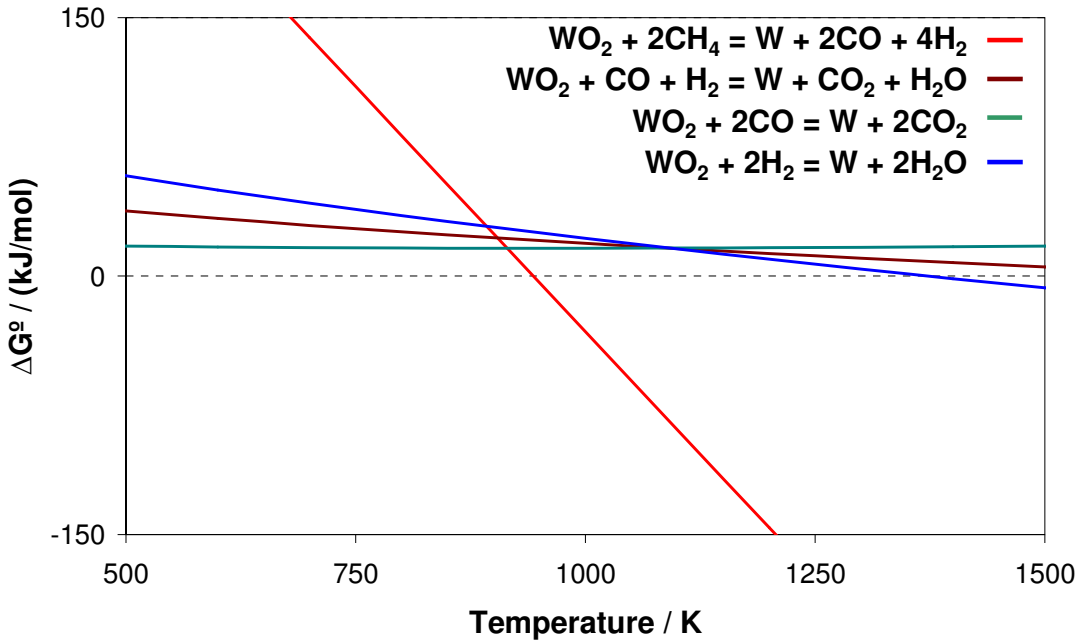

Figure 3.18 Over-reduction of WO_2 to form CO_2 and H_2O

Reduction of WO_3 to WO_2 shows that, at lower temperatures, reduction of WO_3 by CO and H_2 can take place, forming CO_2 and H_2O (**Figure 3.17**). Therefore, to give preferential formation of CO and H_2, it is necessary to perform reduction at higher temperatures, such that these products are thermodynamically more favourable than the former. Reduction of WO_2 shows formation of CO and H_2 products over a wide range of temperatures, rather than formation of CO_2 and H_2O (**Figure 3.18**).

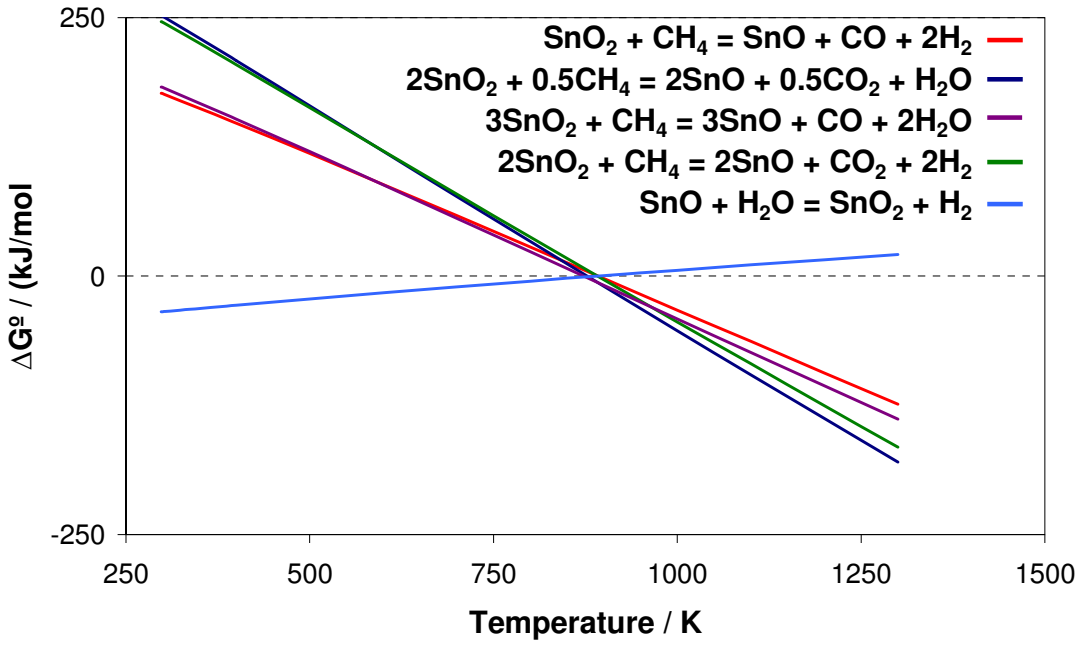

Figure 3.19 Reduction of SnO_2 by CH_4 and re-oxidation of SnO by H_2O

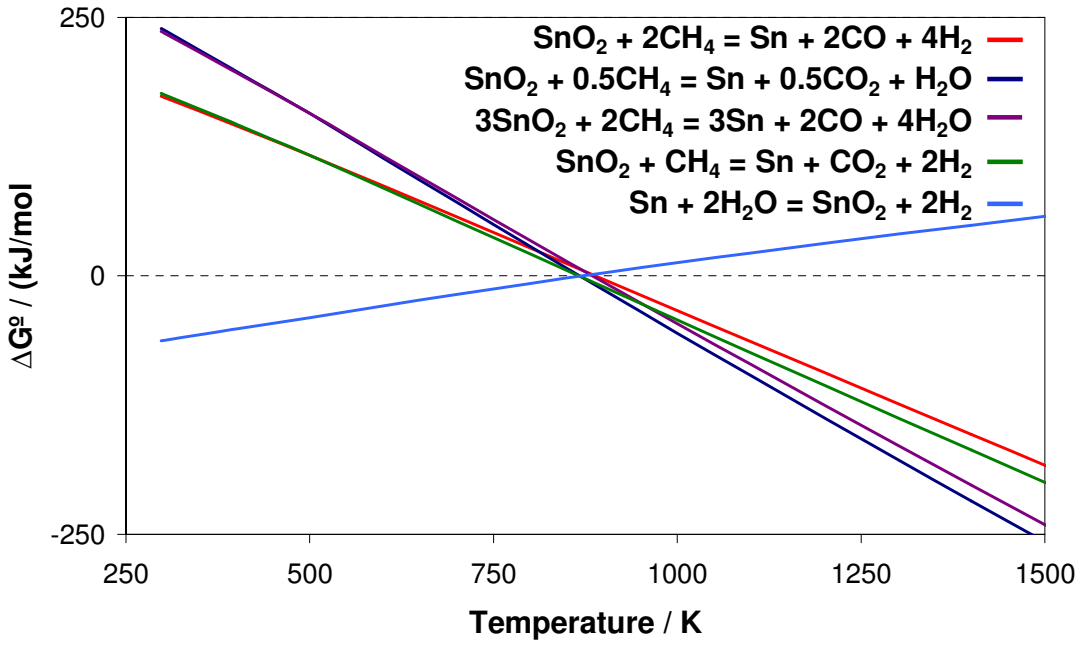

Figure 3.20 Reduction of SnO_2 by CH_4 and re-oxidation of Sn by H_2O

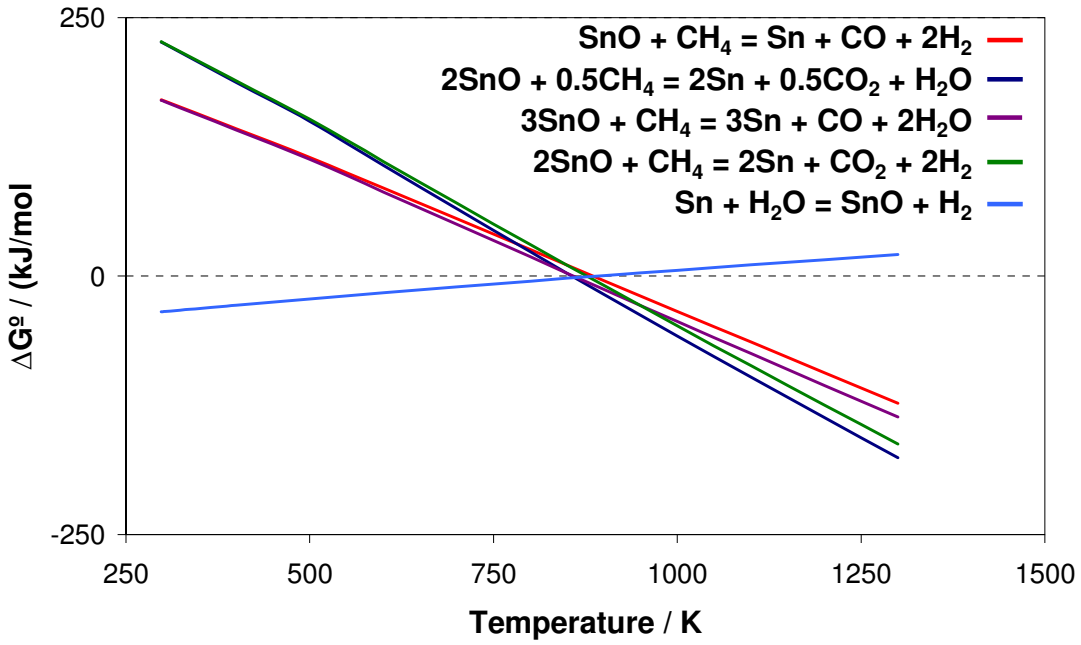

Figure 3.21 Reduction of SnO by CH_4 and re-oxidation of Sn by H_2O

Reduction of SnO_2 to SnO/Sn shows a large degree of overlap between SnO_2 to SnO reduction and SnO_2 to Sn reduction (**Figure 3.19**, **Figure 3.20**). From thermodynamics, it is difficult to determine whether the reduction will take place in a two-step process, initially forming SnO then reducing to Sn (**Figure 3.21**), or reducing directly from SnO_2 to Sn. TPR data shows a single peak, indicative of overlapping between SnO_2 to SnO and SnO to Sn reduction (**Figure 3.3**). Formation of CO_2 + H_2O is highly favoured at all temperatures at which reduction takes place, with re-oxidation indicative that a SnO_2/Sn cycle is achievable. However, due to the low melting point of Sn, it is advantageous to achieve partial oxidation if possible, whereupon a SnO_2/SnO cycle would prevent the extensive sintering associated with complete reduction to form Sn.

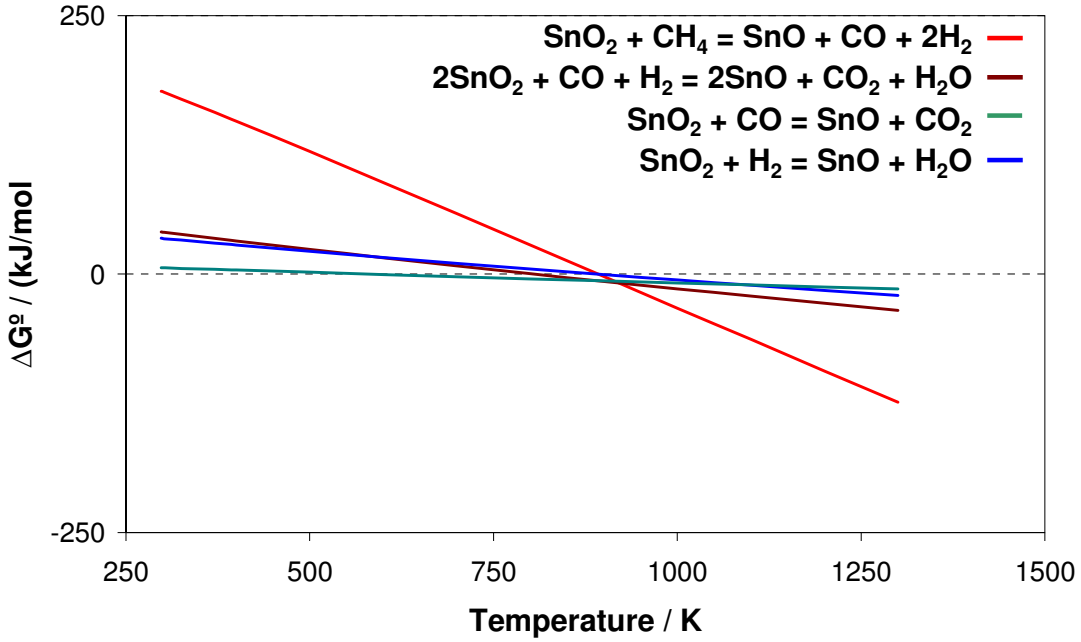

Figure 3.22 Over-reduction of SnO_2/Sn to form CO_2 and H_2O

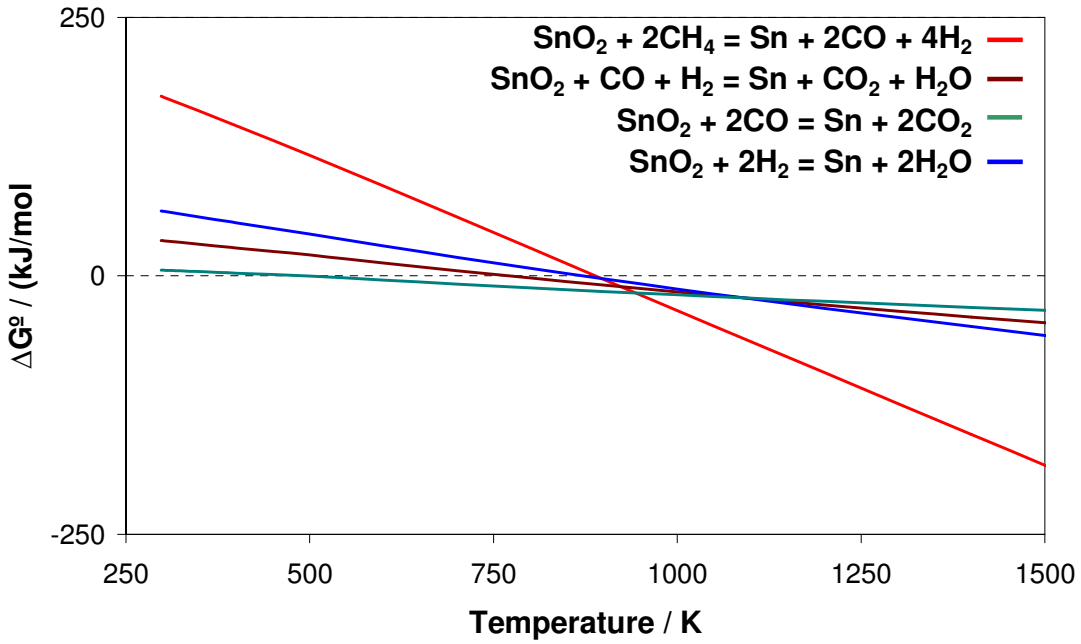

Figure 3.23 Over-reduction of SnO_2/Sn to form CO_2 and H_2O

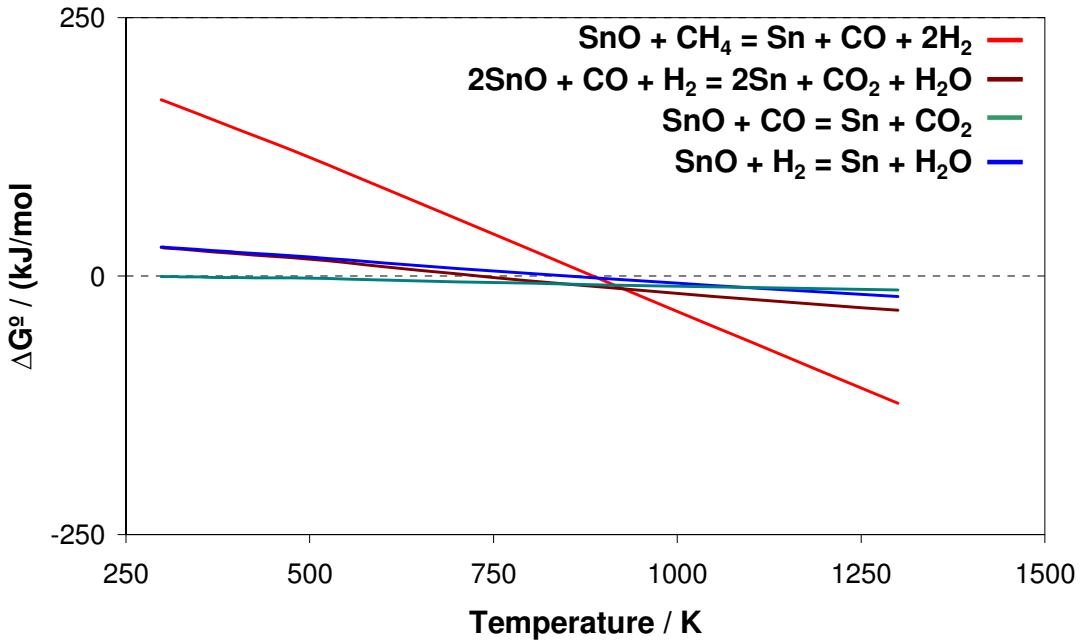

Figure 3.24 Over-reduction of SnO/Sn to form CO_2 and H_2O

In all cases, SnO_x is preferentially reduced by CH_4 to form CO + H_2, as indicated by comparison between **Figure 3.19 - Figure 3.21** and **Figure 3.22 - Figure 3.24**, with complete oxidation of CO and H_2 unlikely until much higher temperatures are reached. Gupta et al. show through calculation of phase equilibrium diagrams, reaction of CO and H_2 over SnO_2 to form CO_2 and H_2O is relatively poor in comparison to other metal oxides examined [31].

3.3.2 Routes to hydrogen product contamination and catalyst deactivation during the Steam-Metal Process

Formation of metal carbide species as a possible reaction from methane reduction of metal oxides is detrimental toward the Steam-Metal process [32, 33], due to the resultant contamination of H_2 produced upon re-oxidation. This arises from the re-oxidation of the metal carbide, resulting in CO_x production.

$$M_xC + yH_2O \rightarrow M_xO_y + yH_2$$

The likelihood of carbide formation may be assessed and minimised by employing certain experimental criteria to help favour specific products whilst limiting the extent of carbide formation [34]. Calculation of possible carbide formation routes from both CH_4 reactant and CO product is tabulated below for reduction of iron and tungsten oxides and compared to reduction of the respective metal oxides to a lower oxidation state or to the metal form (**Table 3-2** - **Table 3-10**). These reaction processes are also presented in graphical form, with plotting of Gibbs Free Energy as a function of temperature highlighting the temperature requirements for the formation of metal carbides to become a favourable process (**Figure 3.25** - **Figure 3.33**).

The formation of tin carbide has been reported as entirely unfavourable with tin carbide found not to be a stable compound [35].

Table 3-2 Carbide formation (Fe_3C) during Fe_3O_4 reduction by CH_4

Key	Reaction	
	$\frac{1}{2}Fe_3O_4 + 2CH_4 \rightarrow \frac{3}{2}Fe + 2CO + 4H_2$	**3.8**
	$Fe_3O_4 + 5CH_4 \rightarrow Fe_3C + 4CO + 10H_2$	**3.28**
	$2Fe_3O_4 + 3CH_4 \rightarrow 2Fe_3C + CO_2 + 6H_2O$	**3.29**
	$3Fe_3O_4 + 5CH_4 \rightarrow 3Fe_3C + 2CO + 10H_2O$	**3.30**
	$Fe_3O_4 + 3CH_4 \rightarrow Fe_3C + 2CO_2 + 6H_2$	**3.31**
	$Fe_3O_4 + 2CO + 4H_2 \rightarrow Fe_3C + CO_2 + 4H_2O$	**3.32**
	$Fe_3O_4 + CO + 5H_2 \rightarrow Fe_3C + 5H_2O$	**3.33**

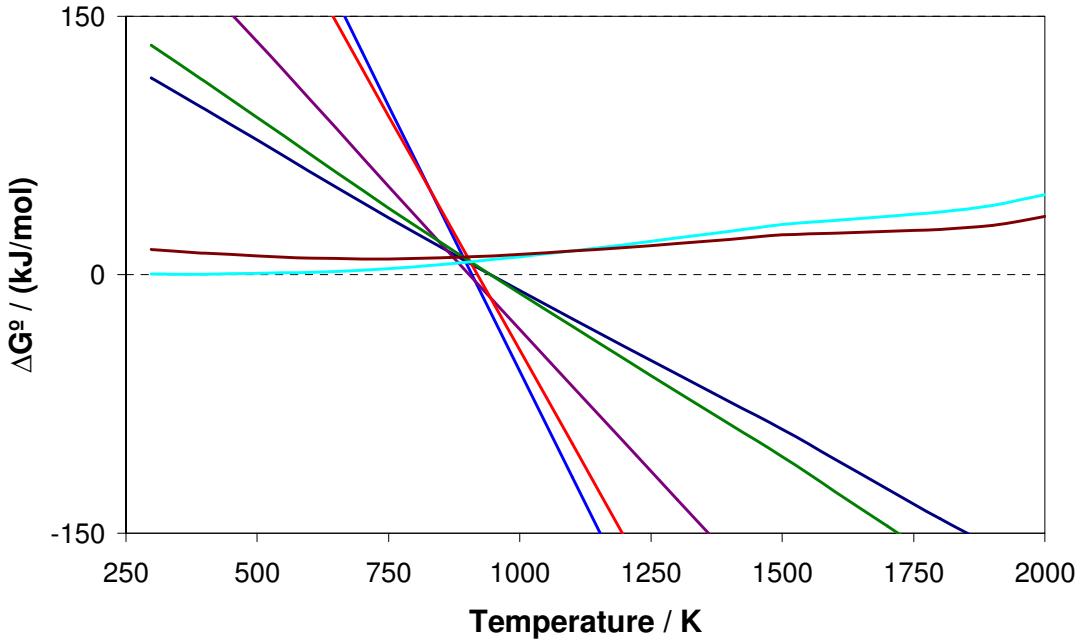

Figure 3.25 Carbide formation (Fe_3C) during Fe_3O_4 reduction by CH_4

Table 3-3 Carbide formation (Fe_3C) during FeO reduction by CH_4

Key	Reaction	
	$FeO + CH_4 \rightarrow Fe + CO + 2H_2$	**3.34**
	$3FeO + 4CH_4 \rightarrow Fe_3C + 3CO + 8H_2$	**3.35**
	$12FeO + 5CH_4 \rightarrow 4Fe_3C + CO_2 + 10H_2O$	**3.36**
	$9FeO + 4CH_4 \rightarrow 3Fe_3C + CO + 8H_2O$	**3.37**
	$3FeO + 2CH_4 \rightarrow Fe_3C + CO_2 + 4H_2$	**3.38**
	$3FeO + 5CO \rightarrow Fe_3C + 4CO_2$	**3.39**
	$3FeO + 2CO + 3H_2 \rightarrow Fe_3C + CO_2 + 3H_2O$	**3.40**
	$3FeO + CO + 4H_2 \rightarrow Fe_3C + 4H_2O$	**3.41**

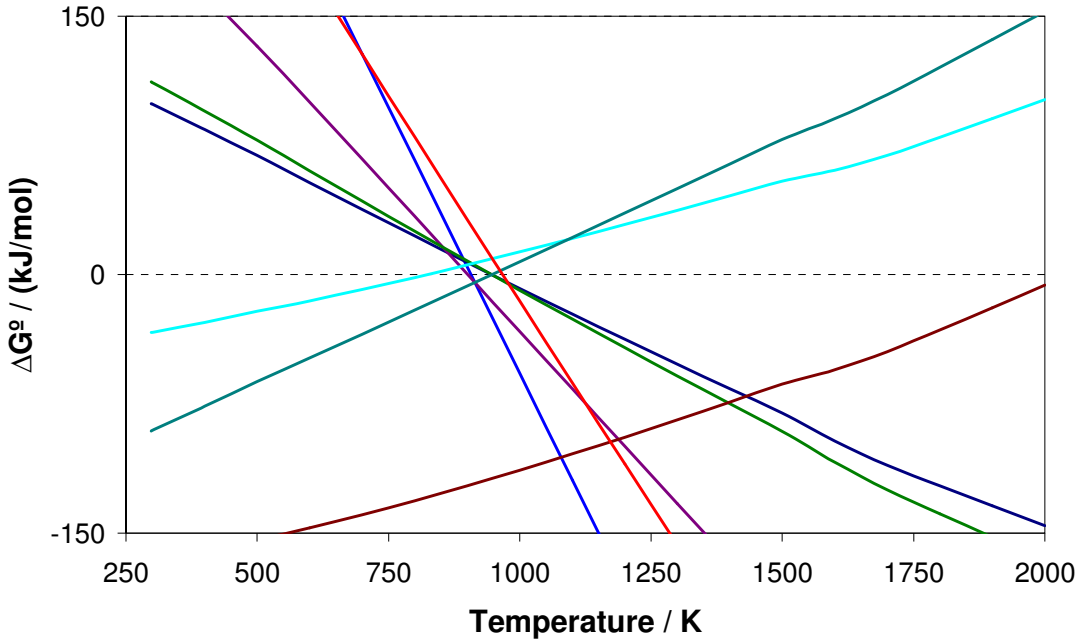

Figure 3.26 Carbide formation (Fe_3C) during FeO reduction by CH_4

Table 3-4 Carbide formation from Fe (Fe_3C) during Fe_3O_4/FeO reduction by CH_4

Key	Reaction	
	$3Fe + CH_4 \rightarrow Fe_3C + 2H_2$	**3.42**
	$3Fe + 2CO \rightarrow Fe_3C + CO_2$	**3.43**
	$6Fe + 3CO + H_2 \rightarrow 2Fe_3C + CO_2 + H_2O$	**3.44**
	$3Fe + CO + H_2 \rightarrow Fe_3C + H_2O$	**3.45**

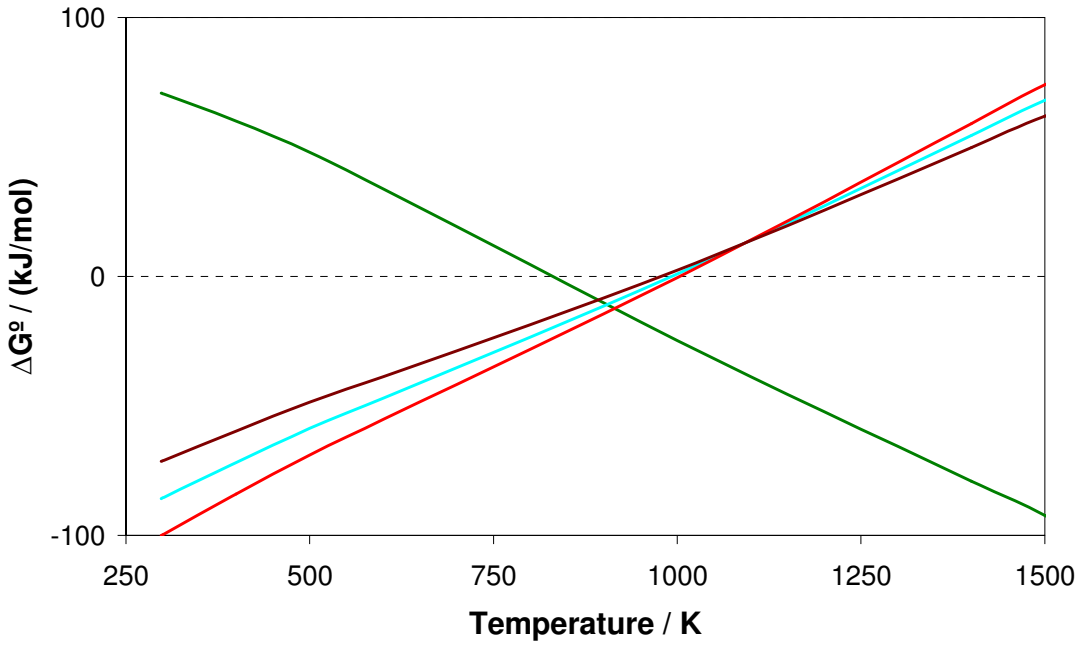

Figure 3.27 Carbide formation (Fe_3C) from Fe during reduction of Fe_3O_4/FeO by CH_4

Table 3-5 Carbide formation (W_2C) during reduction of WO_3 by CH_4

Key	Reaction	
	$\frac{2}{3}WO_3 + 2CH_4 \rightarrow \frac{2}{3}W + 2CO + 4H_2$	**3.10**
	$2WO_3 + 2CH_4 \rightarrow 2WO_2 + 2CO + 4H_2$	**3.11**
	$2WO_3 + 7CH_4 \rightarrow W_2C + 6CO + 14H_2$	**3.46**
	$4WO_3 + 4CH_4 \rightarrow 2W_2C + 2CO_2 + 8H_2O$	**3.47**
	$6WO_3 + 7CH_4 \rightarrow 3W_2C + 4CO + 14H_2O$	**3.48**
	$2WO_3 + 4CH_4 \rightarrow W_2C + 3CO_2 + 8H_2$	**3.49**
	$2WO_3 + 8CO \rightarrow W_2C + 7CO_2$	**3.50**
	$2WO_3 + 2CO + 6H_2 \rightarrow W_2C + CO_2 + 6H_2O$	**3.51**
	$2WO_3 + CO + 7H_2 \rightarrow W_2C + 7H_2O$	**3.52**

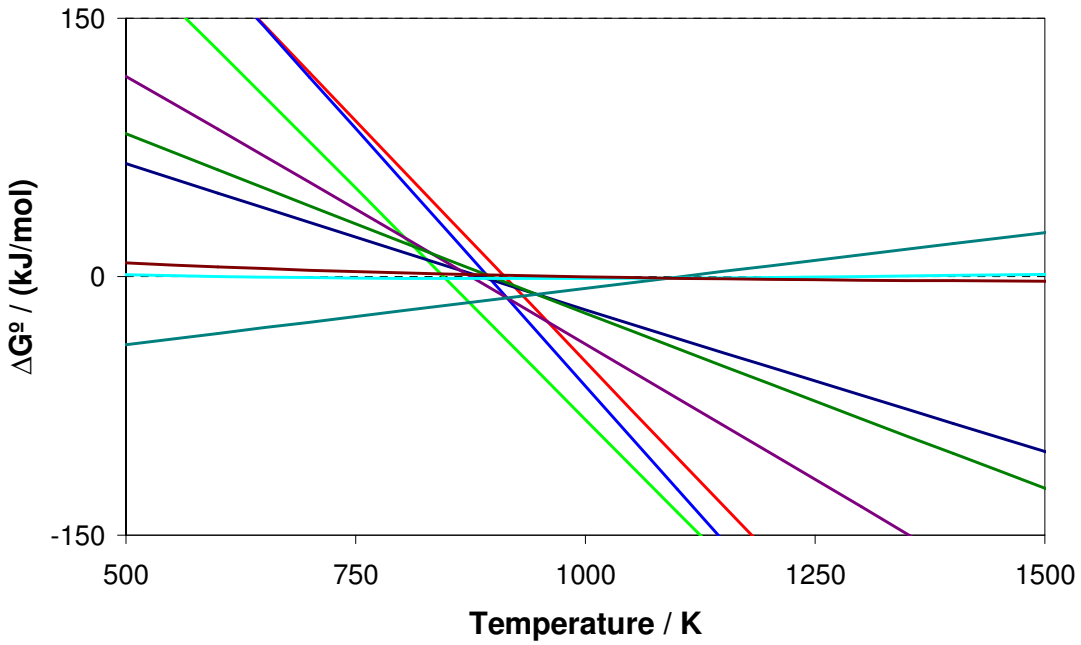

Figure 3.28 Carbide formation (W_2C) during reduction of WO_3 by CH_4

Table 3-6 Carbide formation (WC) during reduction of WO_3 by CH_4

Key	Reaction	
	$\frac{2}{3}WO_3 + 2CH_4 \rightarrow \frac{2}{3}W + 2CO + 4H_2$	**3.10**
	$2WO_3 + 2CH_4 \rightarrow 2WO_2 + 2CO + 4H_2$	**3.11**
	$WO_3 + 4CH_4 \rightarrow WC + 3CO + 8H_2$	**3.53**
	$4WO_3 + 5CH_4 \rightarrow 4WC + CO_2 + 10H_2O$	**3.54**
	$3WO_3 + 4CH_4 \rightarrow 3WC + CO + 8H_2O$	**3.55**
	$2WO_3 + 5CH_4 \rightarrow 2WC + 3CO_2 + 10H_2$	**3.56**
	$WO_3 + 5CO \rightarrow WC + 4CO_2$	**3.57**
	$WO_3 + 2CO + 3H_2 \rightarrow WC + CO_2 + 3H_2O$	**3.58**
	$WO_3 + CO + 4H_2 \rightarrow WC + 4H_2O$	**3.59**

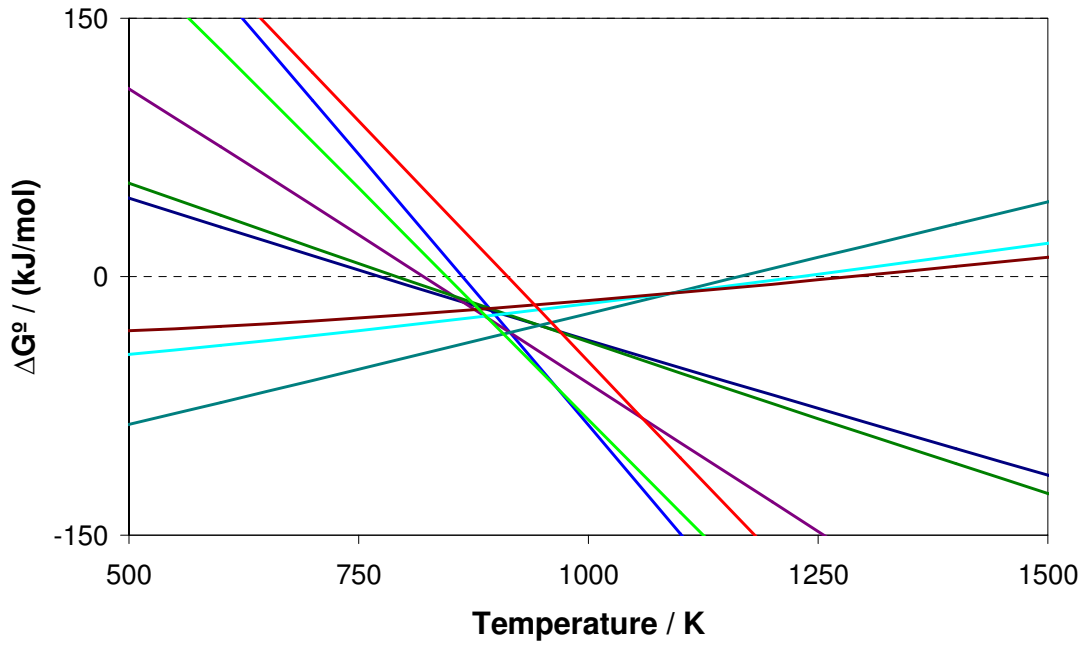

Figure 3.29 Carbide formation (WC) during reduction of WO_3 by CH_4

Table 3-7 Carbide formation (W_2C) during reduction of WO_2 by CH_4

Key	Reaction	
	$WO_2 + 2CH_4 \rightarrow W + 2CO + 4H_2$	**3.60**
	$2WO_2 + 5CH_4 \rightarrow W_2C + 4CO + 10H_2$	**3.61**
	$4WO_2 + 3CH_4 \rightarrow 2W_2C + CO_2 + 6H_2O$	**3.62**
	$6WO_2 + 5CH_4 \rightarrow 3W_2C + 2CO + 10H_2O$	**3.63**
	$2WO_2 + 3CH_4 \rightarrow W_2C + 2CO_2 + 6H_2$	**3.64**
	$2WO_2 + 6CO \rightarrow W_2C + 5CO_2$	**3.65**
	$2WO_2 + 2CO + 4H_2 \rightarrow W_2C + CO_2 + 4H_2O$	**3.66**
	$2WO_2 + CO + 3H_2 \rightarrow W_2C + 3H_2O$	**3.67**

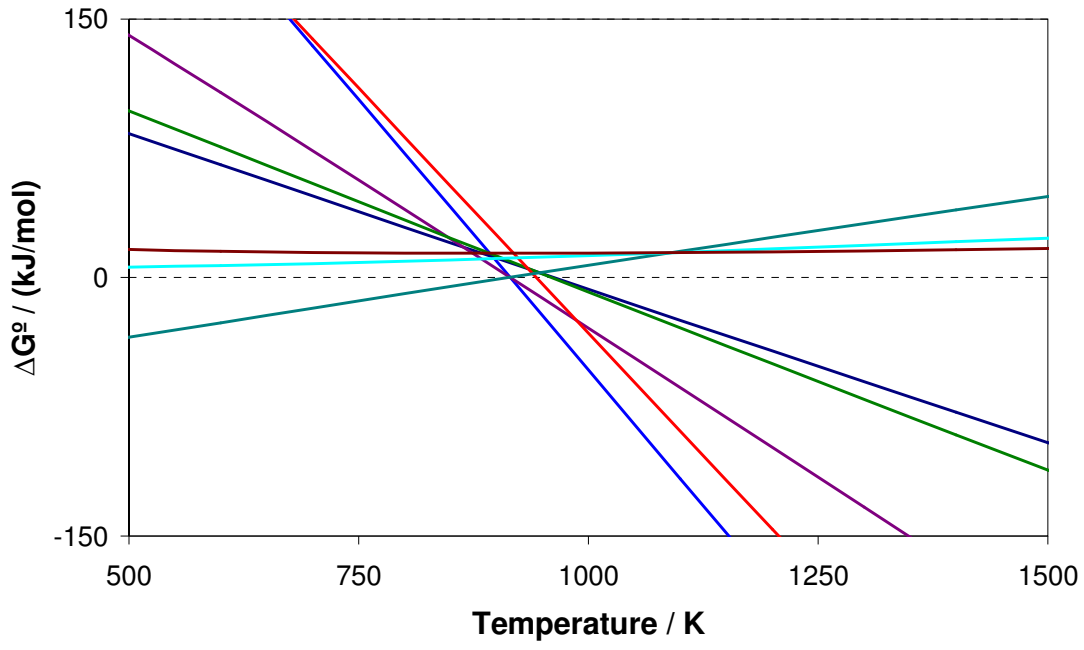

Figure 3.30 Carbide formation (W_2C) during reduction of WO_2 by CH_4

Table 3-8 Carbide formation (WC) during reduction of WO_2 by CH_4

Key	Reaction	
	$WO_2 + 2CH_4 \rightarrow W + 2CO + 4H_2$	**3.60**
	$WO_2 + 3CH_4 \rightarrow WC + 2CO + 6H_2$	**3.68**
	$WO_2 + 2CH_4 \rightarrow WC + CO_2 + 4H_2$	**3.69**
	$WO_2 + CH_4 \rightarrow WC + 2H_2O$	**3.70**
	$WO_2 + 4CO \rightarrow WC + 3CO_2$	**3.71**
	$WO_2 + 2CO + 2H_2 \rightarrow WC + CO_2 + 2H_2O$	**3.72**
	$WO_2 + CO + 3H_2 \rightarrow WC + 3H_2O$	**3.73**

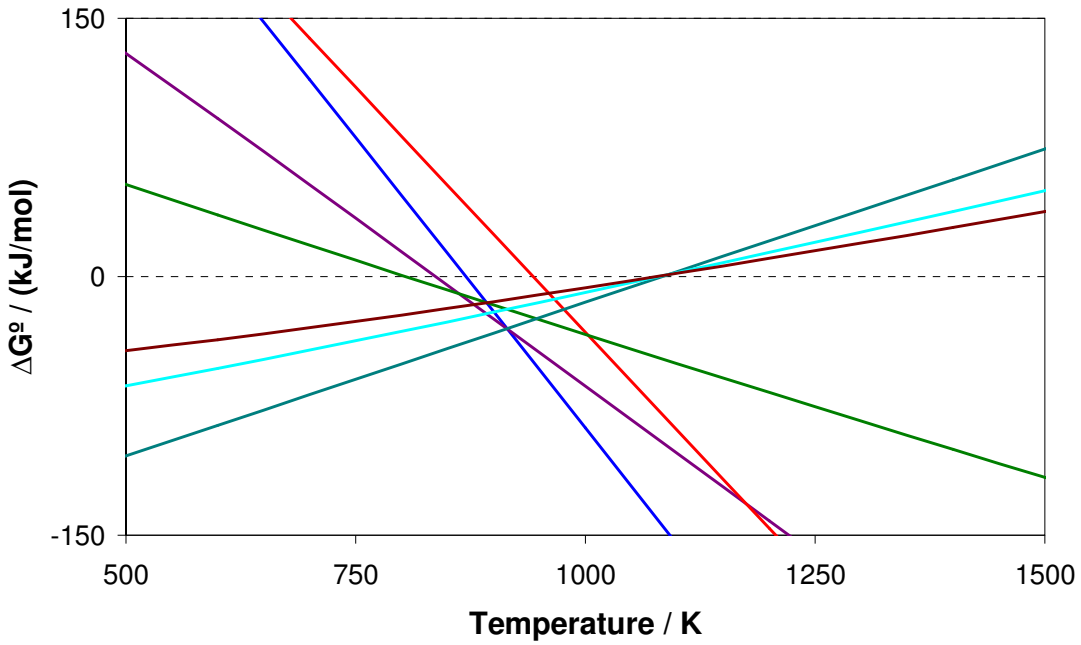

Figure 3.31 Carbide formation (WC) during reduction of WO_2 by CH_4

Table 3-9 Carbide formation from W (W_2C) during WO_3/WO_2 reduction by CH_4

Key	Reaction	
	$2W + CH_4 \rightarrow W_2C + 2H_2$	**3.74**
	$2W + 2CO \rightarrow W_2C + CO_2$	**3.75**
	$6W + 4CO + 2H_2 \rightarrow 3W_2C + CO_2 + 2H_2O$	**3.76**
	$2W + CO + H_2 \rightarrow W_2C + H_2O$	**3.77**

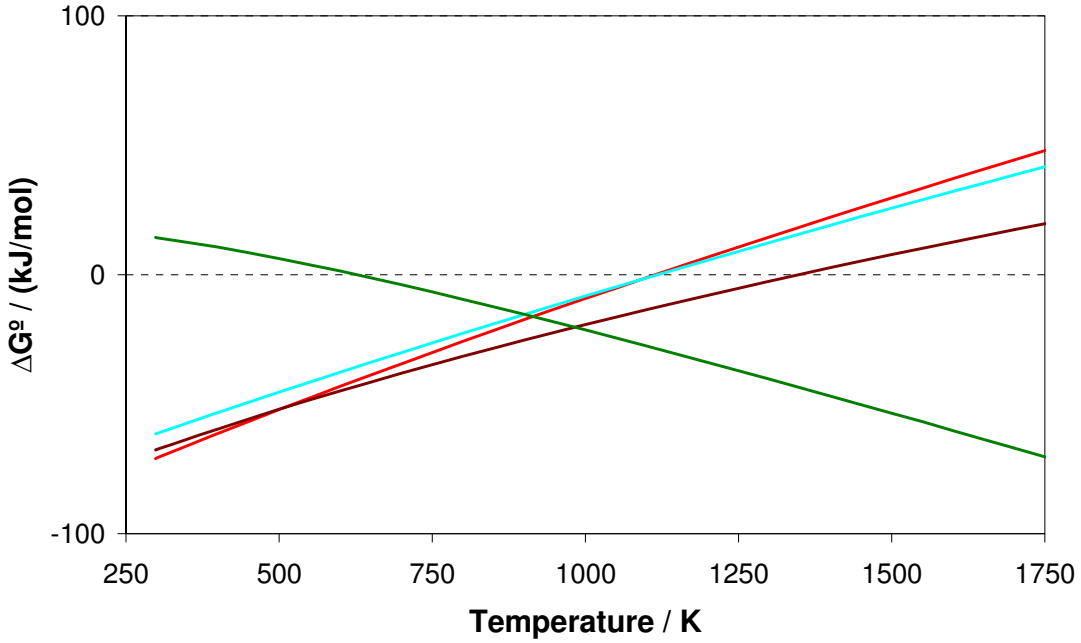

Figure 3.32 Carbide formation from W (W_2C) during WO_2/WO_3 reduction by CH_4

Table 3-10 Carbide formation (WC) from W during WO_3/WO_2 reduction by CH_4

Key	Reaction	
	$W + CH_4 \rightarrow WC + 2H_2$	**3.78**
	$W + 2CO \rightarrow WC + CO_2$	**3.79**
	$2W + 3CO + H_2 \rightarrow 2WC + CO_2 + H_2O$	**3.80**
	$W + CO + H_2 \rightarrow WC + H_2O$	**3.81**

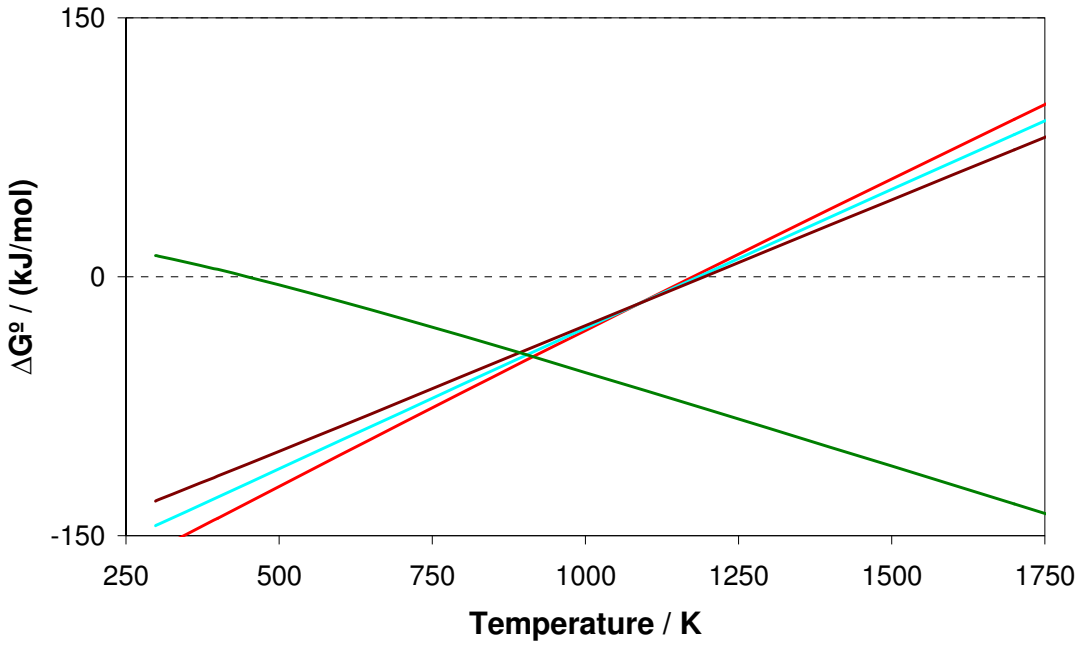

Figure 3.33 Carbide formation (WC) from W during WO_3/WO_2 reduction by CH_4

Based upon the graphing of Gibbs Free Energy versus temperature (**Figure 3.25** - **Figure 3.33**), iron and tungsten oxides show the possibility for metal carbide formation [34]. The reactions for formation of metal carbides show this to be a favourable process at higher temperatures, with the possibility for a number of competing reactions at the temperature of reduction in the reaction process [35-37]. The formation of metal carbide with CO + H_2 competes directly with formation of the corresponding metal and CO + H_2 (**Table 3-2**-**Table 3-10**). In addition, there is also the possibility for formation of CO_2 and/or H_2O in the product gases. Formation of metal carbide from fully reduced metals is high.

To prevent carbide formation it may be possible to achieve partial oxidation to a lower oxidation state and in doing so, not only prevent metal carbide formation, but also limit the occurrence of methane decomposition. Other means of preventing carbide formation could involve the use of promoters which may either aid to stabilise intermediate metal oxides or possibly inhibit formation of metal carbide and/or carbon. Tin oxide shows no evidence of the possibility for metal carbide formation [38].

Formation of unwanted products from CH_4 can occur, with methane decomposition forming C and H_2 (**Equation 3.82**), along with formation of C from CO (Boudouard Reaction) following reduction (**Equation 3.83**):

$$CH_4 \rightarrow C + 2H_2 \qquad \textbf{3.82}$$

$$2CO \rightarrow C + CO_2 \qquad \textbf{3.83}$$

These reactions are shown in **Figure 3.34** along with the effect of increasing chain length upon carbon formation from hydrocarbon decomposition (**Equation 3.84** and **3.85**). Hydrocarbon chain length greater than that of methane results in high likelihood of carbon formation:

$$C_2H_6 \rightarrow 2C + 3H_2 \qquad \textbf{3.84}$$

$$C_3H_8 \rightarrow 3C + 4H_2 \qquad \textbf{3.85}$$

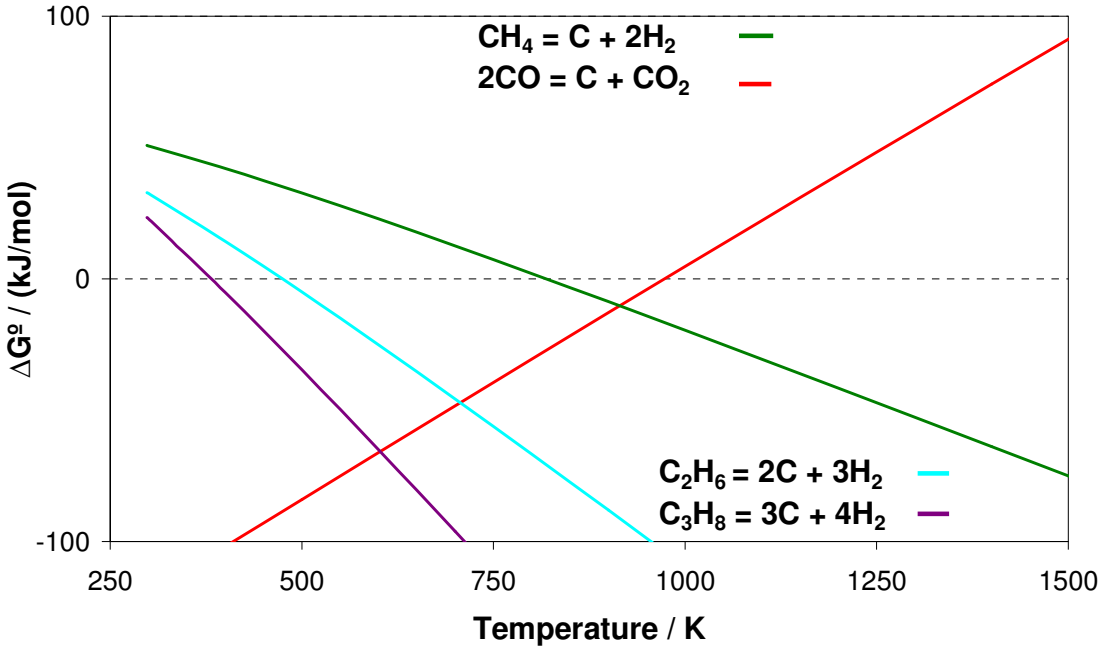

Figure 3.34 Carbon formation during reduction of metal oxides by CH_4

Thermal decomposition of methane is shown to be favourable at temperatures above 820K (**Figure 3.34**). However, methane has proven to decompose via a multi-step process (**Equation 3.87-3.91**) rather than by the direct route shown in **Equation 3.86**. This is due to the strong C-H bond, which requires temperatures in excess of 1000ºC before dissociation of methane can occur [39-41].

$CH_4 \rightarrow C + 2H_2$	ΔHº = +74.8 kJ/mol	**3.86**
$CH_4(ad) \rightarrow CH_3(ad) + H(ad)$	ΔHº = +438.6 kJ/mol	**3.87**
$CH_3(ad) \rightarrow CH_2(ad) + H(ad)$		**3.88**
$CH_2(ad) \rightarrow CH(ad) + H(ad)$		**3.89**
$CH(ad) \rightarrow C(ad) + H(ad)$		**3.90**
$2H(ad) \rightarrow H_2(g)$		**3.91**

Multi-step decomposition of methane is a highly endothermic reaction, thus this should not affect the methane reduction reaction taking place at lower temperature. However, certain metals, including Fe, are known to catalyse decomposition of methane at lower temperature. The oxidation of adsorbed carbon during re-oxidation forms CO and CO_2 along with H_2 in the product gas (**Equations 3.92** and **3.93, Figure 3.35**):

$$C + H_2O \rightarrow CO + H_2 \qquad \textbf{3.92}$$

$$C + 2H_2O \rightarrow CO_2 + 2H_2 \qquad \textbf{3.93}$$

To completely oxidise adsorbed carbon species it may be necessary to re-oxidise at higher temperature (**Figure 3.35**).

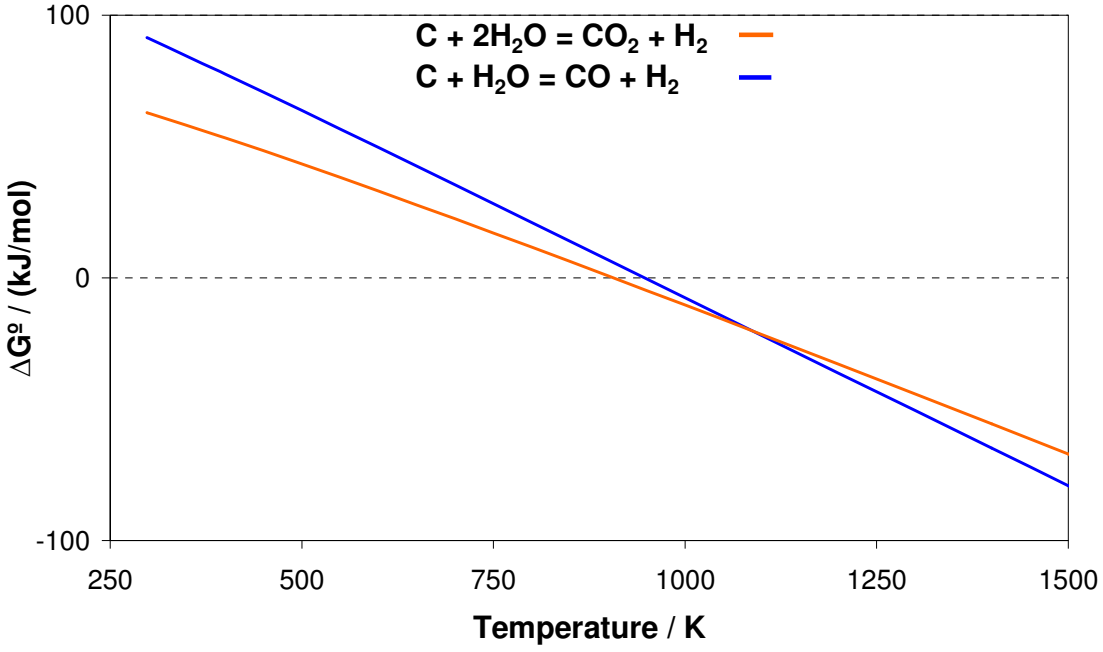

Figure 3.35 CO_x formation from carbon oxidation during re-oxidation of reduced metal oxides

3.4 Conclusions

1. SnO_2, WO_3/WO_2 and Fe_3O_4 have been identified as potential metal oxides suitable for further experimental study in a Steam-Iron type process.
2. Low melting point and the expense of In_2O_3 are limiting factors to further investigation
3. The low oxygen cycling capability of Nb_2O_5 (due to limited reduction at low temperature) will result in low hydrogen production capacity
4. The inability to reduce MoO_2 to a lower oxidation state will limit its potential in the Steam-Metal Process due to catalyst deactivation by sintering and metal carbide formation and/or carbon deposition
5. Methane concentration and temperature control is required to achieve partial oxidation of CH_4 to form useful CO and H_2 products, rather than complete oxidation, resulting in formation of CO_2 and H_2O
6. Stabilisation of intermediate metal oxide phases by introduction of promoters are methods of avoiding carbide formation and coking from decomposition of methane. These two primary routes to catalyst deactivation are likely to occur over completely reduced metals

3.5 References

1. H. Kameyama, K. Yoshida, and D. Kunii, 'A method for screening possible thermochemical decomposition processes for water using δG_0 -T diagrams', *The Chemical Engineering Journal* **1976**, 11(3), 223-229
2. N.W. Hurst, S.J. Gentry, A. Jones, and B.D. McNicol, 'Temperature Programmed Reduction', *Catalysis Reviews - Science and Engineering* **1982**, 24(2), 233-309
3. I. Barin, 'Thermochemical Data of Pure Substances', 3rd ed. *VCH*: Weinheim, **1995**
4. P.B. Tarman, 'Hydrogen by the steam-iron process', *Coal Processing Technology* **1979**, 5, 114-16
5. V. Hacker, R. Fankhauser, G. Faleschini, H. Fuchs, K. Friedrich, M. Muhr, and K. Kordesch, 'Hydrogen production by steam-iron process', *Journal of Power Sources* **2000**, 86(1-2), 531-535
6. S.K. Gangwal, V. Subramani, W. Li, B.S. Turk, R. Gupta, and P.L. Silverston. 'Production of pure hydrogen from syngas by steam-iron process using nanoparticle iron catalysts', in *Abstracts of Papers, 231st ACS National Meeting* (2006) Atlanta, GA, United States: American Chemical Society, Washington, D. C.
7. R. Biljetina and P.B. Tarman, 'Steam-iron process for hydrogen production', *Energy Research Abstracts* **1978**, 3(23),
8. G. Li, J. Ma, H. Ni, Q. Shen, and F. Tsukihashi, 'Influences of Oxide Additions on Formation Reaction of Iron Carbide at 1023 K', *I.S.I.J. International* **2006**, 46(7), 981-986
9. M.A. Ermakova, D.Y. Ermakov, A.L. Chuvilin, and G.G. Kuvshinov, 'Decomposition of Methane over Iron Catalysts at the Range of Moderate Temperatures: The Influence of Structure of the Catalytic Systems and the Reaction Conditions on the Yield of Carbon and Morphology of Carbon Filaments', *Journal of Catalysis* **2001**, 201(22), 183-197

10. A. Steinfeld, A. Frei, P. Kuhn, and D. Wuillemin, 'Solar thermal production of zinc and syngas via combined ZnO-reduction and CH_4-reforming processes', *International Journal of Hydrogen Energy* **1995**, 20(10), 793-804
11. K. Wegner, H.C. Ly, R.J. Weiss, S.E. Pratsinis, and A. Steinfeld, 'In situ formation and hydrolysis of Zn nanoparticles for H_2 production by the 2-step ZnO/Zn water-splitting thermochemical cycle', *International Journal of Hydrogen Energy* **2006**, 31(1), 55-61
12. I. Vishnevetsky and M. Epstein, 'Production of hydrogen from solar zinc in steam atmosphere', *International Journal of Hydrogen Energy* **2007**, 32(14), 2791-2802
13. M. Lundberg, 'Model calculations on some feasible two-step water splitting processes', *International Journal of Hydrogen Energy* **1993**, 18(5), 369-376
14. K. Otsuka, S. Murakoshi, and A. Morikawa, 'Potential Metal-Oxides for the Production of Hydrogen from Water by a Reduction Oxidation Cycle Using Carbon as a Reductant', *Fuel Processing Technology* **1983**, 7(3), 203-211
15. E. Bilgen and C. Bilgen, 'Solar hydrogen production using two-step thermochemical cycles', *International Journal of Hydrogen Energy* **1982**, 7(8), 637-644
16. S. Abanades, P. Charvin, G. Flamant, and P. Neveu, 'Screening of water-splitting thermochemical cycles potentially attractive for hydrogen production by concentrated solar energy', *Energy* **2006**, 31(14), 2805-2822
17. K. Otsuka, S. Murakoshi, and A. Morikawa, 'Hydrogen-Production from Water by Reduced Tin Oxide', *Fuel Processing Technology* **1983**, 7(3), 213-223
18. M. Forster, 'Theoretical investigation of the system SnO_x/Sn for the thermochemical storage of solar energy', *Energy* **2004**, 29(5-6), 789-799
19. P. Charvin, S. Abanades, F. Lemont, and G. Flamant, 'Experimental Study of SnO_2/SnO/Sn Thermochemical Systems for Solar Production of Hydrogen', *AICHE Journal* **2008**, 54(10), 2759-2767
20. K. Otsuka, T. Yasui, and A. Morikawa, 'Reproducible Hydrogen-Production from Water by Indium Oxide', *Journal of Catalysis* **1981**, 72(2), 392-393

21. K. Otsuka, Y. Takizawa, and A. Morikawa, 'Hydrogen-Production from Water on Carbon-Reduced Indium Oxide', *Fuel Processing Technology* **1982**, 6(3), 215-223

22. K. Otsuka, T. Yasui, and A. Morikawa, 'The Decomposition of Water on the Co-Reduced or H_2-Reduced Indium Oxide', *Bulletin of the Chemical Society of Japan* **1982**, 55(6), 1768-1771

23. K. Otsuka, A. Mito, S. Takenaka, and I. Yamanaka, 'Production of hydrogen from methane without CO_2-emission mediated by indium oxide and iron oxide', *International Journal of Hydrogen Energy* **2001**, 26(3), 191-194

24. A. Igarashi, H. Asano, Y. Kikuchi, and Y. Ogino, 'Active metal/oxide systems for water decomposition', *Chemistry Letters* **1982**, 11, 1693-1696

25. T. Kodama, T. Shimizu, T. Satoh, and K.I. Shimizu, 'Stepwise production of CO-rich syngas and hydrogen via methane reforming by a WO_3-redox catalyst', *Energy* **2003**, 28(11), 1055-1068

26. E. Ogata, Y. Kamiya, and N. Ohta, 'The effect of oxidation state of tungsten on hydrocracking of n-heptane over tungsten oxide', *Journal of Catalysis* **1973**, 29(2), 296-307

27. D.C. Vermaire and P.C. Van Berge, 'The preparation of WO_3/TiO_2 and WO_3/Al_2O_3 and characterisation by temperature-programmed reduction', *Journal of Catalysis* **1989**, 116(2), 309-317

28. A. Hanif, T. Xiao, A.P.E. York, J. Sloan, and M.L.H. Green, 'Study on the Structure and Formation Mechanism of Molybdenum Carbides', *Chemistry of Materials* **2002**, 14(3), 1009-1015

29. M. Chambon, S. Abanades, and G. Flamant, 'Kinetic investigation of hydrogen generation from hydrolysis of SnO and Zn solar nanopowders', *International Journal of Hydrogen Energy* **2009**, 34(13), 5326-5336

30. A. Kock, H.M. Fortuin, and J.W. Geus, 'The Reduction Behaviour of Supported Iron Catalysts in Hydrogen or Carbon-Monoxide Atmospheres', *Journal of Catalysis* **1985**, 96(1), 261-275

31. P. Gupta, L. G. Velazquez-Vargas and L-S. Fan, 'Syngas Redox (SGR) Process to Produce Hydrogen from Coal Derived Syngas', *Energy & Fuels* **2007**, 21, 2900-2908

32. G. Li, J. Ma, H. Ni, Q. Shen and F. Tsukihashi, 'Influences of Oxide Additions on Formation Reaction of Iron Carbide at 1023 K', *ISIJ International* **2006**, 46(7), 981–986

33. K-S. Kang, C-H. Kim, W-C. Cho, K-K. Bae, S-W. Woo, C-S. Park, 'Reduction characteristics of $CuFe_2O_4$ and Fe_3O_4 by methane; $CuFe_2O_4$ as an oxidant for two-step thermochemical methane reforming', *International Journal of Hydrogen Energy* **2008**, 33, 4560-4568

34. K. Svoboda, G. Slowinski, J. Rogut, D. Baxter, 'Thermodynamic possibilities and constraints for pure hydrogen production by iron based chemical looping process at lower temperatures', *Energy Conversion and Management* **2007**, 48, 3063-3073

35. W. R Ruston, M.. Warzee, J. Hennaut and J. Waty, 'The Solid Reaction Production of the Catalytic Decomposition of Carbon Monoxide on Iron at 550°C', *Carbon* **1969**, 7, 47-57

36. T. Shimizu, K. Shimizu, Y. Kitiyama, T. Kodama, 'Thermochemical Methane Reforming Using WO_3 as an Oxidant Below 1173 K by a Solar Furnace Simulator', *Solar Energy* **2001**, 71(5), 315–324

37. K-S. Kang, C-H. Kim, W-C. Cho, K-K. Bae, S-W. Woo, C-S. Park, 'Reduction characteristics of $CuFe_2O_4$ and Fe_3O_4 by methane; $CuFe_2O_4$ as an oxidant for two-step thermochemical methane reforming', *International Journal of Hydrogen Energy* **2008**, 33(17), 4560-4568

38. J. Percy, 'The Metallurgy of Lead, including Desiverization and Cupellation', *London*: J. Murray, **1870**, 67

39. G.Q. Zhang and O. Ostrovski, 'Reduction of titania by methane-hydrogen-argon gas mixture', *Metallurgical and Materials Transactions B - Process Metallurgy and Materials Processing Science* **2000**, 31(1), 129-139

40. N.Z. Muradov and T.N. Veziroglu, 'From hydrocarbon to hydrogen-carbon to hydrogen economy', *International Journal of Hydrogen Energy* **2005**, 30(3), 225-237

41. R. Alizadeh, E. Jamshidi, and G. Zhang, 'Transformation of methane to synthesis gas over metal oxides without using catalyst', *Journal of Natural Gas Chemistry* **2009**, 18(2), 124-130

EXPERIMENTAL METHODOLOGY

4.1 Introduction

This chapter describes the synthesis, testing and characterisation of all samples.

4.2 Experimental

4.2.1 Materials

4.2.1.1 Chemicals

The major chemicals used as precursor materials for formation of metal oxide based samples are as follows:

- $(FeNO_3)_3.9H_2O$ – Univar 98%
- $(CeNO_3)_3.6H_2O$ – Aldrich 99%
- $ZrO(NO_3)_2.xH_2O$ – Technical Grade
- $(NH_2)_2CO$ – Biolab Scientific 99.5%
- $SnCl_4.5H_2O$ – Aldrich 98%
- $InCl_3$ – Alfa Products (ultrapure)
- $(NH_4)_2.Mo_7O_{24}.4H_2O$ – Univar 81-83% as MoO_3
- WCl_6 – Aldrich 99.9+% Metals basis
- $NbCl_5$ – Aldrich 99%
- $(NH_4)_2Ce(NO_3)_6$ – Sigma Aldrich 99.99%

4.2.1.2 Gases

9.85 mol% H_2 in He, diluted to approximately 5 mol% total H_2, was used for all Temperature Programmed Reduction (TPR) analyses. 4.0 mol% H_2 in N_2 was used for all Thermogravimetric Analysis (TGA) experiments. 29.9% CO/1.04 mol% Ar in He balance (10%), H_2 (10-30%) and CH_4 (10-50%) were used as reductants in the Steam-Iron/Metal Reaction (SIR), with 1.06 mol% Ar in He as a reference gas and further He added for balance. 0.55 mol% Ar in N_2 and 1.06 mol% Ar in He were employed as carrier gases which were passed through a water saturator for the re-oxidation phase of the Steam-Iron/Metal Reaction. Helium was used as a dilution gas in the Steam-Iron/Metal Reaction and Temperature Programmed Reduction respectively. Argon was used as a reference gas for mass spectrometer analysis and provided a benchmark for fluctuation in reactant gas flow.

Gas concentrations in reduction gases were initially selected on the basis of reproduction of literature based experiments. Change in gas concentration was implemented with respect to performance during reduction; if gas concentration influenced poor reduction or rapid catalyst deactivation, concentrations were altered accordingly.

Table 4-1 Gas Specifications

Gas	Purity	Usage	Manufacturer
Ar/N_2	0.55% Ar/N_2	SIR carrier gas	*Linde*
CH_4	High Purity, 99.99%	SIR reducing gas	*Linde*
Ar/He	1.06% Ar/He	TPR/SIR reference gas SIR carrier gas	*Coregas*
Ar/CO/He	1.04% Ar/29.9% CO/He	SIR reducing gas	*Coregas*
H_2/He	9.85% H_2/ He	TPR reducing gas	*Coregas*
Ar	High Purity, 99.999%	Diluent gas	*Coregas*
He	High Purity, 99.999%	Diluent gas	*Coregas*
H_2	High Purity, 99.999%	SIR reducing gas	*Coregas*
N_2	High Purity, 99.999%	Balance gas	*Coregas*
H_2/N_2	4% H_2/N_2	TGA reducing gas	*BOC*
Zero Grade Air	High Purity	Carrier gas	*BOC*

4.2.2 Synthesis Methodology

4.2.2.1 Urea Hydrolysis

Experimental procedure for preparation of metal oxides by urea hydrolysis was followed as outlined in previous methodology [1, 2]. The method of urea hydrolysis synthesis has demonstrated a means of reproducibly synthesizing homogenous particles with high surface area. The concentrations of metal salt (0.1M) and urea (0.4M) have been shown by Lin, J-D and Duh, J-G [3] to produce particles of the higher surface area in comparison to reactions at lower concentrations of urea. To maximise the effect of ceria for increased reducibility of the promoted metal oxide and zirconia for enhanced particle dispersion, the molar ratio of CeO_2:ZrO_2 was maintained at 1:1. At a ratio of 1:1, CeO_2/ZrO_2 demonstrates the greatest reducibility [4, 5], with the (CeO_2-ZrO_2):MO_x ratio also maintained at 1:1. The preparation procedure was as follows:

1 Dissolve metal salts (nitrates or chlorides) at desired ratios in MilliQ water to form 0.1M solution. Dissolve corresponding amount of urea in MilliQ water to form solution of 0.4M, giving ratio of metal salt solution to urea solution of 2:1 (v/v).
2 Combine both solutions and heat whilst stirring to boil under reflux conditions.
3 Age the precipitate in boiling solution for 24 hours.
4 Allow the solution to cool to room temperature
5 Centrifuge and wash solution using MilliQ water no less than three times. The product was washed by a process of redispersing in fresh MilliQ water and sonicating, then centrifuging to remove the supernatant.
6 Dry the precipitate at 120ºC overnight
7 Calcine by heating dried precipitate to 500ºC at 8ºC/min and holding for 4 hours.
8 Grind calcined particles into suitable particle size between 150-250 microns in diameter.

Extra care was taken when dissolving volatile chloride based metal salts, which react violently when exposed to moisture. All samples were weighed out in a glove box under N_2 atmosphere, and sealed in containers under inert atmosphere. The weighed sample was added directly to the MilliQ water solution to minimise sample loss from atmospheric exposure.

4.2.3 Experimental Setup

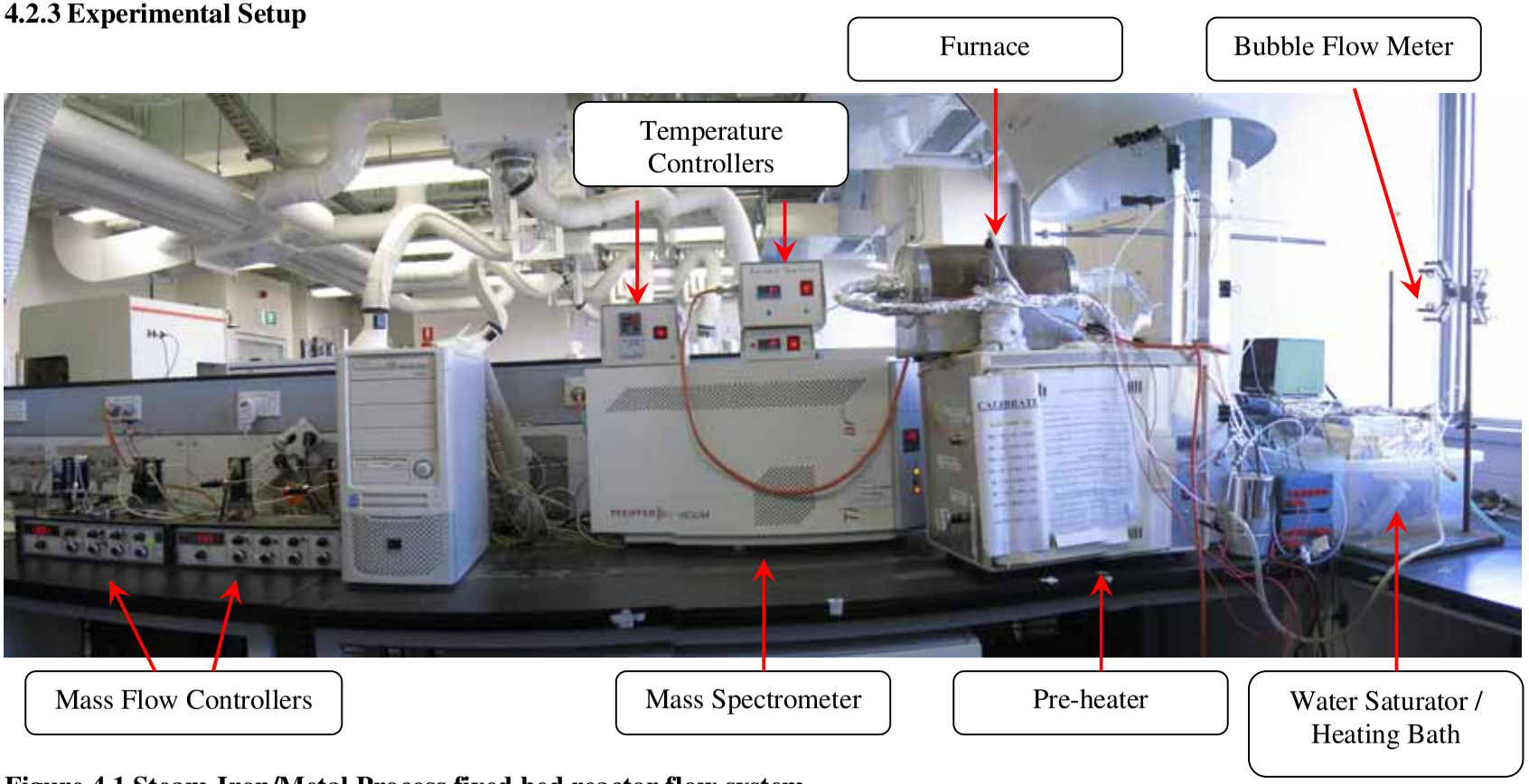

Figure 4.1 Steam-Iron/Metal Process fixed bed reactor flow system

Reactions were conducted within a tubular fixed bed reactor system comprising a quartz tube of dimensions 400mm x 8mm. A thermocouple was placed outside the reactor tube within the furnace for monitoring temperature. Reactant gases were fed into the reactor tube through heated lines. Water was fed into the reactor by means of gas (0.55 mol% Ar in N_2 or 1.06 mol% Ar in He) passing through a heated water saturator to achieve the desired water content. A condenser was used to remove water from the product gas stream prior to passing into the mass spectrometer.

The sample was loaded into the reactor and held by means of quartz wool packing. Flow rates were calibrated using Brooks 5850E mass flow controllers, and flow rates were measured using a soap bubble flow meter. Studies on the effect of mass transfer in the reactor were not carried out.

4.2.4 Furnace and Preheater Setup

An electric furnace was used to heat the reactor, with temperature of the reactor tube monitored by a thermocouple within the furnace at the reactor bed. Shinko temperature controllers were used for temperature programming and monitoring of the system.

The pre-heater was used to heat both incoming and outgoing gases from the reactor tube, with the temperature maintained at 180ºC to achieve complete water evaporation in the gas stream. The gas lines passing the water saturated gas stream into the reactor were heated by means of a heating line controlled by a specially constructed transformer. The temperature of all heated lines was maintained at no less than 150ºC to ensure evaporation of water in the gas stream prior to passing through the reactor tube, and to prevent condensation of water in the product gas stream.

4.2.5 Gas Detection

A Balzers Thermostar Quadropole Mass Spectrometer was used to analyse all incoming and outgoing gases. Mass spectrometry works on the principle of separation of molecules based on their mass to charge ratio. Molecules entering the chamber are ionized to generate charged molecules and molecular fragments, which then pass through an electromagnetic field allowing them to be separated according to their mass to charge ratio.

The molecular weights and their fragmentations for gases H_2(2), He(4), H_2O(18, 17), CO(28, 12), CO_2(44), O_2(32, 16) and Ar(40) were monitored. Detected signals were corrected with respect to their background signal.

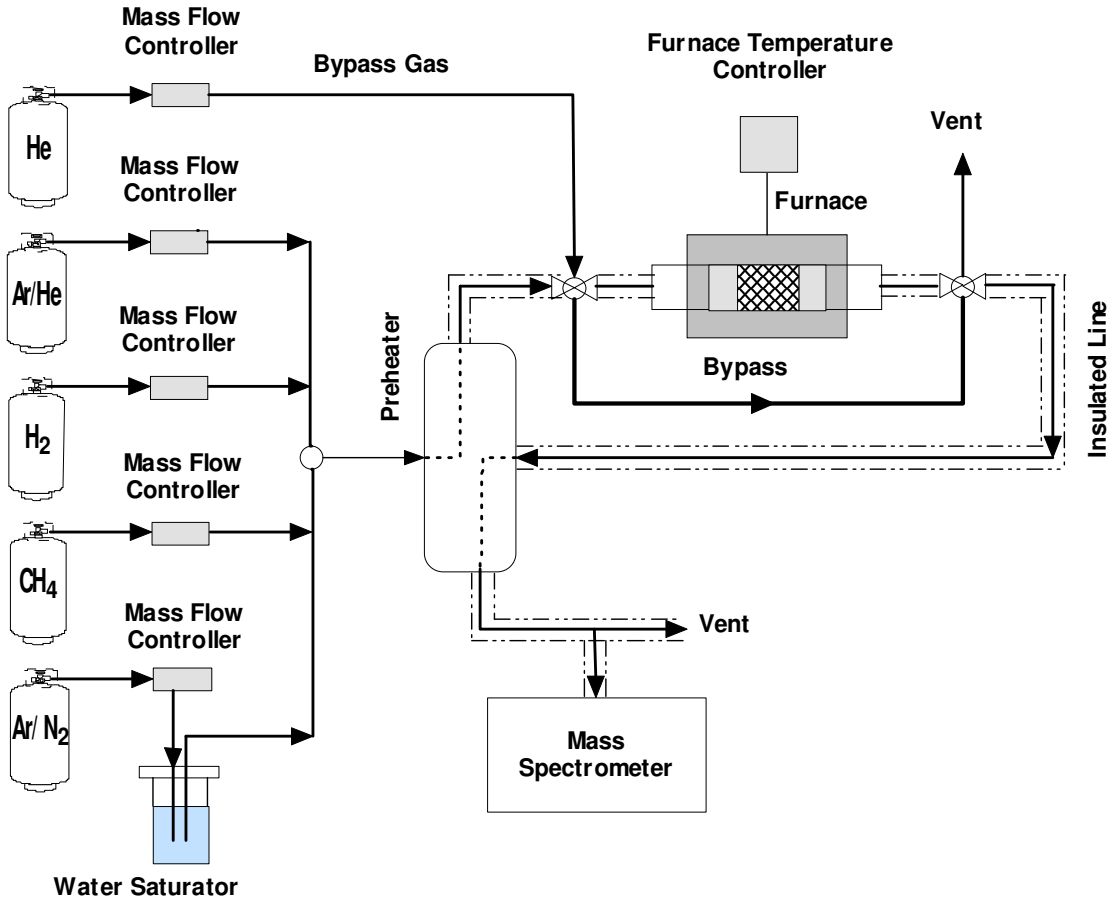

Figure 4.2 Experimental setup for the Steam-Iron/Metal Process reaction

4.2.6 Experimental Conditions

4.2.6.1 Sample Pretreatment

No pre-treatment was employed prior to reaction of catalysts, with the exception of drying the catalyst within the reactor tube. This procedure involves:

1 Loading catalyst into the reactor tube
2 Purging the system by passing He through the reactor tube at 30mL/min whilst simultaneously heating the system to 150ºC and holding at this temperature until observed moisture content in the system has stabilised (1 hr).

4.2.7 Characterisation Techniques

4.2.7.1 Transmission Electron Microscopy (TEM)

TEM works on the principle of an electron beam passing through the sample, with an image formed by the interaction of electrons as they move through the sample. As the sample becomes thicker, the intensity of outgoing electrons is altered, which gives rise to image contrast over the image. The electron beam having passed through the sample is detected and used to form an image.

All sample images were taken using a TEM Philips CM200 with an accelerating voltage of 200kV, spot size of 25 nm and at an objective aperture setting of 4. Samples were prepared by dispersing in methanol by sonication prior to being analysed on a 200 mesh copper grid.

4.2.7.2 Scanning Electron Microscopy (SEM)

SEM works on the principle of a beam of electrons rastered over the sample surface, which produces elastically scattered electrons, inelastically scattered electrons and electromagnetic radiation. From interaction of the electrons with the sample surface, the subsequent detected electrons are used to form an image, giving depth and contrast from the electron intensity following this interaction.

All sample images were taken using a Hitachi S4500 with an accelerating voltage of 5kV, and a working distance of 20mm. Samples were prepared by mounting onto a metal stub with carbon tape then gold coated to improve conductivity.

4.2.7.3 Brunauer-Emmett-Teller (BET) Surface Area

Surface area is determined by calculating the volume of N_2 required to form a monolayer on the sample surface (V_m), using the following formula:

$$\frac{P}{V_a(P_0 - P)} = \frac{1}{V_m C} + \frac{(C-1)}{V_m C}\frac{P}{P_0}$$

where, V_a is the volume of gas adsorbed at pressure P,
P_0 is the gas saturation pressure,
V_m is the volume necessary to cover the entire adsorbing surface by a mono molecular layer,
C is a constant involved with energy of adsorption
Plotting of $P/V_a(P_0-P)$ vs. P/P_0 gives a slope of $(C-1)/V_mC$ and intercept of $1/V_mC$ which can be used for determining a value for V_m. Applying the formula:

$$S = \frac{V_m A_m N_a}{W V_0}$$

where, S is the specific surface area of the sample in m^2g^{-1},
N_a is the Avogadro's number, $6.023x10^{23}$ molecules mol^{-1},
A_m is the area of an adsorbed molecule, m^2,
V_0 is 22414mL mol^{-1}, and
W is the sample weight,
which gives surface area of the sample.

BET surface area and pore volume data was determined by N_2 adsorption using the forty point BET method on the Micrometrics Tristar device. The sample of ca. 150 mg was loaded into the sample tube and degassed at 150°C for 3 hours, followed by purging using nitrogen just prior to BET measurement.

4.2.7.4 X-Ray Diffraction (XRD)

Characterisation of powder samples by XRD is useful for qualitative, and to a lesser extent, quantitative analysis. Bragg's Law states:

$$n\lambda = 2d\sin\theta$$

where, n is an integer,
λ is the wavelength of incident radiation,
d is the d-spacing, crystal plane distance, and
θ is the angle of incidence.
This technique can be used to determine the d spacing within a given crystal lattice for any given angle of incidence, giving a characteristic diffraction spectrum for each sample.

This technique can also be used to determine crystallite size via the Scherrer Equation,

$$t = \frac{0.9\lambda}{B\cos\theta}$$

where, t is particle diameter,

B is width of diffraction curve at FWHM, in radians,

λ is the wavelength of incident radiation,

θ is the angle of incidence.

XRD analysis was taken following grinding of the sample to particle sizes no greater than 60 μm. All samples were measured on the Philips X'pert Multipurpose X-ray Diffraction System (MPD) using Cu Kα radiation over 10° – 100° in the 2θ range at 40mA and 45kV. Analysis of XRD data was performed using the X'Pert Highscore Plus software package, with XRD spectra matched against the International Centre for Diffraction Data (ICDD) database for comparison and phase determination.

4.2.7.5 X-Ray Photoelectron Spectroscopy (XPS)

X-Ray Photoelectron Spectroscopy (XPS) is a highly useful technique for the qualitative surface analysis of powder and thin film samples [6]. The technique involves irradiating the sample via a monochromated (or non-monochromated) x-ray source, whereupon electrons are emitted by the sample with a discrete kinetic energy. By determining the characteristic electron binding energy associated with individual elements, the elemental composition of the sample is thus analysed. Semi-quantitative analysis of the sample is also possible by measurement of comparative intensity of emitted electrons between individual elements contained within the sample.

Samples were analysed with a Thermo Scientific ESCALAB220i-XL using a monochromated Al K α (energy 1486.6 eV) x-ray source at 15 mA and 10 kV. Pass energy of 100 eV was employed for survey scans or 20 eV for region scans, with a step size of 1 eV for surface scans or 0.1 eV for region scans.

4.2.7.6 Thermoanalytical Characterisation

Temperature Programmed Reduction (TPR)

The technique of temperature programmed reduction (TPR) is a highly useful characterisation technique to study the behaviour and properties of metal oxide systems, amongst many others [7]. By simultaneously heating and passing a reducing gas over the sample it is possible to determine the onset temperature of reduction, as well as comparison between different oxide species and the effect of promoter/support addition upon reduction. Using this method, some comparisons can be drawn between thermodynamic predictions and experimental outcomes.

TPR experiments were conducted using a Micromeritics AutoChem II 2920. Approximately 50 mg of sample were loaded into the quartz reactor tube, which was purged using argon gas at a flow rate of 30mL/min and heated to 150ºC to remove moisture. Once the water signal from the sample was observed to stabilise (1 hr), the reducing gas comprising ca. 5% H_2 / He / Ar was flowed over the sample at a rate of 30mL / min whilst ramping the temperature from 150ºC to 1000ºC at a rate of 5ºC / min. The change in H_2 flow and H_2O production was monitored using a MS.

Thermogravimetric Analysis (TGA)

Thermogravimetric analysis (TGA) is a highly useful characterisation technique used to study the degradation of metal oxide systems, amongst other materials. Characterisation is determined by measurement of weight change in relation to temperature as the sample is being reduced. By comparison between changes in weight due to mass loss and known sample mass of oxidation states, it is possible to determine various metal oxidation states within the system, as well as the onset temperature of reduction.

TGA experiments were conducted using a Mettler Toledo, TGA/SDTA851e. 10-50 mg of sample was loaded into the reactor tube then calcined by heating the sample from room temperature to 500ºC at 5ºC/min in air. The sample was held at 500ºC for 1 hr, before N_2 at a flow rate of 20mL/min was introduced into the reactor tube and the sample cooled back to room temperature under a flow of N_2. At this point, 4% H_2 / 96% N_2 at a flow rate of 40mL/min was flowed over the sample for 1 hr before sample reduction by heating from room temperature to 900ºC at 5ºC/min under a flow of 4% H_2 / 96% N_2. The sample was held at 900ºC for 3 hrs to ensure complete reduction by 4% H_2 / 96% N_2, before finally being cooled to room temperature under a flow of N_2 gas.

4.3 References

1. V. Galvita and K. Sundmacher, 'Hydrogen production from methane by steam reforming in a periodically operated two-layer catalytic reactor', *Applied Catalysis A - General* **2005**, 289(2), 121-127
2. S. Pengpanich, V. Meeyoo, T. Rirksomboon, and K. Bunyakiat, 'Catalytic oxidation of methane over CeO_2-ZrO_2 mixed oxide solid solution catalysts prepared via urea hydrolysis', *Applied Catalysis A - General* **2002**, 234(1-2), 221-233
3. J.D. Lin and J.G. Duh, 'Coprecipitation and hydrothermal synthesis of ultrafine 5.5 mol% CeO_2-2 mol% $YO_{1.5}$-ZrO_2 powders', *Journal of the American Ceramic Society* **1997**, 80(1), 92-98
4. T. Murota, T. Hasegawa, S. Aozasa, H. Matsui, and M. Motoyama, 'Production Method of Cerium Oxide with High Storage Capacity of Oxygen and Its Mechanism', *Journal of Alloys and Compounds* **1993**, 193(1-2), 298-299
5. Y.W. Li, D.H. He, Q.M. Zhu, X. Zhang, and B.Q. Xu, 'Effects of redox properties and acid-base properties on isosynthesis over ZrO_2-based catalysts', *Journal of Catalysis* **2004**, 221(2), 584-593
6. J.M. Hollander and W.L. Jolly, 'X-ray photoelectron spectroscopy', *Accounts of Chemical Research* **1970**, 3(6), 193-200
7. N.W. Hurst, S.J. Gentry, A. Jones, and B.D. McNicol, 'Temperature Programmed Reduction', *Catalysis Reviews - Science and Engineering* **1982**, 24(2), 233-309

INVESTIGATION OF SUITABLE PROMOTERS FOR THE STEAM-IRON PROCESS

5.1 Introduction

A primary characteristic of metal oxides surveyed for use in the Steam-Iron Process is the inability to undergo both reduction and re-oxidation at relatively low temperature (**Chapter 3**). A wide range of metal oxides are either easily reduced or re-oxidised at lower temperature, but very few oxides are capable of being both reduced and oxidised within a relatively low narrow range of temperatures. Iron oxide is a suitable metal oxide which has been heavily investigated for its potential in the Steam-Iron Process [1-6].

The use of carbon containing reductants such as methane or carbon monoxide tend to favour coking and catalyst deactivation, a trend which may be minimised by the use of suitable promoters [6]. Whilst iron oxide species show the highest activity when promoted with precious metals such as Rh, Pt and Pd, cheaper alternatives also exist. Ceria and ceria-zirconia are well known for their high oxygen storage capacity (OSC), [7-9]. Use of ceria as a promoter is expected to both enhance the redox of oxide species and the oxidation of adsorbed carbon species [9, 10]. By oxidation of adsorbed carbon during the reduction phase of the reaction, it may be possible to avoid carbon oxide formation during hydrogen production upon re-oxidation. Ceria and ceria/zirconia have also been shown to enhance the thermal stability of the iron-iron oxide system [11, 12].

This chapter investigates the effect of ceria and ceria-zirconia based promoters on the reduction and re-oxidation behaviour of iron oxide. The effect of promoter addition is assessed over a variety of reductants in an attempt to increase reducibility and/or oxidisability, along with metal oxide lifetime.

5.2 Experimental

5.2.1 Metal Oxide Preparation

Unpromoted and promoted Fe_2O_3-based metal oxides were prepared by the method of urea hydrolysis, as described in **Chapter 4** (Experimental Methodology). This method has shown to maximise both homogeneity and surface area of synthesized metal oxide particles when compared to various co-precipitation methods. The composition of promoted Fe_2O_3 was selected at 75mol%Fe_2O_3-25mol%CeO_2 and 50mol%Fe_2O_3-25mol%CeO_2-25mol%ZrO_2. Characterisation techniques involved BET, XRD, TEM, and TPR as described in **Chapter 4** (Experimental Methodology).

5.2.2 Temperature Programmed Reduction (TPR)

An outline of experimental apparatus used for TPR analysis can be found in **Chapter 4** (Experimental Methodology). Prior to analysis, the sample was heated under a flow of Ar to 150ºC for 1 hour to ensure all excess moisture was removed.

The following experimental conditions were employed:

- Flow rate: 30mL/min
- Incoming gas mixture: 5 vol%H_2-95 vol% (1%Ar in He)
- Metal oxide loading: 0.05-0.1g
- Temperature ramping rate: 150-800ºC at 5ºC/min
- Reactor Pressure: 1 atm

5.2.3 Steam-Iron Process

An outline of experimental apparatus used for Steam-Iron reaction studies can be found in **Chapter 4** (Experimental Methodology). Initially the sample was heated under flow of He up to 150ºC and held until no further change in the outgoing H_2O signal was observed. Flow rates of all incoming reactants were maintained at 60 mL/min, with reactor pressure maintained at a constant 1 atm.

The following experimental conditions were employed for all metal oxides during reduction/re-oxidation studies (**Table 5-1**):

Table 5-1. Reaction conditions for redox analysis of promoted iron oxides

Reductant	**Incoming gas mixture**	**Metal Oxide Loading / g**	**Temperature of reduction**
H_2	25 vol% H_2 -13.3 vol% (1%Ar in He) - 61.7 vol% He	0.2 - 0.3	550ºC
CO	10 vol%CO-13.3 vol% (1%Ar in He)-76.7 vol% He	0.2 - 0.3	450ºC
CO + H_2 (syngas)	10 vol% CO - 30 vol% H_2 - 60 vol% He	0.2 - 0.3	450ºC
CH_4	10 vol% CH_4 - 13.3 vol% (1%Ar in He) - 76.7 vol% He	0.2 - 0.3	750ºC
Oxidant	**Incoming gas mixture**	**Metal Oxide Loading / g**	**Temperature of oxidation**
H_2O	2-3 vol% H_2O - 97 vol% (1 vol%Ar in N_2)	0.2 - 0.3	450 - 750ºC

5.3 Results and Discussion

5.3.1 Characterisation

TEM imagery of as prepared unpromoted and promoted Fe_2O_3 is indicative of an overall decrease in particle size with addition of promoters (**Figure 5.1**). Unpromoted Fe_2O_3 particles show a highly porous structure, as evident from TEM imagery with higher contrast observed at interparticle pores compared to particle bulk, and observed particle diameters approximately equal to particle diameters calculated from XRD spectra.

Figure 5.2 shows XRD spectra of as prepared unpromoted and promoted Fe_2O_3, which show the presence of CeO_2 and CeO_2/ZrO_2 as separate phases when added to Fe_2O_3 as promoters. Line broadening is observed in promoted Fe_2O_3, indicative of decreased crystallite size for promoted Fe_2O_3. The crystallite size of Fe_2O_3 with CeO_2 and CeO_2/ZrO_2 was determined via the Scherrer equation, using the approximation of Fe_2O_3 as spherical particles (**Table 5-2**). Surface area was also found to increase with the addition of CeO_2 and CeO_2/ZrO_2 to Fe_2O_3 (**Table 5-2**). The increase in surface area is attributed to an additive effect of the surface areas promoters to Fe_2O_3, rather than surface area change resulting from formation of a new oxide. XRD results show two distinct phases corresponding to the individual oxides, with no peak shift to indicate formation of a solid solution or other structures.

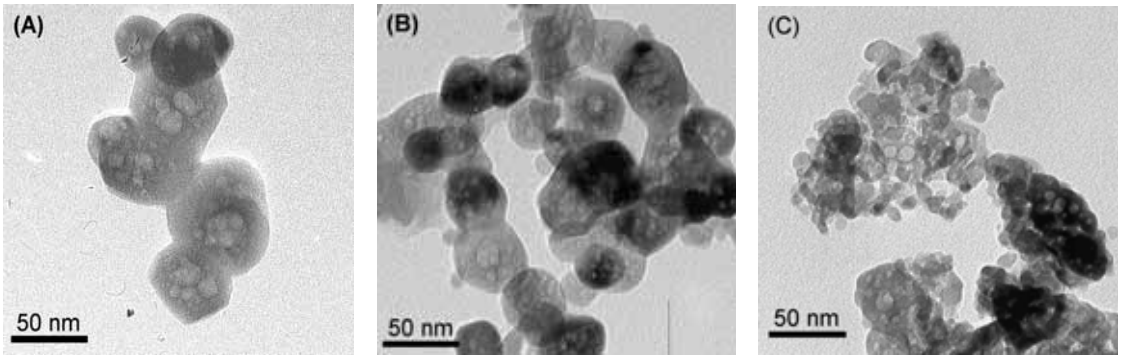

Figure 5.1 TEM imagery of as prepared samples: (A) Fe_2O_3, (B) Fe_2O_3/CeO_2, (C) $Fe_2O_3/[CeO_2/ZrO_2]$

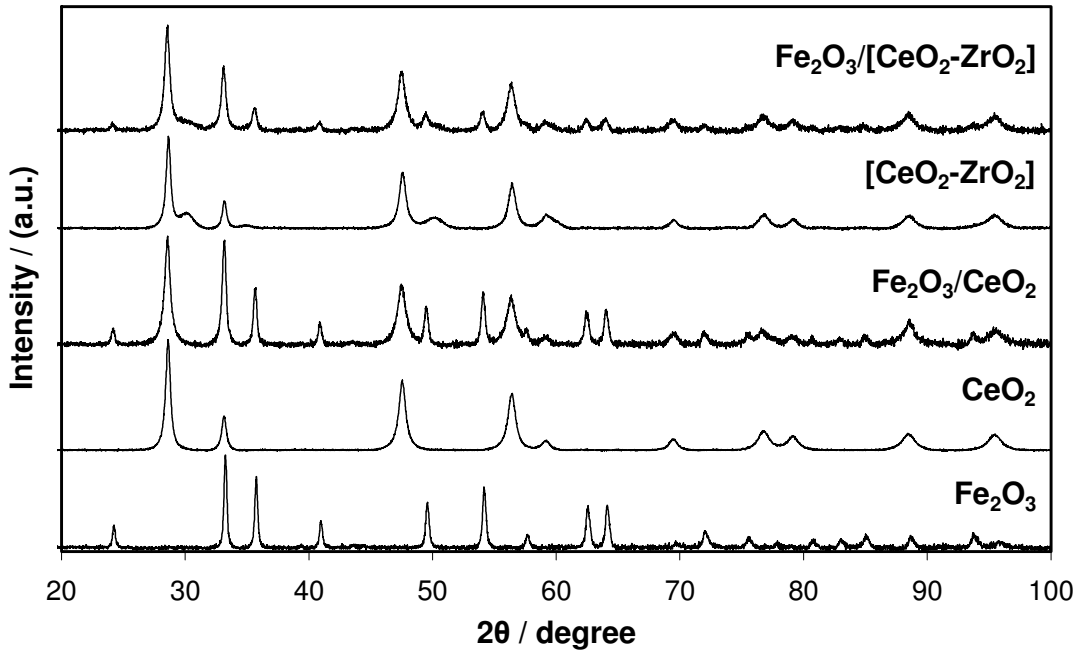

Figure 5.2 XRD spectra of as prepared unpromoted and promoted Fe_2O_3

Table 5-2 Measured crystallite size and surface area of as prepared unpromoted and promoted Fe_2O_3

Sample	Particle Diameter[a,b] / nm	BET_{SA}[b] / (m^2/g)
Fe_2O_3	48	19.8
CeO_2	--	89.5
ZrO_2	--	105.1
CeO_2/ZrO_2	--	88.1
Fe_2O_3/CeO_2	27	51.7
Fe_2O_3/ [CeO_2/ZrO_2]	25	80.3

[a] Determined by Scherrer Equation from XRD spectra, values calculated from major Fe_2O_3 peaks [b] Values determined after calcination in air at 500°C

Temperature programmed reduction (TPR) analysis of unpromoted and promoted Fe_2O_3 is shown in **Figure 5.3**. Unpromoted Fe_2O_3 reduces in three stages, with peaks at 356ºC, 562ºC and 727ºC. These peaks correlate to reduction of Fe_2O_3 to Fe_3O_4, Fe_3O_4 to FeO and FeO to Fe respectively [13, 14]. Due to the metastable nature of the intermediate FeO phase, complete reduction of Fe_3O_4 to FeO was not achieved before reduction of FeO to Fe begins, as evidenced by the large degree of overlap between the final two peaks.

Reduction of CeO_2 promoted Fe_2O_3 shows three peaks at 353ºC, 505ºC and 600ºC (**Figure 5.3**). It has been reported that the three peaks correlate to reduction of Fe_2O_3 to Fe_3O_4 at the lowest temperature peak (353ºC), followed by a combination of reduction of Fe_3O_4 to Fe and reduction of high surface area species of CeO_2 to Ce_2O_3 at the second peak. The final peak at 750ºC is assigned to the reduction of bulk species of CeO_2 to Ce_2O_3 [15, 16].

Deconvolution of CeO_2/ZrO_2 promoted Fe_2O_3 spectra (**Figure 5.3**) shows initial reduction of Fe_2O_3 to Fe_3O_4 (343ºC). The second peak is determined to be reduction of high surface area $2(CeO_2/ZrO_2)$ to $Ce_2O_3/2ZrO_2$ (445ºC), as based on calculation and comparison of Fe_2O_3 based peak area ratios. Subsequent peaks can then be assigned to reduction of Fe_3O_4 to FeO (568ºC), and finally FeO to Fe (750ºC) [11]. In addition, a peak at high temperature, was observed by superposition with peak fitting (>750ºC), which is attributed to reduction of bulk species of CeO_2/ZrO_2 [11]. The higher proportion of 50% CeO_2/ZrO_2 results in a more predominant $2(CeO_2/ZrO_2)$ to Ce_2O_3/ZrO_2 peak at 445ºC prior to reduction of Fe_3O_4 to Fe, as compared to CeO_2 promoted Fe_2O_3.

Identified peaks are assigned to reduction of Fe_2O_3 or promoting oxides alone. Further peaks or peak shifts which may be attributed to reduction of composite oxide species, such as Fe-Ce-O or Fe-Zr-O have not been identified. Strong interactions between Ce and Fe species are not observed except at higher ratios of Ce to Fe (>60%) [15] and deconvolution of CeO_2/ZrO_2 promoted Fe_2O_3 based on peak positions suggest that minimal, if any interactions exist between Fe and Ce or Zr species [11].

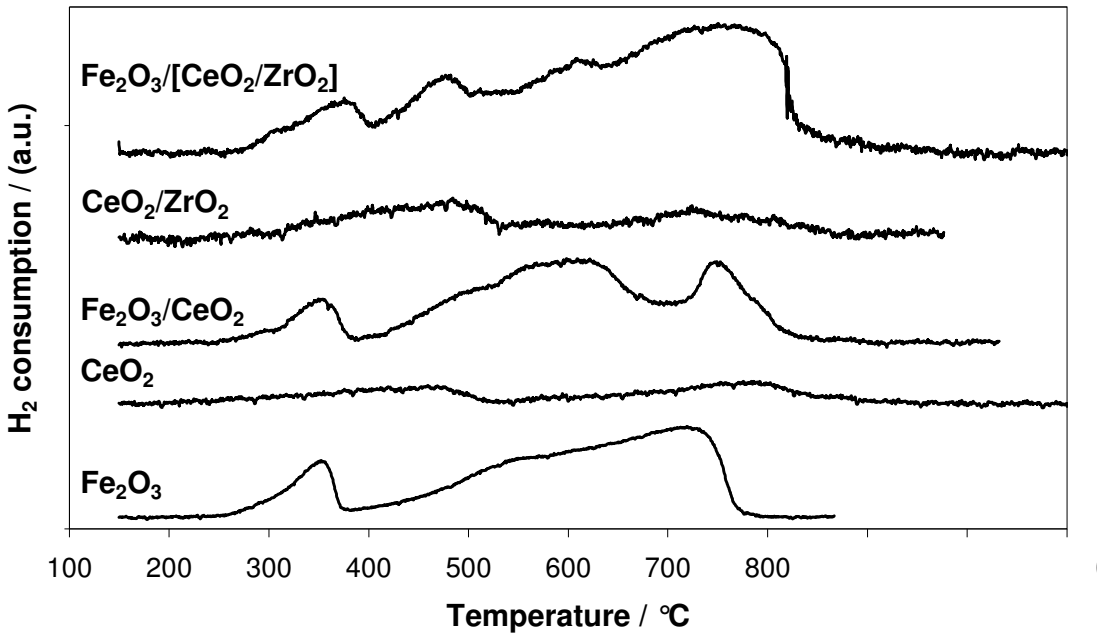

Figure 5.3 5% H_2 TPR of unpromoted and promoted Fe_2O_3 up to 800ºC

Table 5-3 Peak temperatures and assignments of 5% H_2 TPR of unpromoted and promoted Fe_2O_3

Sample	Oxidation State				
	Temperature / (ºC)				
Reduction State	$Fe_2O_3 \rightarrow Fe_3O_4$	$2(CeO_2/ZrO_2) \rightarrow Ce_2O_3/2ZrO_2$	$Fe_3O_4 \rightarrow FeO$	$FeO \rightarrow Fe$	$CeO_2 \rightarrow Ce_2O_3$
Fe_2O_3	356	--	~ 562	727	--
Fe_2O_3/CeO_2	353	--	~ 505	~600	750
Fe_2O_3 / [CeO_2/ZrO_2]	343	445	568	~750	--

5.3.2 Steam-Iron Reaction: H_2 reduction studies on promoted Fe_2O_3

Following TPR studies, metal oxides were studied in a Steam-Iron type process, initially using H_2 as a reductant. Redox was performed at 550ºC, which was determined to be the approximate temperature at which reduction of Fe_2O_3 to form FeO could be achieved [17]. By limiting complete reduction to Fe, it is possible to prevent extensive sintering and increase catalyst lifetime. Initial reduction was performed with a temperature ramp, with H_2 reduction from 150-550ºC. However, as shown below, reduction to Fe did occur in some samples. Subsequent re-oxidation and further reduction cycles were performed isothermally at 550ºC.

5.3.2.1 H_2 reduction/H_2O re-oxidation of unpromoted Fe_2O_3

Hydrogen consumption in the first reduction is consistent with reduction of Fe_2O_3 to Fe, with stoichiometric levels of hydrogen consumption (**Table 5-4**):

$$Fe_2O_3 + 3H_2 \rightarrow 2Fe + 3H_2O \qquad \textbf{5.1}$$

Subsequent reduction cycles show hydrogen consumption indicative of reduction of Fe_3O_4 to Fe:

$$Fe_3O_4 + 4H_2 \rightarrow 3Fe + 4H_2O \qquad \textbf{5.2}$$

A drop in hydrogen consumption is observed, resulting from sintering effects limiting the exposed surface area available for hydrogen to react during reduction.

Re-oxidation of unpromoted Fe_2O_3 is from Fe to Fe_3O_4 (**Table 5-5**):

$$3Fe + 4H_2O \rightarrow Fe_3O_4 + 4H_2 \qquad \textbf{5.3}$$

A progressive decrease in the amount of hydrogen produced results from rapid sintering of completely reduced iron metal with each cycle, resulting in rapid catalyst deactivation (**Figure 5.4**). Sintering is known to be the primary mechanism responsible for deactivation of iron oxide. Bleeker et. al. have shown that the extent of reduction; the degree of oxygen removed from the metal oxide, has a significant effect upon the degree of deactivation [18]. Re-oxidation is made more difficult by a high percentage of bulk Fe, which is more difficult to re-oxidise than intermediate oxide phases of iron, due to larger grain size caused by more extensive sintering as previously mentioned.

Table 5-4 Total H_2 consumption from unpromoted Fe_2O_3 reduction at 550°C

	Cumulative H_2 Consumption (x 10^{-3}) / moles		
	Cycle 1	**Cycle 2**	**Cycle 3**
Reduction state	Fe_2O_3-Fe	Fe_3O_4-Fe	Fe_3O_4-Fe
Stoichiometric	4.67	4.16	4.16
Experimental	4.6	3.7	3.1
	Cumulative H_2O Production (x 10^{-3}) / moles		
Stoichiometric	4.67	4.16	4.16
Experimental	4.6	3.7	3.4

Table 5-5 Total H_2O consumption and H_2 production from unpromoted Fe_2O_3 re-oxidation at 550°C

	Cumulative H_2O Consumption (x 10^{-3}) / moles		
	Cycle 1	**Cycle 2**	**Cycle 3**
Re-oxidation state	Fe-Fe_3O_4	Fe-Fe_3O_4	Fe-Fe_3O_4
Stoichiometric	4.16	4.16	4.16
Experimental	4.1	3.2	2.7
	Cumulative H_2 Production (x 10^{-3}) / moles		
Stoichiometric	4.16	4.16	4.16
Experimental	3.8	2.7	2.4

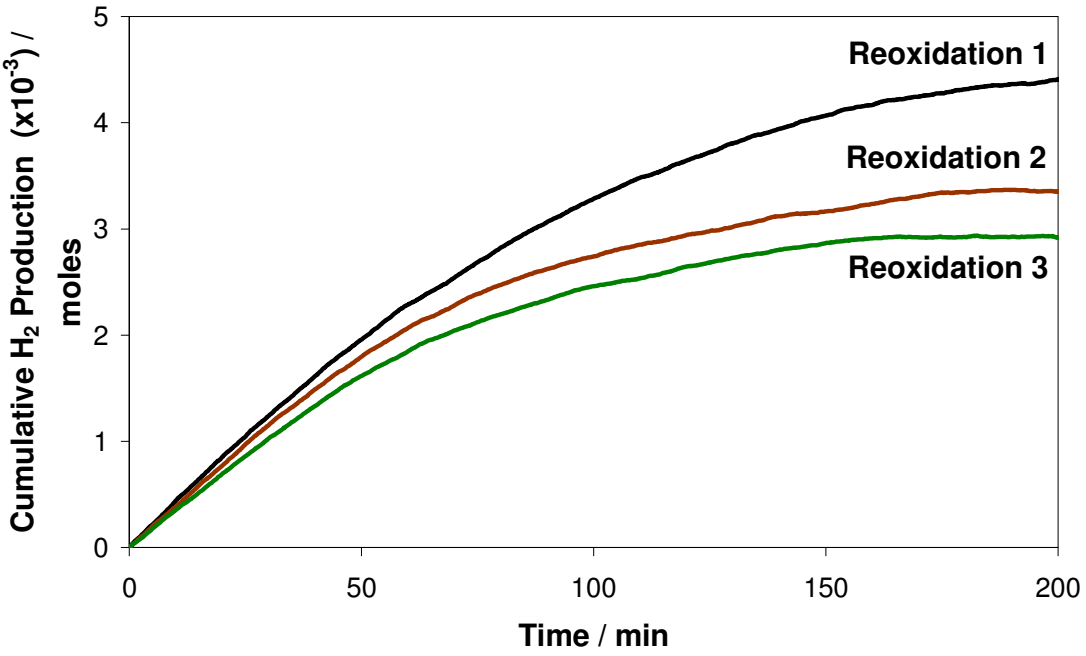

Figure 5.4 H_2O re-oxidation of unpromoted Fe_2O_3 over 3 cycles at 550°C

5.3.2.2 H_2 reduction/H_2O re-oxidation of CeO_2 promoted Fe_2O_3

Initial reduction of CeO_2 promoted Fe_2O_3 is from Fe_2O_3 to Fe. Following this, hydrogen consumption in the second reduction is consistent with a transition of FeO to Fe (**Table 5-6**):

$$FeO + H_2 \rightarrow Fe + H_2O \qquad \textbf{5.4}$$

This observation is based upon calculated H_2 production from the re-oxidation reaction, along with the time taken for re-oxidation to go to completion.

Complete re-oxidation of Fe by H_2O can only form Fe_3O_4 (**Chapter 3**), on the basis of which the final three reductions are determined to correlate to:

$$Fe_3O_4 + 4H_2 \rightarrow 3Fe + 4H_2O \qquad \textbf{5.2}$$

Re-oxidation of CeO_2 promoted Fe_2O_3 shows transition of Fe to FeO for the first two cycles, followed by re-oxidation of Fe to Fe_3O_4 in the following three cycles, as calculated by H_2 production values (**Figure 5.5, Table 5-7**). In addition, the similarity in the re-oxidation times between the first and second cycles compared to latter cycles is indicative of slower re-oxidation of bulk Fe metal. The reason for this incomplete re-oxidation is not completely understood. It is believed this may arise as a result of formation of a new binary oxide between Fe and Ce [16, 19]. The occurrence of such an event may simply arise after a number of cycles due to sintering and diffusion effects from cycling at high temperature.

Excess hydrogen consumption is observed with the addition of CeO_2, resulting in values in the initial reduction that exceed stoichiometric values by up to 2.5 times. Whilst this effect is influenced by the presence of CeO_2, hydrogen consumption is not in direct correlation to CeO_2 and/or Fe_2O_3 reduction. The reason for this is not entirely understood. There is the possibility excess hydrogen consumption effect may arise as a result of the aforementioned formation of a new potential binary oxide between Ce and Fe. It has been reported by Nguyen et. al. that the formation of a solid solution between CeO_2 and SnO_2 resulted in a significant increase in hydrogen consumption from reduction, beyond calculated values for the maximum OSC of the individual oxides [20]. CeO_2 promoted Fe_2O_3 shows good surface area retention, with approximately 75% of maximum hydrogen production produced over all cycles.

Table 5-6 Total H_2 consumption from CeO_2 promoted Fe_2O_3 reduction at 550ºC

	Cumulative H_2 Consumption (x 10^{-3}) / moles				
	Cycle 1	**Cycle 2**	**Cycle 3**	**Cycle 4**	**Cycle 5**
Reduction State	Fe_2O_3-Fe	FeO-Fe	FeO-Fe	Fe_3O_4-Fe	Fe_3O_4-Fe
Stoichiometric	3.31	2.21	2.21	2.93	2.93
Experimental	7.7	2.2	3.9	3.7	3.3
	Cumulative H_2O Production (x 10^{-3}) / moles				
Stoichiometric	3.31	2.21	2.21	2.93	2.93
Experimental	2.9	2.2	2.4	2.6	2.6

Table 5-7 Total H_2O consumption and H_2 production from CeO_2 promoted Fe_2O_3 re-oxidation at 550ºC

	Cumulative H_2O Consumption (x 10^{-3}) / moles				
	Cycle 1	**Cycle 2**	**Cycle 3**	**Cycle 4**	**Cycle 5**
Re-oxidation State	Fe-FeO	Fe-FeO	Fe-Fe_3O_4	Fe-Fe_3O_4	Fe-Fe_3O_4
Stoichiometric	2.21	2.21	2.93	2.93	2.93
Experimental	1.6	1.7	2.1	2.0	2.2
	Cumulative H_2 Production (x 10^{-3}) / moles				
Stoichiometric	2.21	2.21	2.93	2.93	2.93
Experimental	1.6	1.6	2.3	2.3	2.3

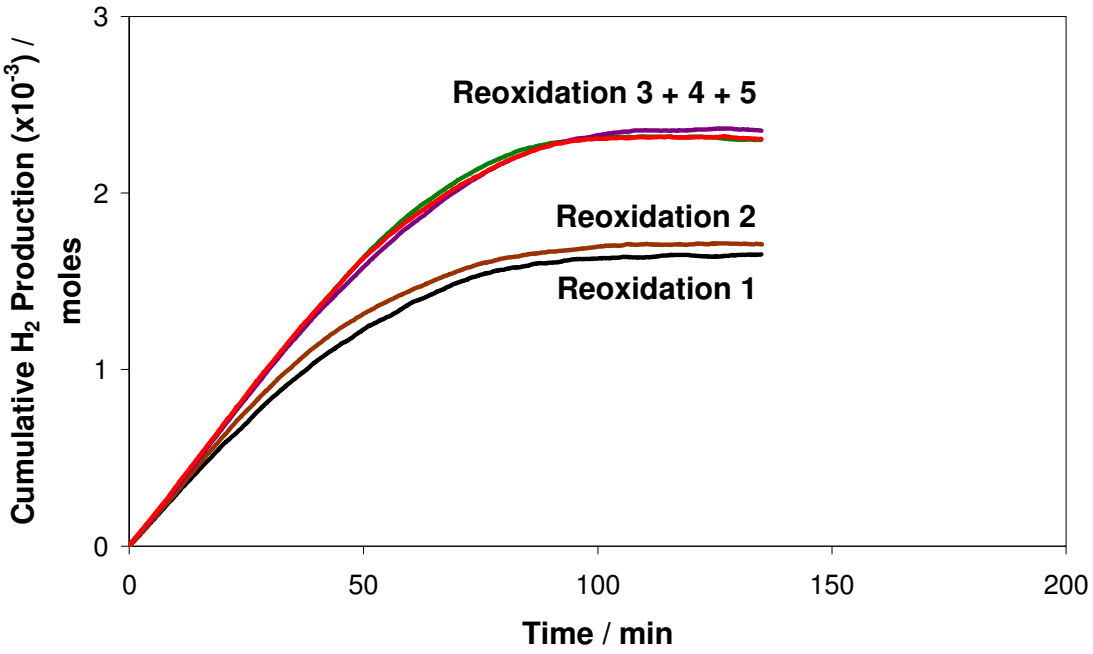

Figure 5.5 H_2O re-oxidation of CeO_2 promoted Fe_2O_3 over 5 cycles at 550°C

5.3.2.3 H_2 reduction/H_2O re-oxidation of CeO_2/ZrO_2 promoted Fe_2O_3

Reduction of CeO_2/ZrO_2 promoted Fe_2O_3 shows only partial reduction of Fe_2O_3 to FeO in the first cycle (**Table 5-8**):

$$Fe_2O_3 + H_2 \rightarrow 2FeO + H_2O \qquad \textbf{5.5}$$

Subsequent reduction cycles transition between Fe_3O_4 and FeO for a further two cycles, before finally reverting to Fe_3O_4-Fe redox cycling behaviour:

$$Fe_3O_4 + H_2 \rightarrow 3FeO + H_2O \qquad \textbf{5.6}$$

$$Fe_3O_4 + 4H_2 \rightarrow 3Fe + 4H_2O \qquad \textbf{5.2}$$

Re-oxidation is consistent with a FeO to Fe_3O_4 transition for the initial three cycles, followed by Fe to Fe_3O_4 redox cycling (**Figure 5.6, Table 5-9**):

$$3FeO + H_2O \rightarrow Fe_3O_4 + H_2 \quad \textbf{5.7}$$

$$3Fe + 4H_2O \rightarrow Fe_3O_4 + 4H_2 \quad \textbf{5.3}$$

Stoichiometric values are consistent with production of hydrogen from both FeO to Fe_3O_4 re-oxidation and from Ce_2O_3/ZrO_2 to CeO_2/ZrO_2 re-oxidation in the first three cycles:

$$2(CeO_2 / ZrO_2) + H_2 \leftrightarrow Ce_2O_3 / 2ZrO_2 + H_2O \quad \textbf{5.8}$$

CeO_2 to Ce_2O_3 reduction is observed in the TPR profile (**Figure 5.3**), where reduction of CeO_2 to Ce_2O_3 inhibits reduction further reduction of FeO to Fe.

Cycle 1-3 – Reduction:

(1^{st} reduction) $3Fe_2O_3 + H_2 \rightarrow 2Fe_3O_4 + H_2O$ **5.9**

$$Fe_3O_4 + 2(CeO_2 / ZrO_2) + 2H_2 \rightarrow 3FeO + Ce_2O_3 / 2ZrO_2 + 2H_2O \quad \textbf{5.10}$$

Re-oxidation:

$$3FeO + Ce_2O_3 / 2ZrO_2 + 2H_2O \rightarrow Fe_3O_4 + 2(CeO_2 / ZrO_2) + 2H_2 \quad \textbf{5.11}$$

Cycle 4, 5 – Reduction:

$$Fe_3O_4 + 4H_2 \rightarrow 3Fe + 4H_2O \quad \textbf{5.2}$$

Re-oxidation:

$$3Fe + 4H_2O \rightarrow Fe_3O_4 + 4H_2 \quad \textbf{5.3}$$

Table 5-8 Total H_2 consumption from CeO_2/ZrO_2 promoted Fe_2O_3 reduction at 550°C

	Cumulative H_2 Consumption (x 10^{-3}) / moles				
	Cycle 1	**Cycle 2**	**Cycle 3**	**Cycle 4**	**Cycle 5**
Reduction State	Fe_2O_3-FeO	Fe_3O_4-FeO	Fe_3O_4-FeO	Fe_3O_4-Fe	Fe_3O_4-Fe
	CeO_2-Ce_2O_3	CeO_2-Ce_2O_3	CeO_2-Ce_2O_3		
Stoichiometric	0.82 + 0.41	0.54 + 0.41	0.54 + 0.41	2.17	2.17
	1.23	**0.95**	**0.95**		
Experimental	11.5	2.9	1.6	5.1	2.9
	Cumulative H_2O Production (x 10^{-3}) / moles				
Stoichiometric	0.82 + 0.41	0.54 + 0.41	0.54 + 0.41	2.17	2.17
	1.23	**0.95**	**0.95**		
Experimental	1.3	1.1	1.2	1.8	2.0

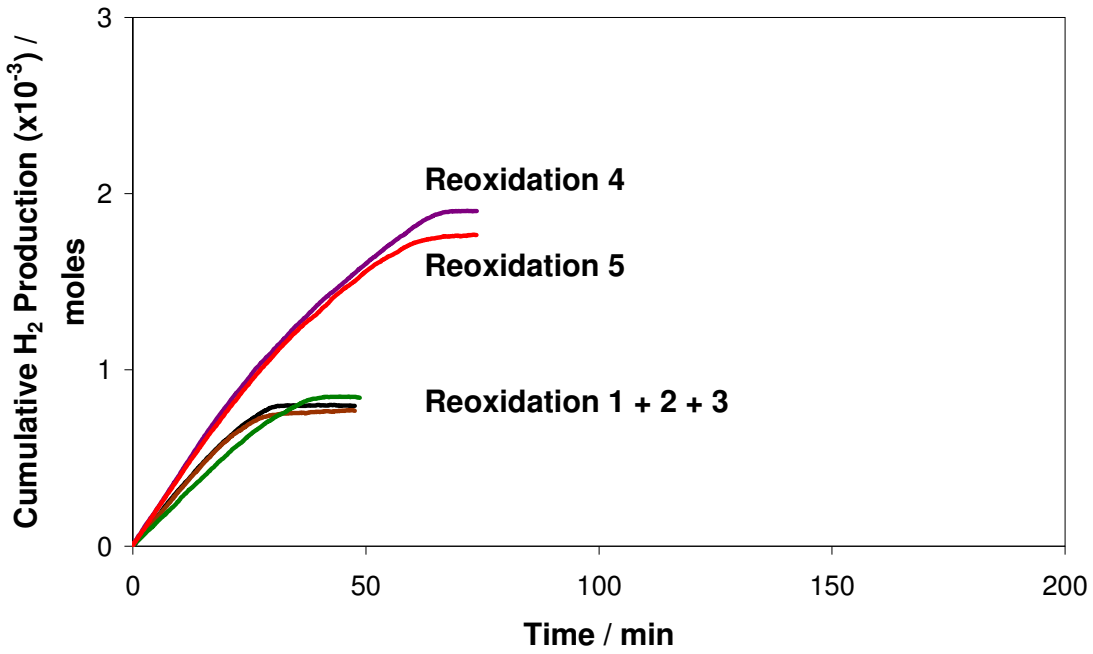

Figure 5.6 H_2O re-oxidation of CeO_2/ZrO_2 promoted Fe_2O_3 over 5 cycles at 550°C

Table 5-9 Total H_2O consumption and H_2 production from CeO_2/ZrO_2 promoted Fe_2O_3 re-oxidation at 550°C

	Cumulative H_2O Consumption (x 10^{-3}) / moles				
	Cycle 1	**Cycle 2**	**Cycle 3**	**Cycle 4**	**Cycle 5**
Re-oxidation State	FeO-Fe_3O_4	FeO-Fe_3O_4	FeO-Fe_3O_4	Fe-Fe_3O_4	Fe-Fe_3O_4
	Ce_2O_3-CeO_2	Ce_2O_3-CeO_2	Ce_2O_3-CeO_2		
Stoichiometric	0.54 + 0.41	0.54 + 0.41	0.54 + 0.41	2.17	2.17
	0.95	**0.95**	**0.95**		
Experimental	0.8	0.8	0.9	1.8	1.6
	Cumulative H_2 Production (x 10^{-3}) / moles				
Stoichiometric	0.54 + 0.41	0.54 + 0.41	0.54 + 0.41	2.17	2.17
	0.95	**0.95**	**0.95**		
Experimental	0.8	0.8	0.9	2.0	1.8

CeO_2/ZrO_2 is preferentially reduced prior to reduction of Fe_3O_4 to Fe (**Figure 5.3**), with CeO_2/ZrO_2 acting to stabilise the metastable FeO phase, allowing for subsequent cycling between FeO and Fe_3O_4. With each cycle, slight over-reduction of FeO results in formation of Fe metal. Following the third cycle, due to the high proportion of Fe formed, complete reduction to form Fe metal becomes favoured over stabilisation of FeO.

Re-oxidation of FeO to Fe_3O_4 in the first three cycles produces stoichiometric amounts of hydrogen, but re-oxidation of Fe to Fe_3O_4 in the fourth and fifth cycles shows progressively decreasing hydrogen production. Minimal sintering is expected for reduction of Fe_3O_4 to FeO, but upon complete reduction of Fe_3O_4 to Fe the degree of sintering in the metallic phase is greater. Re-oxidation is much quicker in the first three cycles, due to re-oxidation of a less sintered intermediate oxide phase (FeO) and the lesser amount of oxygen removed (0.33 moles/mol.Fe), as compared to Fe to Fe_3O_4 re-oxidation (1.33 moles/mol.Fe). This stabilizing effect may arise due to interaction between iron oxide and the promoting species, as found in the reduction of iron oxide

promoted with MgO and CaO species [21, 22]. It is reported by El-Geassy that MgO has a retardation effect upon the reduction of Fe_2O_3, in which a stable wustite phase is formed resulting from interaction with MgO species. No reports of stabilisation due to introduction of CeO_2/ZrO_2 promoters at the loadings used were found.

Reduction of CeO_2/ZrO_2 promoted Fe_2O_3 also shows high levels of hydrogen consumption, with values five times greater than stoichiometric values in the initial reduction. Once again, the reason for this excess hydrogen consumption is not clear, with literature references primarily referring to hydrogen overspill when using precious metals promoters. This phenomenon is not found to be directly related to reduction of either Fe_2O_3 or CeO_2 species. Surface area is likely to be a factor in hydrogen consumption; with increasing surface area from CeO_2 promoted Fe_2O_3 to CeO_2/ZrO_2 promoted Fe_2O_3, there is a two-fold increase in hydrogen consumption, as compared to hydrogen consumption over unpromoted Fe_2O_3.

5.3.2.4 Post-redox characterisation

Figure 5.7 shows post-H_2 reduction/H_2O re-oxidation XRD sample analysis. The final phase composition is consistent with Fe_3O_4 and CeO_2 or CeO_2/ZrO_2. Calculated particle diameters based upon XRD results indicate increased crystallite size due to sintering effects (**Table 5-10**).

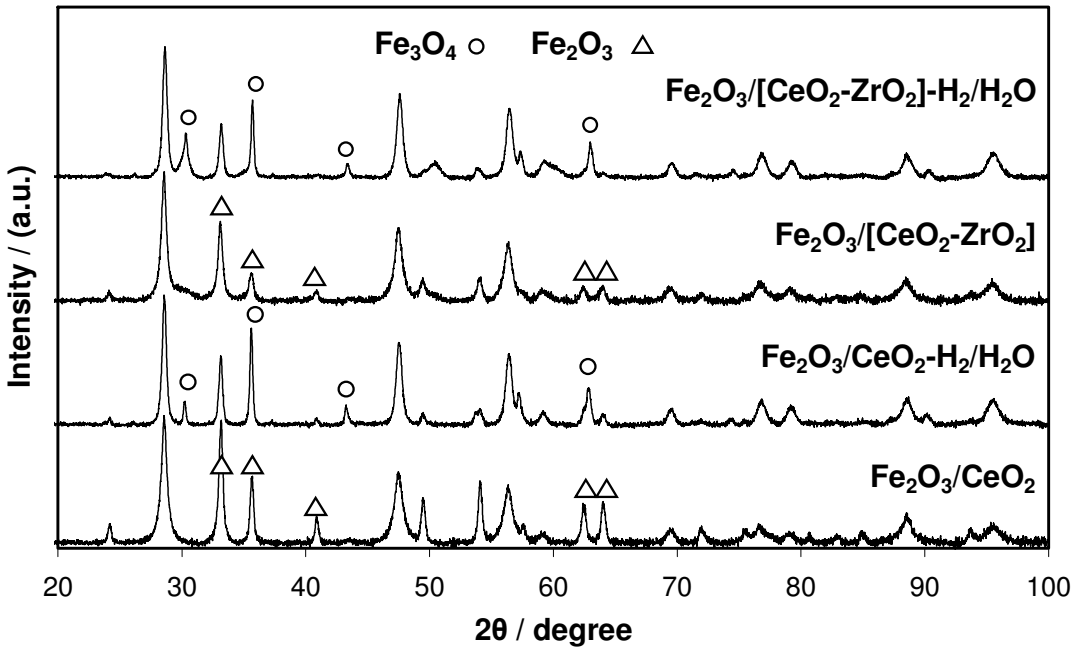

Figure 5.7 XRD spectra of as prepared and H_2/H_2O post-redox of promoted Fe_2O_3

Table 5-10 Measured properties of H_2 post-redox samples

Sample	Crystallite Diameter/ nm Post-Steam-Iron Reaction[a] (5 cycles)	BET_{SA} / (m^2/g) Post-Steam-Iron Reaction (5 Cycles)
Fe_2O_3	--	<1
Fe_2O_3/CeO_2	42	4.2
Fe_2O_3 / [CeO_2/ZrO_2]	50	19.1

[a] Determined by Scherrer Equation from XRD spectra (**Figure 5.7**)

This observation is supported by TEM imagery (**Figure 5.8**) with elimination of interparticle porosity as compared to fresh, unreacted samples. However, smaller particles dispersed throughout the aggregates are also observed. This is indicative of sintering of iron oxide, whilst CeO_2 and CeO_2/ZrO_2 promoted Fe_2O_3 are relatively less sintered, retaining smaller particle size and structure.

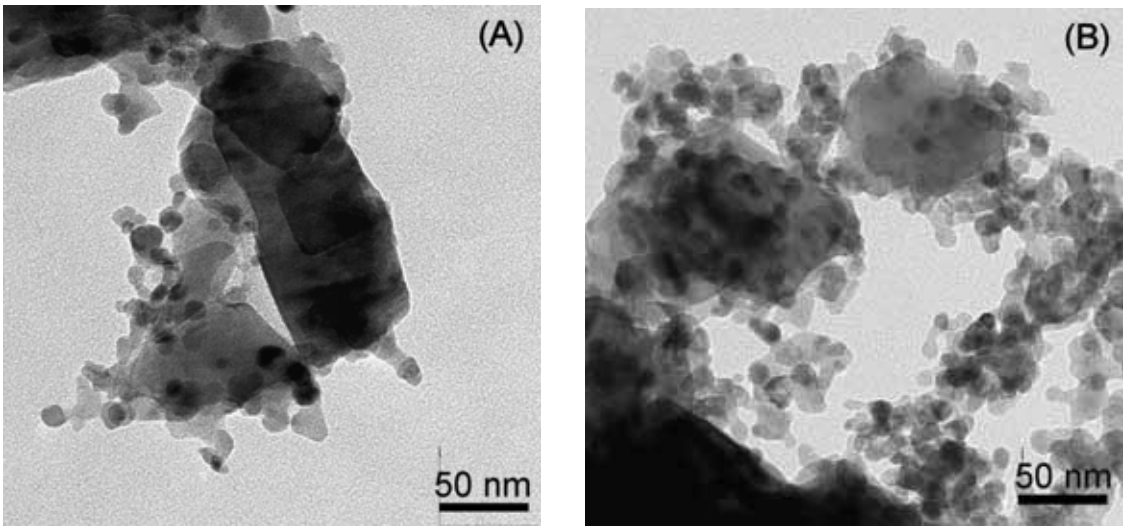

Figure 5.8 TEM imagery of (A) Fe_2O_3/CeO_2 and (B) $Fe_2O_3/[CeO_2/ZrO_2]$, H_2/H_2O post-redox

5.3.2.5 H_2 reduction/H_2O re-oxidation of unpromoted and promoted Fe_2O_3

Redox of Fe_2O_3, CeO_2/Fe_2O_3 and $[CeO_2/ZrO_2]/Fe_2O_3$ using H_2 as the reductant and H_2O as the oxidant was performed at 550ºC over a number of cycles to determine the effects of promoters upon Fe_2O_3 redox behaviour and change in potential OSC. Unpromoted Fe_2O_3 showed initial reduction to Fe metal, followed by redox cycling between Fe ↔ Fe_3O_4 as calculated from hydrogen consumption during the reduction reaction and hydrogen production during the re-oxidation reaction (**Table 5-4**, **Table 5-5**). Re-oxidation of Fe_3O_4 to form Fe_2O_3 is considered to be thermodynamically unfavourable and this transition was not observed during the redox process. Deactivation as a result of sintering effects accounted for an incremental decrease in H_2 production capacity up to 35% between the first and the third cycle, with the same decrease in stoichiometric H_2 production capacity.

CeO_2 promoted Fe_2O_3 showed unexpected redox behaviour. Following initial reduction of Fe_2O_3 to Fe metal, subsequent re-oxidation formed FeO, as determined by calculation of H_2 production and re-oxidation time (**Table 5-9**, **Figure 5.5**). This cycling between Fe

↔ FeO occurred for two cycles, whereupon from the third cycle onward, complete re-oxidation to form Fe_3O_4 was observed and redox cycling between Fe ↔ Fe_3O_4 took place. Redox of CeO_2 species did not occur, as TPR indicated (**Figure 5.3**) reduction of CeO_2 only takes place beyond 700ºC, well above the 550ºC operating temperature for redox. This unusual behaviour was possibly attributed to the formation of a new form of Fe-Ce binary oxide, however this was not confirmed [16, 19]. The final structure is consistent with separate oxides of Fe_3O_4 and CeO_2. Over five cycles approximately 25% reduction in H_2 production capacity was observed. Hydrogen production remained consistent with minimal decline following the first cycle, with the exception of the increase in H_2 production due to a transition to higher oxidation state upon Fe_3O_4 formation (previously FeO formation).

Addition of CeO_2/ZrO_2 to Fe_2O_3 demonstrates limited stabilising behaviour upon reduction of Fe_2O_3, forming metastable FeO and subsequently allowing for cycling between FeO ↔ Fe_3O_4 for up to three cycles (**Table 5-9**, **Figure 5.6**). Reduction and re-oxidation times were more rapid as compared to Fe ↔ Fe_3O_4 cycling, with calculation of H_2 production from each cycle consistent with this observation. Similar stabilisation of intermediate iron oxide (FeO) has been observed with addition of MgO and CaO as reported by El-Geassy [21, 22]. From the fourth cycle onward, cycling behaviour reverted once more to form Fe ↔ Fe_3O_4. Reduction of CeO_2 species also took place, giving additional OSC and H_2 production. High H_2 production capacity was retained over numerous cycles, with only 15% reduction in H_2 production between experimental and stoichiometric values.

Addition of CeO_2 and CeO_2/ZrO_2 promoters increase the rate of re-oxidation of Fe_2O_3 even when taking into account the difference in Fe_2O_3 percentage within unpromoted and promoted samples (**Figure 5.4 – Figure 5.6**). High surface area retention allows for a greater proportion of reduced iron oxide to be re-oxidised over a number of cycles, maintaining increased hydrogen production during re-oxidation. This conclusion is based on higher percentage of hydrogen produced per mole of Fe over promoted iron oxide.

Addition of CeO_2 and CeO_2/ZrO_2 allows for Fe_3O_4 to form a greater proportion of surface oxygen species, resulting in more rapid reduction as compared to unpromoted Fe_3O_4 which is contains a greater proportion of bulk oxygen that is more slowly reduced. Additionally, complete reduction to Fe metal shows increased sintering effects and catalyst deactivation even for promoted Fe_2O_3, whereas stabilisation of FeO aids to retain surface area and maximise hydrogen production.

5.3.3 Steam-Iron Reaction: CO reduction studies on promoted Fe_2O_3

Reduction of unpromoted and promoted Fe_2O_3 by CO was investigated at 450ºC. The possibility of CO decomposition over Fe at higher temperature would result in undesired coking and rapid catalyst deactivation, thus temperature was limited in an effort to prevent such effects. Following reduction of Fe_2O_3 from 150-450ºC in the first cycle, subsequent reduction and re-oxidation processes were performed isothermally at 450ºC. **Figure 5.9** shows the CO reduction profiles of unpromoted and promoted Fe_2O_3 up to 450ºC. Unpromoted Fe_2O_3 reduces in two steps, yet the CO signal does not return to the original value, possibly due to ongoing reduction. As it unlikely that unpromoted Fe_2O_3 is reduced to FeO and remains stable, it is probable that Fe_2O_3 has reduced to Fe, whereupon CO decomposition over Fe metal accounts for continuous CO consumption over time. CeO_2 promoted Fe_2O_3 shows reduction in two distinct steps, Fe_2O_3 to Fe_3O_4 followed by Fe_3O_4 to FeO. In contrast, CeO_2/ZrO_2 promoted Fe_2O_3 shows complete reduction, with three distinguishable peaks correlating to reduction from Fe_2O_3 to Fe_3O_4, Fe_3O_4 to FeO and FeO to Fe. Again, the CO signal does not return to its original value, indicative of the reaction yet to reach completion with ongoing CO consumption.

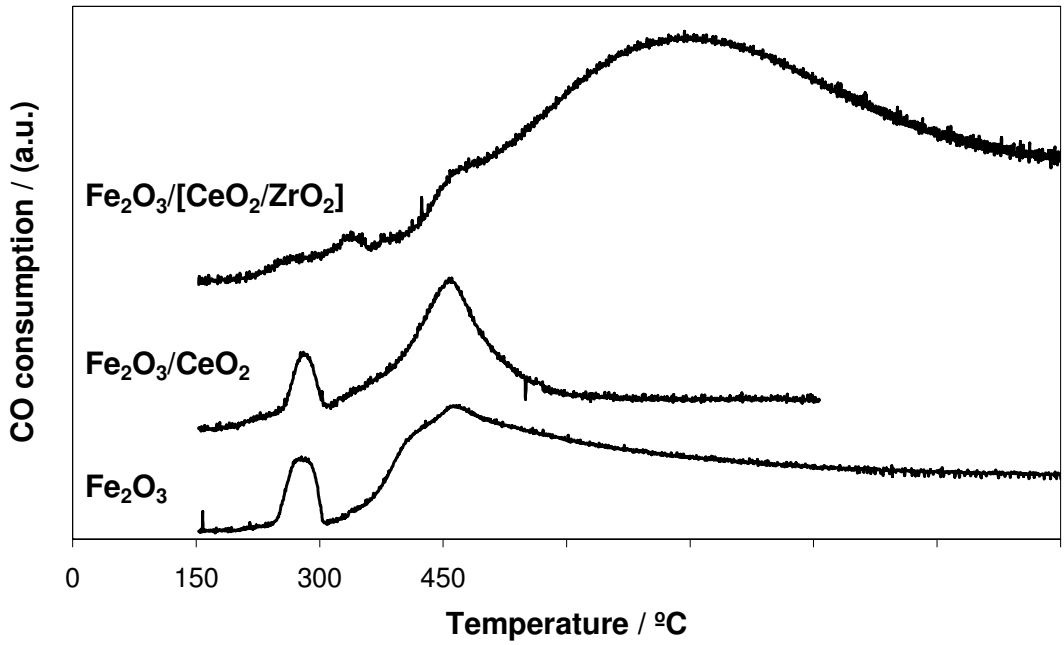

Figure 5.9 10% CO reduction of unpromoted and promoted Fe_2O_3 up to 450ºC

5.3.3.1 CO reduction/H_2O re-oxidation of unpromoted Fe_2O_3

Table 5-11 summarises CO consumption and CO_2 production from the reduction of unpromoted Fe_2O_3. Consumption of CO is observed to be greater than CO_2 production. According to the predicted reaction process, CO and CO_2 should be produced in a 1:1 ratio for CO consumption correlating to reduction of Fe_3O_4 to Fe.

$$Fe_3O_4 + 4CO \rightarrow 3Fe + 4CO_2 \qquad \textbf{5.12}$$

Upon formation of Fe metal, further reactions which could take place include the formation of Fe_3C and/or CO decomposition catalysed by Fe metal, resulting in carbon deposition. Either of these two reactions would result in excess CO consumption in comparison to CO_2 formation. Thermodynamic assessment of reduction of iron oxide by CO suggests that at relatively low temperatures of reduction (<1000ºC) carbon deposition

is the highly favourable reaction upon formation of Fe metal [23]. Thus it is assumed that this excess CO consumption correlates to CO decomposition over reduced Fe metal to form carbon. The sharp drop in CO consumption and CO_2 production from reduction in the following cycles indicates that carbon deposition and sintering cause substantial decrease in cyclic activity. **Table 5-12** shows H_2 and CO_2 production from re-oxidation of reduced Fe_2O_3. There is approximately stoichiometric production of hydrogen from Fe re-oxidation in the first cycle, along with limited hydrogen produced from carbon oxidation. Subsequent cycles show significant drops in hydrogen production.

Table 5-11 Total CO consumption and CO_2 production from unpromoted Fe_2O_3 reduction up to 450ºC

	Cumulative CO Consumption (x 10^{-3}) / moles		
	Cycle 1	**Cycle 2**	**Cycle 3**
Reduction State	Fe_2O_3-Fe	Fe_3O_4-Fe	Fe_3O_4-Fe
Stoichiometric	4.71	4.18	4.18
Experimental	4.9	0.7	0.3
	Cumulative CO_2 Production (x 10^{-3}) / moles		
Stoichiometric	4.71	4.18	4.18
Experimental	4.2	0.5	0.3

Table 5-12 Total H_2O consumption, H_2 production and CO_2 production from unpromoted Fe_2O_3 re-oxidation at 450ºC

	Cumulative H_2O Consumption (x 10^{-3}) / moles		
	Cycle 1	**Cycle 2**	**Cycle 3**
Re-oxidation State	Fe-Fe_3O_4	Fe-Fe_3O_4	Fe-Fe_3O_4
Stoichiometric	4.18	4.18	4.18
Experimental	4.2	1.1	1.0
	Cumulative H_2 Production (x 10^{-3}) / moles		
Stoichiometric	4.18	4.18	4.18
Experimental	4.7	1.1	0.9
H_2-Fe re-oxidation	**4.1**		
	Cumulative CO_2 Production (x 10^{-3}) / moles		
Experimental	0.3	0.04	0.04

5.3.3.2 CO reduction/H_2O re-oxidation of CeO_2 promoted Fe_2O_3

Table 5-13 shows slightly greater than stoichiometric consumption of CO in the first cycle, with stoichiometric CO_2 production, consistent with Fe_2O_3-FeO reduction together with some carbon deposition. In the second reduction cycle, CO consumption is in excess of stoichiometric quantities required for complete reduction of Fe_3O_4 to Fe alone, due to CO decomposition over completely reduced Fe.

H_2O consumption and H_2 production upon re-oxidation correlate to FeO-Fe_3O_4 re-oxidation, with minimal CO_2 production from carbon oxidation (**Table 5-14**):

$$C + 2H_2O \rightarrow CO_2 + 2H_2 \qquad \textbf{5.13}$$

In the second re-oxidation cycle, carbon deposition on the metal oxide surface from the previous reduction cycle inhibits Fe to Fe_3O_4 re-oxidation, thereby preventing further hydrogen production. At the relatively low temperature used for re-oxidation (450ºC), these adsorbed carbon species are unable to be re-oxidised by H_2O.

Carbon burn off was not performed to verify the extent of carbon deposition. However, XRD analysis of CeO_2 promoted Fe_2O_3 following two redox cycles of CO reduction and H_2O re-oxidation shows a structure predominantly comprising Fe metal and carbon (**Figure 5.12**).

Table 5-13 Total CO consumption and CO_2 production from CeO_2 promoted Fe_2O_3 reduction up to 450ºC

	Cumulative CO Consumption (x 10^{-3}) / moles	
	Cycle 1	**Cycle 2**
Reduction State	Fe_2O_3-FeO	Fe_3O_4-Fe
Stoichiometric	1.15	3.07
Experimental	1.6	5.9
	Cumulative CO_2 Production (x 10^{-3}) / moles	
Stoichiometric	1.15	3.07
Experimental	1.2	2.6

Table 5-14 Total H_2O consumption, H_2 production and CO_2 production from CeO_2 promoted Fe_2O_3 re-oxidation at 450°C

	Cumulative H_2O Consumption (x 10^{-3}) / moles	
	Cycle 1	**Cycle 2**
Re-oxidation State	FeO-Fe_3O_4	Fe-Fe_3O_4
Stoichiometric	0.76	3.07
Experimental	1.3	1.2
	Cumulative H_2 Production (x 10^{-3}) / moles	
Stoichiometric	0.76	3.07
Experimental	1.3	0
	Cumulative CO_2 Production (x 10^{-3}) / moles	
Experimental	0.1	0.1

5.3.3.3 CO reduction/H_2O re-oxidation of CeO_2/ZrO_2 promoted Fe_2O_3

Table 5-15 shows high levels of CO consumption from reduction of CeO_2/ZrO_2 promoted Fe_2O_3, with **Figure 5.9** showing continued consumption of CO after reduction of FeO to Fe has taken place. CO_2 production is approximately 50% of CO consumption, indicating the Boudouard Reaction as the primary reaction, producing CO_2 and C:

$$2CO \rightarrow CO_2 + C \qquad \textbf{5.14}$$

Figure 5.10 shows lack of any H_2 production in the re-oxidation step, with some CO_2 being produced. Subsequent re-oxidation yields minimal CO_2, with carbon oxidation unfavourable at lower temperature.

Table 5-15 Total CO consumption and CO_2 production from CeO_2/ZrO_2 promoted Fe_2O_3 reduction up to 450ºC

	Cumulative CO Consumption (x 10^{-3}) / moles
	Cycle 1
Reduction State	Fe_2O_3-Fe
Stoichiometric	2.45
Experimental	12.1
	Cumulative CO_2 Production (x 10^{-3}) / moles
Stoichiometric	2.45
Experimental	5.4

Table 5-16 Total H_2O consumption, H_2 production and CO_2 production from CeO_2/ZrO_2 promoted Fe_2O_3 re-oxidation at 450ºC

	Cumulative H_2O Consumption (x 10^{-3}) / moles
	Cycle 1
Re-oxidation State	Fe-Fe_3O_4
Stoichiometric	2.17
Experimental	0.5
	Cumulative H_2 Production (x 10^{-3}) / moles
Stoichiometric	2.17
Experimental	0
	Cumulative CO_2 Production (x 10^{-3}) / moles
Experimental	0.04

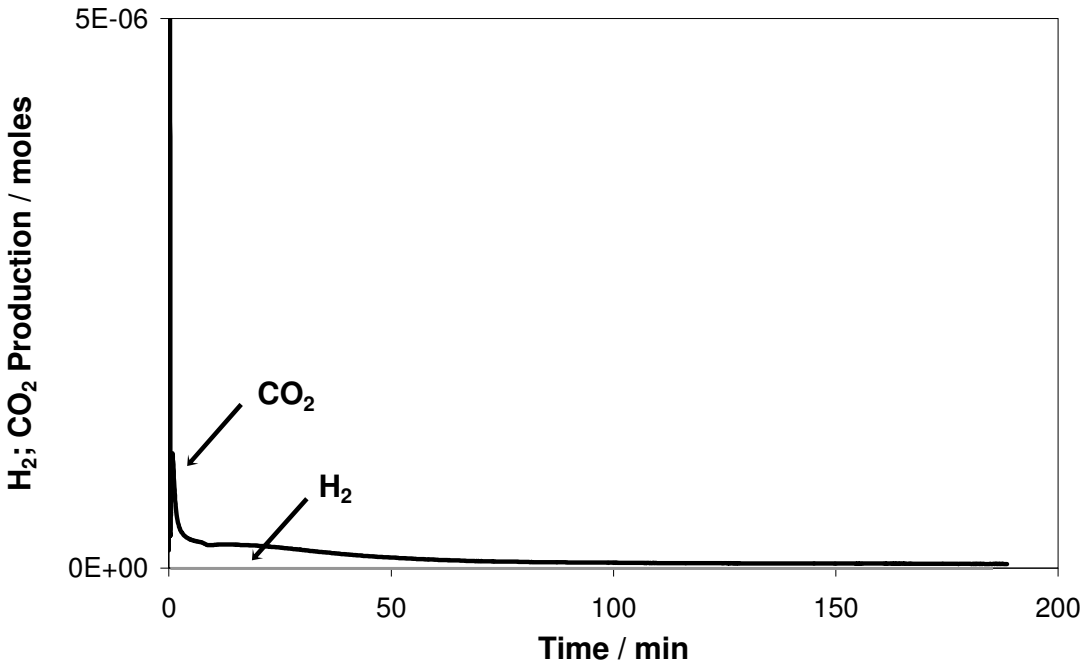

Figure 5.10 H_2 and CO_2 production from H_2O re-oxidation of CeO_2/ZrO_2 promoted Fe_2O_3 at 450ºC

5.3.3.4 Post-redox characterisation

H_2 production from one redox cycle of unpromoted Fe_2O_3 shows stoichiometric H_2 production however, H_2 production in subsequent redox cycles is minimal due to limited repeatable redox capability (**Figure 5.11**). CeO_2 promoted Fe_2O_3 demonstrates fast re-oxidation for one redox cycle, albeit, with lower H_2 production due to limited reduction compared to unpromoted Fe_2O_3. Beyond the first cycle coking results in catalyst deactivation.

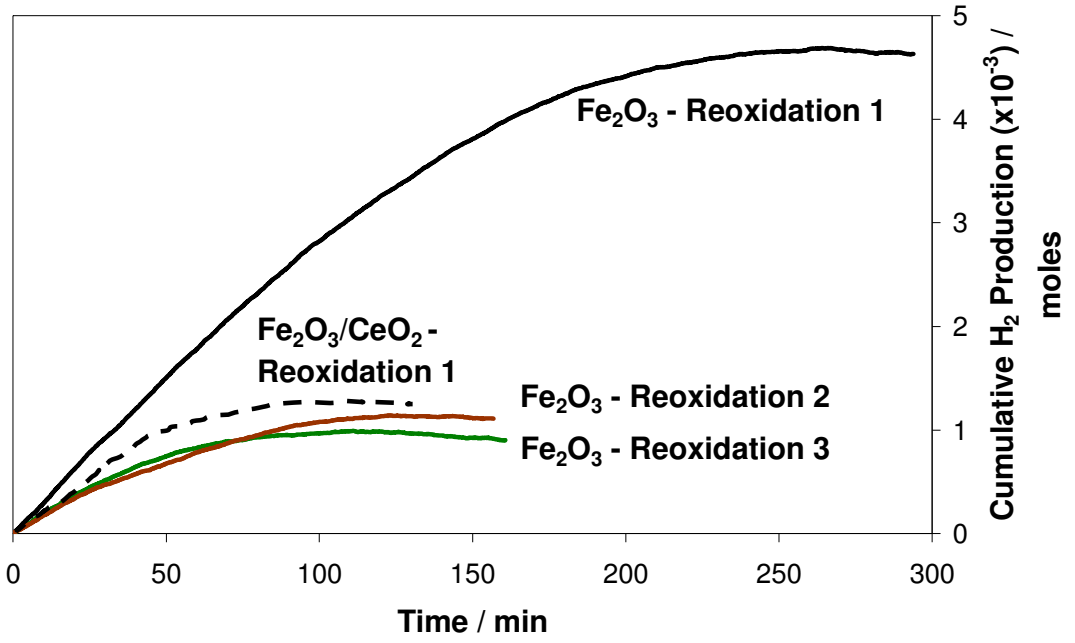

Figure 5.11 H_2 production from H_2O re-oxidation of unpromoted and CeO_2 promoted Fe_2O_3 at 450°C

Post-redox XRD (**Figure 5.12**) shows unpromoted Fe_2O_3 with a Fe_3O_4 composition. The first reduction of Fe_2O_3 to Fe is followed by subsequent re-oxidation of Fe to Fe_3O_4, due to complete re-oxidation to Fe_2O_3 being thermodynamically unfavourable. CeO_2 and CeO_2/ZrO_2 promoted Fe_2O_3 show predominantly Fe metal composition post-redox, indicating of a lack of re-oxidation. Due to carbon on the surface reduced Fe is unable to be re-oxidised, preventing hydrogen production over promoted Fe_2O_3. All samples show carbon, due to adsorbed carbon species that are unable to be oxidised at lower temperature.

Higher surface area retention promoted Fe_2O_3 is also observed by post-SIR BET (**Table 5-17**). However, the high surface area can also be attributed to deposition of high surface area carbon on unpromoted and promoted Fe_2O_3 samples.

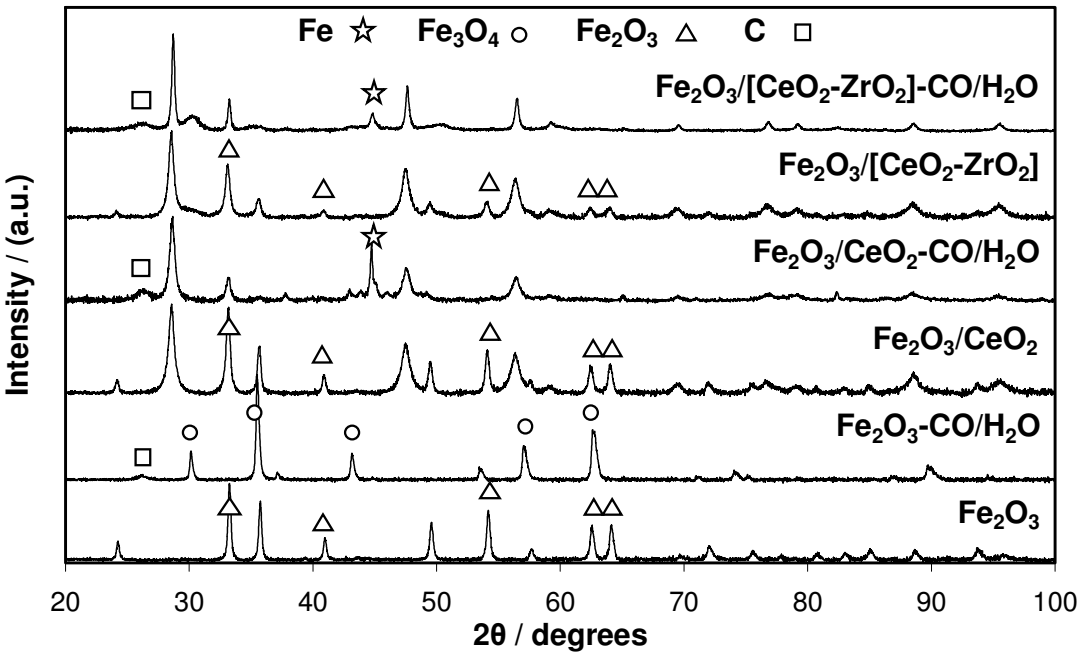

Figure 5.12 XRD spectra of as prepared and CO/H_2O post-redox of unpromoted and promoted Fe_2O_3

Table 5-17 Measured properties of CO/H_2O post-redox unpromoted and promoted Fe_2O_3 at 450ºC

Sample	Particle Diameter/ nm Post-SIR[a] (5 cycles)	BET_{SA} / (m^2/g) Post-SIR (5 Cycles)
Fe_2O_3	54.6	43.2
Fe_2O_3/CeO_2	55.1	53.0
Fe_2O_3 / [CeO_2/ZrO_2]	39.7	89.9

[a] Determined by Scherrer Equation from XRD spectra (**Figure 5.12**)

Calculation of Gibbs Free Energy (**Table 5-18**) indicates at 450ºC, oxidation of carbon by H_2O is not a favoured reaction. At this lower temperature, the Boudouard reaction is favoured, resulting in extensive carbon deposition when using CO as a reductant.

Table 5-18 Gibbs Free Energy of reaction at 450ºC

Equation	Reaction	ΔG^{o}_{450} / (kJ/mol)
5.12	$C + 2H_2O \rightarrow CO_2 + 2H_2$	24.88
5.15	$C + H_2O \rightarrow CO + H_2$	38.64
5.13	$2CO \rightarrow CO_2 + C$	-44.20

CeO_2 and CeO_2/ZrO_2 promoters increase reducibility of Fe_2O_3 and, as a result, promoted Fe_2O_3 shows greater levels of coking compared to unpromoted Fe_2O_3. Complete and rapid reduction of Fe_2O_3 to Fe in promoted samples, coupled with higher surface areas, results in high levels of CO decomposition. Carbon oxidation is not observed upon re-oxidation due to low temperature of reaction. In comparison, whilst unpromoted Fe_2O_3 still shows hydrogen production after a number of cycles, there is a significant decrease in percentage hydrogen production due to catalyst deactivation.

5.3.3.5 CO reduction/H_2O re-oxidation of unpromoted and promoted Fe_2O_3

Redox of Fe_2O_3, CeO_2/Fe_2O_3 and $[CeO_2/ZrO_2]/Fe_2O_3$ using CO as the reductant and H_2O as the oxidant was performed at 450ºC over a number of cycles to compare CO as a reductant. Unpromoted Fe_2O_3 shows ongoing CO consumption beyond 200 minutes following reduction of Fe_2O_3 to Fe_3O_4, followed by Fe_3O_4 to Fe reduction, which is attributed to CO decomposition following reduction to Fe metal (**Figure 5.9**). Re-oxidation produces CO_2 from oxidation of deposited carbon with close to stoichiometric H_2 production in the first redox cycle (**Table 5-12**). Subsequent redox cycles show minimal CO consumption during reduction and subsequently, minimal H_2 production during oxidation due to blockage of active sites by carbon deposits at the catalyst surface. Carbon oxidation is not possible at the relatively low temperature of re-oxidation.

CeO_2 promoted Fe_2O_3 shows excess CO consumption in the first reduction, according to the calculated FeO final oxidation state, with greater than stoichiometric hydrogen production from re-oxidation (**Figure 5.9**, **Table 5-14**). This is attributed to oxidation of deposited carbon, which produces CO_2 and H_2. Beyond the first cycle, complete reduction to Fe metal is observed, whereupon excess CO consumption from CO decomposition to form carbon occurs. Introduction of CeO_2 to Fe_2O_3 stabilises the formation of intermediate FeO. CO decomposition catalysed over Fe metal is considered to be the primary cause for catalyst deactivation and contamination of H_2 production.

CeO_2/ZrO_2 promoted Fe_2O_3 shows deactivation following the first reduction cycle, in which up to six times the stoichiometric level of CO is consumed, resulting in excessive carbon deposition (**Figure 5.9**). Subsequent re-oxidation yields no H_2 with minimal CO_2 production (**Table 5-16**). Unlike reduction of unpromoted Fe_2O_3 and CeO_2 promoted Fe_2O_3, the rapid reduction of CeO_2/ZrO_2 promoted Fe_2O_3 forms Fe metal which catalyses CO decomposition by the Boudouard Reaction. The high level of carbon formation prevents further re-oxidation of reduced Fe_2O_3 species, thereby limiting H_2 production.

5.3.4 Steam-Iron Reaction: CO + H_2 reduction studies on promoted Fe_2O_3

Reduction using a syngas mixture (CO + $3H_2$) resulted in high levels of coking and rapid catalyst deactivation of both unpromoted and promoted Fe_2O_3. Once temperatures reached 450ºC, CO and H_2 consumption increased to a maximum level at which they remained, indicative of reactor blockage (**Figure 5.13**). Re-oxidation of both unpromoted and promoted Fe_2O_3 at 450ºC resulted in negligible levels of hydrogen production due to complete reactor blockage, as well as the inability to oxidise adsorbed carbon at low temperature. Syngas is highly reactive as a reductant, but without means of limiting carbon formation from CO decomposition, catalyst deactivation is inevitable. The possibility for lower temperature reduction in an effort to prevent carbon deposition was considered improbable, due to inefficiency of the subsequent re-oxidation step at lower temperature.

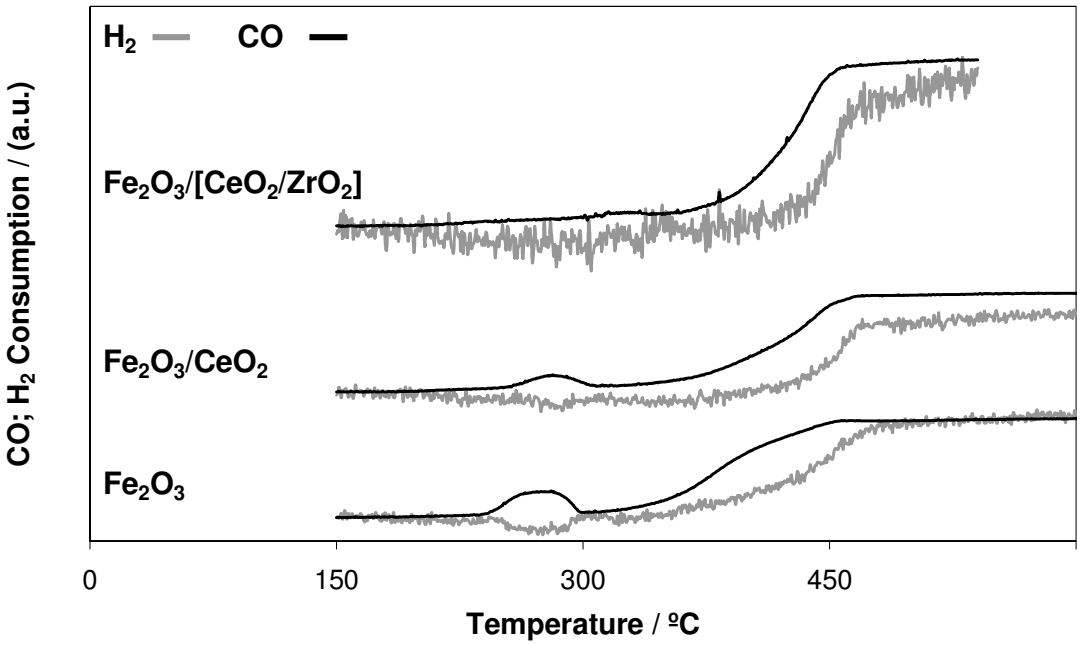

Figure 5.13 10% CO / 30% H_2 reduction of unpromoted and promoted Fe_2O_3 up to 450ºC

5.3.5 Steam-Iron Reaction: CH_4 reduction studies on promoted Fe_2O_3

Higher concentration of methane results in preferential partial oxidation of methane, to give CO + H_2 rather than CO_2 and H_2O (**Equation 5.15-5.18**):

$$3Fe_2O_3 + CH_4 \rightarrow 2Fe_3O_4 + CO + 2H_2 \quad \textbf{5.16}$$

$$Fe_3O_4 + 4CH_4 \rightarrow 3Fe + 4CO + 8H_2 \quad \textbf{5.17}$$

$$6Fe_2O_3 + \tfrac{1}{2}CH_4 \rightarrow 4Fe_3O_4 + \tfrac{1}{2}CO_2 + H_2O \quad \textbf{5.18}$$

$$Fe_3O_4 + CH_4 \rightarrow 3Fe + CO_2 + 2H_2O \quad \textbf{5.19}$$

Due to methane decomposition over Fe beyond ca 750ºC [24], it is necessary to limit methane concentration such that severity of carbon deposition is mitigated. Methane concentration was set to 10% CH_4 in Ar/He, at a flow rate of 60mL/min.

As shown in **Figure 5.14**, reduction of unpromoted Fe_2O_3 by methane up to 750ºC is incomplete, with two peaks at 530ºC and 750ºC+ being assigned to Fe_2O_3 to Fe_3O_4 and Fe_3O_4 to FeO reduction. CeO_2 promoted Fe_2O_3 showed two peaks at 612ºC and 750ºC+, assigned to the same aforementioned peaks for unpromoted Fe_2O_3. A third peak that emerges after the temperature is held at 750ºC for 60 minutes corresponds with complete reduction of FeO to Fe. Reduction of CeO_2/ZrO_2 promoted Fe_2O_3 shows extensive CH_4 decomposition at 750ºC+, with reactor blockage due to carbon deposition. This is evidenced by the sudden decrease in the methane signal (**Figure 5.14**), which is not accompanied by a corresponding increase in product gases, as would be expected for high methane consumption due to decomposition (**Figure 5.15**). There is a sudden fluctuation in Ar reference gas signal (not shown) also corresponding with limited methane gas flow.

Figure 5.15 more clearly illustrates the reduction profile of each sample from CH_4 reduction, showing CO_2 and H_2O production. These products provide the most distinct profile with these gases produced at all reduction peaks therefore they provide the most accurate depiction of the reduction profile during CH_4 reduction. A broad peak at low temperature observed for CeO_2/ZrO_2 promoted Fe_2O_3 (and to a lesser extent, CeO_2 promoted Fe_2O_3), can be assigned to reduction of CeO_2 and CeO_2/ZrO_2 by CH_4, shown in **Figure 5.15**. CH_4 reduction occurred more rapidly on CeO_2/ZrO_2 promoted Fe_2O_3 in 150 min, compared to 200+ min for CeO_2 promoted Fe_2O_3 (**Figure 5.14, Figure 5.15**). Unpromoted Fe_2O shows incomplete reduction with only two distinct peaks observed. The primary products from CH_4 reduction are CO_2 and H_2O, produced at each reduction peak. CO and H_2 production (not shown) are produced upon complete reduction of FeO $\rightarrow$ Fe in the final reduction peak situated beyond 750°C.

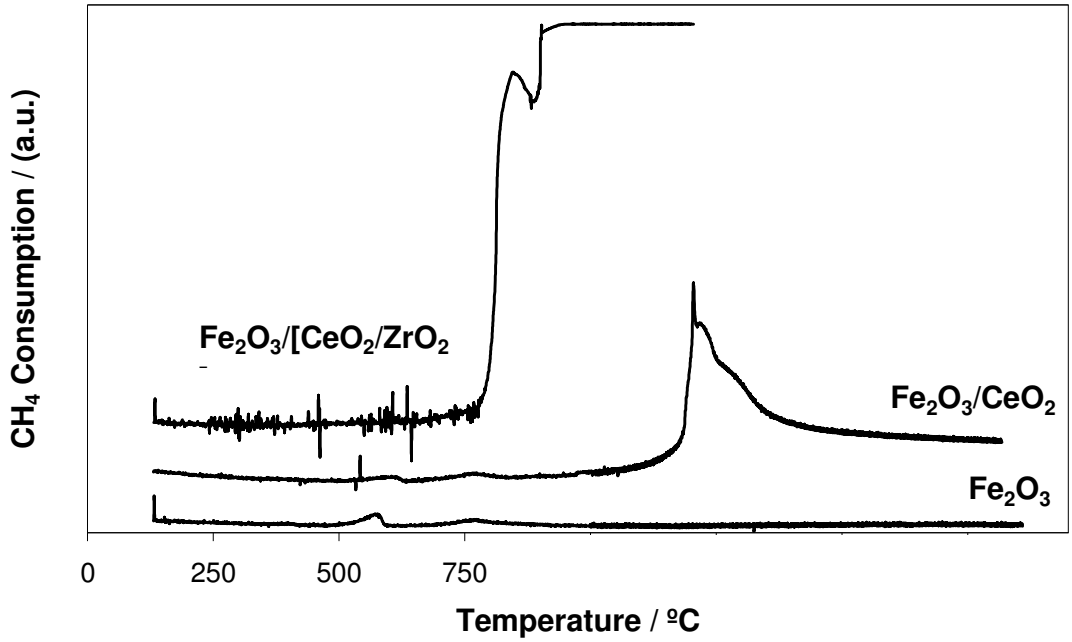

Figure 5.14 10% CH_4 reduction of unpromoted and promoted Fe_2O_3 up to 750ºC

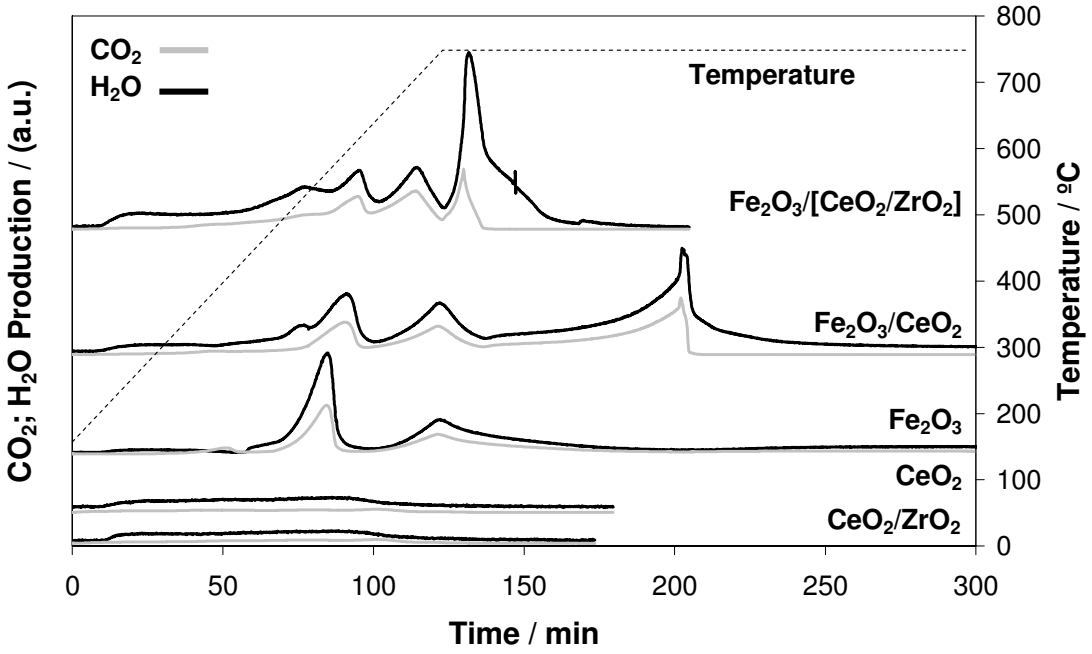

Figure 5.15 CO_2; H_2O production from 10% CH_4 reduction of unpromoted and promoted Fe_2O_3 up to 750ºC

5.3.5.1 CH_4 reduction/H_2O re-oxidation of unpromoted Fe_2O_3

Table 5-19 Total CH_4 consumption and CO_2 and H_2O production from unpromoted Fe_2O_3 reduction up to 750ºC

Peaks 1 + 2	CH_4 Consumption ($x10^{-3}$) / moles	Cumulative Gas Production ($x10^{-3}$) / moles	
	CH_4	H_2O	CO_2
Reduction State	Fe_2O_3-FeO	Fe_2O_3-FeO	Fe_2O_3-FeO
Stoichiometric	0.39	0.78	0.39
Experimental	0.4	0.7	0.4

CH_4 consumption and H_2O and CO_2 production in the peaks at 570ºC and 750ºC, from reduction of unpromoted Fe_2O_3, are consistent with reduction of Fe_2O_3 to Fe_3O_4 and Fe_3O_4 to FeO (**Table 5-19**). Subsequent re-oxidation produces negligible amounts of H_2 (not shown), possibly resulting from extensive sintering of unpromoted Fe_2O_3, and partial reduction to metastable FeO.

5.3.5.2 CH_4 reduction/H_2O re-oxidation of CeO_2 promoted Fe_2O_3

Reduction of CeO_2 promoted Fe_2O_3 gives CH_4 consumption and CO_2 and H_2O production consistent with a Fe_2O_3 to FeO transition, via Fe_3O_4, in the first two peaks at 590ºC and 750ºC (**Table 5-20**). In the third reduction peak, following holding at 750ºC over a period of time, CO and H_2 are also produced along with CO_2 and H_2O (**Table 5-21**):

$$4FeO + CH_4 \rightarrow 4Fe + CO_2 + 2H_2O \qquad \textbf{5.20}$$

$$FeO + CH_4 \rightarrow Fe + CO + 2H_2 \qquad \textbf{5.21}$$

According to experimental results (**Table 5-21**), **Equation 5.20** is the favoured reaction, producing four times greater CO in comparison to CO_2 production. Thermodynamic assessments confirms this observation (**Figure 3.9**), showing CO and H_2 formation (**Equation 5.20**) to be favoured over CO_2 and H_2O production (**Equation 5.19**). CH_4 consumption is approximately 200% of CH_4 consumed from reduction, due to subsequent CH_4 decomposition following reduction.

Table 5-20 Total CH_4 consumption and CO_2 and H_2O production over CeO_2 promoted Fe_2O_3 reduction up to 750ºC, Peaks 1 + 2 (Figure 5.15)

	CH_4 Consumption ($x10^{-3}$) / moles	**Cumulative Gas Production ($x10^{-3}$) / moles**	
Peaks 1 + 2	**CH_4**	**H_2O**	**CO_2**
Reduction State	Fe_2O_3-FeO	Fe_2O_3-FeO	Fe_2O_3-FeO
Stoichiometric	0.29	0.58	0.29
Experimental	0.2	0.4	0.2

Table 5-21 Total CH_4 consumption and CO_2 and H_2O production over CeO_2 promoted Fe_2O_3 reduction up to 750ºC, Peak 3 (Figure 5.15)

	CH_4 Consumption ($x10^{-3}$) / moles	**Cumulative Gas Production ($x10^{-3}$) / moles**			
Peak 3	**CH_4**	**H_2O**	**CO_2**	**H_2**	**CO**
Reduction State	FeO-Fe	FeO-Fe	FeO-Fe	FeO-Fe	FeO-Fe
Stoichiometric	1.44	0.58	0.29	2.30	1.15
Experimental	3.0	0.5	0.3	2.5	1.2

CeO_2 promoted Fe_2O_3 was re-oxidised at lower temperature (550ºC), and compared to re-oxidation at temperatures used in reduction (750ºC). Re-oxidation at 550ºC (**Figure 5.16, Table 5-22**) yielded clean hydrogen, with less than 50% of the total stoichiometric hydrogen expected. When re-oxidised at 750ºC (**Figure 5.16, Table 5-23**), production of CO, CO_2 and H_2 was observed.

CO_x formation can take place due to oxidation of adsorbed carbon species, or through re-oxidation of iron carbide species:

$$C + 2H_2O \rightarrow CO_2 + 2H_2 \qquad \textbf{5.13}$$

$$C + H_2O \rightarrow CO + H_2 \qquad \textbf{5.15}$$

$$Fe_3C + H_2O \rightarrow 3Fe + CO + H_2 \qquad \textbf{5.22}$$

$$Fe_3C + 2H_2O \rightarrow 3Fe + CO_2 + 2H_2 \qquad \textbf{5.23}$$

Carbon deposition becomes more pronounced with increasing degree of oxygen conversion in the metal oxide being reduced [25, 26]. Based upon **Figure 5.15**, CeO_2 promoted Fe_2O_3 shows high percentage oxygen conversion, with complete reduction to form iron metal, thus resulting in carbon deposition from methane reduction over Fe metal. Galvita et. al. do not report the formation of iron carbides, instead mentioning only carbon deposition as the primary source of CO_x formation during re-oxidation studies [26]. Akiyama et. al. report the primary product arising from oxidation via steam to be CO_2, especially in the initial stages, as compared to minimal CO production in latter stages of oxidation, in accordance with change in Gibbs Free Energy with temperature [27]. The ability of ceria to oxidise deposited carbon via lattice oxygen, is dependent upon the degree of oxygen conversion; for higher oxygen conversion, available ceria lattice oxygen for carbon oxidation is reduced and carbon deposition is increased. Based upon the primary production of CO along with the complete reduction of iron oxide, it is surmised that carbon deposition is the primary contributor to CO_x formation during H_2O oxidation.

H_2O consumption is consistent with oxidation of both carbon and Fe:

$$\text{Moles.}H_2O = \text{Moles.CO} + [2 \times \text{moles.}CO_2] + \text{Moles.}H_2\text{(Fe reoxidation)} \quad \textbf{5.24}$$

Hydrogen production from re-oxidation of reduced Fe_2O_3/CeO_2 alone can be calculated as the difference in total hydrogen production less hydrogen produced by carbon oxidation (**Figure 5.16, Table 5-23**):

$$H_2\text{(Fe reoxidation)} = H_2\text{(Total)} - H_2\text{(CO)} - 2H_2(CO_2) \quad \textbf{5.25}$$

At 750ºC, oxidation of carbon allows for complete re-oxidation of reduced Fe_2O_3/CeO_2. Re-oxidation at 550ºC produces clean hydrogen, but the amount of hydrogen produced is much lower than stoichiometric re-oxidation of Fe to Fe_3O_4, indicative of incomplete re-oxidation. Adsorbed carbon species remaining on the metal surface that are unable to be oxidised will result in catalyst deactivation.

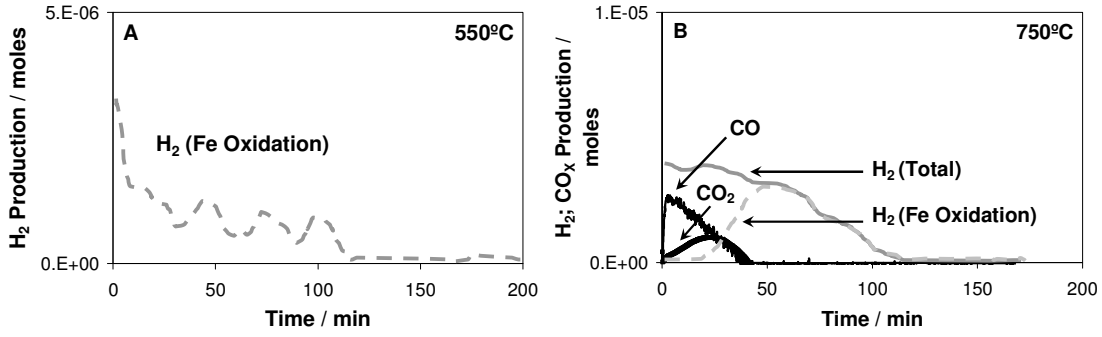

Figure 5.16 H_2O re-oxidation of CeO_2 promoted Fe_2O_3 showing, (A) H_2 production at 550ºC, and (B) H_2, CO and CO_2 production at 750ºC

Table 5-22 Total H_2O consumption and H_2, CO, CO_2 production from CeO_2 promoted Fe_2O_3 re-oxidation at 550ºC

	H_2O Consumption ($x10^{-3}$) / moles	Cumulative Gas Production ($x10^{-3}$) / moles		
	H_2O	H_2	CO	CO_2
Re-oxidation state	Fe-Fe_3O_4	Fe-Fe_3O_4	C + H_2O	C + H_2O
Stoichiometric	3.07	3.07	--	--
Experimental	1.6	**1.2**	0	0

Table 5-23 Total H_2O consumption and H_2, CO, CO_2 production over CeO_2 promoted Fe_2O_3 during re-oxidation at 750ºC

	H_2O Consumption ($x10^{-3}$) / moles	Cumulative Gas Production ($x10^{-3}$) / moles		
	H_2O	H_2	CO	CO_2
Re-oxidation State	Fe-Fe_3O_4	Fe-Fe_3O_4	C + H_2O	C + H_2O
Stoichiometric	3.07	3.07	3.07	3.07
Experimental	4.4	4.0	1.2	0.2
H_2-Fe re-oxidation		**2.4**		

5.3.5.3 CH_4 reduction/H_2O re-oxidation of CeO_2/ZrO_2 promoted Fe_2O_3

Reduction by CH_4 gives H_2O and CO_2 production consistent with Fe_2O_3 to FeO reduction, via Fe_3O_4, in the two peaks at 610ºC and 730ºC (**Table 5-24**). Following this, CH_4 decomposition following holding the temperature at 750ºC produces CO and H_2, as well as H_2O and CO_2, with complete reduction of the oxide to Fe (**Table 5-25**). CO and H_2 production is the favoured reaction, with product ratios skewed toward partial oxidation. In assuming that 30% of the reaction process results in formation of CO_2 and

H_2O, and the remaining 70% of the processes favors CO and H_2 production, the product ratios can be calculated as shown below:

$$0.3\times[4FeO + CH_4 \rightarrow 4Fe + CO_2 + 2H_2O] \quad \textbf{5.26}$$

$$0.7\times[FeO + CH_4 \rightarrow Fe + CO + 2H_2] \quad \textbf{5.27}$$

CH_4 consumption in excess of the calculated consumption for FeO to Fe results from carbon deposition, and H_2O production is greater than stoichiometric ratios predict.

Table 5-24 Total CH_4 consumption and CO_2 and H_2O production from CeO_2/ZrO_2 promoted Fe_2O_3 reduction up to 750ºC, Peaks 1 + 2 (Figure 5.14)

	CH_4 Consumption ($x10^{-3}$) / moles	**Cumulative Gas Production ($x10^{-3}$) / moles**	
Peaks 1 + 2	**CH_4**	**H_2O**	**CO_2**
Reduction State	Fe_2O_3-FeO	Fe_2O_3-FeO	Fe_2O_3-FeO
Stoichiometric	0.20	0.41	0.20
Experimental	--[a]	0.4	0.2

[a] Unable to be determined due to noise to background ratio

Table 5-25 Total CH_4 consumption and CO_2 and H_2O production from CeO_2/ZrO_2 promoted Fe_2O_3 reduction up to 750ºC, Peak 3 (Figure 5.14)

	CH_4 Consumption ($x10^{-3}$) / moles	**Cumulative Gas Production ($x10^{-3}$) / moles**			
Peak 3	**CH_4**	**H_2O**	**CO_2**	**H_2**	**CO**
Reduction State	FeO-Fe	FeO-Fe	FeO-Fe	FeO-Fe	FeO-Fe
Stoichiometric	1.0	0.12	0.061	2.28	1.14
Experimental	2.8[a]	0.3	0.05	2.3	1.1

[a] Value calculated up to reactor blockage observed

Figure 5.17 shows re-oxidation of CH_4 reduced CeO_2/ZrO_2 promoted Fe_2O_3. The reaction shows an initial steady stream of CO and H_2 at equal ratios, following which enhanced hydrogen production is observed, along with CO_2. The formation of CO and CO_2 is attributed to oxidation of deposited carbon species resulting from CH_4 decomposition during the reduction reaction, similar to re-oxidation of CeO_2 promoted Fe_2O_3:

$$C + H_2O \rightarrow CO + H_2 \quad \textbf{5.15}$$

$$C + 2H_2O \rightarrow CO_2 + 2H_2 \quad \textbf{5.13}$$

H_2O consumption is consistent with carbon oxidation and re-oxidation of Fe (**Table 5-26**):

$$\text{Moles.}H_2O = \text{Moles.CO} + [2 \times \text{moles.}CO_2] + \text{Moles.}H_2\text{(Fe reoxidation)} \quad \textbf{5.28}$$

Hydrogen production from re-oxidation of reduced $Fe_2O_3/[CeO_2/ZrO_2]$ is calculated as follows:

$$H_2\text{(Fe reoxidation)} = H_2\text{(Total)} - H_2\text{(CO)} - 2H_2(CO_2) \quad \textbf{5.29}$$

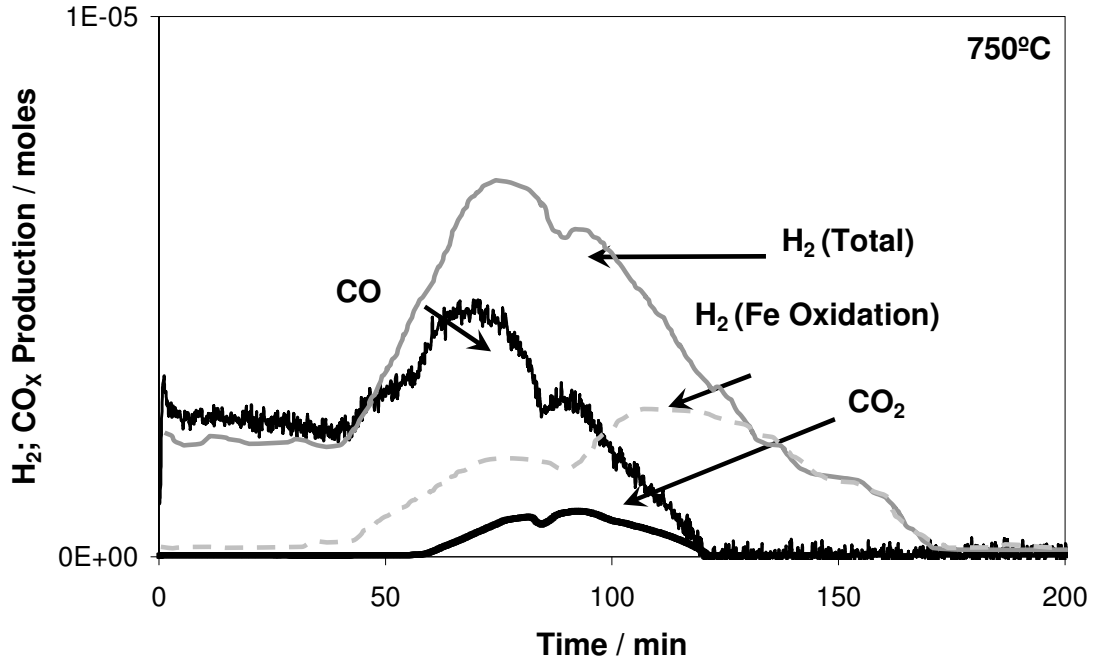

Figure 5.17 H_2O re-oxidation of CeO_2/ZrO_2 promoted Fe_2O_3 showing H_2, CO and CO_2 production at 750ºC

Table 5-26 Total H_2O consumption and H_2, CO, CO_2 production from CeO_2/ZrO_2 promoted Fe_2O_3 re-oxidation at 750ºC

	H_2O Consumption ($x10^{-3}$) / moles	Cumulative Gas Production ($x10^{-3}$) / moles		
	H_2O	H_2	CO	CO_2
	Fe-Fe_3O_4	Fe-Fe_3O_4	Fe-Fe_3O_4	Fe-Fe_3O_4
Stoichiometric	2.17	2.17	2.17	2.17
Experimental	5.4	5.3	2.9	0.3
H_2-Fe re-oxidation		**1.8**		

5.3.5.4 Post-redox characterisation

Figure 5.18 shows H_2 production from unpromoted and promoted Fe_2O_3 with measurements based on absolute H_2 production according to sample weight. Negligible H_2 production over unpromoted Fe_2O_3 is observed. CeO_2 promoted Fe_2O_3 re-oxidises more rapidly than CeO_2/ZrO_2 promoted Fe_2O_3, but this is due to more severe coking over the latter, resulting in longer re-oxidation time to completely oxidise all adsorbed carbon and subsequently re-oxidise Fe. **Figure 5.19** shows XRD spectra of post-CH_4-H_2O redox on CeO_2 and CeO_2/ZrO_2 promoted Fe_2O_3. Post-redox XRD of CeO_2 promoted Fe_2O_3 shows CeO_2 and Fe_2O_3 as the primary phases. Fe is expected to re-oxidise only to form Fe_3O_4 with presence of Fe_2O_3 in the final composition unexpected. This may arise from donation of oxygen in the CeO_2 lattice to Fe_3O_4, allowing for formation of Fe_2O_3. Neither iron carbide nor carbon was detected, indicative of complete oxidation of adsorbed carbon species on both CeO_2 and CeO_2/ZrO_2 promoted Fe_2O_3.

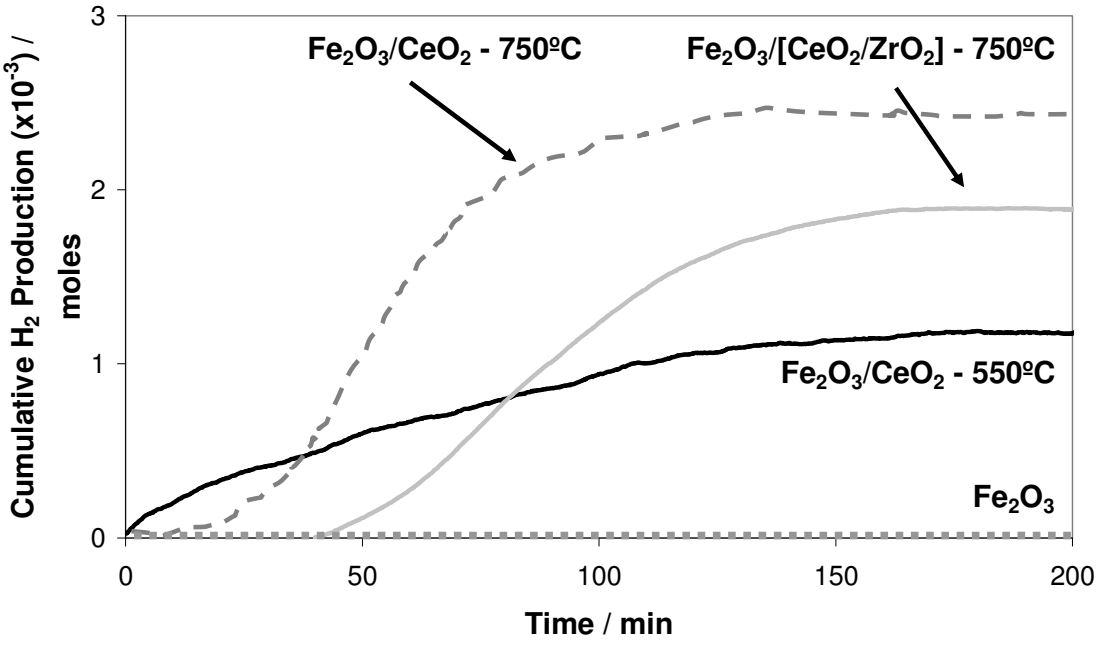

Figure 5.18 H_2 production from H_2O re-oxidation of CH_4-reduced unpromoted and promoted Fe_2O_3 at 750ºC

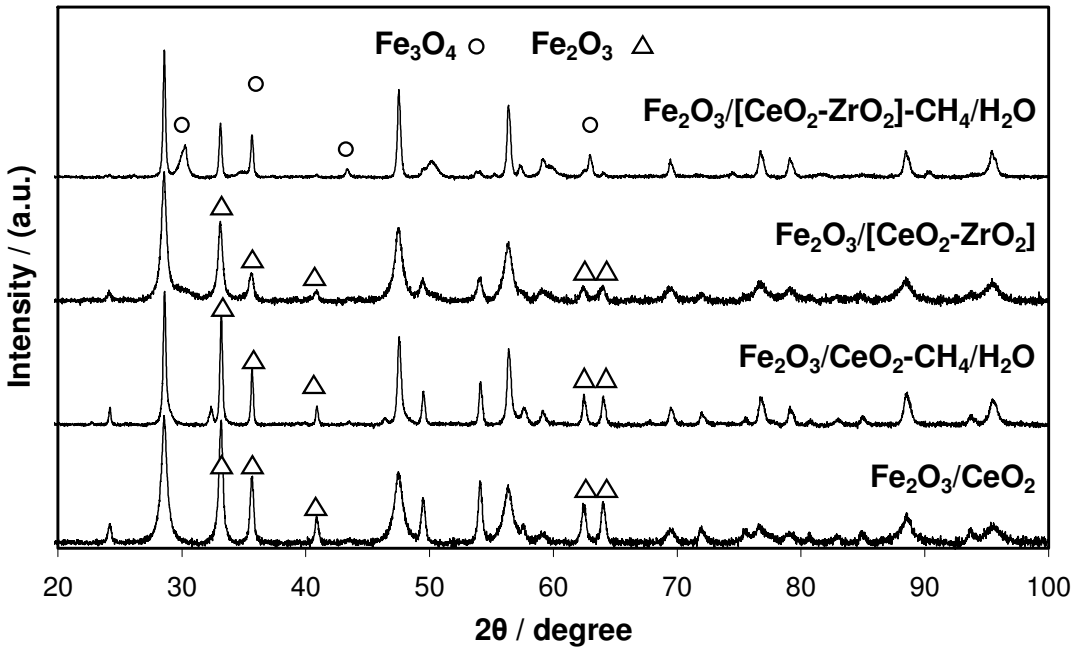

Figure 5.19 XRD spectra of fresh and CH_4/H_2O post-redox promoted Fe_2O_3

Table 5-27 Measured properties of CH_4/H_2O post-redox unpromoted and promoted Fe_2O_3

Sample	Particle Diameter/ nm Post-SIR[a] (5 cycles)	BET_{SA} / (m^2/g) Post-SIR (5 Cycles)
Fe_2O_3	--	<1
Fe_2O_3/CeO_2	50.0	15.0
Fe_2O_3 /[CeO_2/ZrO_2]	45.0	10.7

[a] Determined by Scherrer Equation from XRD spectra (**Figure 5.19**)

In summary, both CeO_2 and CeO_2/ZrO_2 promoters increase the rate of CH_4 reduction, compared to unpromoted Fe_2O_3, which does not undergo complete reduction up to 750ºC. Re-oxidation at lower temperature (550ºC) allows for production of clean hydrogen over CeO_2 promoted Fe_2O_3, however, carbon remains on the surface, as shown when further re-oxidation is performed at 750ºC. Limited hydrogen production is also observed at

550ºC, due to carbon inhibiting complete re-oxidation of Fe. In comparison, re-oxidation at 750ºC of CeO_2 and CeO_2/ZrO_2 promoted Fe_2O_3 show high levels of hydrogen production, but with co-production of CO and CO_2. CeO_2/ZrO_2 promoted Fe_2O_3 is particularly affected by high levels of coking, primarily due to accelerated reduction, favouring complete reduction to Fe metal. CH_4 decomposition over Fe metal at 750ºC is a known issue.

Whilst it is possible to increase rate of reduction at higher CH_4 concentration, coking at higher concentration is also much more severe. In order to use CH_4 as a reductant it is necessary to find methods of preventing CH_4 decomposition, such that use of higher CH_4 concentration is advantageous rather than a cause of catalyst deactivation.

5.3.5.5 CH_4 reduction/H_2O re-oxidation of unpromoted and promoted Fe_2O_3

Redox of Fe_2O_3, CeO_2/Fe_2O_3 and $[CeO_2/ZrO_2]/Fe_2O_3$ using CH_4 as the reductant and H_2O as the oxidant was performed at 750ºC over a number of cycles to compare CH_4 as a reductant. Unpromoted Fe_2O_3 shows incomplete reduction up to 750ºC with CH4, with minimal H_2 production upon H_2O re-oxidation (**Figure 5.14**, **Figure 5.18**).

CeO_2 promoted Fe_2O_3 undergoes complete reduction by CH_4 up to 750ºC, forming Fe metal which catalyses CH_4 decomposition and subsequent carbon deposition (**Figure 5.14**). The formation of Fe_3C as the final product of this reaction is ruled out based on post-reduction XRD results and literature findings confirming formation of carbon is generally the favoured reaction route. Subsequent re-oxidation at 550ºC shows substoichiometric hydrogen production, with no evidence of CO_x formation (**Figure 5.16A**). Repeated reduction in a second cycle, followed by re-oxidation this time at 750ºC shows the formation of CO and CO_2 (**Figure 5.16A**). Therefore, in the first cycle, formation of CO_x is not observed due to inability to oxidise deposited carbon at the low temperature of reaction. Subsequently substoichiometric hydrogen production is due to catalyst deactivation from blockage of active sites by this deposited carbon. In the second

cycle, this carbon is able to be removed at the higher temperature of re-oxidation, forming CO and CO_2. Whilst low temperature re-oxidation produces clean hydrogen, this is not a sustainable redox cycle; with increasing deposition of carbon over each reduction phase, deactivation of the metal oxide will rapidly ensue, thus it is necessary to burn off or remove this carbon.

CeO_2/ZrO_2 promoted Fe_2O_3 shows more rapid reduction up to 750ºC when reduced by CH_4 (**Figure 5.14**), forming Fe metal with high levels of carbon deposited on the catalyst surface, as evidenced by the substantial contamination of hydrogen produced upon re-oxidation (**Figure 5.17**). Complete oxidation of this deposited carbon is necessary before oxidation of Fe metal takes place, due to excessive coverage of the catalyst surface following reduction.

Comparison between all reductants used for reduction and re-oxidation of Fe_2O_3, CeO_2/Fe_2O_3 and $[CeO_2/ZrO_2]/Fe_2O_3$ shows H_2 to be the most effective reductant with $[CeO_2/ZrO_2]/Fe_2O_3$ the best performing oxide. The H_2 reduction and H_2O re-oxidation cycle on CeO_2/ZrO_2 promoted Fe_2O_3 is able to reproducibly form close to stoichiometric levels of hydrogen and high surface area retention is observed over numerous cycles. Use of carbon based reductants CO and CH_4 show carbon deposition over Fe metal formed during the reduction phase, which subsequently contaminates the H_2 production stream during re-oxidation. It is necessary to limit the degree of oxygen species removed, with a greater degree of oxygen removal correlating with higher levels of carbon formation [26]. Formation of Fe metal is known to catalyse CO and/or CH_4 decomposition, therefore, preventing its formation by reduction to FeO will allow for clean reduction and re-oxidation of iron based metal oxides using carbon based reductants.

5.4 Conclusions

1. Addition of CeO_2 and CeO_2/ZrO_2 to Fe_2O_3 results in improved reducibility and increased surface area retention
2. Addition of CeO_2/ZrO_2 to Fe_2O_3 inhibits complete reduction of Fe_2O_3 to Fe during H_2 reduction, by stabilising intermediate oxide FeO for a number of cycles.
3. CO reduction of CeO_2 promoted Fe_2O_3 allows for clean H_2 production for one cycle, by stabilisation of FeO, prior to catalyst deactivation due to coking.
4. Use of CO reductant results in coke formation on both unpromoted and promoted Fe_2O_3 samples. Better reducibility of promoted samples show complete reduction to Fe metal, catalysing CO decomposition. Both unpromoted and promoted Fe_2O_3 samples reduced by CO and CO + H_2 show poor hydrogen production upon subsequent oxidation.
5. CeO_2 and CeO_2/ZrO_2 promoted Fe_2O_3 show better reducibility when reduced by CH_4, compared to incomplete reduction of unpromoted Fe_2O_3.
6. CeO_2 and CeO_2/ZrO_2 promoters prevent formation of iron carbide when reduced by CH_4, with complete oxidation of adsorbed coke when re-oxidised with H_2O at 750ºC.

Fe catalyses carbon formation by facilitating decomposition of CO and CH_4. Carbon formation during partial reduction of promoted Fe_2O_3 species to FeO may result from some Fe being formed. Limiting reduction temperatures during CH_4 reduction is one possible solution, but the limited reactivity of CH_4 at lower temperature remains a barrier. CO and CO + H_2 reduction promote carbon formation at relatively low temperature. By decreasing the temperature of reduction, it may be possible to limit formation of Fe which catalyses CO decomposition however, this would severely limit the rate of H_2O re-oxidation. Thermodynamics indicate that increasing process temperature above 750ºC may render the CO decomposition reaction unfavourable, thereby limiting carbon formation (**Chapter 3**).

Whilst catalytic activity is not directly proportional to surface area, maximising surface area results in a greater percentage of reduction and re-oxidation. Increased surface area, achieved by addition of promoting species, helps to limit sintering over a number of cycles, thus maintaining higher levels of H_2 production, as evident by the significant drop in hydrogen production of non-promoted Fe_2O_3.

FeO stabilisation upon H_2 reduction of CeO_2/ZrO_2 promoted Fe_2O_3 has been shown here. CH_4 reduction of CeO_2/ZrO_2 promoted Fe_2O_3 does not exhibit the same stabilised formation of FeO. Reduction of CeO_2/ZrO_2 alone by CH4 occurs at much lower temperature than does the commencement of Fe_2O_3 reduction. H_2 reduction of CeO_2/ZrO_2 promoted Fe_2O_3 shows that reduction of CeO_2/ZrO_2 and reduction of FeO overlap, with CeO_2/ZrO_2 reduction taking place following initial reduction of Fe_2O_3 to Fe_3O_4. It is possible that H_2 reduction of CeO_2/ZrO_2 at similar temperature to Fe_3O_4 to FeO acts to inhibit further reduction of FeO to form metallic Fe. By reducing CeO_2/ZrO_2 promoted Fe_2O_3 with CH4 at lower temperature stabilised formation of FeO may occur. However, as observed in reduction of CeO_2 promoted Fe_2O_3 reduction, FeO is not stabilised, with complete reduction of FeO to metallic Fe over a period of time of maintaining process temperature at 750ºC.

The effect of CeO_2/ZrO_2 promoter addition as reported here may be applied to various metal/metal oxide systems in the hope that stabilisation of intermediate metal oxide phases can be achieved. The effect of increased metal oxide stability will allow for resistance to deactivation as well as prevention of carbon and/or metal carbide formation resulting from over-reduction to the metallic form.

5.5 References

1. V. Hacker, R. Fankhauser, G. Faleschini, H. Fuchs, K. Friedrich, M. Muhr, and K. Kordesch, 'Hydrogen production by steam-iron process', *Journal of Power Sources* **2000**, 86(1-2), 531-535
2. V. Hacker, 'A novel process for stationary hydrogen production: the reformer sponge iron cycle (RESC)', *Journal of Power Sources* **2003**, 118(1-2), 311-314
3. P.B. Tarman. 'The status of the steam-iron process for hydrogen production', in *Proceedings of Synthetic Pipeline Gas Symposium* (1976).
4. P.B. Tarman, 'Hydrogen by the steam-iron process', *Coal Processing Technology* **1979**, 5, 114-16
5. S.K. Gangwal, V. Subramani, W. Li, B.S. Turk, R. Gupta, and P.L. Silverston. 'Production of pure hydrogen from syngas by steam-iron process using nanoparticle iron catalysts', in *Abstracts of Papers, 231st ACS National Meeting* (2006) Atlanta, GA, United States: American Chemical Society, Washington, D. C.
6. K. Otsuka and S. Takenaka, 'Storage and supply of pure hydrogen mediated by the redox of iron oxides', *Journal of Japan Petroleum Institute* **2004**, 47(6), 377-386
7. A. Trovarelli, 'Catalytic properties of ceria and CeO_2-containing materials', *Catalysis Reviews* **1996**, 38(4), 439-520
8. H.C. Yao and Y.F.Y. Yao, 'Ceria in automotive exhaust catalysts: I. Oxygen storage', *Journal of Catalysis* **1984**, 86(2), 254-265
9. E. Aneggi, M. Boaro, C. De Leitenburg, G. Dolcetti, and A. Trovarelli, 'Insights into the redox properties of ceria-based oxides and their implications in catalysis', *Journal of Alloys and Compounds* **2006**, 408, 1096-1102
10. A. Trovarelli, C. De Leitenburg, M. Boaro, and G. Dolcetti, 'The utilisation of ceria in industrial catalysis', *Catalysis Today* **1999**, 50(2), 353-367

11. V. Galvita and K. Sundmacher, 'Redox behaviour and reduction mechanism of Fe_2O_3-$CeZrO_2$ as oxygen storage material', *Journal of Materials Science* **2007**, 42(22), 9300-9307

12. V. Galvita, T. Hempel, H. Lorenz, L.K. Rihko-Struckmann, and K. Sundmacher, 'Deactivation of modified iron oxide materials in the cyclic water gas shift process for CO-free hydrogen production', *Industrial & Engineering Chemistry Research* **2008**, 47(2), 303-310

13. J. Bessières, A. Bessières, and J.J. Heizmann, 'Iron oxide reduction kinetics by hydrogen', *International Journal of Hydrogen Energy* **1980**, 5(6), 585-595

14. O.J. Wimmers, P. Arnoldy, and J.A. Moulijn, 'Determination of the Reduction Mechanism by Temperature-Programmed Reduction: Application to Small Fe_2O_3 Particles', *Journal of Physical Chemistry* **1986**, 90, 1331-1337

15. K. Li, H. Wang, Y. Wei, M. Liu, 'Preparation and characterisation of $Ce_{1-x}Fe_xO_2$ complex oxides and its catalytic activity for methane selective oxidation', *Journal of Rare Earths* **2008**, 26(2), 245-249

16. K. Li, H. Wang, Y. Wei, D. Yan, 'Direct conversion of methane to synthesis gas using lattice oxygen of CeO_2–Fe_2O_3 complex oxides', *Chemical Engineering Journal* **2010**, 156, 512-518

17. O.J. Wimmers, P. Arnoldy, and J.A. Moulijn, 'Determination of the Reduction Mechanism by Temperature-Programmed Reduction: Application to Small Fe_2O_3 Particles', *Journal of Physical Chemistry* **1986**, 90, 1331-1337

18. M.F. Bleeker, H.J. Veringa, S.R.A. Kersten, 'Deactivation of iron oxide used in the steam-iron process to produce hydrogen', *Applied Catalysis A: General* **2009**, 357, 5-17

19. K. Li, H. Wang, Y. Wei, M. Liu, 'Catalytic performance of cerium iron complex oxides for partial oxidation of methane to synthesis gas', *Chemical Engineering Journal* **2010**, 156, 512-518

20. T.B. Nguyen, J.P. Deloume, V. Perrichon, 'Study of the redox behaviour of high surface area CeO_2-SnO_2 solid solutions', *Applied Catalysis A: General* **2003**, 249(2), 273-284

21. A.A. El-Geassy, ‘Gaseous Reduction of MgO-doped Fe_2O_3 Compacts with Carbon-monoxide at 1173-1 473K’, *ISIJ International* **1996**, 36(11) 1328-1337

22. A.A. El-Geassy, ‘Stepwise Reduction of CaO and/or MgO Doped-Fe_2O_3 Compacts to Magnetite Then Subsequently to lron at 1173-1 473K’, *ISIJ International* **1997**, 37(9), 844-853

23. K. Mondal, H. Lorethova, E. Hippo, T. Wiltowski, S.B. Lalvani, ‘Reduction of iron oxide in carbon monoxide atmosphere-reaction controlled kinetics’, *Fuel Processing Technology*, **2004**, 86 33-47

24. S. Takenaka, M. Serizawa, and K. Otsuka, 'Formation of filamentous carbons over supported Fe catalysts through methane decomposition', *Journal of Catalysis* **2004**, 222(2), 520-531

25. K.Z. Li, H. Wang, Y.G. Wei, D.X. Yan, ‘Selective Oxidation of Carbon Using Iron-Modified Cerium Oxide’, *Journal of Physical Chemistry C* **2009**, 113, 15288-15297

26. V. Galvita, T. Schröder, B. Munder, K. Sundmacher, ‘Production of hydrogen with low CO_x-content for PEM fuel cells by cyclic water gas shift reactor’, *International Journal of Hydrogen Energy* **2008**, 33, 1354-1360

27. T. Akiyama, A. Miyazaki, H. Nakanishi, M. Hisa, A. Tsutsumi, 'Thermal and gas analyses of the reaction between iron carbide and steam with hydrogen generation at 573K', *International Journal of Hydrogen Energy* **2004** 29, 721-724

INVESTIGATION OF PROMOTED TIN OXIDE FOR THE STEAM-METAL PROCESS

6.1 Introduction

Thermodynamic calculations indicate that the use of tin oxide for the production of hydrogen in the Steam-Metal Process is favourable (**Chapter 3**) [1, 2]. Preliminary studies have focused primarily upon high temperature thermochemical reduction of tin oxide via solar energy [1, 3] due to its comparably low temperature of thermal decomposition, in contrast to solar thermochemical reduction of zinc oxide [4, 5] and iron oxide [6, 7]. Re-oxidation of reduced tin oxide and/or tin metal by water has also shown to proceed readily at relatively low temperature [3, 8, 9].

Few studies have reported on the use of methane [10, 11] and carbon monoxide [12] in tin oxide reduction. In the previous chapter (**Chapter 5**), promoted iron oxide showed good reducibility using CO and CO + H_2 as reductants. However, use of methane as a reductant is favoured given that CO and CO + H_2 (syngas) are derived from methane via the steam reforming reaction:

$$CH_4 + H_2O \rightarrow CO + 3H_2 \qquad \textbf{6.1}$$

$$SnO_2 + CO + H_2 \rightarrow Sn + CO_2 + H_2O \qquad \textbf{6.2}$$

$$SnO_2 + 2CH_4 \rightarrow Sn + 2CO + 4H_2 \qquad \textbf{6.3}$$

The effect of CeO_2 on SnO_2 has been shown to increase reducibility of SnO_2, with a reported oxygen storage capacity (OSC) greater than that of ceria-zirconia [13, 14]. Promotion of SnO_2 by CeO_2/ZrO_2, as yet unreported, is proposed to be equally as effective, if not more so than addition of CeO_2 alone. However, the low melting point of Sn metal (230°C) will result in significant sintering upon complete reduction of the sample, drastically reducing the available surface area and limiting subsequent hydrogen production. As such, the aim of CeO_2/ZrO_2 addition is to produce a threefold effect:

- Increase in H_2 production by increasing SnO_2 OSC
- Greater thermal stability and resistance to sintering
- Possible stabilisation of intermediate oxidation state (SnO) during reduction

By stabilised formation of SnO during reduction, it may be possible to prevent Sn metal formation and hinder sintering. A similar effect was reported in the previous chapter (**Chapter 5**), with addition of CeO_2/ZrO_2 allowing for stabilised reduction of Fe_2O_3 to form FeO.

6.2 Experimental

6.1.1 Metal Oxide Preparation

Unpromoted and promoted SnO_2 samples were prepared by the method of urea hydrolysis, as described in **Chapter 4** (Experimental Methodology). Ceria-zirconia was added to SnO_2 at concentrations of 10mol%, 20mol%, 25mol%, 30mol%, 40mol% and 50mol%. The composition of SnO_2 was adjusted to make up the difference. Characterisation techniques include BET, XRD and TPR as described in Chapter 4 - Experimental Methodology.

6.2.1 Temperature Programmed Reduction (TPR)

An outline of the experimental apparatus used for TPR analysis can be found in **Chapter 4** (Experimental Methodology). Prior to analysis, the sample was heated under a flow of Ar to 150ºC for 1 hour to ensure all excess moisture was removed.

The following experimental conditions were used:

- Flow rate: 30mL/min
- Incoming gas mixture: 5 vol%H_2-95 vol% (1%Ar in He)
- Metal oxide loading: 0.05-0.1g
- Temperature ramping rate: 150-750ºC at 5ºC/min
- Reactor Pressure: 1 atm

6.2.2 Steam-Metal Process

An outline of the experimental apparatus used for Steam-Metal reaction studies can be found in **Chapter 4** (Experimental Methodology). Initially the sample was heated under flow of He up to 150ºC and held until no further change in the outgoing H_2O signal was observed. Flow rates of all incoming reactants were maintained at 60 mL/min, with reactor pressure maintained at a constant 1 atm.

The following experimental conditions were employed for all metal oxides during reduction/re-oxidation studies (**Table 6-1**):

Table 6-1 Reaction conditions for redox analysis of promoted tin oxide

Reductant	**Incoming gas mixture**	**Metal Oxide Loading / g**	**Temperature of reduction**
CH_4	10 vol% CH_4 -13.3 vol% (1% Ar in He) - 76.7 vol% He	0.2 - 0.3	150 - 750ºC
Oxidant	**Incoming gas mixture**	**Metal Oxide Loading / g**	**Temperature of oxidation**
H_2O	2-3 vol% H_2O - 97 vol% (1% Ar in N_2)	0.2 - 0.3	600ºC

6.3 Results and Discussion

6.3.1 Characterisation

Figure 6.1 shows the XRD pattern of unpromoted and CeO_2/ZrO_2 (CZ) promoted SnO_2, with CeO_2/ZrO_2 shown for comparison. At low CeO_2/ZrO_2 addition (10 mol% [CeO_2/ZrO_2] / 90 mol% SnO_2) the structure is characteristic of tetragonal SnO_2. With increasing addition of CeO_2/ZrO_2, characteristic CeO_2/ZrO_2 peaks become more predominant indicating formation of a mixed oxide comprised of SnO_2 and CeO_2/ZrO_2.

Surface area increases with increased addition of CeO_2/ZrO_2 (**Table 6-2**). Corresponding crystallite sizes calculated from XRD spectra using the Scherrer Equation (**Table 6-2**) show increasing SnO_2 crystallite size with higher CeO_2/ZrO_2 addition, up to 20 mol% loading of CeO_2/ZrO_2. Similarity of XRD spectra between unpromoted SnO_2 and low percentage addition of CeO_2/ZrO_2 ($Sn_{(0.9)}CZ$), suggests that formation of a SnO_2 based solid solution may be possible. This is further evidenced by the similarity in crystallite size between $Sn_{(0.9)}CZ$ and SnO_2. As increasing amounts of CeO_2/ZrO_2 are added, SnO_2 crystallite size shows a sudden increase to a constant value. The consistent increase in surface area which is not reflected in a corresponding change in crystallite size shows a lack of interaction between SnO_2 and CeO_2/ZrO_2 that would otherwise influence crystallite size of SnO_2. Thus the change in surface area comes about as an additive effect due to addition of increasing amounts of higher surface area CeO_2/ZrO_2.

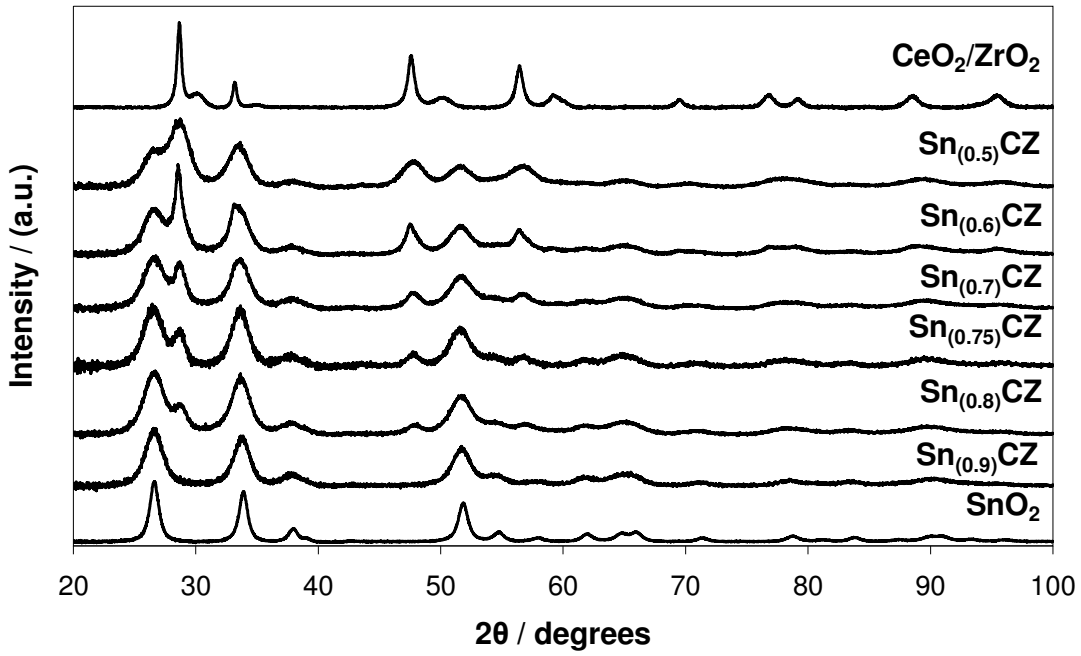

Figure 6.1 XRD spectra of unpromoted and promoted SnO_2, shown with CeO_2/ZrO_2

Table 6-2 Measured crystallite size and surface area of as prepared unpromoted and promoted SnO_2

Sample	Crystallite Diameter / nm	BET_{SA} / (m^2/g)
SnO_2	11.0	36.0
$Sn_{0.9}CZ$	13.0	62.1
$Sn_{0.8}CZ$	25.8	65.0
$Sn_{0.75}CZ$	24.6	66.5
$Sn_{0.7}CZ$	25.0	73.8
$Sn_{0.6}CZ$	23.3	77.3
$Sn_{0.5}CZ$	23.9	82.6
CeO_2/ZrO_2	--	88.1

[a] Determined by Scherrer Equation from XRD spectra, values calculated from major SnO_2 peaks

6.3.2 H_2 Temperature Programmed Reduction (TPR)

Figure 6.2 shows H_2 TPR of unpromoted and CeO_2/ZrO_2 promoted SnO_2 up to 750ºC. A low temperature shoulder peak is observed, starting from approximately 200ºC in unpromoted SnO_2. This shoulder can be assigned to surface reduction of oxygen species on SnO_2, with the predominant high temperature peak at 680ºC assigned to bulk reduction of SnO_2 [12]. The reduction of Sn^{4+} to Sn^{2+} is not observed as an intermediate peak prior to complete reduction to Sn metal.

With increasing addition of CeO_2/ZrO_2 the main reduction peak decreases in temperature from 680ºC for unpromoted SnO_2 down to 570ºC for 50 mol% [CeO_2/ZrO_2]/50 mol% SnO_2 (**Table 6-3**). It is surmised this results from the added reducibility from addition of CZ to SnO_2 along with the lower starting temperature of reduction for CZ alone. Increasing CeO_2/ZrO_2 results in lower hydrogen consumption due to limited OSC, with minimal hydrogen consumption at 50 mol% [CeO_2/ZrO_2]/50 mol% SnO_2. It is also observed that with increasing addition of CeO_2/ZrO_2, surface area retention following reduction is increased (**Table 6-3**). The results shown are not normalised against the proportion of SnO_2 present in the sample, thus the results are a reflection of the performance of each promoted oxide based upon the effects of added proportion of CZ.

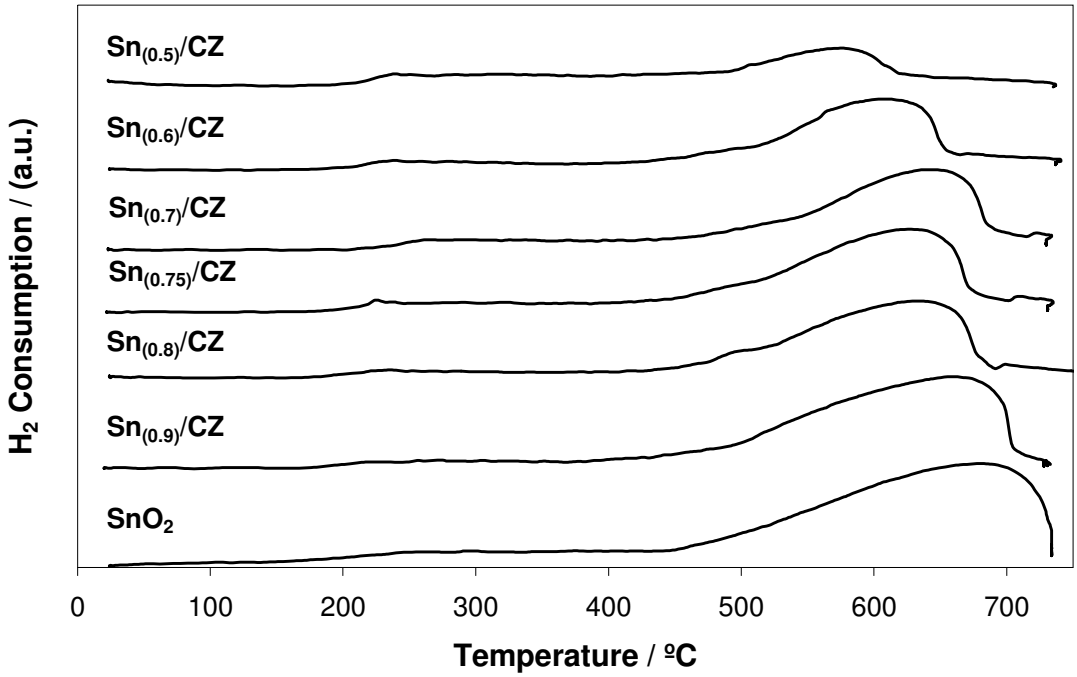

Figure 6.2 5% H_2 TPR of unpromoted and promoted SnO_2 up to 750ºC

Table 6-3 Peak temperatures from 5% H_2 TPR of unpromoted and promoted SnO_2 up to 750ºC

Sample	Peak Temperature / ºC	BET_{SA} / (m^2/g)	
		Pre-TPR	Post-TPR
SnO_2	680	36.0	--
$Sn_{0.9}CZ$	663	62.1	5.6
$Sn_{0.8}CZ$	634	65.0	18.9
$Sn_{0.75}CZ$	623	66.5	26.8
$Sn_{0.7}CZ$	648	73.8	14.4
$Sn_{0.6}CZ$	612	77.3	17.6
$Sn_{0.5}CZ$	570	82.6	48.8

TPR results show the major reduction peak reaches a minimum temperature at a composition of 25 mol% [CeO_2/ZrO_2] / 75 mol% SnO_2. Further increase of CeO_2/ZrO_2 loading up to 40 mol% shows minimal decrease in reduction temperature of SnO_2 to Sn. The sample consisting of 25 mol% [CeO_2/ZrO_2] loading on SnO_2 was selected as the composition for further investigation. This loading shows a good compromise between reducibility, surface area retention and OSC.

Although further increasing CeO_2/ZrO_2 addition shows greater reducibility and possibly higher surface area retention, the limited proportion of SnO_2 results in low OSC and limited H_2 production potential, resulting in less H_2 production per gram of catalyst used. In addition, the reduction of CeO_2 and/or CeO_2/ZrO_2 by carbon based reductants shows high levels of CO_x production upon re-oxidation by water. This results from carbon deposition on the CeO_2 surface, along with the formation of carbonaceous material during the reduction phase, which is favoured in the presence of Ce [17]. Furthermore, with deeper reduction of CeO_2, a greater degree of carbon and carbonaceous material is deposited at the catalyst surface, resulting in CO_x contamination upon H_2O re-oxidation [18]. Therefore, in the interest of producing clean hydrogen and eliminating potential formation of CO_x species, it is desirable maximise the amount of SnO_x as the primary oxide phase in the material.

6.3.3 Transmission Electron Microscopy (TEM)

TEM imagery of unpromoted SnO_2 shows larger particle sizes compared to 25 mol% [CeO_2/ZrO_2] / 75 mol% SnO_2 (**Figure 6.3**). In comparison, 25 mol% [CeO_2/ZrO_2] / 75 mol% SnO_2 shows a larger calculated crystallite size from XRD spectra, along with higher surface area from BET measurements, as compared to unpromoted SnO_2 (**Table 6-2**). This would result from higher porosity of the promoted sample, where calculated surface area may be greater, despite larger crystallite sizes. The less porous nature of unpromoted SnO_2 subsequently has a lower surface area in comparison due to lesser sites available for gas adsorption during BET measurements.

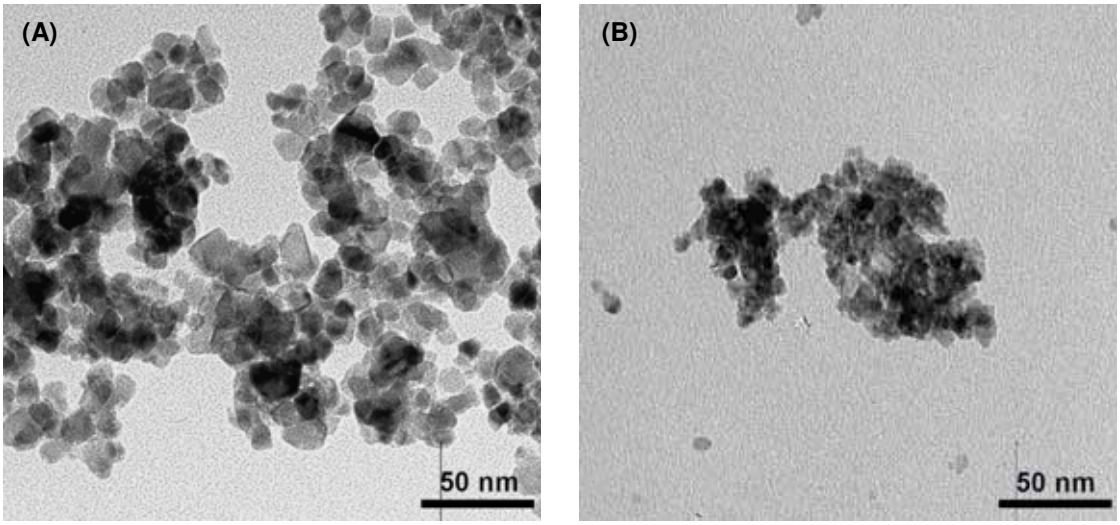

Figure 6.3 TEM imagery of (A) unpromoted SnO_2 and (B) 25 mol% [CeO_2/ZrO_2] / 75 mol% SnO_2

6.3.4 CH_4 Temperature Programmed Reduction (TPR)

Reduction of unpromoted SnO_2 shows two peaks, which are attributed to the reduction of surface oxygen species (**Figure 6.4**) [10]. The two peaks are unable to be assigned individually. The difference in methane consumption calculated between the first and second peaks eliminates assignment of SnO_2 to SnO reduction, followed by SnO to Sn reduction. Methane consumption of each peak in the aforementioned process would be equivalent. Calculation of methane consumption indicates minimal reduction of SnO_2, with approximately 16 times lower methane consumption than stoichiometric values expected for complete reduction of SnO_2 to Sn (**Table 6-4**). Increasing temperature up to 750ºC shows no further reduction of SnO_2, suggesting reduction of bulk SnO_2 oxygen species does not take place below 750ºC [19, 20].

TPR of $SnO_{2(0.75)}$/$[CeO_2/ZrO_2]_{(0.25)}$ shows a similar degree of methane consumption to unpromoted SnO_2, albeit with a single reduction peak at slightly higher temperature (465ºC) (**Figure 6.4**).

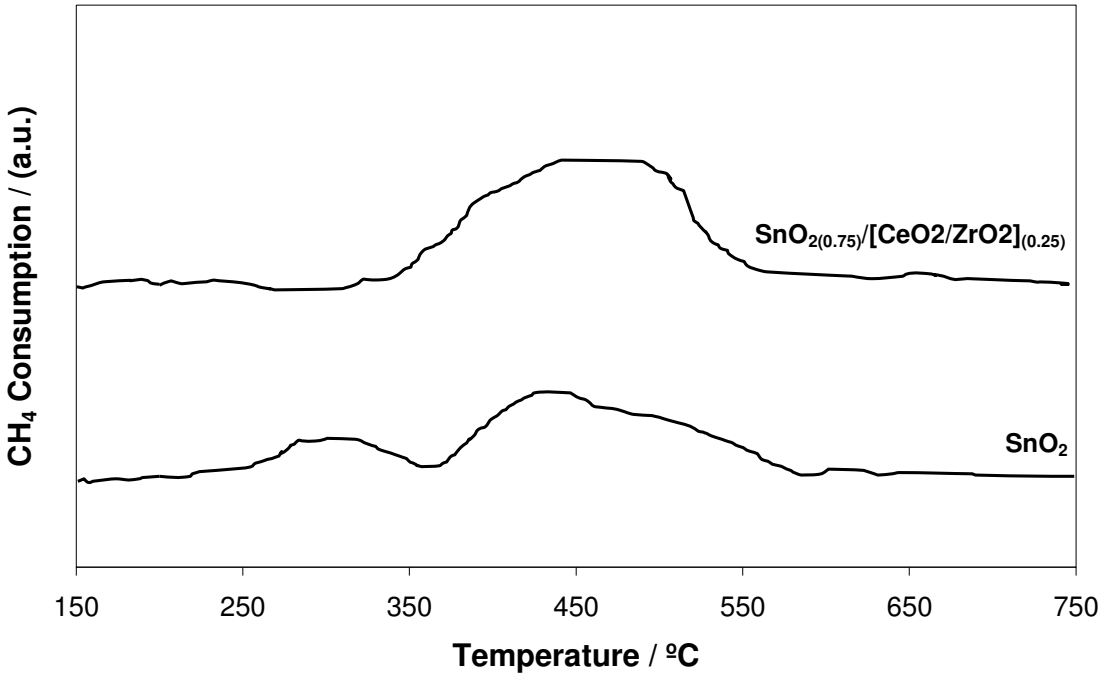

Figure 6.4 10% CH_4 TPR of unpromoted SnO_2 and $SnO_{2(0.75)}/[CeO_2/ZrO_2]_{(0.25)}$

Table 6-4 Peak temperature and assignment of unpromoted SnO_2 and $SnO_{2(0.75)}/[CeO_2/ZrO_2]_{(0.25)}$ TPR

	Oxidation State		
	SnO_2		$SnO_{2(0.75)}$ / $[CeO_2/ZrO_2]_{(0.25)}$
	$SnO_2 \rightarrow SnO/Sn$		$SnO_2 \rightarrow SnO/Sn$ $CeO_2 \rightarrow Ce_2O_3$
Temperature / ºC	310	440	465
	CH_4 Consumption / (moles/g.SnO_2)		
Stoichiometric	1.33×10^{-3}		1.04×10^{-3}
Experimental	0.08×10^{-3}		0.08×10^{-3}

Experimentally, total methane consumption is identical between the two samples despite the fact that methane consumption over $SnO_{2(0.75)}/[CeO_2/ZrO_2]_{(0.25)}$ is expected to be less due to partial substitution of higher OSC SnO_2 with CeO_2. As such, CeO_2/ZrO_2 promoted

SnO_2 shows proportionally higher methane consumption per gram of SnO_2. Addition of CeO_2/ZrO_2 does not facilitate deeper bulk reduction of SnO_2 oxygen species. Wang and Xie report that through the formation of a higher surface area solid solution based on SnO_2 doped with Cr and/or Fe, a reduction in structural crystallinity and the resultant introduction of structural defects allows the lattice oxygen species to become more active [15, 19-21]. This in turn increases CH_4 reducibility of the Sn based solid solution, thereby facilitating deeper reduction of the bulk. It is surmised that the lack of interaction between CeO_2/ZrO_2 and SnO_2 lattice oxygen species prevents deeper reduction of SnO_2 from occurring.

The ratio of H_2 production to CH_4 consumption from oxidation and subsequent reduction of unpromoted SnO_2 is most likely attributed to cycling of surface oxygen species between SnO_2 and SnO (**Table 6-5**). $SnO_{2(0.75)}/[CeO_2/ZrO_2]_{(0.25)}$ shows minimal H_2 production following re-oxidation, with CO_2 production observed. Calculation of CO_2 production during re-oxidation shows approximately 1.2×10^{-5} moles of CO_2 produced per gram of $SnO_{2(0.75)}/[CeO_2/ZrO_2]_{(0.25)}$ (**Figure 6.5**). This would suggest the same number of moles of carbon is deposited at the catalyst surface, which is subsequently removed during re-oxidation. Addition of CeO_2/ZrO_2 does not show improved reducibility of SnO_2 by methane, and results in coke deposition from CeO_2/ZrO_2 reduction alongside SnO_2 reduction, producing CO_x contaminants. The carbon deposits do not facilitate reduction of SnO_2/SnO, as evidenced by the minimal hydrogen production during re-oxidation (**Table 6-5**).

Table 6-5 H_2 production from H_2O re-oxidation of unpromoted SnO_2 and $SnO_{2(0.75)}/[CeO_2/ZrO_2]_{(0.25)}$ at 600ºC

	Oxidation State	
	SnO_2	**$SnO_{2(0.75)}$ / $[CeO_2/ZrO_2]_{(0.25)}$**
	$SnO/Sn \rightarrow SnO_2$	*$SnO/Sn \rightarrow SnO_2$ / $Ce_2O_3 \rightarrow CeO_2$*
	H_2 Production / (moles/g.SnO_2)	
Stoichiometric	3.99×10^{-3}	3.12×10^{-3}
Experimental	0.09×10^{-3}	0.08×10^{-3}

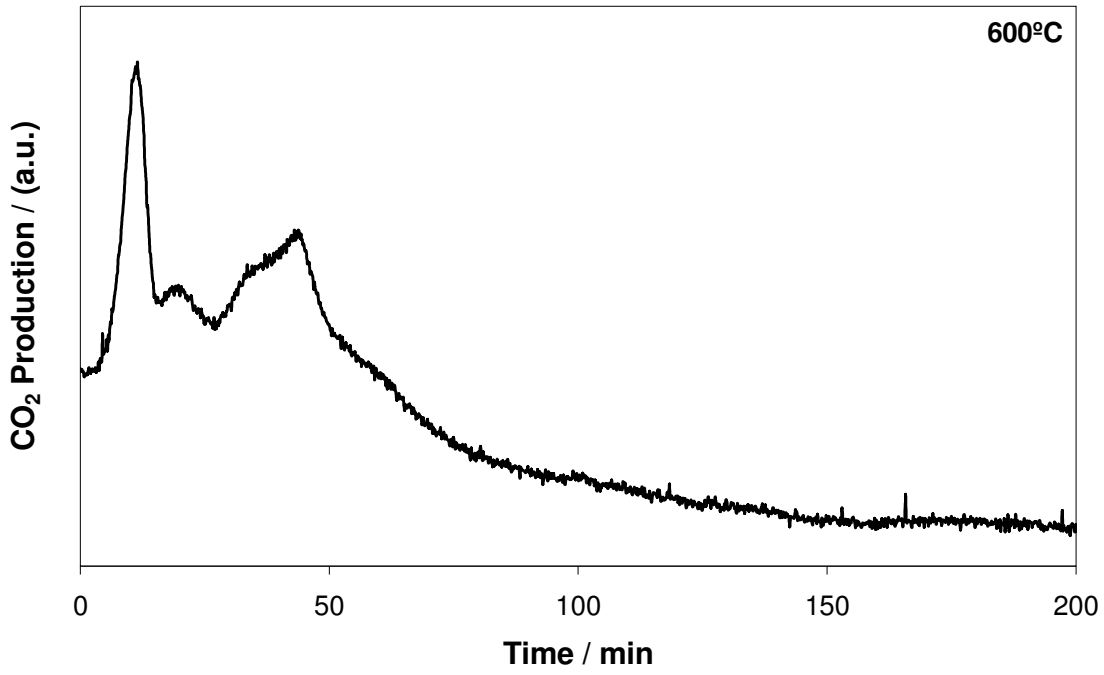

Figure 6.5 CO_2 production from H_2O re-oxidation of $SnO_{2(0.75)}/[CeO_2/ZrO_2]_{(0.25)}$

6.4 Conclusions

1. Addition of CeO_2/ZrO_2 retards sintering of SnO_2 upon reduction, as well as improving reducibility, with a decrease in the temperature of H_2 reduction
2. Unpromoted SnO_2 and 25 mol% [CeO_2/ZrO_2] / 75 mol% SnO_2 show only limited reduction of surface oxygen species by methane, up to 750ºC
3. Re-oxidation of 25 mol% [CeO_2/ZrO_2] / 75 mol% SnO_2 reduced by methane shows CO_2 production, with negligible H_2 production
4. Stabilisation of intermediate SnO upon reduction of SnO_2 is not observed for CeO_2/ZrO_2 promoted SnO_2

Methane is a poor reductant over unpromoted SnO_2. Addition of CeO_2/ZrO_2 shows slightly improved reducibility of surface oxygen species, but does not catalyse further reduction of bulk SnO_2 oxygen species. It is clear that ceria/zirconia promoted tin oxide is not a good system for the Steam-Metal Process.

6.5 References

1. S. Abanades, P. Charvin, F. Lemont, and G. Flamant, 'Novel two-step SnO_2/SnO water-splitting cycle for solar thermochemical production of hydrogen', *International Journal of Hydrogen Energy* **2008**, 33(21), 6021-6030
2. M. Forster, 'Theoretical investigation of the system SnO_x/Sn for the thermochemical storage of solar energy', *Energy* **2004**, 29(5-6), 789-799
3. P. Charvin, S. Abanades, F. Lemont, and G. Flamant, 'Experimental Study of SnO_2/SnO/Sn Thermochemical Systems for Solar Production of Hydrogen', *AICHE Journal* **2008**, 54(10), 2759-2767
4. R. Palumbo, J. Lede, O. Boutin, E.E. Ricart, A. Steinfeld, S. Moller, A. Weidenkaff, E.A. Fletcher, and J. Bielicki, 'The production of Zn from ZnO in a high-temperature solar decomposition quench process - I. The scientific framework for the process', *Chemical Engineering Science* **1998**, 53(14), 2503-2517
5. A. Steinfeld, 'Solar hydrogen production via a two-step water-splitting thermochemical cycle based on Zn/ZnO redox reactions', *International Journal of Hydrogen Energy* **2002**, 27(6), 611-619
6. T. Nakamura, 'Hydrogen Production from Water Utilizing Solar Heat at High-Temperatures', *Solar Energy* **1977**, 19(5), 467-475
7. A. Steinfeld, S. Sanders, and R. Palumbo, 'Design aspects of solar thermochemical engineering - A case study: Two-step water-splitting cycle using the Fe_3O_4/FeO redox system', *Solar Energy* **1999**, 65(1), 43-53
8. K. Otsuka, S. Murakoshi, and A. Morikawa, 'Hydrogen-Production from Water by Reduced Tin Oxide', *Fuel Processing Technology* **1983**, 7(3), 213-223
9. M. Chambon, S. Abanades, and G. Flamant, 'Kinetic investigation of hydrogen generation from hydrolysis of SnO and Zn solar nanopowders', *International Journal of Hydrogen Energy* **2009**, 34(13), 5326-5336

10. X. Wang and Y.-C. Xie, 'CH_4 deep oxidation over active and thermally stable catalysts based on Sn-Cr composite oxide', *New Journal of Chemistry* **2001**, 25, 1621-1626

11. K. Omata, T. Ehara, I. Kawai, and M. Yamada, 'Methane-water redox reaction on A_2SnO_4 (A = Mg, Ca, Sr, Ba) oxide to produce C_2 hydrocarbons', *Catalysis Letters* **1997**, 45 245-248

12. R. Sasikala, N.M. Guptab, and S.K. Kulshreshtha, 'Temperature-programmed reduction and CO oxidation studies over Ce–Sn mixed oxides', *Catalysis Letters* **2001**, 71(1-2), 69-73

    Journal **2001**, 82, 21-31

13. T.B. Nguyen, J.P. Deloume, and V. Perrichon, 'Study of the redox behaviour of high surface area CeO_2-SnO_2 solid solutions', *Applied Catalysis A - General* **2003**, 249(2), 273-284

14. R. Sasikala, N.M. Gupta, and S.K. Kulshreshtha, 'Temperature-programmed reduction and CO oxidation studies over Ce–Sn mixed oxides', *Catalysis Letters* **2001**, 71(1), 69-73

15. X. Wang and Y.-C. Xie, 'Total oxidation of CH_4 on Sn-Cr composite oxide catalysts', *Applied Catalysis B - Environmental* **2001**, 35, 85–94

16. X. Wang and Y.-C. Xie, 'Low-Temperature CH_4 Total Oxidation on Catalysts based on High Surface Area SnO_2', *Reaction Kinetics and Catalysis Letters* **2001**, 72(1), 115-123

17. F.B. Noronha, E.C. Fendley, R.R. Soares, W.E. Alvarez, D.E. Resasco, 'Correlation between catalytic activity and support reducibility in the CO_2 reforming of methane over $Pt/Ce_xZr_{1-x}O_2$ catalysts', *Chemical Engineering*

18. M. Fathi, E. Bjorgum, T. Viig, O.A. Rokstad, 'Partial oxidation of methane to synthesis gas: Elimination of gas phase oxygen', *Catalysis Today* **2000**, 63, 489-497

19. X. Wang and Y-C. Xie, 'CH_4 Deep Oxidation on SnO_2-Based Composite Oxides: Novel, Active, and Stable Catalysts', *Chemistry Letters* **2001**, 3, 216-217

20. X. Wang and Y-C. Xie, 'Total Oxidation of CH_4 on Iron-Promoted Tin Oxide: Novel and Thermally Stable Catalysts', *Reaction Kinetics and Catalysis Letters* **2001**, 72(2), 229-237

21. X. Wang and Y-C. Xie 'Study on Sn-Fe-Cr composite oxides: Novel, active and thermally stable catalysts for CH_4 total oxidation', *Zeitschrift fur Physikalische Chemie-International Journal of Research in Physical Chemistry & Chemical Physics*, **2002** 216(7), 919-929

INVESTIGATION OF PROMOTED TUNGSTEN OXIDE FOR THE STEAM-METAL PROCESS

7.1 Introduction

Thermodynamic assessment of tungsten oxide (**Chapter 3**) has shown it to be suitable in the Steam-Metal Process and this has been confirmed by preliminary work by Kodama et al [1-3]. Tungsten oxide shows high selectivity for methane oxidation in this process, with addition of zirconia leading to improved performance. Tungsten metal and its oxides possess high melting point, resulting in greater resistance to sintering and making it an ideal candidate for high temperature redox reactions.

In the previous chapter (**Chapter 5**), promoted iron oxide showed good reducibility using CO and CO + H_2 as reductants, but carbon formation from CO decomposition over Fe metal and formation of iron carbide are problems. CO and CO + H_2 (syngas) can be derived from methane via the steam reforming reaction (**Chapter 2**). By achieving reduction by methane, the intermediate syngas production step is eliminated. However, methane decomposition over W formed during reduction of WO_3 results in carbon deposition and tungsten carbide formation [4, 5]. As a result, it is necessary to prevent decomposition or to limit further reduction of WO_3 to WO_2.

Ceria-zirconia has been proven to stabilise Fe_2O_3/Fe_3O_4 reduction to form an intermediate FeO phase (**Chapter 5**). It was suggested that addition of ceria-zirconia to tungsten oxide may produce a similar effect and hence achieve redox cycling between higher and lower tungsten oxidation states ($WO_3 \leftrightarrow WO_2$). Ceria-zirconia would also aid in maintaining greater surface area with repeated redox cycling and limiting catalyst deactivation.

This chapter investigates the effect of ceria-zirconia promoters on the reduction and/or re-oxidation behaviour of tungsten trioxide, employing methane as a reductant.

7.2 Experimental

7.2.1 Metal Oxide Preparation

A series of ceria-zirconia promoted tungsten oxide samples and unpromoted tungsten oxide were prepared by the method of urea hydrolysis, as described in **Chapter 4** (Experimental Methodology). Ceria-zirconia was added to tungsten trioxide at doping concentrations of 10mol%, 15mol%, 20mol%, 25mol%, 31mol%, 50mol%, with the concentration of tungsten trioxide adjusted accordingly. The ratio of CeO_2 to ZrO_2 was maintained at 1:1, with [CeO_2-ZrO_2] (hereby designated as CZ) equivalent to a single mole of CeO_2 alone. The inconsistency in promoter addition was due to $2Ce_2O_3.9WO_3$ (31mol%Ce_2O_3-69mol%WO_3) corresponding to a known compound [6, 7]. By replicating this level of promoter addition, albeit using CZ in place of CeO_2, it was sought to form a stable compound with unique structural characteristics. Catalyst characterisation involved BET, XRD, SEM, XPS, TPR and TGA as described in Chapter 4 (Experimental Methodology).

7.2.2 Temperature Programmed Reduction (TPR)

An outline of experimental apparatus used for TPR analysis can be found in Chapter 4 (Experimental Methodology). Initially the sample was heated up to 150ºC under a flow of He and held until no further change in outgoing H_2O signal was observed.

The following experimental conditions were employed:

- Flow rate: 30mL/min
- Incoming gas mixture: 5 vol%H_2-95 vol% (1%Ar in He)
- Catalyst loading: 0.05g
- Temperature ramping rate: 150-1000ºC at 5ºC/min
- Reactor Pressure: 1 atm

7.2.3 Thermogravimetric Analysis (TGA)

An outline of experimental apparatus used for TGA analysis can be found in **Chapter 4** (Experimental Methodology). Initially the sample was heated under air at 5ºC/min to a temperature of 500ºC and held for 1 hour, whereupon N_2 was introduced into the system at 20mL/min as the sample was cooled back to 30ºC. 4% H_2 in N_2 was then flowed over the sample at 30ºC for 1 hour prior to the analysis.

The following experimental conditions were used:

- Flow rate: 40mL/min
- Incoming gas mixture: 4 vol%H_2-96 vol% N_2
- Catalyst loading: 0.01-0.05g
- Temperature ramping rate: 30-900ºC at 5ºC/min; 900ºC for 3hrs
- Reactor Pressure: 1 atm

7.2.4 Steam-Metal Process

An outline of experimental apparatus used for Steam-Metal reaction studies can be found in **Chapter 4** (Experimental Methodology). Initially the sample was heated under flow of He up to 150ºC and held until no further change in the outgoing H_2O signal was observed. Reactor pressure was maintained at a constant 1 atm.

The following experimental conditions were employed for all samples during reduction/re-oxidation studies (**Table 7-1, Table 7-2**):

Table 7-1. Reaction conditions for redox analysis of promoted tungsten oxide (Initial experimental conditions)

Reductant	**Incoming gas mixture**	**Metal Oxide Loading / g**	**Flow Rate / mL/min**	**Temperature of reduction**
CH_4	50 vol% CH_4 - 13.3 vol% (1% Ar in He) - 36.7 vol% He	0.19 - 0.2	60	750ºC
Oxidant	**Incoming gas mixture**	**Metal Oxide Loading / g**	**Flow Rate / mL/min**	**Temperature of oxidation**
H_2O	19.8 vol% H_2O - 80.2 vol% (1% Ar in N_2)	0.19 - 0.2	120	750ºC

Table 7-2. Reaction conditions for redox analysis of promoted tungsten oxide (Redox cycling)

Reductant	**Incoming gas mixture**	**Metal Oxide Loading / g**	**Flow Rate / mL/min**	**Temperature of reduction**
CH_4	50 vol% CH_4 - 13.3 vol% (1% Ar in He) - 36.7 vol% He	0.19 - 0.2	60	750ºC
Oxidant	**Incoming gas mixture**	**Metal Oxide Loading / g**	**Flow Rate / mL/min**	**Temperature of oxidation**
H_2O	46.8 vol% H_2O - 53.2 vol% (1% Ar in N_2)	0.19 - 0.2	120	750ºC

7.3 Results

7.3.1 Characterisation

Figure 7.1 shows XRD spectra of as prepared unpromoted and promoted WO_3. All peaks in the pattern of unpromoted WO_3 were assigned to the stoichiometric monoclinic phase (JCPDS 43-1035). With addition of CZ there is minimal change observed with respect to appearance of CZ peaks, indicating a primarily WO_3 based structure. The Ce and Zr may be of an amorphous form or exist as very small particles such that their diffraction lines are too broad to be observed. At a loading of 31 mol% CZ / 69 mol% WO_3, additional peaks to those of WO_3 alone are observed. The pattern of this additional phase present in 31 mol% CZ / 69 mol% WO_3, was analysed separately (not shown), however a matching spectra for this unknown phase could not be found in the literature. Yoshimura et. al. have reported formation of various Ce(III)W_xO_y phases however, the peaks cannot be assigned to any of these [7].

Further increased loading of CZ to 35 mol% displays similar spectral characteristics to lower loading of CZ (less than 25 mol% CZ) and unpromoted WO_3. At 50 mol% CZ / 50 mol% WO_3 the spectra shows very broad peaks, most likely due to the amorphous nature of the zirconia phase within the compound, and specific spectral characteristics relating to neither WO_3 nor CZ were not observable. Armendáriz et. al. have reported similar behaviour, in which addition of tungsten to zirconia showed broad and undefined peaks of similar characteristic to **Figure 7.1**, consistent with retaining a zirconia based amorphous structure [8, 9]. With greater proportion of Zr present within this compound, the structure tends toward that of ZrO_2, rather than that of WO_3 as found at lower concentration of CZ. Crystalline ZrO_2 is not observed except with an increase in calcination temperature and decrease in WO_3 loading.

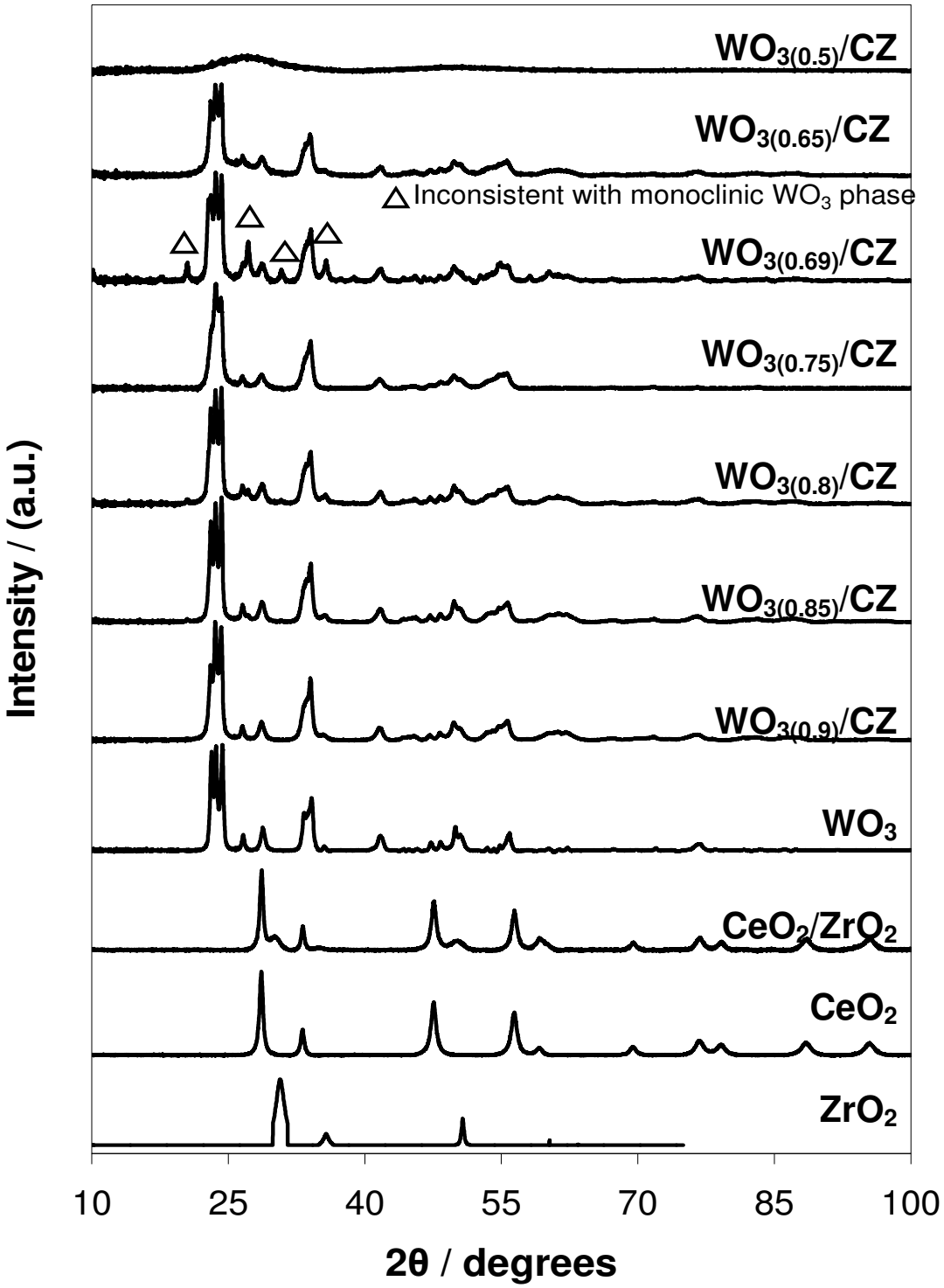

Figure 7.1 XRD spectra of unpromoted and promoted tungsten trioxide with CeO_2/ZrO_2. Peaks inconsistent with monoclinic WO_3 structure are marked

Table 7-3 Measured crystallite size and surface area of as prepared samples

Sample	Particle Diameter[a] / nm	BET_{SA} / (m^2/g)
WO_3	32.9	19.1
WO_3(0.9)/CZ	34.9	20.0
WO_3(0.85)/CZ	39.9	40.1
WO_3(0.8)/CZ	32.5	49.6
WO_3(0.75)/CZ	28.5	51.6
WO_3(0.69)/CZ	31.3	47.6
WO_3(0.65)/CZ	31.1	60.8
WO_3(0.5)/CZ	--	89.2
CeO_2	--	89.5
ZrO_2	--	105.1
CeO_2/ZrO_2	--	88.1

[a] Determined by Scherrer Equation from XRD spectra, values calculated from major WO_3 peaks

Surface area was found to increase with increasing loading of CZ to WO_3 up to 20 mol% CZ. At this point surface area remained similar despite increasing CZ loading with the exception of 50 mol% CZ (**Table 7-3**). Crystallite size calculated by the Scherrer Equation showed minimal variation in crystallite size over a range of CZ loading. This lack of change in crystallite size would suggest that the increase in surface area results from greater dispersion of WO_3 species due to introduction of CZ promoters, rather than formation of a solid solution, which may alter crystallite size.

SEM imagery of 'as prepared' unpromoted and promoted WO_3 is indicative of increasing agglomerate size with addition of CZ (**Figure 7.2**). Unpromoted WO_3 shows high concentration of small particle agglomerates and, following addition of CZ, overall particle size increases. There is very little change in overall structure with increasing loading of CZ.

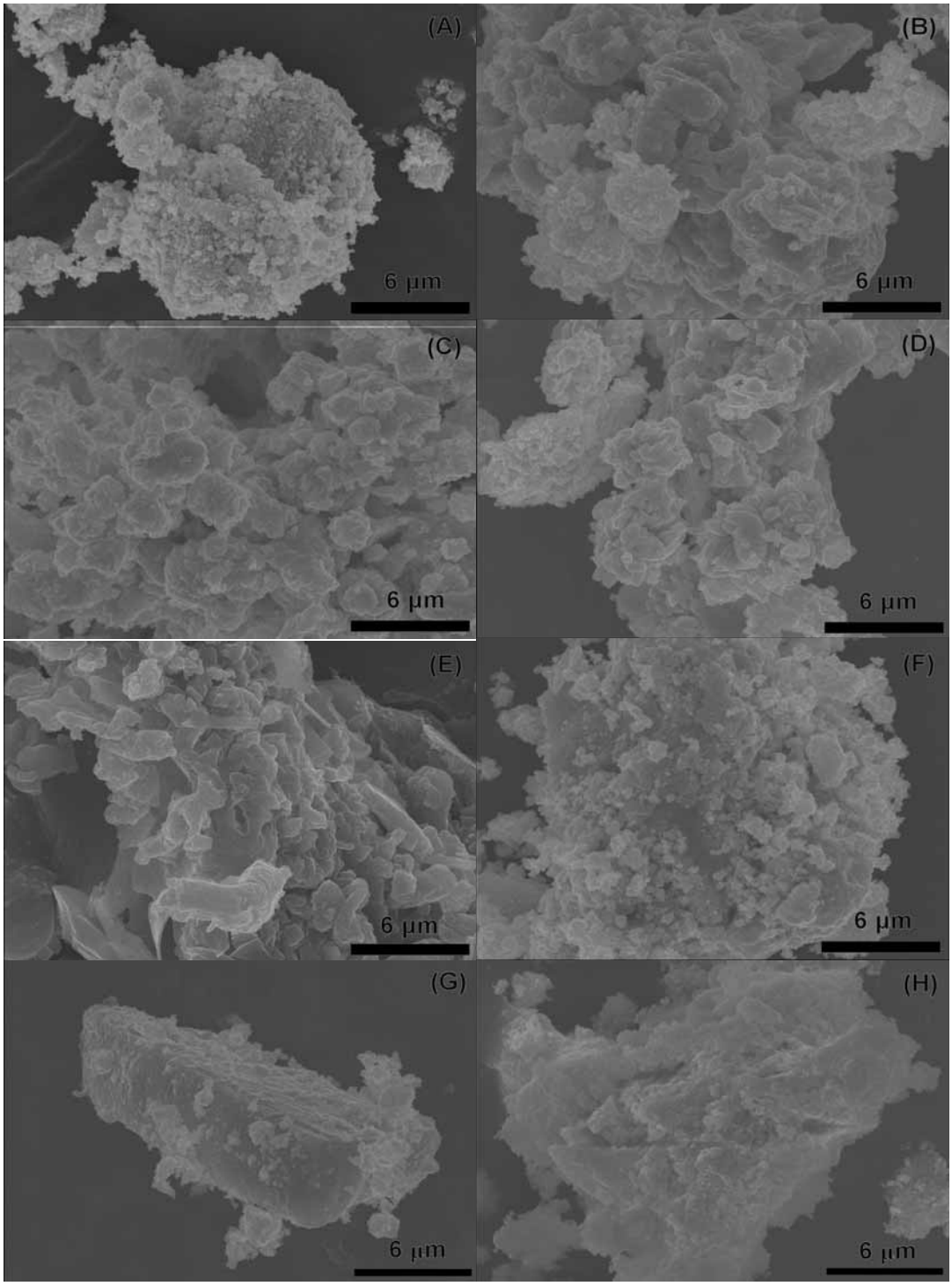

Figure 7.2 SEM imagery of fresh samples, accelerating voltage 20kV and 5000 times magnification: (A) WO_3, (B) WO_3(0.9)/CZ, (C) WO_3(0.85)/CZ, (D) WO_3(0.8)/CZ, (E) WO_3(0.75)/CZ, (F) WO_3(0.69)/CZ, (G) WO_3(0.65)/CZ, (H) WO_3(0.5)/CZ

At 31 mol% CZ / 69 mol% WO_3 and 35 mol% CZ / 65 mol% WO_3 the observed structure is more similar to that of unpromoted WO_3, indicating a change in structure as compared to lower concentrations of CZ addition (<25 mol% CZ). This is also the case with 50 mol% CZ / 50 mol% WO_3.

7.3.2 Hydrogen Temperature Programmed Reduction (TPR)

Temperature programmed reduction (TPR) analysis of unpromoted and promoted WO_3 with increasing loading of CZ is shown in **Figure 7.3**. Unpromoted WO_3 reduces in a multi-step process, with peaks at 573ºC, 679ºC, 735ºC and 956ºC. There is overlap of the second and third reduction peaks, followed by complete reduction of WO_2 to W. The observation of multiple intermediate oxidation phases of tungsten during reduction of WO_3 has been previously reported [10, 11], resulting in a reduction process that can be broken down into $WO_3 \rightarrow WO_{2.9} \rightarrow WO_{2.72} \rightarrow WO_2 \rightarrow W$ (**Table 7-4**). Following addition of CZ to WO_3, the $WO_{2.9} \rightarrow WO_{2.72} \rightarrow WO_2$ reduction steps are no longer separable, reducing in a single step. This is preceded by a small peak arising at ~600C which is attributed to the $WO_3 \rightarrow WO_{2.9}$ reduction step. Following these two steps is the complete reduction of WO_2 to W for all CZ promoted WO_3 samples. Reduction of $WO_{2.9}$ to WO_2 is observed to occur at increasing temperature following addition of CZ at 10%, with a slight shift to lower temperatures at increasing additions of CZ.

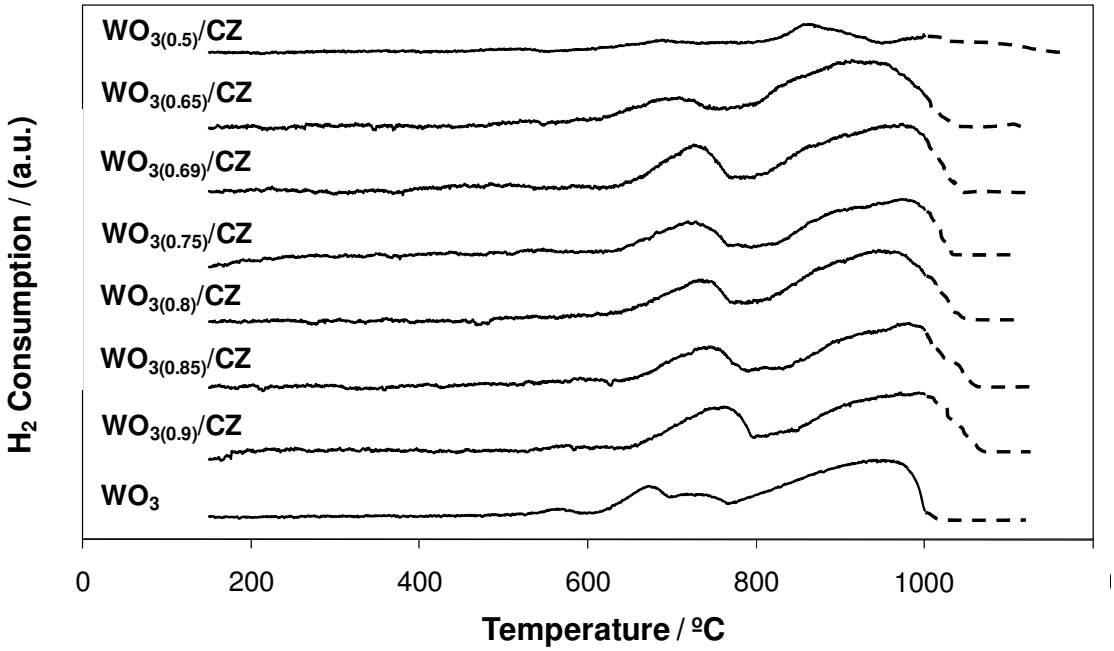

Figure 7.3 H_2 TPR of unpromoted and promoted WO_3 up to 1000ºC

Table 7-4 Peak temperatures and assignments of 5% H_2 TPR of unpromoted and promoted WO_3

Sample	Temperature / (ºC)			
Reduction State	$WO_3 \rightarrow WO_{2.9}$ $2(CeO_2/ZrO_2) \rightarrow Ce_2O_3/2ZrO_2$	$WO_{2.9} \rightarrow WO_{2.72}$	$WO_{2.72} \rightarrow WO_2$	$WO_2 \rightarrow W$
WO_3[a]	573	679	735	956
WO_3(0.9)/CZ	581	764		1000
WO_3(0.85)/CZ	587	749		986
WO_3(0.8)/CZ	544	742		954
WO_3(0.75)/CZ	541	729		977
WO_3(0.69)/CZ	489	729		976
WO_3(0.65)/CZ	537	705		927
WO_3(0.5)/CZ	512	694		866

[a] Reduction of unpromoted WO_3 does not include reduction of CeO_2/ZrO_2

With increasing CZ loading, the initial peak in the TPR profile is observed as a broad shoulder. Based on calculated peak area comparison, this shoulder cannot be assigned to reduction of WO_3 to $WO_{2.9}$ but it may be defined as a combination of both the aforementioned reduction, along with $2(CeO_2/ZrO_2)$ to $Ce_2O_3/2ZrO_2$ reduction. H_2 reduction of CeO_2/ZrO_2 shows reduction to occur at similarly low temperature but, at such low loadings and low levels of H_2 consumption, it is difficult to resolve this peak within the reduction profile.

There is minimal change discernable in the behaviour of H_2 reduction with increasing addition of CZ up to 35%. At a 1:1 ratio of WO_3 to CZ (50 mol% CZ / 50 mol% WO_3), the observed hydrogen consumption is markedly decreased, indicative of lower OSC as compared to both unpromoted WO_3 and lower loadings of CZ. As stated earlier, in the interest of maximising potential hydrogen production, it is necessary to limit the percentage of CZ addition.

7.3.3 Methane Temperature Programmed Reduction (TPR)

With the primary reductant of interest being methane, it is necessary to determine how the methane reduction profile for unpromoted and promoted WO_3 differs from H_2 reduction. **Figure 7.4** shows the H_2O production profile from methane reduction of WO_3 with increasing loading of CZ. The outgoing water signal gives the clearest signal, and thus was chosen over other product gases or methane consumption signal as a means for gauging the reduction process. In the interest of limiting potential carbon formation from methane decomposition, the reduction temperature did not extend beyond 750ºC. After holding the temperature constant at 750ºC for approximately 50 minutes, unpromoted WO_3 is further reduced to form W metal, where subsequent methane decomposition occurs and formation of WC is observed (**Figure 7.6**). With increasing addition of CZ, there is longer time taken for the outgoing gas signal to stabilise at 750ºC, as an indicator of complete reduction, at which point methane decomposition over W produces carbon and/or tungsten carbide.

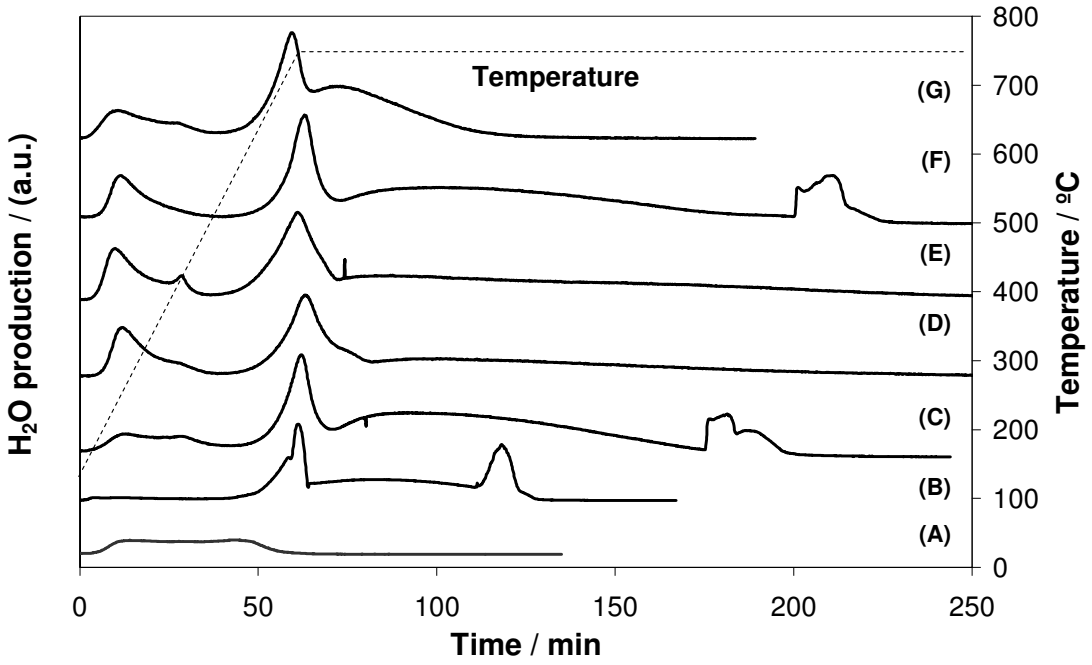

Figure 7.4 H_2O output signal of 50% CH_4 TPR of unpromoted and promoted WO_3 up to 750ºC: (A) CeO_2/ZrO_2, (B) WO_3, (C) WO_3(0.9)CZ, (D) WO_3(0.85)CZ, (E) WO_3(0.8)CZ, (F) WO_3(0.75)CZ, (G) WO_3(0.69)CZ

Table 7-5 Peak temperatures and assignments of 50% CH_4 TPR of unpromoted and promoted WO_3

Sample	**Temperature / (ºC)**		
Reduction State	$WO_3 \rightarrow WO_{2.72}$ $2CeO_2/ZrO_2 \rightarrow Ce_2O_3/2ZrO_2$	$WO_{2.72} \rightarrow WO_2$	$WO_2 \rightarrow W$
WO_3[a]	737	750	750
WO_3(0.9)/CZ	281	750	750
WO_3(0.85)/CZ	280	750	--
WO_3(0.8)/CZ	259	750	--
WO_3(0.75)/CZ	270	750	750
WO_3(0.69)/CZ	264	740	--
CeO_2/ZrO_2	315; 590		

[a] Reduction of unpromoted WO_3 does not include the reduction of CeO_2/ZrO_2

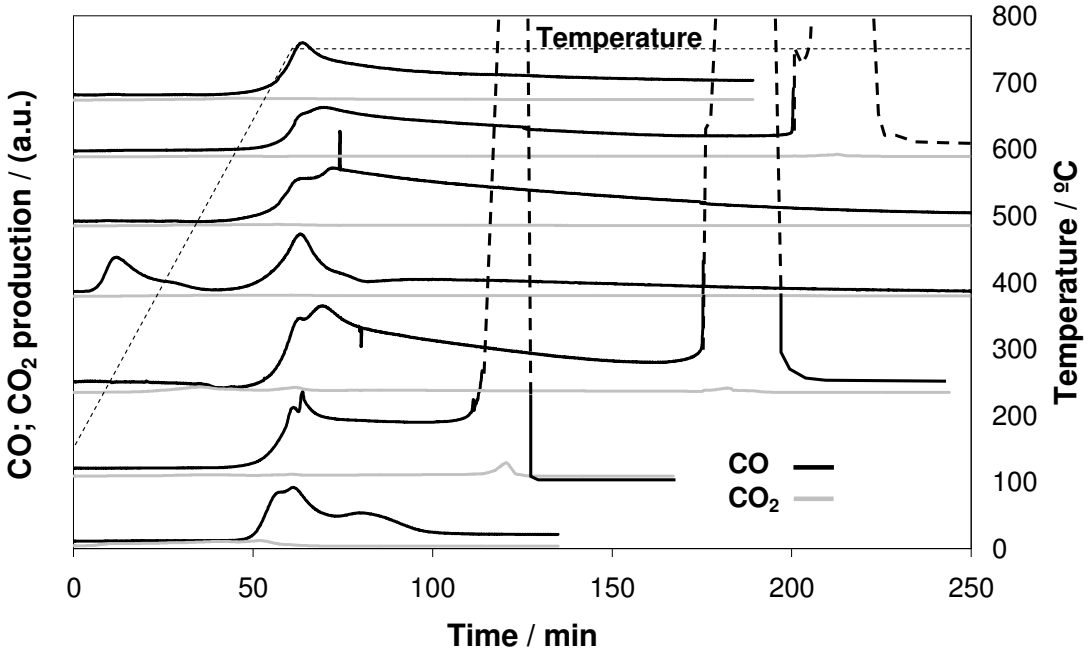

Figure 7.5 CO; CO_2 output signal of 50% CH_4 TPR of unpromoted and promoted WO_3 up to 750ºC: (A) CeO_2/ZrO_2, (B) WO_3, (C) WO_3(0.9)CZ, (D) WO_3(0.85)CZ, (E) WO_3(0.8)CZ, (F) WO_3(0.75)CZ, (G) WO_3(0.69)CZ

Reduction of CeO_2/ZrO_2 shows a broad peak between 150-600ºC, assigned to reduction of Ce species (**Figure 7.4**). Lower temperature peaks between 150-600ºC are also observed during reduction of all CZ promoted WO_3 samples. These peaks are assigned to a combination of the aforementioned reduction of CeO_2/ZrO_2 for promoted WO_3 along with reduction of WO_3 to $WO_{2.72}$ (**Table 7-5**). Following on from this initial peak, reduction of CZ promoted WO_3 to form WO_2 at ~750ºC ($CZ_x.WO_{2(x-1)}$) for all samples shows no evidence of CO_x formation upon re-oxidation with H_2O (not shown). In the reduction of unpromoted WO_3, initial transition of WO_3 to $WO_{2.72}$ occurs at ~730ºC, as indicated by a small shoulder preceding the reduction of $WO_{2.72}$ to WO_2 beyond 750ºC (**Figure 7.4**, **Table 7-5**). CO output results reflect the results shown by H_2O signal from reduction (**Figure 7.5**). CO_2 production is minimal.

At 15 mol% CZ and 20 mol% CZ loading on WO_3, it is observed that H_2O production is not stabilised up to 250 min, with reduction taking place beyond 250 min (not shown). It is surmised that the reduction peak arising beyond 200 min for 25 mol% CZ loading on WO_3 may be a discrepancy, given that with increasing CZ addition, the time taken for reduction to go to completion increases accordingly. At a loading of 31 mol% CZ, hereby designated as 4CZ.9WO_3, complete stabilisation of the outgoing gas signal is observed, indicative of stabilised formation of the intermediate WO_2 phase. For all other samples, complete reduction by methane takes place to form W/WC. Stabilisation of the intermediate WO_2 phase within 4CZ.9WO_3 limits the need for further investigation of methane reduction at higher CZ loading, due to further decrease in oxygen storage capacity with increased addition of CZ. In the interest of maximising hydrogen production, minimal CZ loading on WO_3 is sought.

7.3.4 Post methane TPR analysis

Post CH_4 TPR analysis was limited to unpromoted WO_3 and 4CZ.9WO_3. It was assumed that for all other samples (WO_3(0.9)CZ, WO_3(0.85)CZ, WO_3(0.8)CZ, WO_3(0.75)CZ), final sample composition was comparable with unpromoted WO_3 in terms of undergoing complete reduction. The sample of interest was primarily 4CZ.9WO_3 due to its stabilised reduction and unique structure (**Figure 7.1**). XRD analysis of reduced, unpromoted WO_3 shows formation of a primarily WC phase with some W and a small amount of WC_{1-x} (**Figure 7.6**). XRD analysis of the reduced state of 4CZ.9WO_3 shows the structure is comprised primarily of WO_2 (JCPDS 32-1393) with some $WO_{2.72}$ present (JCPDS 05-0392) (**Figure 7.7**). Separate peaks associated with Ce and Zr species were not observed, and there was no indication of any phase separation between the promoting species and WO_3, with the structure retaining a predomoninantly WO_x phase. The results show that reduction of 4CZ.9WO_3 produces WO_2 without reducing completely to form W, thereby preventing formation of WC and/or carbon through methane decomposition. Elimination of these products allows for production of clean hydrogen during re-oxidation with water by limiting potential formation of CO and/or CO_2. Due to the sensitive nature of reduced

WO_2 and Ce_2O_3, exposure to the atmosphere most likely results in some degree of oxidation, accounting for formation of some $WO_{2.72}$.

Both unpromoted and promoted WO_3 were reduced under the same conditions, as in CH_4 reduction above in **Figure 7.4**, with reduction continuing to the point at which the H_2O signal stabilised and reduced to a minimum value, at which point it was assumed the reduction had gone to completion. According to **Figure 7.4**, the reduction times for both samples were not significantly different, however the XRD spectra of unpromoted WO_3 shows line broadening (**Figure 7.6**), consistent with smaller particles, as compared to post-reduction XRD of $4CZ.9WO_3$, which has sharper peaks indicative of larger crystallite size due to sintering (**Figure 7.7**). Particle fragmentation has been observed upon formation of WC by Medeiros et. al., resulting in smaller particle size as compared to the oxide precursor, whilst Madhav Reddy et. al. have reported the formation of amorphous WC upon reduction [12, 13].

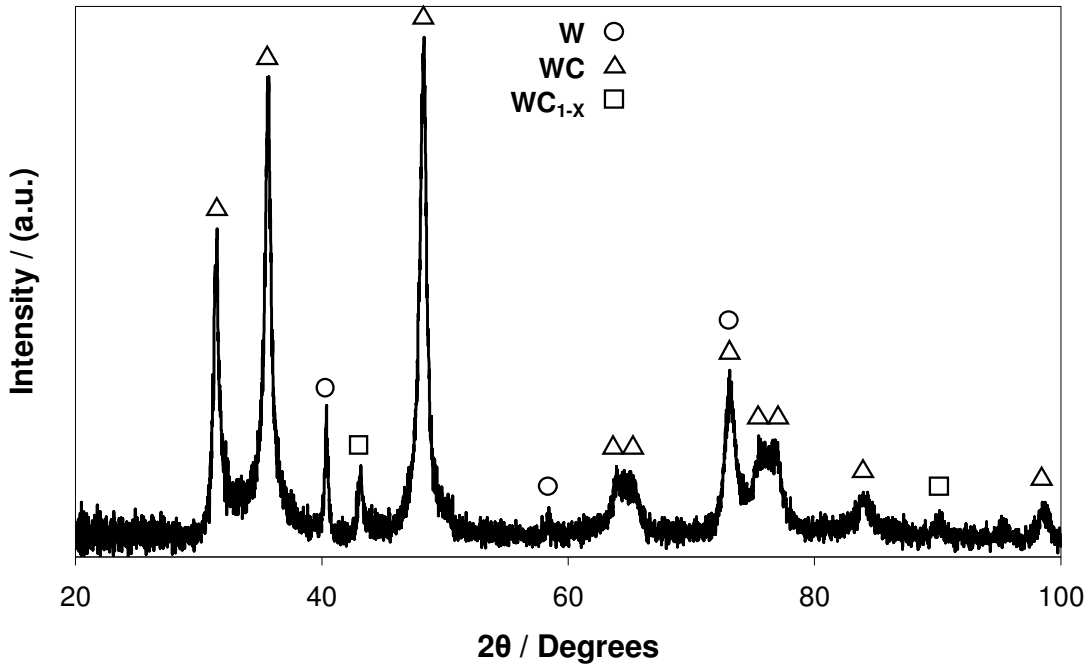

Figure 7.6 Post methane reduction XRD spectra of WO_3

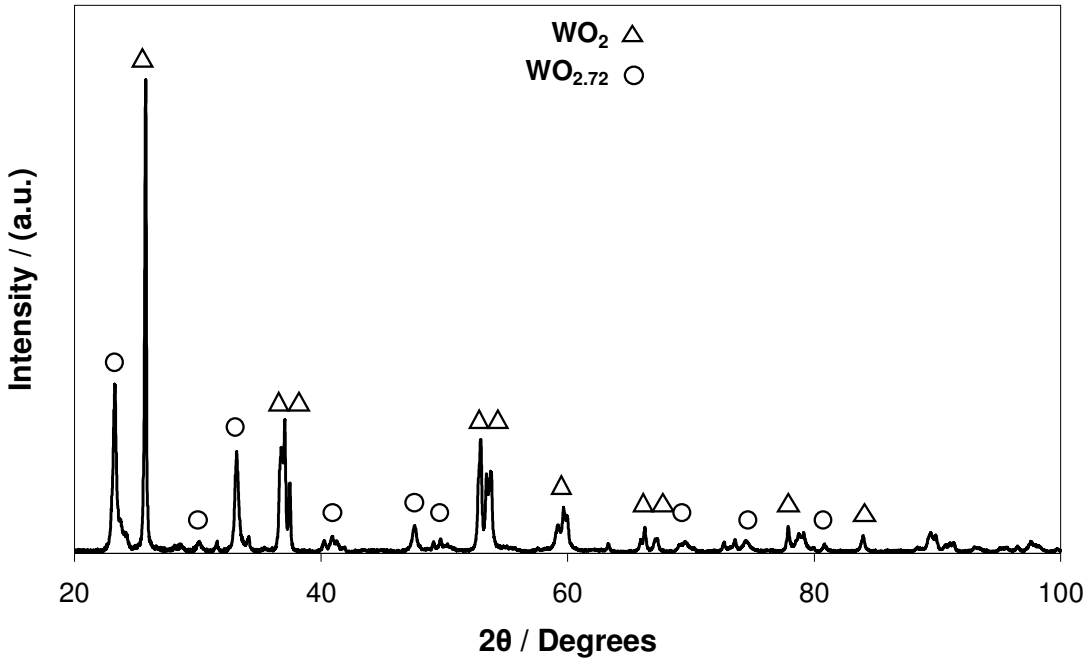

Figure 7.7 Post methane reduction XRD spectra of 4CZ.9WO_3

XPS analysis of fresh unpromoted WO_3 and 4CZ.9WO_3 shows minimal variation in the W4f W^{6+} doublet at binding energies of 35.81 eV (WO_3) and 35.71 eV (4CZ.9WO_3) respectively (**Figure 7.8**, **Figure 7.9**, **Table 7-6**). Based on literature values, this shift of 0.1 eV is not considered to be of significance, with binding energy values for W4f peaks of WO_3 ranging between 35.5-35.8 eV [14-16]. In the case of significant interaction between the promoting oxide species and WO_3, it has been reported that peak broadening is observed due to greater dispersion of WO_3 species, however, peak broadening is not observed in this case [17]. XPS analysis of peaks in the Ce3d region of 4CZ.9WO_3 (**Table 7-6**) produced minimal intensities, thus more detailed analysis and comparison of Ce3d species between CZ promoted WO_3 and CeO_2/ZrO_2 alone was not possible. **Table 7-6** shows minimal variation in calculation of oxygen species (O1s) atomic percentage between unpromoted and promoted WO_3, indicating that substitution of 31 mol% WO_3 with CZ still shows high OSC retention. Minimal Ce3d species are detected at the surface, perhaps resulting from Ce species present as very small particles or primarily within the bulk, which also renders them undetectable by XRD (**Figure 7.1**).

Table 7-6 Measured XPS peaks and corresponding binding energies

Sample	Element	Binding Energy / eV	[AT] / %
WO_3	O1s	532.9	2.37
	O1s	531.68	6.24
	O1s	530.72	50.56
	W 4f	35.81	22.27
4CZ.9WO_3	O1s	533.51	1.73
	O1s	532.1	7.36
	O1s	530.69	47.80
	W 4f	35.71	17.42
	Ce 3d5	886.32	0.39
	Ce 3d5	882.42	0.26

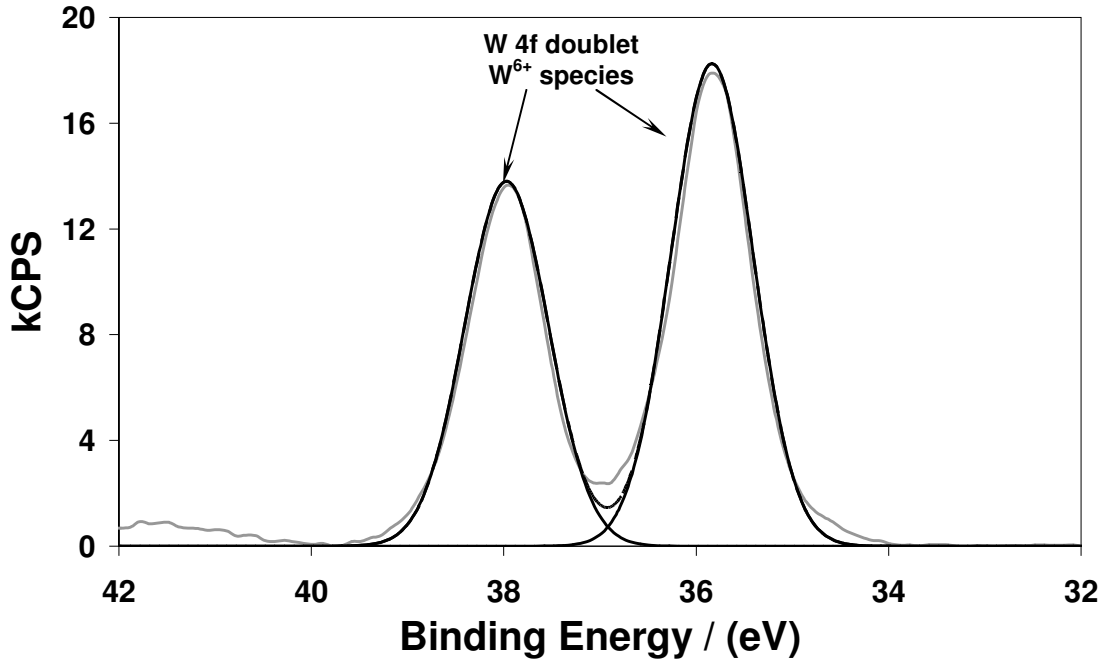

Figure 7.8 W 4f peaks from XPS spectra of fresh unpromoted WO_3

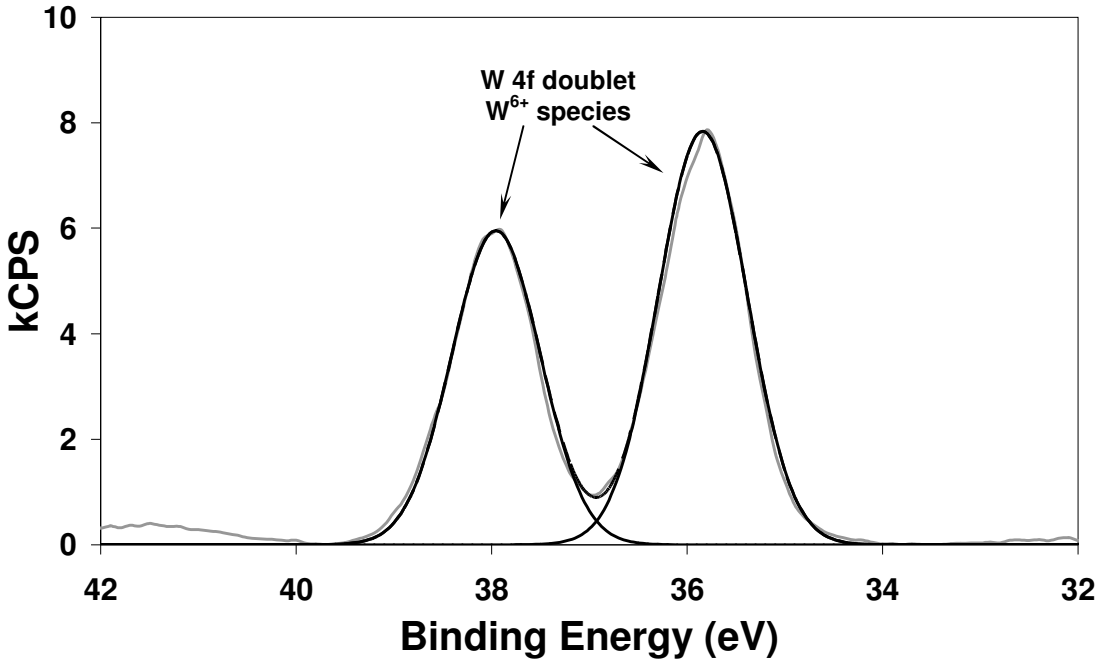

Figure 7.9 W 4f peaks from XPS spectra of fresh 4CZ.9WO$_3$

Surface analysis of reduced 4CZ.9WO$_3$ by XPS (**Figure 7.10**) shows W 4f peaks of W^{6+} doublet at a binding energy of 36.34 eV. W 4f doublets which emerge at 34.67 eV and 33.51 eV can be assigned to W^{5+} and W^{4+} respectively (**Table 7-7**) [18, 19]. Surface oxidation occurs upon sample exposure to the atmosphere, thus it is difficult to gain an accurate sample composition from XPS, due to the surface analysis limitation of this technique. By quantification of the amount of W^{4+} and W^{5+} in the sample with respect to W^{6+}, more precise determination of the exact oxidation state would be possible. Relatively large amounts of W^{4+} observed from XPS coupled with XRD data identifies the reduced state of 4CZ.9WO$_3$ as comprised primarily of WO_2. Comparison between reduced 4CZ.9WO$_3$ and 'as prepared' 4CZ.9WO$_3$ shows a decrease in the W^{6+} W4f atomic percentage due to its removal during reduction to form W^{4+} and W^{5+}, and a slight increase in Ce3d species resulting from greater exposure of Ce species at the surface following reduction (**Table 7-6**, **Table 7-7**). Comparison between reduced 4CZ.9WO$_3$ and 'as prepared' 4CZ.9WO$_3$ shows only a slight decrease in atomic percentage of oxygen species (O1s), however, this may result from unavoidable surface oxidation.

Table 7-7 Measured XPS peaks and corresponding binding energies post-redox

Sample	Element	Binding Energy / eV	[AT] / %
4CZ.9WO_3 Reduced State	O1s	532.80	5.19
	O1s	531.30	45.06
	W 4f	36.34	14.38
	W 4f	34.67	3.41
	W 4f	33.51	1.22
	Ce 3d	886.46	0.60
	Ce 3d	882.60	0.49

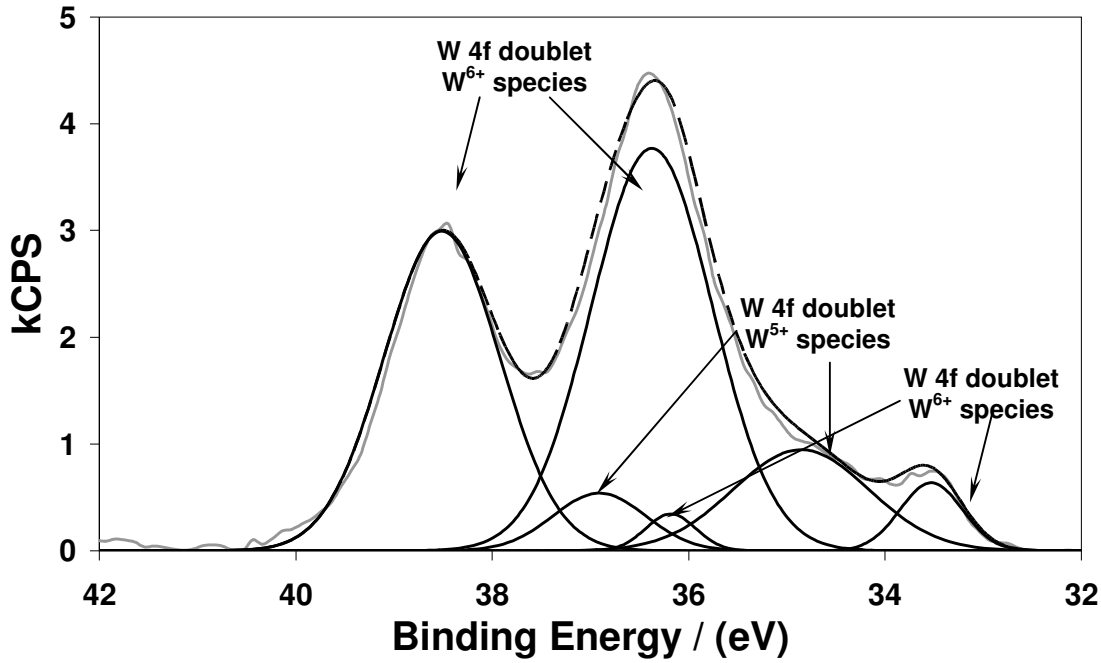

Figure 7.10 W 4f peaks from XPS spectra of reduced 4CZ.9WO_3

These results show partial reduction of 4CZ.9WO_3 to 4CZ.9WO_2 to be stable, as compared to lower loading of CZ on WO_3. Complete reduction of unpromoted WO_3 forms WC, which is thermodynamically unfavourable for re-oxidation to form WO_3 [2].

Contamination of hydrogen production due to CO_x formation during H_2O re-oxidation would also result.

$$WC + H_2O \rightarrow W + CO + H_2 \quad \textbf{7.1}$$

$$WC + 2H_2O \rightarrow W + CO_2 + 2H_2 \quad \textbf{7.2}$$

7.3.5 Thermogravimetric Analysis (TGA)

To gain a better understanding of the reduction pathway and various intermediate oxidation states of unpromoted and CZ promoted WO_3, thermogravimetric analysis (TGA) was used to determine the precise mass loss during sample reduction. Given the choice of 4CZ.9WO_3 as the primary candidate for further investigation, TGA studies were limited to unpromoted WO_3, 4CZ.9WO_3 and CeO_2/ZrO_2 for comparison.

Prior to reduction, samples were calcined in air at 500ºC for 1 hr. All samples showed some degree of mass loss during calcination, however, upon cooling back to room temperature, mass gain was observed. The initial sample mass was taken as the measured mass of the sample during the calcination step at 500ºC, as this mass loss was not attributed to sample reduction when H_2 was introduced. This resulted in an initial mass greater than 100% prior to reduction by H_2.

As per H_2 TPR studies on WO_3, TGA confirms reduction in a four step process from $WO_3 \rightarrow WO_{2.9} \rightarrow WO_{2.72} \rightarrow WO_2 \rightarrow W$ based on weight loss calculations, which is consistent with previous findings (**Figure 7.11, Table 7-8**) [10, 11]. The available OSC of CeO_2/ZrO_2 is shown to be much less than that of WO_3, with approximately 2% total mass loss in CeO_2/ZrO_2, resulting from $2(CeO_2/ZrO_2)$ to $Ce_2O_3/2ZrO_2$ reduction, as compared to 7.4% for reduction of WO_3 to WO_2 at 810-820ºC. 4CZ.9WO_3 demonstrates similar OSC to unpromoted WO_3 for the reduction of WO_3 to WO_2, with final OSC for complete reduction of WO_3 greater than complete reduction of 4CZ.9WO_3 (**Table 6-4**).

Reduction of CZ within 4CZ.9WO_3 occurs alongside conversion of WO_3 to WO_2 at low temperature.

The similarity between final mass loss for WO_3 and 4CZ.9WO_3 is unexpected, given that substitution of CZ into 4CZ.9WO_3 should show a decrease in total OSC equivalent to approximately 81% of total OSC of WO_3 compared to the 0.85% difference in final mass loss between the two samples. The more pronounced shoulder that appears at 810-820ºC for 4CZ.9WO_3 and unpromoted WO_3 demonstrates increased stabilisation of intermediate WO_2 in 4CZ.9WO_3 over a larger temperature range. Initial reduction of 4CZ.9WO_3 from WO_3 to WO_2 shows a more pronounced effect from addition of CZ, with increased OSC, following which reduction of WO_2 to W occurs at reasonably similar rates for both CZ promoted WO_3 and unpromoted WO_3 once the sample reaches 900ºC.

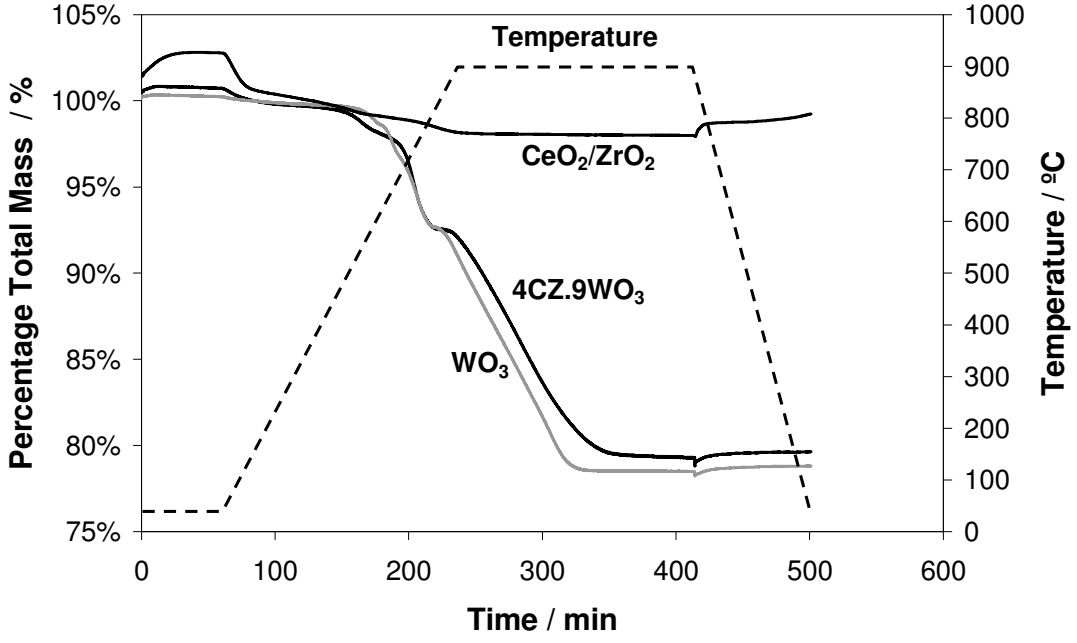

Figure 7.11 TGA of unpromoted WO_3, 4CZ.9WO_3 and CeO_2/ZrO_2

Table 7-8 Peak temperatures and assignments of unpromoted WO_3 TGA

	Oxidation State			
WO_3	$WO_3 \rightarrow WO_{2.9}$	$WO_{2.9} \rightarrow WO_{2.72}$	$WO_{2.72} \rightarrow WO_2$	$WO_2 \rightarrow W$
Temperature / ºC	160	473	612	812
	% Mass Remaining / %			
Stoichiometric	99.31	98.07	93.10	79.30
Experimental	99.52	98.42	92.57	78.52

Table 7-9 Peak temperatures and assignments of 4CZ.9WO_3 TGA

	Oxidation State			
4CZ.WO_3	$WO_3 \rightarrow WO_{2.9}$	$WO_{2.9} \rightarrow WO_{2.72}$ $2[CeO_2/ZrO_2] \rightarrow Ce_2O_3/ZrO_2$	$WO_{2.72} \rightarrow WO_2$	$WO_2 \rightarrow W$
Temperature / ºC	150	387	644	817
	% Mass Remaining / %			
Stoichiometric	99.46	97.90	94.03	83.27
Experimental	99.52	97.75	92.50	79.33

7.3.6 Theoretical Calculation of Potential Oxygen Storage Capacity (OSC)

To quantify the hydrogen production potential of 4CZ.9WO_3 redox compared to unpromoted WO_3 and CZ addition at various loadings, a theoretical calculation method is employed. **Table 7-10** shows calculations of the theoretical potential maximum hydrogen production from tungsten oxides and cerium oxides. Hydrogen production from oxidation of Ce_2O_3 to CeO_2 yields only 65% of potential hydrogen compared to hydrogen production from oxidation of WO_2 to WO_3. With addition of ZrO_2, hydrogen production from CeO_2/ZrO_2 is further halved to 32.5%. Based on these calculations, in the interest of maximising hydrogen production it is necessary to limit addition of CZ to the $CZ_x.WO_{3(x-1)}$ system.

Table 7-10 Potential H_2 production from H_2O re-oxidation of various metal oxides

Eq.	Reaction	H_2 Production		
		mol.H_2/ mol.(sample)[a]	mol.H_2/ g.(sample)[a]	L.H_2/ kg.(sample)[a]
7.3	$W + 3H_2O \rightarrow WO_3 + 3H_2$	3	12.9 x 10^{-3}	287.9
7.4	$W + 2H_2O \rightarrow WO_2 + 2H_2$	2	8.63 x 10^{-3}	192.0
7.5	$WO_2 + H_2O \rightarrow WO_3 + H_2$	1	4.31 x 10^{-3}	96.0
7.6	$Ce_2O_3 + H_2O \rightarrow 2CeO_2 + H_2$	0.5	3.39 x 10^{-3}	75.4
7.7	$[Ce_2O_3 - 2ZrO_2] + H_2O \rightarrow 2[CeO_2 - ZrO_2] + H_2$	0.25	1.69 x 10^{-3}	37.7
7.8	$[Ce_2O_3 - 2ZrO_2]_{(0.1)}.WO_{2(0.9)} + H_2O$ $2[CeO_2 - ZrO_2]_{(0.1)}.WO_{3(0.9)} + H_2$	0.925	4.14 x 10^{-3}	92.1
7.9	$[Ce_2O_3 - 2ZrO_2]_{(0.15)}.WO_{2(0.85)} + H_2O$ $2[CeO_2 - ZrO_2]_{(0.15)}.WO_{3(085)} + H_2$	0.888	4.06 x 10^{-3}	90.3
7.10	$[Ce_2O_3 - 2ZrO_2]_{(0.2)}.WO_{2(0.8)} + H_2O$ $2[CeO_2 - ZrO_2]_{(0.2)}.WO_{3(0.8)} + H_2$	0.85	3.95 x 10^{-3}	87.9
7.11	$[Ce_2O_3 - 2ZrO_2]_{(0.25)}.WO_{2(0.75)} + H_2O$ $2[CeO_2 - ZrO_2]_{(0.25)}.WO_{3(0.75)} + H_2$	0.813	3.85 x 10^{-3}	85.7
7.12	$2[Ce_2O_3 - 2ZrO_2].9WO_2 + 11H_2O \rightarrow 4[CeO_2 - ZrO_2].9WO_3 + 11H_2$	0.769	3.73 x 10^{-3}	83.0
7.13	$[Ce_2O_3 - 2ZrO_2]_{(0.35)}.WO_{2(0.65)} + H_2O$ $2[CeO_2 - ZrO_2]_{(0.35)}.WO_{3(0.65)} + H_2$	0.738	3.64 x 10^{-3}	81.1
7.14	$[Ce_2O_3 - 2ZrO_2]_{(0.5)}.WO_{2(0.5)} + H_2O$ $2[CeO_2 - ZrO_2]_{(0.5)}.WO_{3(0.5)} + H_2$	0.625	3.29 x 10^{-3}	73.2

[a] The sample referred to corresponds to all metal oxides incorporated within the system (W, Ce, Zr). In the case of CeO_2-ZrO_2 the sample referred to is both Ce and Zr.

Based upon these results, total hydrogen production from $W + 3H_2O \rightarrow WO_3 + 3H_2$ (287.9L/kg.W) is 3.5 times greater compared to $4CZ.9WO_2 + H_2O \rightarrow 4CZ.9WO_3 + H_2$ (83L/kg.[W + Ce + Zr]). Given the potential for clean hydrogen production using the latter resulting from incomplete reduction from WO_3 to WO_2, complete reduction of unpromoted or promoted WO_3 is not feasible due to WC formation and subsequent CO_x contamination. Comparison between $WO_2 + H_2O \rightarrow WO_3 + H_2$ (96L/kg.W) and $4CZ.9WO_2 + H_2O \rightarrow 4CZ.9WO_3 + H_2$ (83L/kg.[W+Ce+Zr]) shows only a 13.5% decrease in total potential hydrogen production. The actual potential hydrogen production may be greater, as TGA results show possible increased OSC (**Figure 7.11**). In addition, the increased resistance to sintering from CZ in $4CZ.9WO_3$ allows for higher levels of hydrogen production to be maintained over numerous cycles, as compared to unpromoted WO_3, which would sinter more readily, thus limiting potential hydrogen production.

7.4 CH_4-H_2O redox cycling of $4CZ.9WO_3$

7.4.1 Optimisation of $4CZ.9WO_3$ Redox Process

Following selection of $4CZ.9WO_3$ as an optimal CZ loading on WO_3, further studies were conducted to determine ideal experimental conditions at which the system was optimised. This study was conducted in two separate phases, reduction and re-oxidation. In the reduction phase, the reduction parameters were altered whilst the oxidation parameters were kept constant. Similarly, in the oxidation phase, reduction parameters were kept constant with alteration of the oxidation parameters between experiments. The experimental parameters of importance were defined as flow rate, reactant concentration and operating temperature for both phases of the process. The nature of the Steam-Metal Oxide Process is such that reduction is immediately followed by re-oxidation, thus it is desired to select an optimal temperature at which both reduction and re-oxidation are to be conducted, making the process more energy efficient.

Reduction of 4CZ.9WO_3 was performed at different temperatures to assess the extent of reduction (**Figure 7.12**), and the effect of reduction temperature upon subsequent hydrogen production (**Figure 7.13**). Re-oxidation parameters were kept constant with isothermal re-oxidation at 750ºC via 19.8% H_2O in Ar/He at 60mL/min. Reduction at 650ºC is incomplete, as observed by low levels of product gases observed. Subsequent re-oxidation of this sample produces minimal amounts of H_2. At 750ºC, outgoing CO and H_2O gases show small reduction peaks which are ongoing up to 100 minutes of residence time. The reaction shows production of H_2 and CO_2 are minimal. These results are indicative of a greater degree of reduction than at 650ºC and a final product consistent with WO_2. Re-oxidation of this sample confirms this analysis, producing hydrogen in amounts close to the stoichiometric amounts of hydrogen expected for $WO_2 \rightarrow WO_3$ re-oxidation. At 850ºC, much more prominent peaks associated with product gases are observed, with an initial peak arising in the first 25 minutes of reduction, which is followed by generation of large amounts of CO, H_2 and H_2O. Once again the production of CO_2 is considered minimal. This rapid reduction peak following approximately 25 minutes at 850ºC results in formation of W metal and tungsten carbide. The initial peak is ascribed to a $WO_3 \rightarrow WO_2$ transition, as per reduction at 750ºC. Re-oxidation by H_2O shows greater than stoichiometric amount of hydrogen produced due to tungsten carbide oxidation producing both CO_x and H_2.

These findings demonstrate isothermal reduction at 750ºC to be the ideal temperature for stabilised reduction of 4CZ.9WO_3 to form 4CZ.9WO_2, allowing for clean hydrogen production upon re-oxidation with H_2O.

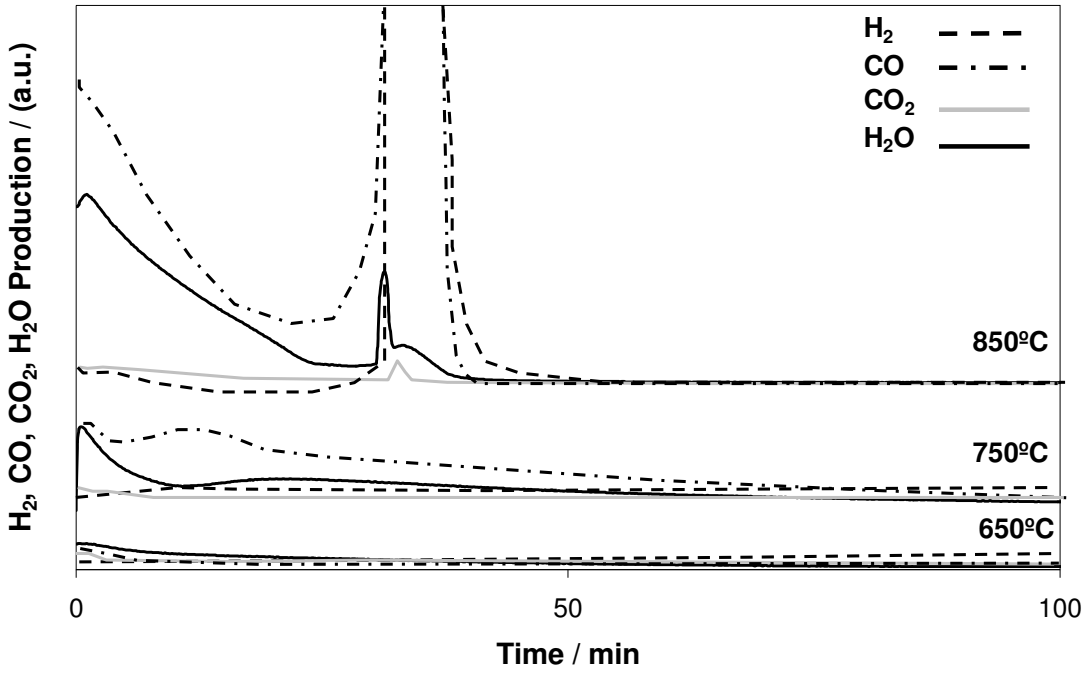

Figure 7.12 Normalised H_2, CO, CO_2, H_2O production from isothermal reduction of 4CZ.9WO_3 with 50% CH_4 in Ar/He at various temperatures

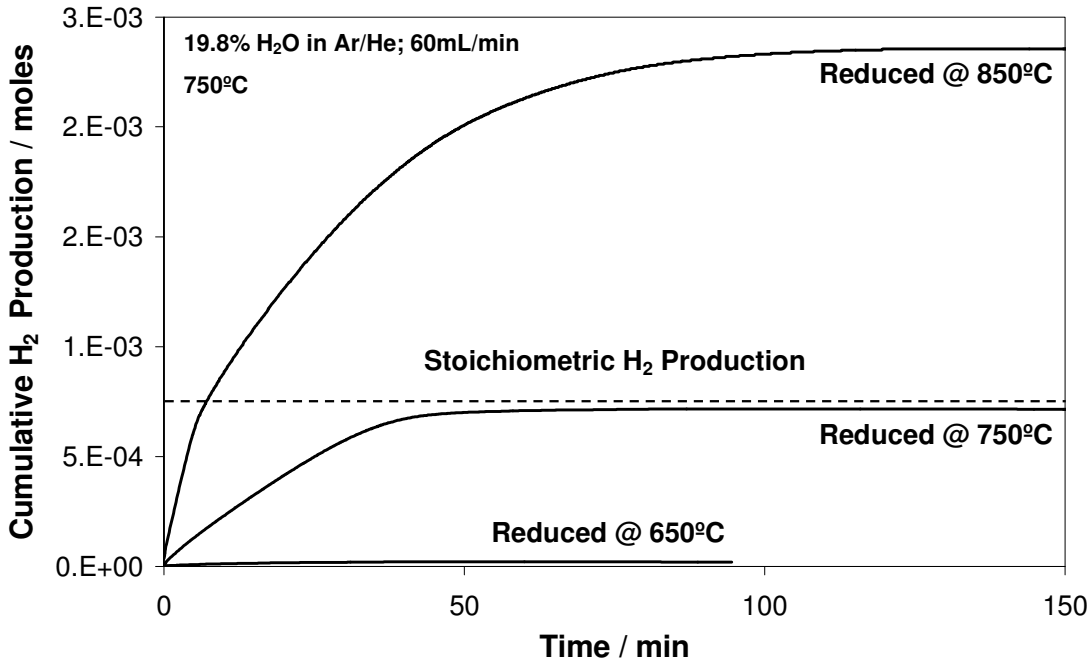

Figure 7.13 Total hydrogen production from isothermal re-oxidation of 4CZ.9WO_3 reduced at various temperatures with 19.79% H_2O in Ar/He

Figure 7.14 shows hydrogen production from isothermal re-oxidation of reduced 4CZ.9WO_3. Reduction parameters were kept constant with isothermal reduction at 750ºC via 50% CH_4 in Ar/He at 60mL/min. Re-oxidation at 650ºC results in incomplete re-oxidation of 4CZ.9WO_3, and minimal hydrogen production. Increasing temperature to 750ºC and 850ºC shows stoichiometric amounts of hydrogen production, with respect to re-oxidation of partially reduced 4CZ.9WO_3. Higher temperature shows increased rate of re-oxidation. In the interest of maintaining reduction and re-oxidation at a constant temperature, 750ºC was selected, allowing for complete re-oxidation along with partial reduction of 4CZ.9WO_3.

The effect of flow rate and reactant concentration was determined by experimental design in which the chosen parameters were varied simultaneously with each reaction (**Table 7-11-Table 7-14**). The experimental order was randomized to ensure that time was not a significant factor in the overall design and the results remained unbiased.

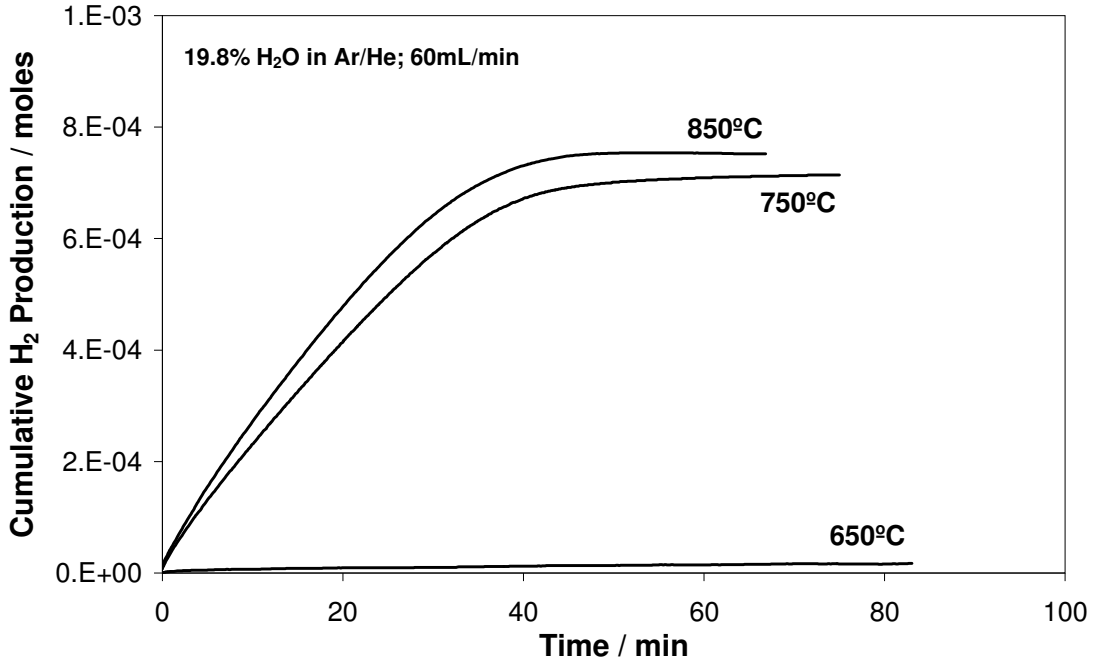

Figure 7.14 Total hydrogen production from isothermal re-oxidation of 4CZ.9WO_3 at various temperatures with 19.8% H_2O in Ar/He

Table 7-11 Experimental conditions and randomised order for optimisation of methane reduction parameters

		Methane Concentration / % CH_4		
	750ºC	**10**	**25**	**50**
Flow Rate / (mL/min)	**30**	1	2	3
	60	4	5	6
	120	7	8	9

Table 7-12 Constant water oxidation experimental conditions during optimisation of methane reduction parameters

Flow Rate / (mL/min)	H_2O Concentration / % H_2O	Reactor Temperature / ºC
60	19.8	750

Table 7-13 Experimental conditions and randomised order for optimisation of water oxidation parameters

		H_2O Concentration / % H_2O (Water saturator temperature / ºC)		
	750ºC	**19.8 (60ºC)**	**30.9 (70ºC)**	**46.8 (80ºC)**
Flow Rate / (mL/min)	**30**	5	9	1
	60	2	7	8
	120	3	4	6

Table 7-14 Constant methane reduction experimental conditions during optimisation of water oxidation parameters

Flow Rate / (mL/min)	CH_4 Concentration / % CH_4	Temperature / ºC
60	50	750

Reduction experiments show that increasing flow rate and methane concentration results in more rapid reduction (**Figure 7.15**). Low methane concentration (10%) results in incomplete reduction despite varying flow rate. Stabilised reduction of $4CZ.9WO_3$ is observed at 25% methane. Further increasing methane concentration to 50% results in more rapid reduction whilst still showing stabilised partial reduction of $4CZ.9WO_3$. The exception is 50% methane concentration at 120 mL/min which shows rapid and complete reduction, resulting in CO_x production from H_2O re-oxidation.

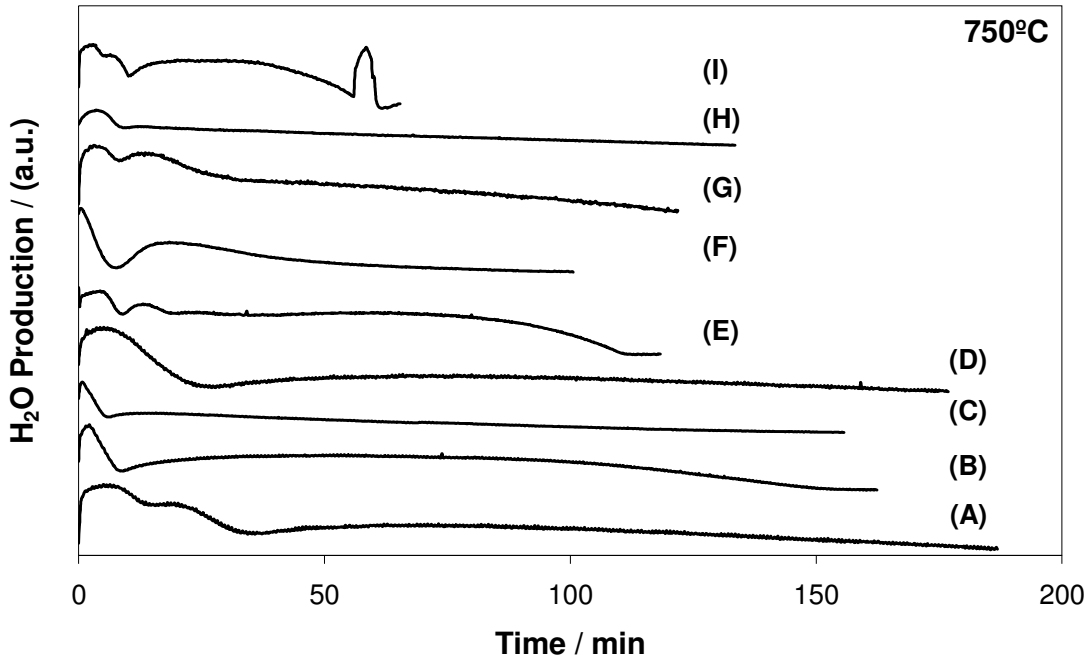

Figure 7.15 Normalised H_2O production from isothermal CH_4 reduction of $4CZ.9WO_3$ at 750ºC with: (A) 30mL/min; 10% CH_4, (B) 30mL/min; 25% CH_4, (C) 30mL/min; 50% CH_4, (D) 60mL/min; 10% CH_4, (E) 60mL/min; 25% CH_4, (F) 60mL/min; 50% CH_4, (G) 120mL/min; 10% CH_4, (H) 120mL/min; 25% CH_4, (I) 120mL/min; 50% CH_4

H_2 production shows the extent of reduction coupled with varying reduction parameters (**Table 7-15**). At 10% methane concentration, sub-stoichiometric hydrogen production during H_2O re-oxidation indicates incomplete reduction. Increasing methane concentration during reduction produces higher levels of hydrogen from re-oxidation due to more complete reduction. Time taken for reduction is proportional to both methane concentration and flow rate.

Table 7-15 H_2 production from 19.8% H_2O re-oxidation of 4CZ.9WO_3 at 750ºC, reduced by varying flow rate and CH_4 concentration

Reduction Parameters			**Re-oxidation**	
CH_4 Concentration / % CH_4	**Flow Rate / (mL/min)**	**Time / min**	**H_2 Production / moles Stoichiometric**	**H_2 Production / moles Experimental**
10	30	187	7.47×10^{-4}	3.3×10^{-4}
25	30	158		5.2×10^{-4}
50	30	147		7.0×10^{-4}
10	60	177		6.1×10^{-4}
25	60	113		7.3×10^{-4}
50	60	95		6.9×10^{-4}
10	120	122		7.5×10^{-4}
25	120	130		7.4×10^{-4}
50	120	63		[a] 9.4×10^{-4}

[a] Over-reduction of WO_3 resulted in formation of WC, thereby producing greater than theoretical H_2 concentration upon re-oxidation due to CO & CO_2 formation.

Variation of re-oxidation parameters shows minimal difference in total hydrogen production, with influence primarily upon the rate of re-oxidation (**Table 7-16**). The rate of re-oxidation is proportional to flow rate and H_2O concentration (**Figure 7.16**). Stoichiometric hydrogen production is determined as the potential hydrogen production of 4CZ.9WO_3 comprising, $WO_2 + H_2O \rightarrow WO_3 + H_2$ and $Ce_2O_3 + H_2O \rightarrow 2CeO_2 + H_2$.

Selected experimental parameters for reduction were then chosen with 50% CH_4 in Ar/He at a flow rate of 60mL/min, and reduction conducted isothermally at 750ºC. Re-oxidation experimental parameters were selected as 46.8% H_2O in Ar/He (water saturator temperature of 80ºC) at a flow rate of 120mL/min, and an isothermal re-oxidation temperature of 750ºC.

Table 7-16 H_2 production from H_2O re-oxidation of 4CZ.9WO_3 at varying flow rate and H_2O concentration at 750ºC

H_2O Concentration / % H_2O	**Flow Rate / (mL/min)**	**H_2 Production / moles Stoichiometric**	**H_2 Production / moles Experimental**	**Time / min**
19.79	30	7.47×10^{-4}	7.2×10^{-4}	50
30.87	30		7.2×10^{-4}	30
46.79	30		7.2×10^{-4}	28
19.79	60		7.8×10^{-4}	45
30.87	60		7.2×10^{-4}	24
46.79	60		7.2×10^{-4}	20
19.79	120		7.4×10^{-4}	37
30.87	120		7.1×10^{-4}	24
46.79	120		7.7×10^{-4}	16

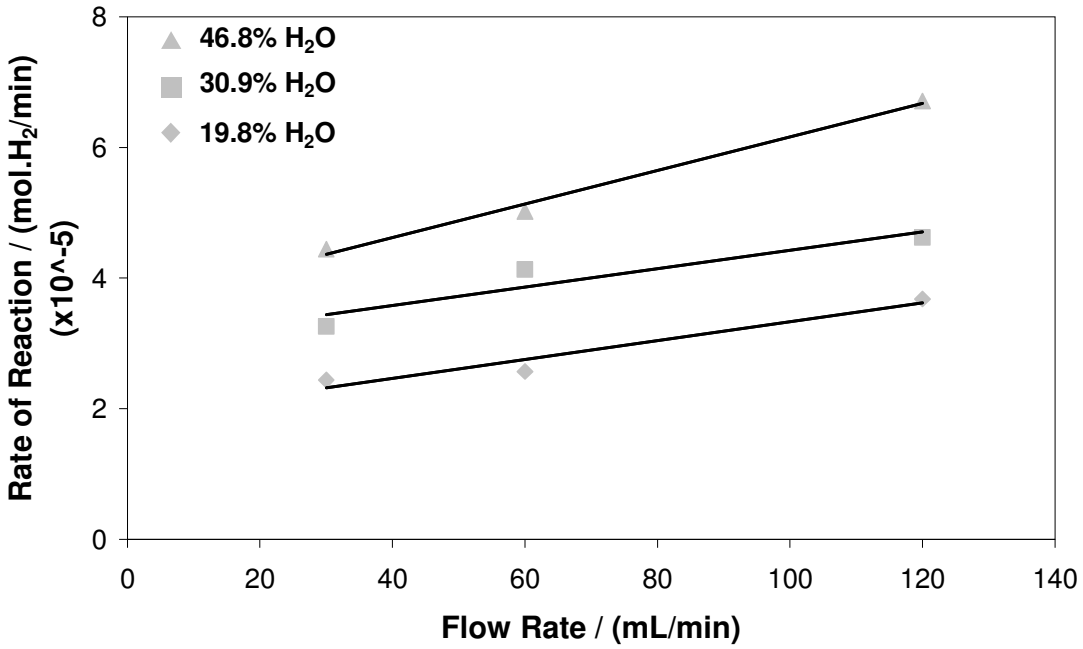

Figure 7.16 Rate of reaction vs. flow rate of H_2O re-oxidation of 4CZ.9WO_3 at 750ºC

7.4.2 Post-Redox Characterisation of 4CZ.9WO_3

There is an observed structural change in redox cycled 4CZ.9WO_3 following the first cycle, with XRD analysis of post-redox samples showing a different structure of 4CZ.9WO_3 compared to the initial spectra (**Figure 7.17**). Most notably, the three most prominent tungsten peaks have been replaced by a single peak. The new spectra can be defined as $WO_{2.9}$ or a sub-stoichiometric form of tungsten trioxide (JCPDS 05-0386). This is also evident by the colour change between fresh 4CZ.9WO_3 and its cycled counterpart, from a green-yellow colour which corresponds to monoclinic WO_3, to a predominantly blue colouring. Tungsten 'blue' oxide is a well known and well characterised form of tungsten oxide, corresponding to sub-stoichiometric tungsten trioxide, of which $WO_{2.9}$ is one form [20, 21]. This is indicative of the inability of H_2O to completely re-oxidise WO_2 and form WO_3, leading to a slight loss in total OSC.

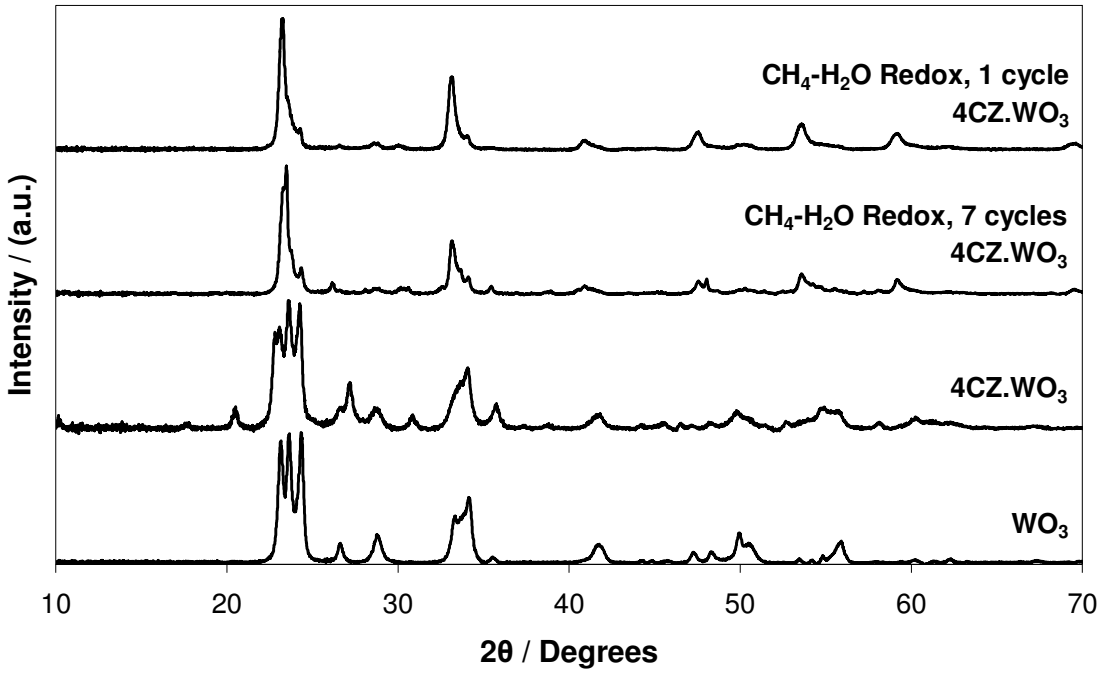

Figure 7.17 XRD analysis of 4CZ.9WO_3 following CH_4-H_2O redox, with fresh 4CZ.9WO_3 and unpromoted WO_3

XPS surface analysis of H_2O re-oxidised 4CZ.9WO_3 (**Figure 7.18**) shows W 4f peaks assigned to W^{6+} doublet at a binding energy of 36.26. The presence of sub-stoichiometric tungsten oxide in the form of W^{5+} is also detected at binding energy of 34.51. Quantification of relative amounts of W^{6+} compared to W^{5+} shows approximately 3.3% W^{5+} as a proportion of all W oxidation states present.

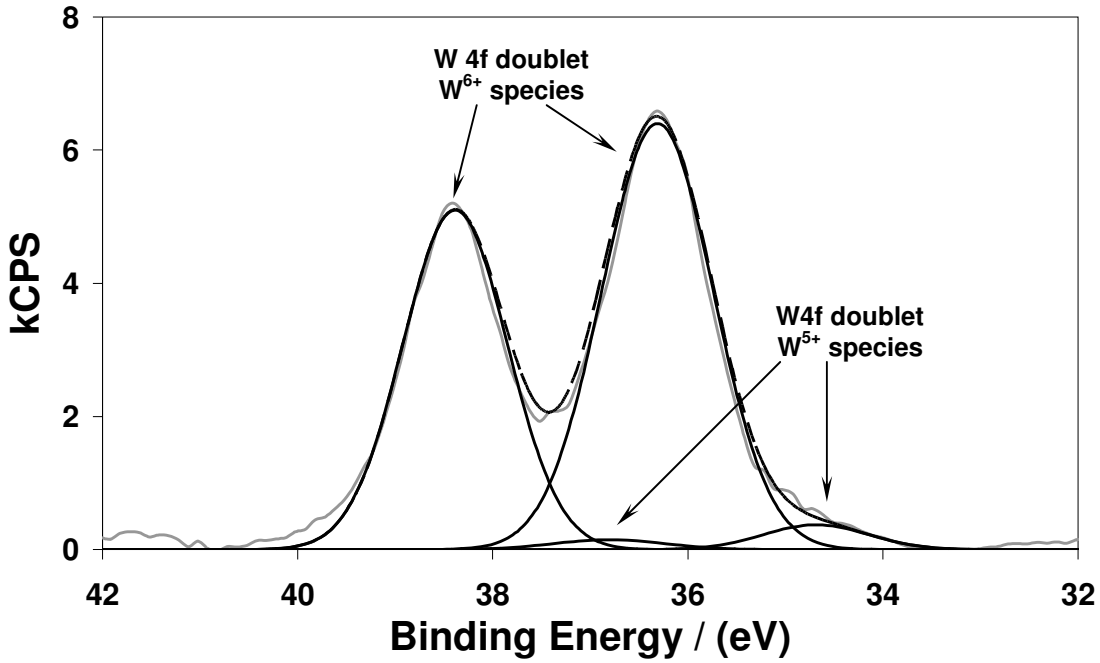

Figure 7.18 W 4f peaks from XPS spectra of re-oxidised 4CZ.9WO_3

Table 7-17 Measured XPS peaks and corresponding binding energies post-redox

Sample	Element	Binding Energy / eV	[AT] / %
4CZ.9WO_3 Re-oxidised State	O1s	533.63	2.41
	O1s	532.38	5.47
	O1s	531.18	42.75
	W 4f	36.26	14.55
	W 4f	34.51	0.50
	Ce 3d	886.69	0.31
	Ce 3d	882.36	0.14

Following CH_4-H_2O redox cycling of 4CZ.9WO_3, oxygen was passed over the sample to achieve complete re-oxidation. XRD spectra of this oxidised sample shows a monoclinic WO_3 phase comparable to the fresh sample, indicating that it is the oxidizing ability of H_2O which affects complete re-oxidation (**Figure 7.19**).

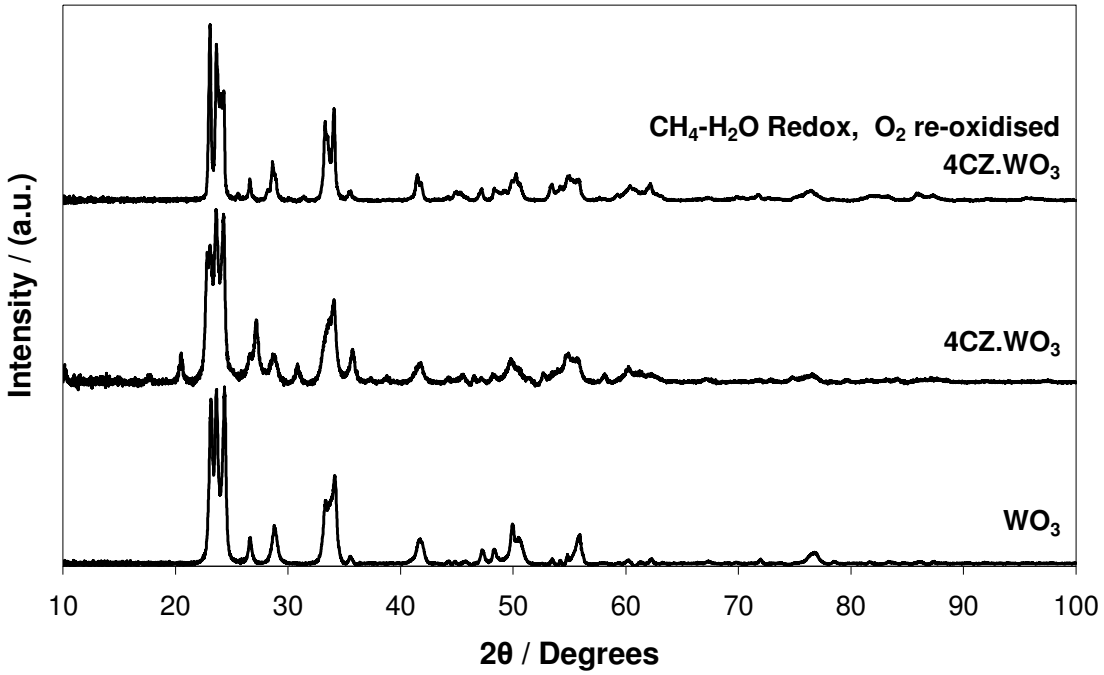

Figure 7.19 XRD analysis of O_2 oxidation of 4CZ.9WO_3 following CH_4-H_2O redox, with fresh 4CZ.9WO_3 and unpromoted WO_3

7.4.3 Optimised CH_4-H_2O Redox Cycling of 4CZ.9WO_3

Following selection of optimal reduction and re-oxidation parameters, sample redox was repeated twenty times to determine cyclic stability and hydrogen production potential with multiple cycles (**Table 7-18**). Rate of reduction and total time taken for reduction to stabilise did not have an influence upon rate of re-oxidation or total hydrogen production. Total hydrogen production remained relatively consistent throughout the 20 cycles, with only 6% difference in H_2 production potential between the first and last cycle, and an overall fluctuation of up to 18% in final H_2 production over all cycles.

Table 7-18 H_2 production from H_2O re-oxidation of 4CZ.9WO_3 (0.2g) over 20 cycles

Cycle	Reduction	Re-oxidation		
	Time / min	H_2 Production ($x10^{-4}$) / moles Stoichiometric	H_2 Production ($x10^{-4}$) / moles Experimental	Time / min
1	180	7.47	7.5	17.4
2	127		6.14	23.1
3	137		7.61	20.1
4	129		7.29	18.8
5	89		7.19	19.9
6	87		6.8	19.5
7	81		6.2	23.2
8	89		7.12	19
9	80		7.22	23.6
10	87		7.26	20.6
11	97		7	24
12	97		6.2	20.5
13	95		7.12	19
14	100		7.23	19.4
15	101		7.4	20.3
16	103		6.91	20.3
17	101		7.6	17.2
18	96		7.25	17.5
19	100		7.25	18.1
20	95		7.16	15.7

[a] Values determined following reduction by CH_4, re-oxidation by H_2O at 750ºC

The relatively low hydrogen production for a number of cycles may indicate that experimental hydrogen production is less than stoichiometric calculations. Given the formation of the final phase of $4CZ.9WO_3$ as a sub-stoichiometric tungsten oxide comprised of $WO_{2.9}$ (**Figure 7.17**), it is likely that hydrogen production would be less than that of complete re-oxidation calculations predict for WO_2 to WO_3 re-oxidation. This would give a value of 6.80×10^{-4} moles H_2 production from re-oxidation of partially reduced $4CZ.9WO_3$. Therefore, it is presumed that the final tungsten oxide phase is a mixture of multiple oxidation states.

Final surface area of samples cycled for various lengths is shown **Table 7-19**. Following operation for 20 cycles at 750ºC under constant redox, $4CZ.9WO_3$ retains relatively high surface area, which accounts for the high levels of hydrogen production throughout the 20 cycles. In comparison, surface area of unpromoted tungsten oxide is measured at 19.1 m^2/g which is not significantly greater than 13.1 m^2/g measured for $4CZ.9WO_3$ after 20 redox cycles. CZ promoted Fe_2O_3 also shows reasonable surface area retention however, the higher melting point of tungsten oxide aids to maintain much higher relative surface area in comparison to Fe_2O_3, irregardless of CZ promotion. Unpromoted Fe_2O_3 shows surface area of <1 m^2/g after only 3 redox cycles at much lower cycling temperature (550ºC) (**Table 5-2**, **Table 5-10**).

Table 7-19 Measured surface area of samples post-redox

Sample	Number of Cycles	BET_{SA}[a] / (m^2/g)
$4CZ.9WO_3$	0	47.6
$4CZ.9WO_3$	1	40.0
$4CZ.9WO_3$	5	30.2
$4CZ.9WO_3$	10	23.3
$4CZ.9WO_3$	20	13.1

[a] Values determined following reduction by CH_4, re-oxidation by H_2O at 750ºC

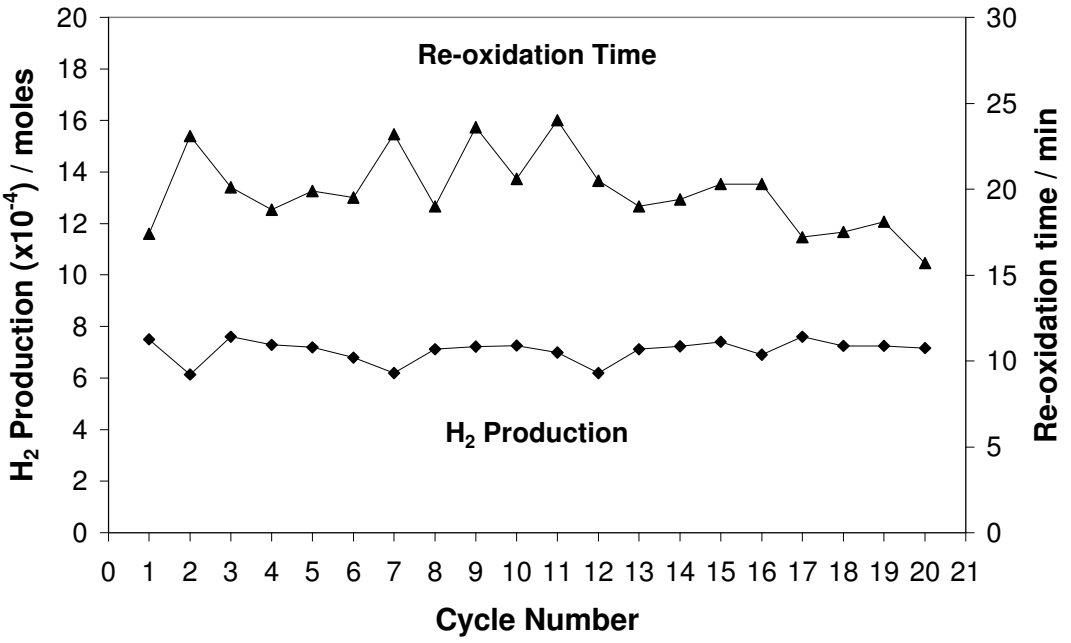

Figure 7.20 Variation in H_2 production and re-oxidation time from H_2O re-oxidation of 4CZ.9WO_3 (0.2g) over 20 cycles

Figure 7.20 shows hydrogen production and time of hydrogen production with minimal variation, as surface area decreases over twenty cycles (**Table 7-19**). Surface area remains independent of both hydrogen production and re-oxidation kinetics, as a progressive decrease in hydrogen production and increase in re-oxidation time would be expected from the first to last cycle due to sintering effects. Kodama et. al. show similar behaviour with CH_4-H_2O redox of ZrO_2 promoted WO_3 under similar experimental conditions [3], however this behaviour is only reported over five cycles, therefore it is difficult to establish whether a different trend might emerge upon further cycling. Subsequent surface areas are not reported which would give further insight toward surface area from the first and last cycles. Balducci et. al. report unusual behaviour of CeO_2-ZrO_2 solid solutions following numerous redox cycles, in which improved reduction behaviour is observed despite sintering effects [22]. In this case, availability of active sites is not considered to be a rate limiting step in the redox of 4CZ.WO_3.

7.5 Conclusions

1. Addition of CeO_2/ZrO_2 increases stability of WO_3, giving higher surface area and a structure predominantly based upon monoclinic WO_3.
2. Precise loading of 31mol% CZ / 69 mol% WO_3 ($4CZ.9WO_3$) allows for stabilisation of WO_3 to form WO_2 when reduced by methane, as compared to unpromoted WO_3, which forms WC.
3. Optimal operating conditions for this process were found to be 50% CH_4 at a flow rate of 60mL / min for reduction, and 46.8% H_2O saturation in He/Ar at a flow rate of 120 mL / min for oxidation. Both reduction and oxidation were performed at a temperature of 750ºC.
4. $4CZ.9WO_3$ shows no evidence of methane decomposition or tungsten carbide formation upon reduction, with re-oxidation producing comparable amount of clean hydrogen up to 20 cycles.

Reduction of unpromoted WO_3 by methane results in tungsten carbide formation upon complete reduction to W. This carbide formation proceeds by decomposition of methane over W. Hydrogen produced upon H_2O re-oxidation of this species is subsequently contaminated by co-production of CO_x.

Use of CeO_2/ZrO_2 as a promoter allows for stabilisation of partially reduced $4CZ.9WO_3$ to form WO_2, thereby limiting formation of W and enabling reproducible clean hydrogen production. Addition of CeO_2/ZrO_2 also aids to impede WO_3 deactivation by maintaining higher surface area over time at high temperature. By limiting further reduction of WO_2 sintering is also prevented, which otherwise take would place by way of W metal nucleation.

7.6 References

1. T. Kodama, et al., 'Thermochemical methane reforming using a reactive WO_3/W redox system', *Energy* **2000**, 25(5), 411-425
2. T. Shimizu, et al., 'Thermochemical methane reforming using WO_3 as an oxidant below 1173 K by a solar furnace simulator', *Solar Energy* **2001**, 71(5), 315-324
3. T. Kodama, et al., 'Stepwise production of CO-rich syngas and hydrogen via methane reforming by a WO_3-redox catalyst', *Energy* **2003**, 28(11), 1055-1068
4. E. Iglesia, et al., 'Synthesis, characterisation, and catalytic properties of clean and oxygen-modified tungsten carbides', *Catalysis Today* **1992**, 15(2), 307-337
5. J.M. Giraudon, et al., 'Synthesis of Tungsten Carbides by Temperature-Programmed Reaction with CH_4-H_2 Mixtures. Influence of the CH_4 and Hydrogen Content in the Carburizing Mixture', *Journal of Solid State Chemistry* **2000**, 154(2), 412-426
6. M. Yoshimura, T. Sata, and T. Nakamura, 'Preparation of Cerium-Tungsten Binary Oxides', *Nippon Kagaku Kai-shi (Journal of the Chemical Society of Japan)* **1973**, (12), 2287-2294
7. M. Yoshimura, et al., 'Identification of binary compounds in the system Ce_2O_3-WO_3', *Journal of Solid State Chemistry* **1976**, 16(3-4), 219-232
8. M.A. Cortés-Jácome, J.A. Toledo-Antonio, H. Armendáriz, I. Hernández, X. Bokhimi, 'Solid Solutions of WO_3 into Zirconia in WO_3-ZrO_2 Catalysts', *Journal of Solid State Chemistry*, **2002** 164, 339-344
9. H. Armendáriz, M.A. Cortés, I. Hernández, J. Navarrete, A. Vázquez, 'One-step synthesis and characterisation of ZrO_2-WO_x prepared by hydrothermal method at autogenous pressure', *Journal of Materials Chemistry*, **2003**, 13, 143-149
10. I. Szilágyi, et al., 'Partial thermal reduction of ammonium paratungstate tetrahydrate', *Journal of Thermal Analysis and Calorimetry* **2007**, 88(1), 139-144
11. N.E. Fouad, K.M.E. Attyia, and M.I. Zaki, 'Thermogravimetry of WO_3 reduction in hydrogen: Kinetic characterisation of autocatalytic effects', *Powder Technology* **1993**, 74(1), 31-37

12. F.F.P. Medeiros, S.A. De Oliveira, C.P. De Souza, A.G.P. Da Silva, U.U. Gomes, J.F. De Souza 'Synthesis of tungsten carbide through gas–solid reaction at low temperatures', *Materials Science and Engineering*, **2001** A315, 58-62

13. K. Madhav Reddy, T.N. Rao, K. Radha, J. Joardar, 'Nanostructured tungsten carbides by thermochemical processing', *Journal of Alloys and Compounds*, **2010** 494, 404-409

14. M. Valigi, D. Gazzoli, I. Pettiti, G. Mattei, S. Colonna, S. De Rossi, G. Ferraris, 'WO_x/ZrO_2 catalysts Part 1. Preparation, bulk and surface characterisation', *Applied Catalysis A: General* **2002**, 231, 159-172

15. M.M. Natile, F. Tomaello, A. Glisenti, 'WO_3/CeO_2 Nanocomposite Powders: Synthesis, Characterisation, and Reactivity', *Chemistry of Materials* **2006**, 18, 3270-3280

16. M.M. Natile, A.Glisenti, 'WO_3/CeO_2/YSZ nanocomposite as a potential catalyst for methanol reforming', *Journal of Power Sources* **2005**, 145 644-651

17. P. Biloen and G.T. Pott, 'X-Ray Photoelectron Spectroscopy Study of Supported Tungsten Oxide', *Journal of Catalysis*, **1973** 30(2), 169-174

18. B.A. De Angelis and M. Schiavello, 'X-ray photoelectron spectroscopy study of nonstoichiometric tungsten oxides', *Journal of Solid State Chemistry* **1977**, 21(1), 67-72

19. S. Penner, et al., 'The structure and composition of oxidised and reduced tungsten oxide thin films', *Thin Solid Films* **2008**, 516(10), 2829-2836

20. H.-J. Lunk, et al., 'What is Behind 'Tungsten Blue Oxides'?' *Refractory Metals & Hard Materials* **1993-1994**, 12, 17-26

21. E. Lassner and W. Schubert, 'Tungsten Blue Oxide', *International Journal of Refractory Metals & Hard Materials* **1995**, 13(1-3), 111-117

22. G. Balducci, P. Fornasiero, R. Di Monte, J. Kaspar, S. Meriani, M. Graziani, 'An unusual promotion of the redox behaviour of CeO_2-ZrO_2 solid solutions upon sintering at high temperatures', *Catalysis Letters*, **1995** 33, 193-200

KINETIC STUDY OF CERIA-ZIRCONIA PROMOTED TUNGSTEN OXIDE FOR THE STEAM-METAL PROCESS

8.1 Introduction

This kinetic study was designed to gain a better understanding of the influence of reaction conditions during the oxidation and reduction reactions on promoted tungsten oxide and to gain a greater understanding of the reaction mechanism and how it best fits with existing kinetic models. The kinetics of reduction and re-oxidation are taken into consideration, with each treated as an individual process.

Literature pertaining to the kinetics of the reduction phase in the Steam-Iron Process is primarily focused on iron oxide reduction [1-4] and to some extent, on the kinetics of zinc oxide reduction [5, 6]. There is some discrepancy between proposed kinetic models for reduction of iron oxide but there is agreement that the kinetics of Fe_2O_3 to Fe_3O_4 reduction differs from the kinetics of Fe_3O_4 to FeO/Fe reduction. A limited amount of literature can be found pertaining to the reduction kinetics of promoted iron oxide [2, 7]. Due to the multi-step reduction mechanism of a number of metal oxides (Fe_2O_3, WO_3) reduction kinetics are to be obtained via a non-isothermal TPR method.

Knowledge of the kinetics of oxidation of reduced metal oxides by steam in the Steam-Iron Process is fairly limited with discrepancy between various studies [8-10]. Oxidation kinetics can possibly be derived from Chemical Looping Combustion data, which is comparable to the Steam-Metal Process [11, 12]. Re-oxidation proceeds as a rapid single step process, with oxidation kinetics calculated by isothermal oxidation methods.

This chapter investigates the kinetics of CeO_2/ZrO_2 promoted WO_3 (4CZ.9WO_3) during both reduction and re-oxidation.

8.2 Experimental

8.2.1 Metal Oxide Preparation

Ceria-zirconia promoted tungsten oxide samples and unpromoted tungsten oxide samples were prepared by the method of urea hydrolysis, as described in **Chapter 4** (Experimental Methodology). Ceria-zirconia was added to tungsten trioxide at a concentration of 31mol%, with the concentration of tungsten trioxide adjusted accordingly. This ceria-zirconia promoted tungsten oxide sample is hereby referred to as 4CZ.9WO_3. The ratio of CeO_2 to ZrO_2 was maintained at 1:1, with [CeO_2-ZrO_2] (hereby designated as CZ) equivalent to a single mole of CeO_2 alone.

8.2.2 Reduction Kinetics - Temperature Programmed Reduction (TPR)

An outline of experimental apparatus used for TPR analysis can be found in **Chapter 4** (Experimental Methodology). Initially the sample was heated up to 150ºC under a flow of He and held until no further change in the outgoing H_2O signal was observed.

The following experimental conditions were employed:

- Flow rate: 30mL/min
- Incoming gas mixture: 5 vol%H_2-95 vol% (1%Ar in He)
- Catalyst loading: 0.05g
- Temperature ramping rate: 150-1000ºC at 3, 4 and 5ºC/min
- Reactor Pressure: 1 atm

Both unpromoted WO_3 and 4CZ.9WO_3 were tested for comparison, using a particle size of 150 – 250 μm. Apparent activation energy was determined by variation of the ramping rate of TPR measurements.

With many metal oxides reducing through a series of oxidation phases before being completely reduced, it is necessary to determine the reduction mechanism for each of these phases. As a result, the kinetics of metal oxide reduction processes can be determined by thermo-analytical means such as temperature programmed reduction (TPR), which is an important characterisation technique for determining the reducibility of metal oxides [7, 13, 14]. The technique of TPR allows for the observation of various oxidation phases during the reduction of a given metal oxide.

The general kinetic rate equation applied to the reduction process is as follows:

$$r = \frac{d\alpha}{dt} = k(T) \cdot f(\alpha) \cdot f'(P_{H2}, P_{H2O}) \qquad \textbf{8.1}$$

where α is the degree of conversion of oxygen within the metal oxide and *k(T)* is the temperature dependent rate co-efficient which can be expressed via the Arrhenius Equation. *f(α)* represents the dependence of reduction kinetics upon the degree of solid conversion, whilst $f(P_{H2}, P_{H2O})$ represents the dependence of reduction kinetics upon the concentrations of H_2 and H_2O in the gas phase. The term *k(T)* can be represented by the equation:

$$k(T) = A \cdot e^{(-E_a / RT)} \qquad \textbf{8.2}$$

where *A* is the pre-exponential factor, E_a is apparent activation energy and *R* is the ideal gas constant (8.314 $Jmol^{-1}K^{-1}$).
For a constant heating rate, the term for temperature change can be expressed as:

$$dT = \phi \cdot dt \qquad \textbf{8.3}$$

where ϕ is temperature ramping rate. Combining **Equations 8.1** to **8.3** gives:

$$r = \frac{d\alpha}{dT} = \frac{A}{\phi} \cdot e^{(-E_a/RT)} \cdot f(\alpha) \cdot f'(P_{H2}, P_{H2O}) \qquad \textbf{8.4}$$

Under differential conditions, the term $f'(P_{H2}, P_{H2O})$ can be approximated as a constant [14], reducing **Equation 8.4** to the form:

$$r = \frac{d\alpha}{dT} = \frac{A'}{\phi} \cdot e^{(-E_a/RT)} \cdot f(\alpha) \qquad \textbf{8.5}$$

By integration of **Equation 8.5**, a theoretical TPR profile can be obtained and compared to experimental results to assign an appropriate kinetic model to individual reduction peaks.

$$\int_0^\alpha \frac{d\alpha}{f(\alpha)} = g(\alpha) = \frac{A'}{\phi} \cdot \int_{T_0}^{T} e^{(-E_a/RT)} \cdot dT \qquad \textbf{8.6}$$

Reduction models can be classified into three categories which include phase boundary controlled processes, diffusion controlled processes, and random nucleation (**Table 8-1**) [7, 13, 14]. The phase boundary controlled mechanism is also defined as the shrinking core model, with the chemical reaction process as the rate-determining step. In a diffusion-controlled process, the rate of reaction is controlled by the movement of reactant species to or a product from a reaction interface inside the material. Nucleation-controlled processes proceed by internal reduction and removal of lattice oxygen atoms. When a critical concentration of vacancies is reached, rearrangement of the lattice takes place to eliminate these vacancies and form metal nuclei. Nuclei growth and expansion gives rise to an increase in the reduction process due to the increasing metal–metal oxide interface. When the sample-product interface decreases, so does the reduction process.

Table 8-1 Common controlling mechanisms for solid-state reactions [7, 13, 14]

Model	f(α)	g(α)
Unimolecular Decay[a]	$(1-\alpha)$	$-\ln(1-\alpha)$
2D Phase Boundary[a]	$(1-\alpha)^{1/2}$	$2(1-(1-\alpha)^{1/2})$
3D Phase Boundary[a]	$(1-\alpha)^{1/3}$	$3(1-(1-\alpha)^{1/3})$
1D Nucleation Avrami-Erofeyev	$2(1-\alpha)(-\ln(1-\alpha))^{1/2}$	$(-\ln(1-\alpha))^{1/2}$
2D Nucleation Avrami-Erofeyev	$3(1-\alpha)(-\ln(1-\alpha))^{2/3}$	$(-\ln(1-\alpha))^{1/3}$
3D Nucleation Avrami-Erofeyev	$4(1-\alpha)(-\ln(1-\alpha))^{3/4}$	$(-\ln(1-\alpha))^{1/4}$
One-Dimensional Diffusion	$\frac{1}{2\alpha}$	α^2
Two-Dimensional Diffusion	$-\ln(1-\alpha)-1$	$(1-\alpha)\ln(1-\alpha)+\alpha$
Three-Dimensional Diffusion (Jander)	$\frac{3(1-\alpha)^{2/3}}{2(1-(1-\alpha)^{1/3}))}$	$(1-(1-\alpha)^{1/3})^2$

[a] The phase boundary controlled mechanism is also defined as the shrinking core model, with chemical reaction as the rate-determining step [14].

A method for calculating apparent activation energy from reduction data has been proposed by Kissinger [15], calculated by shifts in peak temperature, T_{MAX}, with changing heating rate, ϕ. At the maximum of the TPR peak, the following equation can be applied:

$$\left[\frac{d}{dT}\left(\frac{d\alpha}{dT}\right)\right]_{T=T_{MAX}} = 0 \qquad \textbf{8.7}$$

whereupon, combining **Equation 8.5** with **Equation 8.7** gives:

$$\left[\frac{d}{dT}\left(\frac{A'}{\phi}\cdot e^{(-Ea/RT)}\cdot f(\alpha)\right)\right]_{T=T_{MAX}} = 0 \qquad \textbf{8.8}$$

forming:

$$\left(\frac{d\alpha}{dT}\right)_{T=T_{MAX}}\left[\frac{E_a}{RT^2{}_{MAX}}+\left(\frac{df(\alpha)}{d\alpha}\right)_{T=T_{MAX}}\left(\frac{A'}{\phi}\cdot e^{(-E_a/RT_{MAX})}\right)\right]=0 \qquad \textbf{8.9}$$

Equation 8.9 can be reduced to **Equation 8.10** by way of the fact that $\left(\frac{d\alpha}{dT}\right)_{T=T_{MAX}} \neq 0$:

$$\frac{\phi E_a}{A'RT^2{}_{MAX}}=-e^{(-E_a/RT_{MAX})}\left(\frac{df(\alpha)}{d\alpha}\right)_{T=T_{MAX}} \qquad \textbf{8.10}$$

which further reduces to:

$$\ln\left(\frac{\phi}{T^2{}_{MAX}}\right)+\ln\left(\frac{E_a}{A'R}\right)=\frac{-E_a}{RT_{MAX}}+\ln\left(-\frac{df(\alpha)}{d\alpha}\right)_{T=T_{MAX}} \qquad \textbf{8.11}$$

$f(\alpha)$ and $\alpha_{T=T_{MAX}}$ remain independent of heating rate, allowing for **Equation 8.11** to be expressed as:

$$\ln\left(\frac{\phi}{T^2{}_{MAX}}\right)=\frac{-E_a}{RT_{MAX}}+\ln\left(\frac{A'R}{E_a}\right)+C \qquad \textbf{8.12}$$

By plotting $\ln\left(\frac{\phi}{T^2{}_{MAX}}\right)$ vs. $\frac{1}{T_{MAX}}$ at various heating rates, an Arrhenius plot can be obtained, in which the slope of the curve is defined as $\left(\frac{-E_a}{R}\right)$ from which an apparent activation energy, E_a, can be calculated [14].

8.2.3 Oxidation Kinetics

An outline of experimental apparatus used for oxidation kinetics studies can be found in **Chapter 4** (Experimental Methodology). Initially the sample was heated up to 150ºC under a flow of He and held until no further change in the outgoing H_2O signal was observed. Reactor pressure was maintained at a constant 1 atm. 4CZ.9WO_3 was tested at a particle size of 150 – 250 μm. Particle size less than 150 μm was also tested to determine the effect of particle size upon re-oxidation time.

The reaction order with respect to H_2O was obtained by varying flow rates at 30, 60 and 120 mL/min, with the H_2O concentration varied at 19.8 vol%, 30.9 vol% and 46.8 vol% in the gas mixture. H_2O was introduced into the reactor by a flow of 1 vol% Ar in N_2 through a water saturator, with the temperature of the water saturator used to alter H_2O concentration. The apparent activation energy was determined by varying oxidation temperature at 700, 750 and 800ºC whilst maintaining flow rate and incoming H_2O concentration as constants.

In all oxidation kinetics experiments, reduction was achieved using methane as the reductant between each oxidation cycle, as outlined in **Table 8-2**. The following experimental conditions were employed for all samples during oxidation studies:

Table 8-2. Reaction conditions for redox analysis of promoted tungsten oxide (Redox cycling)

Reductant	**Incoming gas mixture**	**Metal Oxide Loading / g**	**Flow Rate / mL/min**	**Temperature of reduction**
CH_4	50 vol% CH_4 - 13.3 vol% (1% Ar in He) - 36.7 vol% He	0.19 - 0.2	60	750ºC
Oxidant	**Incoming gas mixture**	**Metal Oxide Loading / g**	**Flow Rate / mL/min**	**Temperature of oxidation**
H_2O	19.8-46.8 vol% H_2O - 80.2-53.2 vol% (1% Ar in N_2)	0.19 - 0.2	30 - 120	700-800ºC

8.3 Results and Discussion

8.3.1 Reduction Kinetics

The TPR of unpromoted WO_3 (**Figure 8.1**) at various ramping rates was compared with that of 4CZ.9WO_3 (**Figure 8.2**). TPR of unpromoted WO_3 shows four distinct peaks, assigned to reduction steps following $WO_3 \rightarrow WO_{2.9} \rightarrow WO_{2.72} \rightarrow WO_2 \rightarrow W$. At lower ramping rate, the reduction profile of WO_3 shows less separation between the second and third reduction peaks ($WO_{2.9} \rightarrow WO_{2.72} \rightarrow WO_2$). With increasing ramping rate, the separation between the second and third reduction peaks becomes more prominent. In contrast, reduction of 4CZ.9WO_3 shows only two major peaks consistent with direct $WO_3/WO_{2.9} \rightarrow WO_2$ reduction, with no intermediate $WO_{2.9} \rightarrow WO_{2.72} \rightarrow WO_2$ reduction, followed by $WO_2 \rightarrow W$. The initial peak in the 4CZ.9WO_3 reduction profile is not easily resolved, and is observed as a broad shoulder which may be defined as a combination of both $WO_3 \rightarrow WO_{2.9}$ with $2(CeO_2/ZrO_2)$ to $Ce_2O_3/2ZrO_2$ reduction. Both unpromoted WO_3 and 4CZ.9WO_3 show increasing peak temperature, T_{MAX}, with increasing ramping rate.

The choice of minimal increase in temperature ramping rate arises from the equation $P = \beta S_0/FC_0$, where β = Ramping rate (ºC/min), S_0 = Amount of reducible species (mg), and $F.C_0$ = Hydrogen flow rate ($cm^3.H_2$/min). Based upon this equation, it is desired to minimise the value of P [16]. With higher ramping rates, peak resolution is decreased due to rapid temperature increase overrunning peak temperatures, and in addition, peak distortion may arise. The shift in T_{MAX} is sufficiently spaced and reproducible to give accurate results.

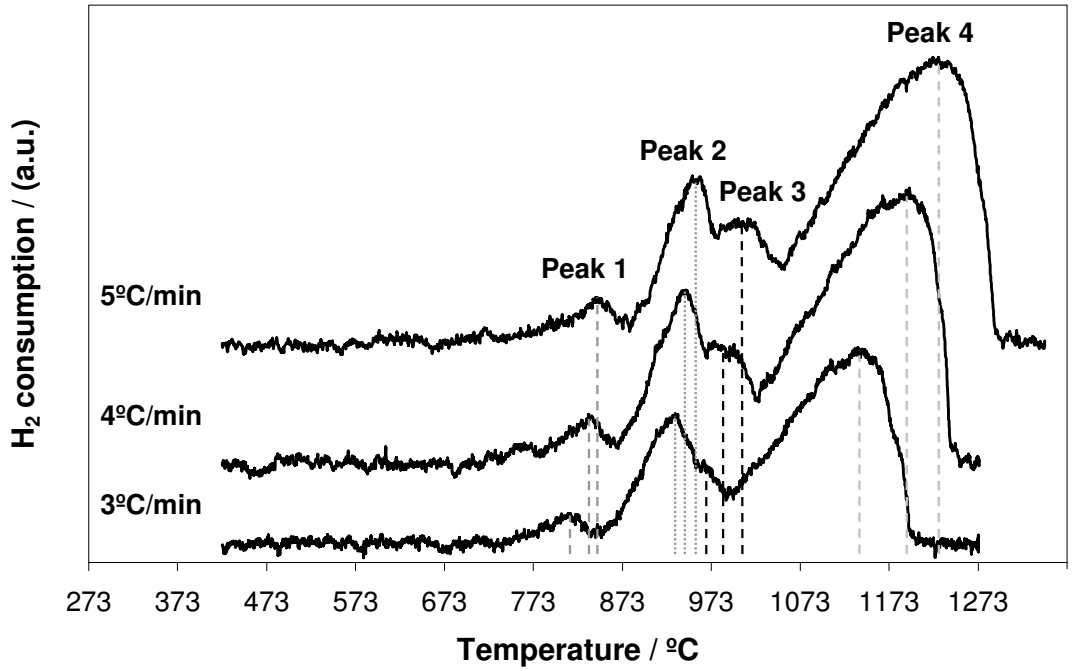

Figure 8.1 5% H_2 TPR of unpromoted WO_3 at various ramping rates, up to 1000ºC

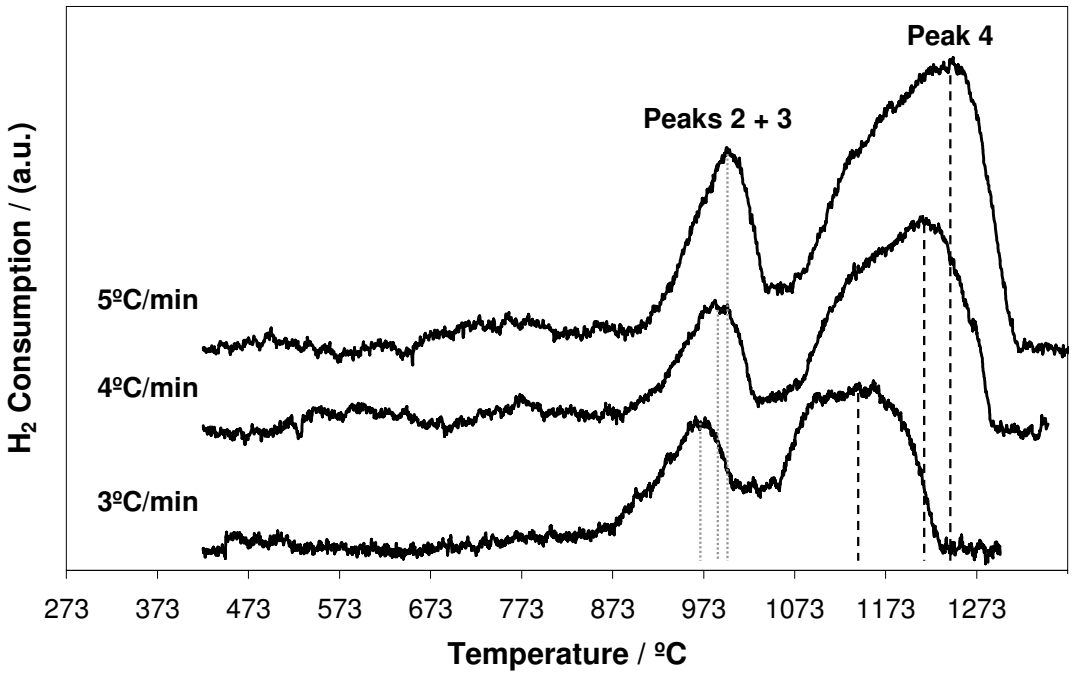

Figure 8.2 5% H_2 TPR of 4CZ.9WO_3 at various ramping rates, up to 1000ºC

Plotting [ln(ramping rate) / T_{MAX}^2] against T_{MAX}^{-1} gives Arrhenius plots of reduction peaks for unpromoted WO_3 (**Figure 8.3**) and 4CZ.9WO_3 (**Figure 8.4**) with the slope of the line equating to $\left(-\frac{E_a}{R}\right)$, where R = 8.314 $Jmol^{-1}K^{-1}$.

The fraction of total WO_3 or 4CZ.9WO_3 converted at each reduction peak is shown below (**Table 8-3**), as calculated via TGA (**Figure 7.11**, not shown). Apparent activation energies for oxidation states of unpromoted WO_3 are calculated, giving activation energies for reduction of WO_3, $WO_{2.9}$, $WO_{2.72}$ and WO_2 as 74 ± 1* kJ/mol, 189 ± 4* kJ/mol, 90 ± 1* kJ/mol and 52 ± 1* kJ/mol respectively (**Table 8-4**). 4CZ.9WO_3 shows an apparent activation energy for the reduction of WO_3/$WO_{2.9}$ → WO_2, hereby assigned as peak 2 + 3, (142 ± 3* kJ/mol, **Table 8-5**), to be less than the activation energy of reduction of $WO_{2.9}$ → $WO_{2.72}$ (189 ± 4* kJ/mol), peak 2, and reduction of $WO_{2.72}$ → WO_2 (90 ± 1* kJ/mol), peak 3, for unpromoted WO_3.

Table 8-3 Peak assignments of unpromoted WO_3 and 4CZ.9WO_3 TGA

	Oxidation State			
WO_3	$WO_3 \rightarrow WO_{2.9}$	$WO_{2.9} \rightarrow WO_{2.72}$	$WO_{2.72} \rightarrow WO_2$	$WO_2 \rightarrow W$
	% Mass Remaining / %			
Stoichiometric	99.31	98.07	93.10	79.30
Experimental	99.52	98.42	92.57	78.52
	Oxidation State			
4CZ.9WO_3	$WO_3 \rightarrow WO_{2.9}$	$WO_{2.9} \rightarrow WO_{2.72}$ $CeO_2/ZrO_2 \rightarrow ½CeO_2/ZrO_2$	$WO_{2.72} \rightarrow WO_2$	$WO_2 \rightarrow W$
	% Mass Remaining / %			
Stoichiometric	99.46	97.90	94.03	83.27
Experimental	99.52	97.75	92.50	79.33

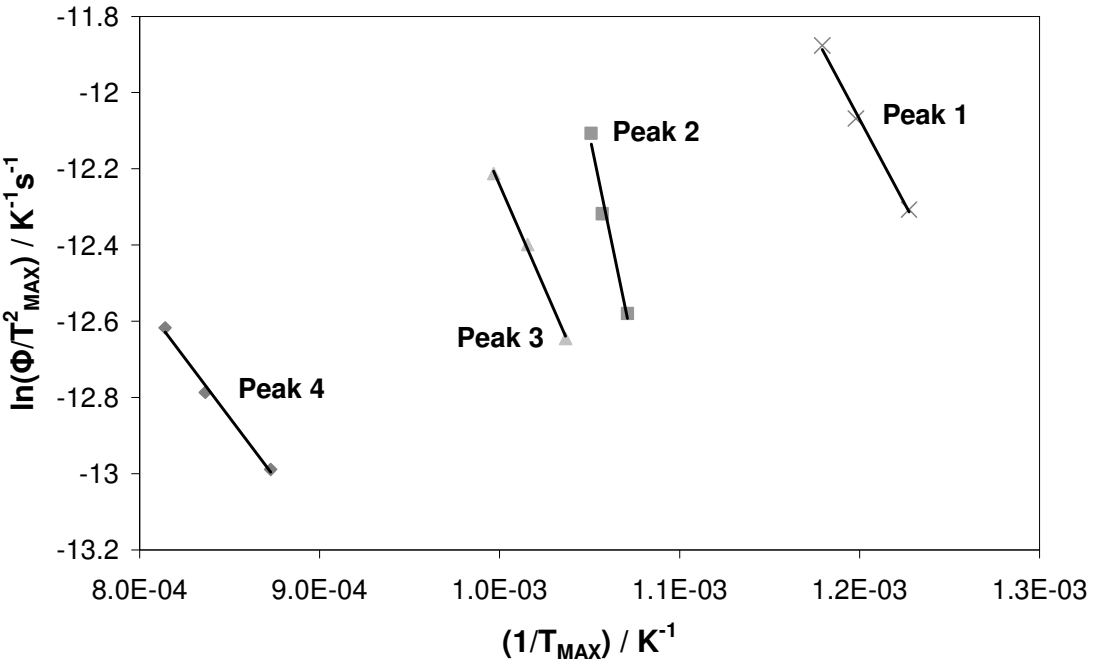

Figure 8.3 Arrhenius plots for unpromoted WO_3, with data obtained from Figure 8.1

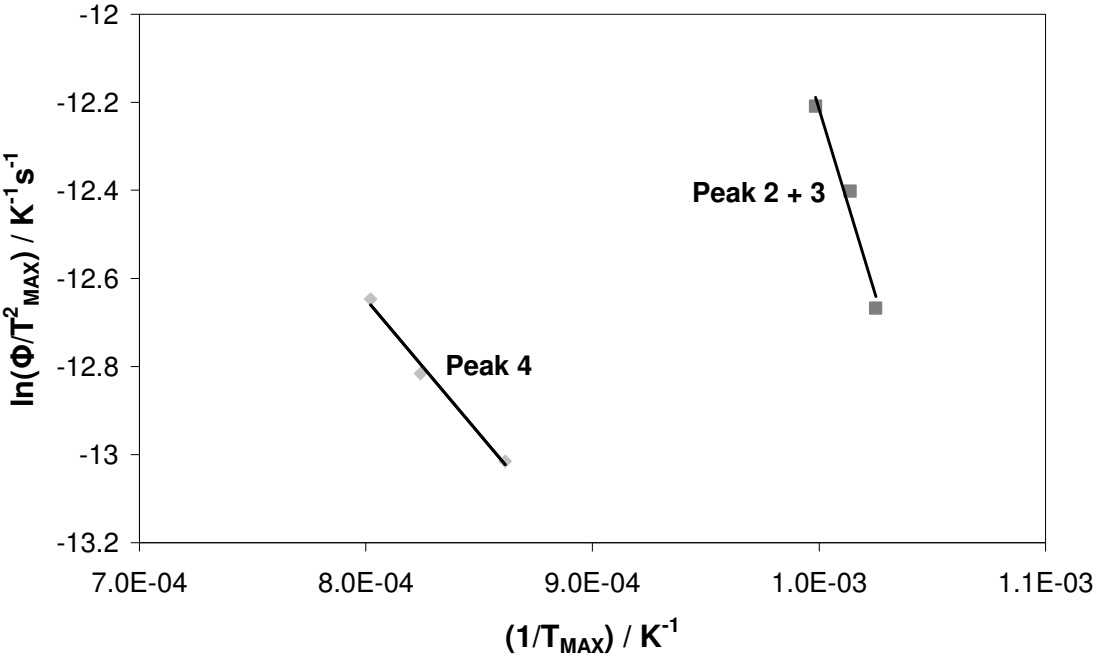

Figure 8.4 Arrhenius plots for 4CZ.9WO_3, with data obtained from Figure 8.2

Table 8-4 Peak temperature, T_{MAX}, at various ramping rates determined from 5% H_2 TPR of unpromoted WO_3 (Figure 8.1), with calculated apparent activation energies, E_a.

Ramping Rate / Ks^{-1}	Temperature, T_{MAX} / K			Apparent Activation Energy / (kJ/mol)
	3	4	5	
Peak 1 ($WO_3 \rightarrow WO_{2.9}$)	814.7	834.8	848.0	**74 ± 1***
Peak 2 ($WO_{2.9} \rightarrow WO_{2.72}$)	933.7	946.0	951.6	**189 ± 4***
Peak 3 ($WO_{2.72} \rightarrow WO_2$)	964.7	984.7	1003.3	**90 ± 1***
Peak 4 ($WO_2 \rightarrow W$)	1145.8	1195.6	1228.3	**52 ± 1***

Table 8-5 Peak temperature, T_{MAX}, at various ramping rates determined from 5% H_2 TPR of 4CZ.9WO_3 (Figure 8.2), with calculated apparent activation energy, E_a.

	Temperature, T_{MAX} / K			Apparent Activation Energy / (kJ/mol)
Ramping Rate / Ks^{-1}	3	4	5	
Peak 2 + 3 ($WO_{3/2.9} \rightarrow WO_2$)	975.6	986.5	1001.5	**142 ± 3***
Peak 4 ($WO_2 \rightarrow W$)	1160.8	1213.4	1246.7	**51 ± 1***

Based upon kinetic models from **Table 8-1**, theoretical TPR curves for 4CZ.9WO_3 reduction can be calculated by application of **Equation 8.6,** and fitted to experimental data to determine the kinetic model governing the reduction process. Experimental TPR profiles obtained at the lowest heating rate (3K/min) are preferable for comparison due to minimal instrumental peak broadening, and comparatively large sample size [17].

Theoretical TPR curves obtained from various models show for peak 2 + 3 reduction ($WO_3/WO_{2.9} \rightarrow WO_2$) of 4CZ.9$WO_3$, the 1D Phase Boundary / Unimolecular Decay model best describes reduction behaviour (**Figure 8.5, Table 8-6**). This equates to a total fraction of 5.4% conversion of 4CZ.9WO_3

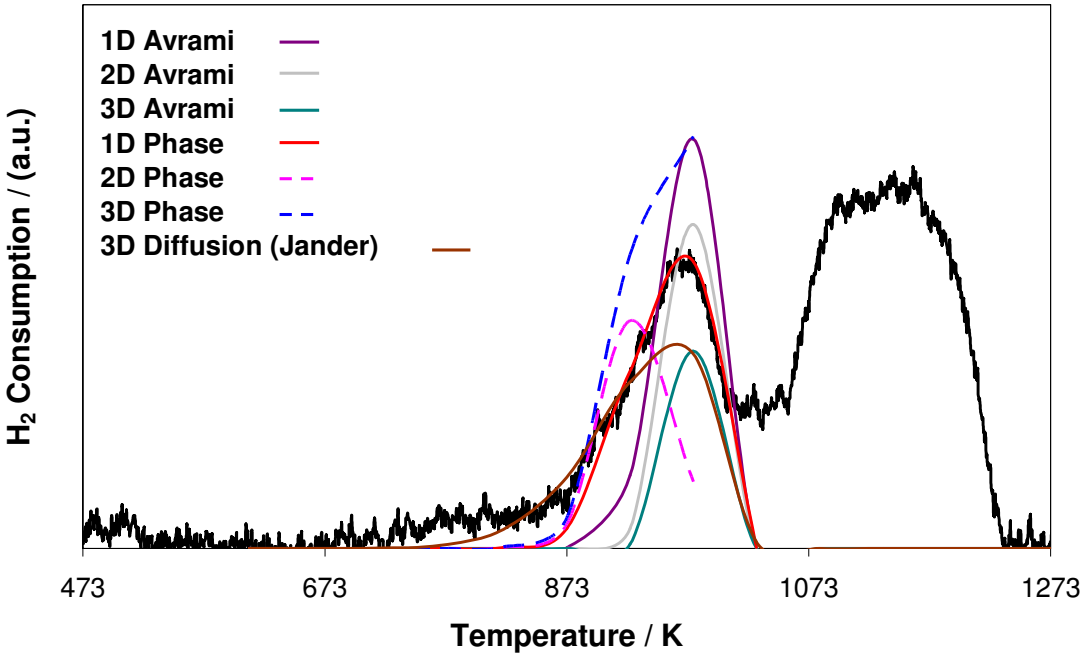

Figure 8.5 Comparison between experimental and calculated H_2 TPR curves based on various reduction mechanisms (Table 8-1) for peak 2 + 3 of 4CZ.9WO_3, heating rate 3K/min

Various models fit against experimental data for reduction of peak 4 of 4CZ.9WO_3 (WO_2 → W) indicate that the 3D Phase Boundary model provides a reasonably suitable fit for this peak (**Figure 8.6, Table 8-6**). This equates to a total of 16.14% conversion of total 4CZ.9WO_3.

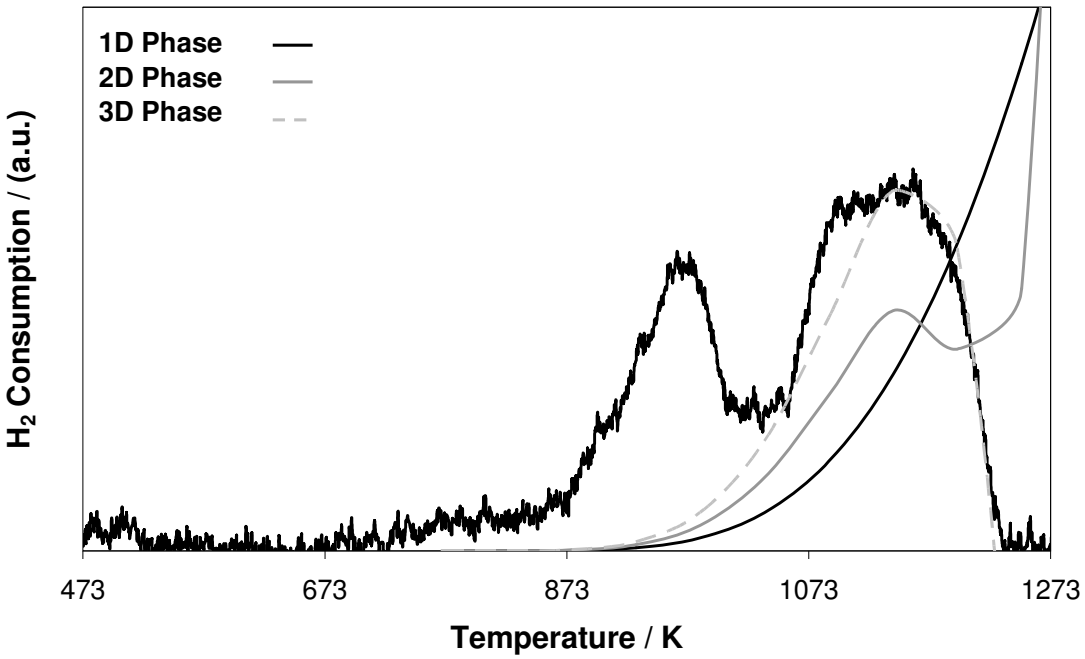

Figure 8.6 Comparison between experimental and calculated 5% H_2 TPR curves based on reduction mechanisms (Table 8-1) for peak 4 of 4CZ.9WO_3, heating rate 3K/min.

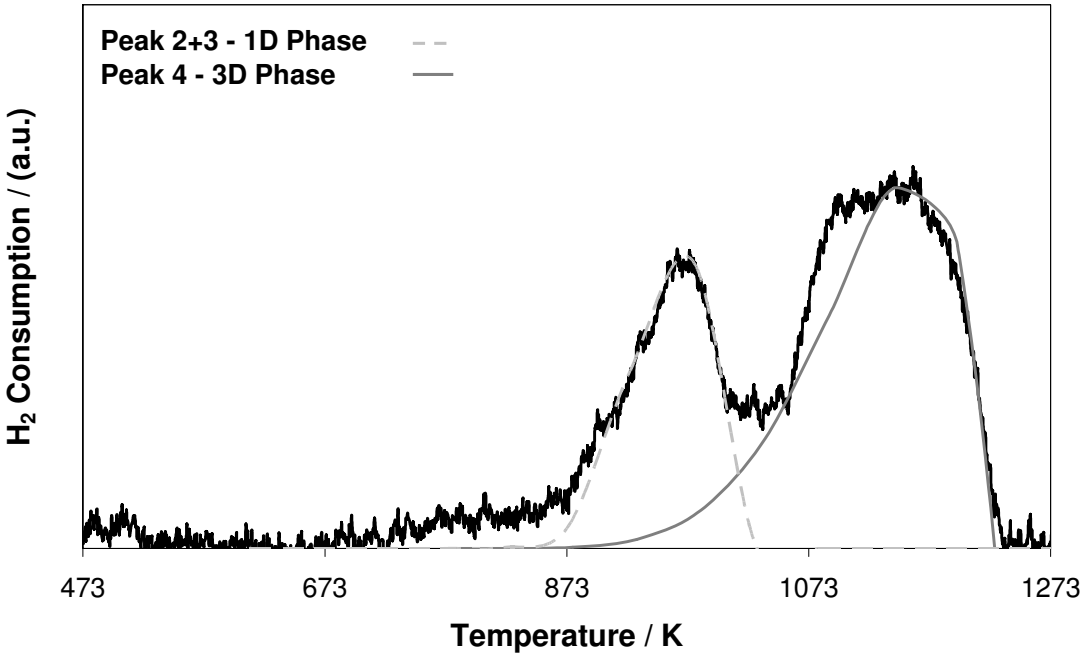

Figure 8.7 Overall peak fitted 5% H_2 TPR profile for 4CZ.9WO_3

Table 8-6 Reduction mechanisms and pre-exponential factor, A, for individual reduction steps, determined from H_2 TPR of 4CZ.9WO_3 (Figure 8.2)

	Reduction Mechanism	A / s^{-1}
Peak 2 ($WO_{3/2.9} \rightarrow WO_2$)	Unimolecular Decay	2.07 x 10^6
Peak 3 + 4 ($WO_2 \rightarrow W$)	3D Phase Boundary	7.84

Peak fitting of kinetic models to TPR of unpromoted WO_3 shows peak 1 to fit to a 1D Phase Boundary / Unimolecular Decay model, whilst peak 2 fits to the 3D Phase Boundary model (**Figure 8.8, Table 8-7**). At a ramping rate of 3K/min, peak 3 is unable to be resolved, and thus its reduction cannot be assigned. Peak 4 conforms to 3D Phase Boundary reduction kinetics.

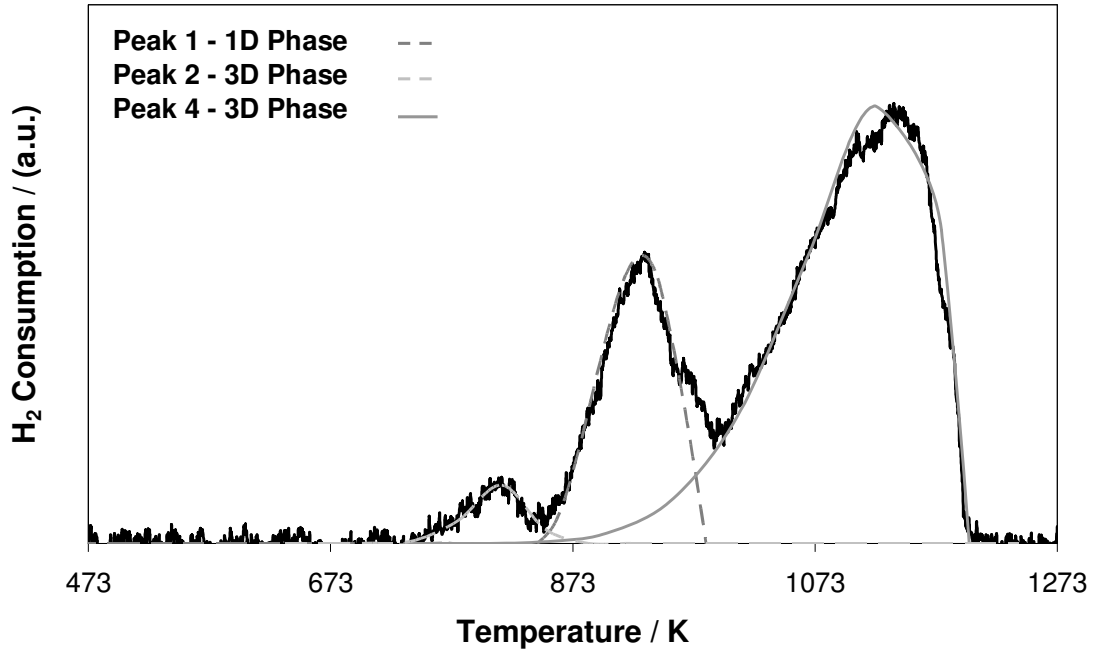

Figure 8.8 Comparison between experimental and calculated 5% H_2 TPR curves based on various reduction mechanisms (Table 8-1) for unpromoted WO_3, heating rate 3K/min.

Table 8-7 Reduction mechanisms and pre-exponential factor, A, for individual reduction steps, determined from 5% H_2 TPR of unpromoted WO_3 (Figure 8.1)

	Reduction Mechanism	A / s^{-1}
Peak 1 ($WO_3 \rightarrow WO_{2.9}$)	Unimolecular Decay	2108
Peak 2 ($WO_{2.9} \rightarrow WO_{2.72}$)	3D Phase Boundary	1.71×10^9
Peak 3 ($WO_{2.72} \rightarrow WO_2$)	--	**--**
Peak 4 ($WO_2 \rightarrow W$)	3D Phase Boundary	10.2

Addition of CeO_2/ZrO_2 shows a largely similar reduction mechanism, with the exception of 3D Phase Boundary reduction of unpromoted WO_3 in comparison to 1D Phase Boundary reduction of 4CZ.9WO_3 for the reduction step of importance ($WO_3/WO_{2.9} \rightarrow WO_2$). Reduction of $WO_2 \rightarrow W$ remains the same in both samples conform to the 3D Phase Boundary mechanism. Comparison between the reduction of unpromoted and promoted WO_3 shows the reduction of WO_3 to WO_2 is influenced with the inclusion of CeO_2/ZrO_2. However, the reduction mechanism remains the same as phase boundary or chemical reaction controlled reduction. The reduction kinetics of CeO_2/ZrO_2 in 4CZ.9WO_3 are unable to be calculated due to largely indiscernible peaks in the TPR profile.

By this method, it is possible to determine an approximation of the governing kinetics for each stage of metal oxide reduction. Although this does not exclude the possibility of other kinetic processes controlling the reduction reaction, the strong correlation between theoretical and experimentally plotted data does give weight to its selection.

8.3.2 Oxidation Kinetics

When determining the oxidation kinetics, it is first necessary to establish the controlling mechanism, allowing for a suitable rate equation to be derived [18]. Gas-solid reactions can be broadly classified into one of two models, those being the progressive conversion model and the unreacted core model. The former dictates that gas enters and reacts throughout the particle, progressively converting solid reactant. In the latter model, the incoming gas first reacts at the outer layer of the particle, before reacting inward toward the unreacted core following complete reaction of the outer layers. In this particular case, the oxidation of a metal oxide, the unreacted core model is known to be the closest approximation to oxidation behaviour.

The three main resistances which govern the unreacted core model are gas phase diffusion, ash layer diffusion and chemical reaction controlled. In gas phase diffusion the reaction is limited by the diffusion of reacting gas through the gas film created at the surface of the solid reactant. Ash layer diffusion is controlled by the diffusion of reacting gas through the ash layer, which is the reacted and inert solid surrounding the unreacted core. Chemical reaction control is unaffected by the surrounding ash layer, thus the reaction rate is dependent upon the available surface area of the unreacted core as the reaction proceeds.

The rate controlling step can be determined by dependence of reaction rate upon various factors including temperature, flow rate and reactant concentration. Diffusion controlled processes have a low dependence on temperature, whilst chemical reaction controlled processes are highly influenced by temperature change (**Figure 8.9**) [18]. **Figure 8.10** shows theoretical conversion of solid reactant with various rate controlling mechanisms. Comparison of experimental results (**Figure 8.11**) with theoretical plots is consistent with a chemical reaction controlling mechanism.

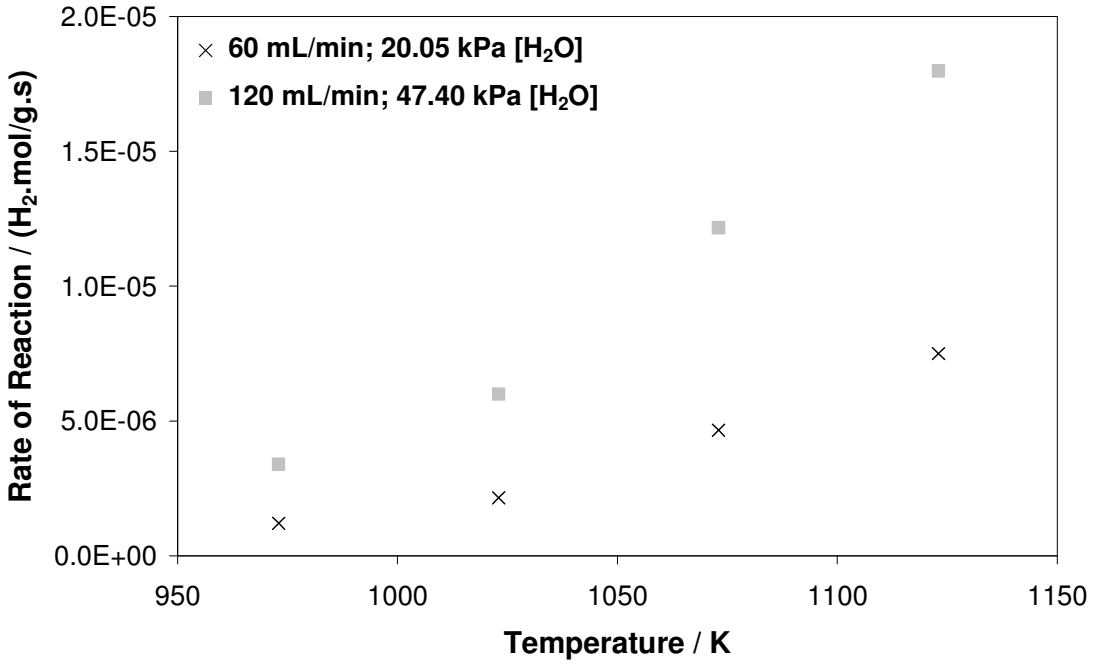

Figure 8.9 Dependence of reaction rate upon temperature at various flow rates and H_2O partial pressures

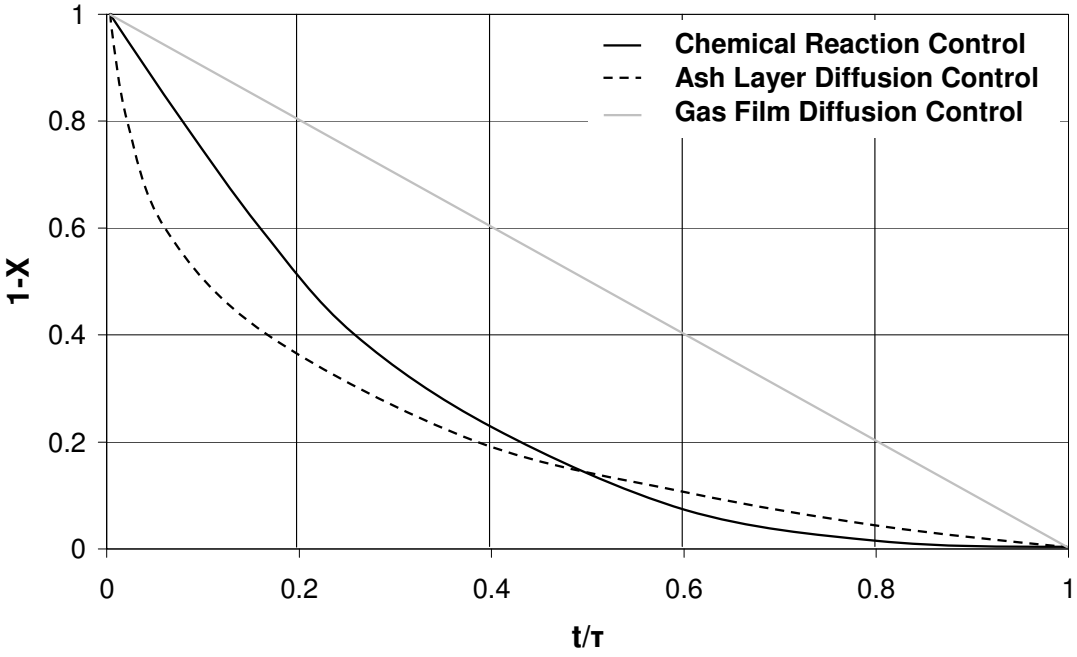

Figure 8.10 Reaction progress with respect to time for various rate controlling processes [18]

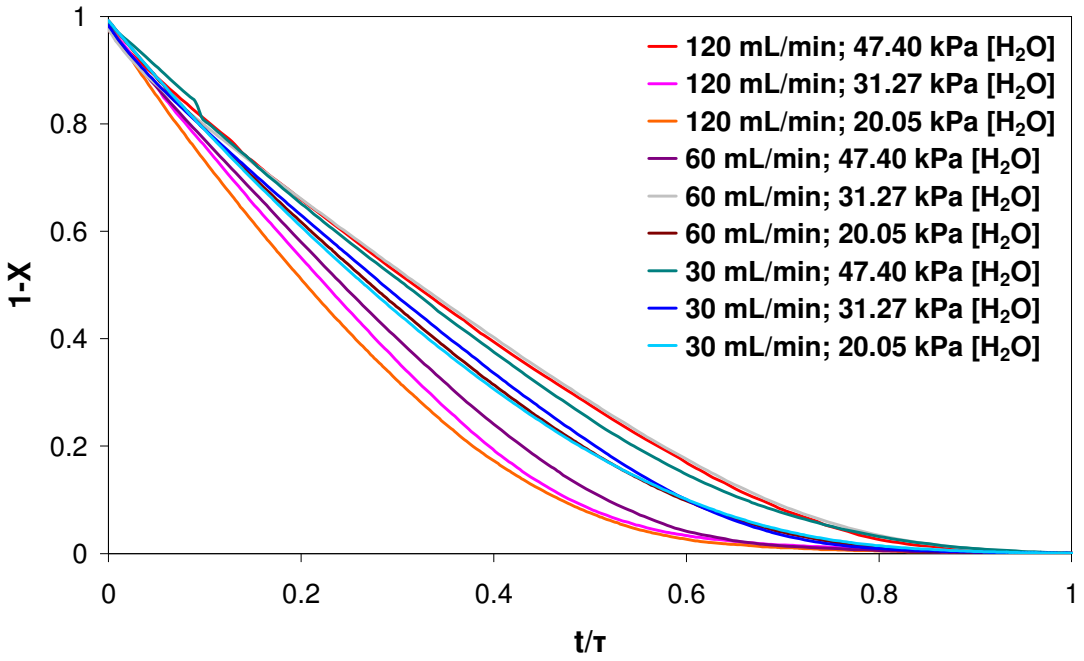

Figure 8.11 Experimental reaction progress with respect to time

Where **X** is defined as the amount of oxide converted, **t** is defined as time at a given conversion, and **τ** is defined as time taken for complete conversion.

The rate of reaction over different particle size can give an indication of the rate controlling mechanism. For diffusion controlled mechanism, time taken for complete conversion is given as $t \propto R^2$ whilst for chemical reaction controlling, $t \propto R$. Particle size, x, was maintained at between 150 μm to 250 μm for all reactions, with an assumed average particle size of 200 μm. Experiments conducted using particles ground to less than 150 μm shows that time is approximately proportional to particle size, with reaction time for x < 150 μm approximately 76% of reaction time for 150 μm < x < 250 μm (**Figure 8.12**).

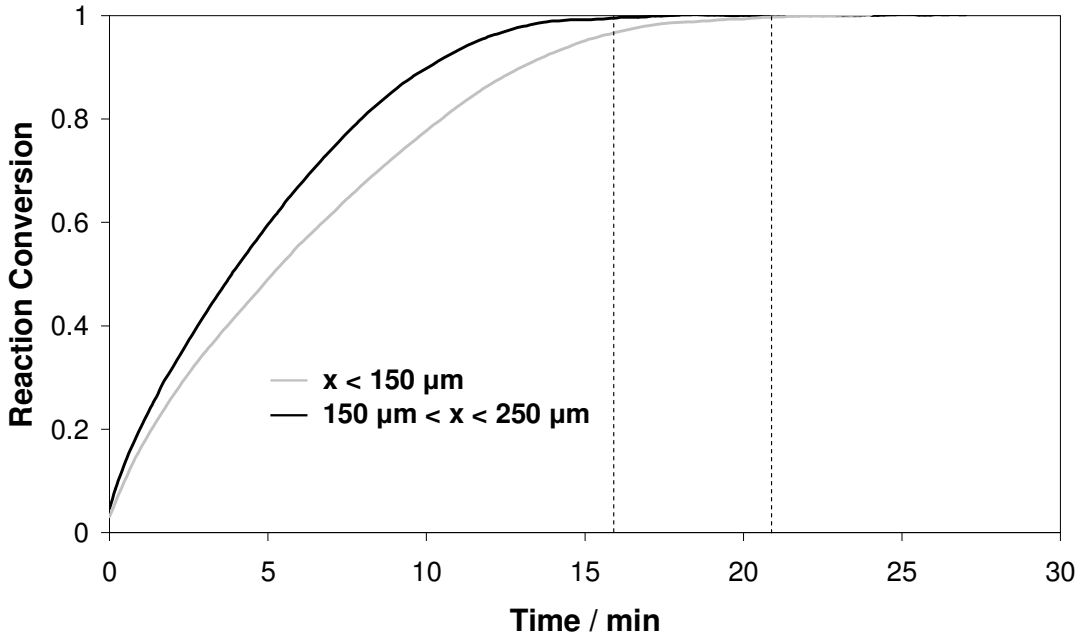

Figure 8.12 Effect of particle size upon time of reaction

Establishing the reaction rate controlling mechanism as one of chemical reaction controlling allows for application of a general rate equation of the form:

$$r = \frac{d\alpha}{dt} = k(T) \cdot [P_{H_2O}]^a \qquad \textbf{8.13}$$

where

$$k(T) = A \cdot e^{(-E_a/RT)} \qquad \textbf{8.14}$$

r is reaction rate, α is the fraction of metal (or metal oxide) converted, t is time, k is rate constant, T is reaction temperature, $[P_{H2O}]$ is the partial pressure of H_2O, ^{a} is the reaction order in H_2O, A is the pre-exponential factor, E_a is apparent activation energy and R is the ideal gas constant (8.314 $Jmol^{-1}K^{-1}$).

The reaction order in H_2O can be determined by measuring the rate of reaction at different partial pressures of H_2O. At constant partial pressure of H_2O and varying temperature, reaction rates can be determined. Then by plotting $\ln[r_{H2}]$, (r_{H2} being rate of H_2 production) against $\ln[P_{H2O}]$, the slope of $\left(-\frac{E_a}{R}\right)$ can be used to obtain the apparent activation energy, E_a.

The effect of H_2O partial pressure upon rate of reaction is shown in **Table 8-8**. Plotting $\ln(r_{H2})$ against $\ln(P_{H2O})$ gives a value for reaction order of H_2O (**Figure 8.13**). Average values at various flow rates gives a reaction order of H_2O of 0.75. A value for reaction rate constant *k(T)* can then be calculated using experimentally obtained data for reaction rate with respect to changing H_2O partial pressure (**Table 8-8**):

Table 8-8 Reaction rate of oxidation at varying H_2O partial pressure and flow rate, with calculated reaction rate constants

Flow Rate / (mL/min)	P_{H2O} / kPa	Rate of Reaction / (x10^{-6} H_2.mol/g.s)	k(T) / (x 10^{-7} H_2.mol/g.s.kPa)
30	20.05	2.03	3.07
	31.27	2.80	
	47.4	3.52	
60	20.05	2.14	2.46
	31.27	3.44	
	47.4	4.34	
120	20.05	2.82	2.10
	31.27	4.05	
	47.40	5.49	

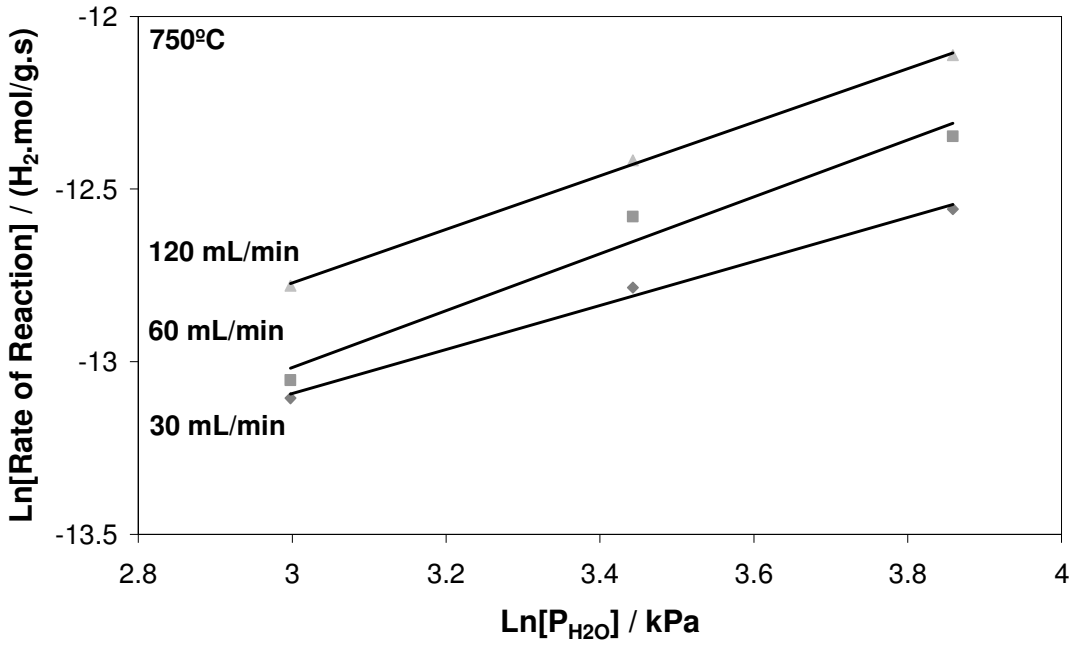

Figure 8.13 Effect of H_2O partial pressure upon rate of reaction

The apparent activation energy was calculated by varying reaction temperature whilst keeping flow rate and H_2O partial pressure constant. Activation energy data was obtained at two sets of conditions to determine the effect, if any, of varying flow rate and H_2O partial pressure (**Table 8-9**). Arrhenius plots of $\ln(r_{H2})$ vs. 1/T shown in **Figure 8.14** give value of apparent activation energy, E_a, of 109 ± 7$^+$ kJ/mol.

$^+$: Standard error based upon one standard deviation.

Table 8-9 Experimental data of effect of reaction temperature upon rate of reaction

Flow Rate / (mL/min)	P_{H2O} / kPa	Temperature / K	Rate of Reaction / ($x10^{-6}$ H_2.mol/g.s)	Apparent Activation Energy / (kJ/mol)
60	20.05	973	1.21	114
		1023	2.15	
		1073	4.66	
		1123	7.50	
120	47.40	973	3.39	104
		1023	5.99	
		1073	12.16	
		1123	17.98	
				109 ± 7[+]

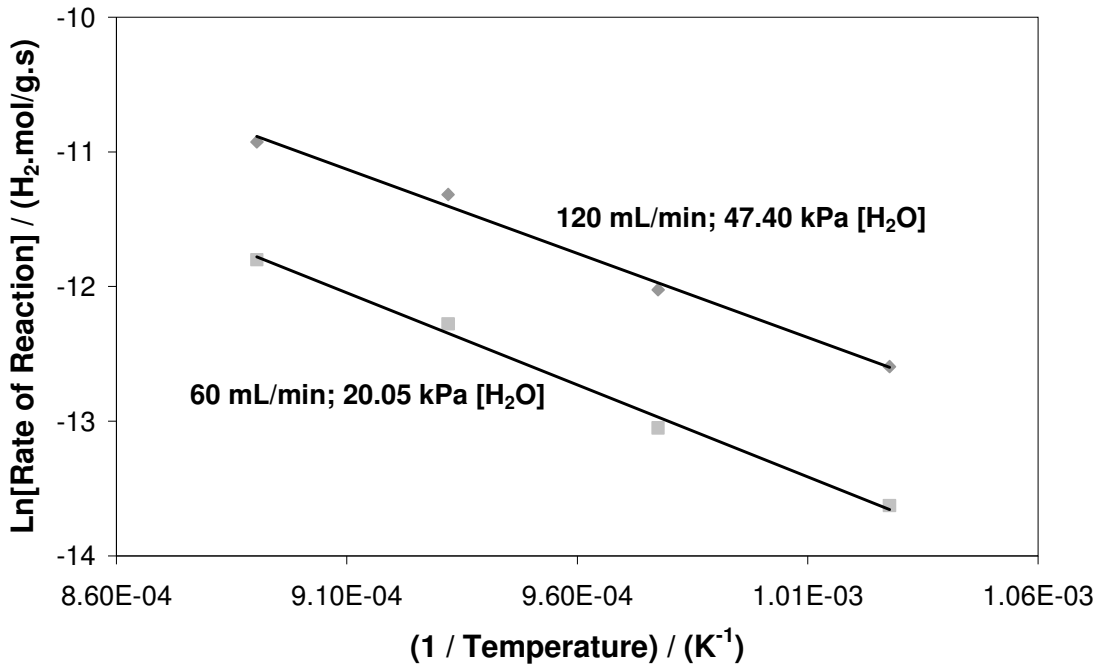

Figure 8.14 Arrhenius plots for the oxidation reaction of 4CZ.9WO_3 at varying flow rate and H_2O partial pressures

From the values of *k(T)* derived in **Table 8-8**, values for A, the pre-exponential constant, and its dependence upon flow rate can be calculated. These values were found to be 0.109, 0.087 and 0.075 at flow rates of 120 mL/min, 60 mL/min and 30 mL/min respectively. By plotting these values against flow rate, the dependence of flow rate upon pre-exponential constant A can be determined, to give a rate equation (**Figure 8.14**):

$$r_{H_2} = [0.064 + (F \times 0.00038)] \cdot e^{(-108750/8.314 \times T)} \cdot [P_{H_2O}]^{0.75} \qquad \textbf{8.15}$$

where *F* is flow rate in mL/min. **Equation 8.15** shows a good fit to experimental data, as shown in **Figure 8.16**.

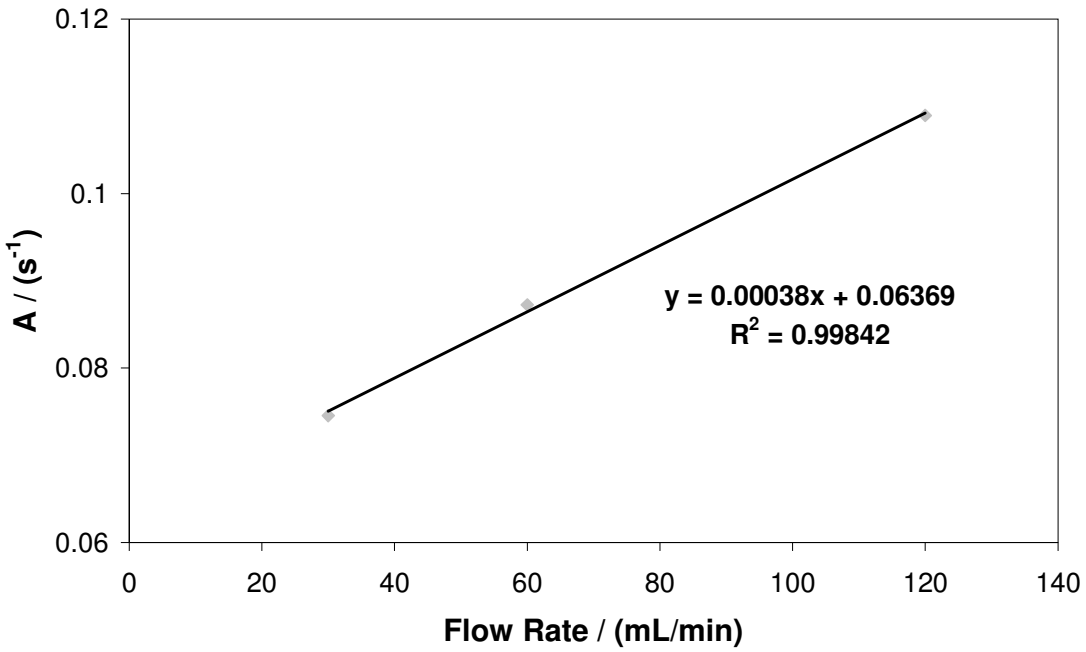

Figure 8.15 Dependence of the pre-exponential constant, A, upon flow rate

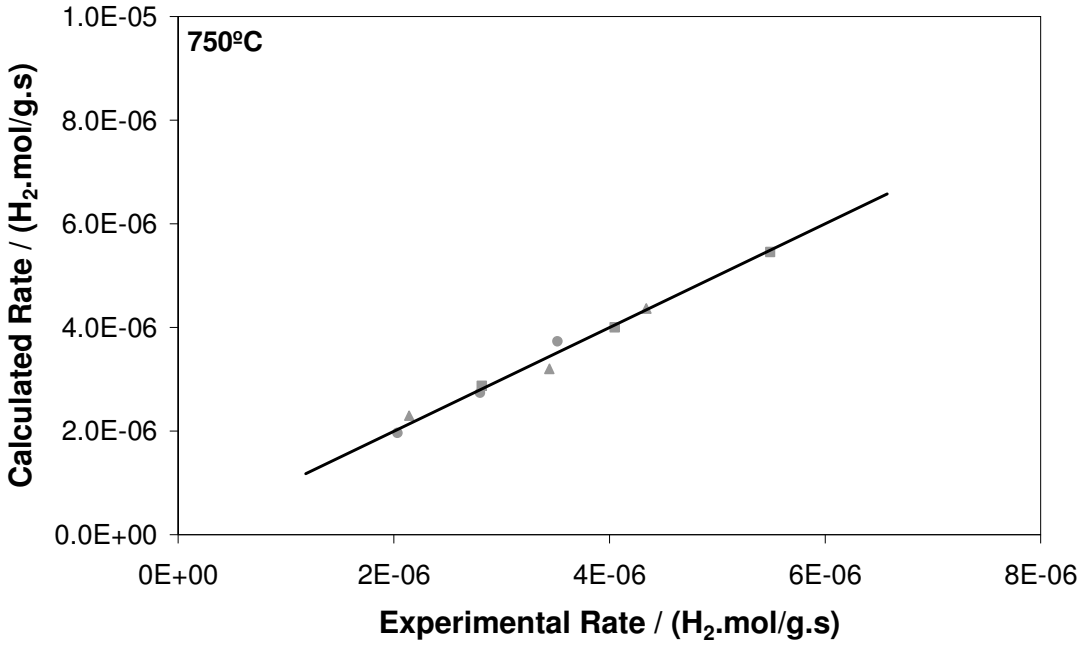

Figure 8.16 Theoretical reaction rate against predicted reaction rate for oxidation of 4CZ.9WO_3

8.3.3 Comparison of Promoted Tungsten Oxide Reduction-Oxidation Kinetics

Results show that the kinetics of both reduction and oxidation are controlled primarily by a chemical reaction mechanism (**Figure 8.11**, **Figure 8.12**). The rate of chemical reaction is directly proportional to, and highly dependent upon temperature. In the interest of limiting sintering and maximising metal oxide lifetime, it is desirable to minimise reaction temperature. Formation of WO_2 from methane reduction of 4CZ.9WO_3 is temperature dependent, with stability of WO_2 compromised with reduction at higher temperature, resulting in formation of W and WC (**Figure 7.12**, **Figure 7.13**). 750ºC (1023K) has shown to be the optimal temperature for operating the overall process, giving compromise between stabilised reduction of 4CZ.9WO_3 to form WO_2, whilst maintaining a high rate of re-oxidation.

Based upon these results, a comparison between the W based Steam-Metal system and Fe based Steam-Iron system can be made. Reduction of Fe_3O_4 is governed by a nucleation controlling mechanism however, the reduction mechanism is found to be dependent upon particle size; as particle size increases the mechanism can shift to one of phase boundary controlled reduction [7, 17]. The nucleation based mechanism is initially governed by uniform internal reduction of the particle, whereupon removal of enough lattice oxygen atoms to achieve a critical concentration of vacancies shows acceleration in reaction rate due to lattice rearrangement to facilitate metal formation and eliminate vacancies. As reduction proceeds further, once a high degree of oxygen has been consumed and there is a greater proportion of metal product to initial metal oxide sample, the reaction decelerates due to limited vacancies to allow for further lattice rearrangement. Experimental results show a phase boundary controlled mechanism for reduction of WO_3, with the reaction rate dependent upon the reaction itself between the sample and reactant, thus such factors as temperature and gas concentrations which control the reaction are rate dependent factors. In comparison, reaction rate dependence in the nucleation mechanism is based upon concentration of vacancies. Based on this, it is presumed that the activation energy for a nucleation based mechanism, in this case Fe_3O_4 reduction, should be lower than that of a phase boundary controlled mechanism, WO_3 reduction.

Oxidation of reduced FeO_x to Fe_3O_4 has been determined to be diffusion based [9]. Diffusion based kinetics remain independent of temperature and gas concentration, and reaction rate is influenced by the rate at which the reactant can diffuse through the reacted layer or product at the surface to react at the unreacted core. This mechanism is expected to have high activation energy; as the metal oxide is oxidised, reaction rate decreases due to the requirement for H_2O to penetrate the increasingly thick oxide layer. WO_2 to WO_3 oxidation for 4CZ.9WO_3 is primarily chemical reaction based, similar to reduction.

Activation energies for reduction of 4CZ.9WO_3 by H_2 (142 ± 3 kJ/mol) has a higher calculated activation energy than reduction of Fe_3O_4 by H_2, with literature values for

activation energy ranging from 70-111 kJ/mol [7, 17], dependent upon experimental conditions. Reduction by H_2 gives lower activation energies than would be expected for reduction by CH_4, due to the greater reducing capability of H_2. Activation energy of Fe to Fe_3O_4 oxidation (78 kJ/mol) [9] is higher than that of 4CZ.WO_2 to 4CZ.9WO_3 oxidation by water (109 ± 7 kJ/mol). Redox of Fe_3O_4 ↔ Fe shows lower activation energy compared to redox of 4CZ.WO_3 ↔ 4CZ.9WO_2 irregardless of governing kinetics. Addition of CeO_2/ZrO_2 promoters to WO_3 shows a decrease in activation energy from 189 ± 4 kJ/mol for reduction of unpromoted WO_3 to 142 ± 3 kJ/mol for CeO_2/ZrO_2 promoted WO_3. In contrast, a significant decrease in activation energy is not observed for reduction of unpromoted Fe_3O_4 (59-70 kJ/mol) compared to reduction of CeO_2/ZrO_2 promoted Fe_2O_3 (78 ± 12 kJ/mol) [7]. It is difficult to discern promoter addition significantly alters activation energy or governing redox kinetic mechanism, which is highly dependent upon experimental conditions [1, 7, 9, 14], suffice to say promoter addition has demonstrated increased reducibility and oxidisability through experimental studies (**Chapter 5, 7, 8**).

Despite lower activation energy of Fe_3O_4 reduction by hydrogen as compared to WO_3 reduction, WO_3 shows better reducibility using methane as a reductant under the same conditions as methane reduction of Fe_3O_4 (**Chapter 5** and **7**). The ability to stabilise reduction of 4CZ.9WO_3 for repeated formation of WO_2 during methane reduction is a significant advantage over methane reduction of Fe_3O_4. Whilst H_2 reduction of promoted Fe_2O_3 is able to be stabilised to some degree (**Chapter 5.3.2.2** and **5.3.2.3**), methane reduction shows reduction to Fe metal even with addition of promoters.

The Fe_3O_4-Fe cycle has the capacity to produce up to 384 L.H_2/kg of Fe_3O_4, however, due to the carbon formation from methane decomposition over Fe metal, a Fe_3O_4-FeO cycle may be used to limit carbon formation [19]. Further investigation will be necessary to determine more precise experimental conditions allowing for stabilised formation of FeO with methane as a reductant. Similarly, despite the high hydrogen production capacity of the WO_3-W cycle (288 L.H_2/kg of WO_3) formation of WC is a problem. Both

the Fe_3O_4-FeO and WO_3-WO_2 cycles are capable of producing up to 96 L.H_2/kg of their respective oxides. Addition of CeO_2/ZrO_2 to WO_3 to form 4CZ.9WO_3 shows slightly decreased hydrogen production at 83 L.H_2/kg of 4CZ.9WO_3 due to the lower oxygen storage capacity of 2[CeO_2/ZrO_2]-[$Ce_2O_3/2ZrO_2$] redox, compared to WO_3-WO_2 redox.

8.4 Conclusions

1. The kinetics for the reduction of 4CZ.9WO_3 (WO_3/$WO_{2.9}$ → WO_2) has shown the system to conform to a 1D phase boundary/unimolecular decay model. The 1D phase boundary/unimolecular decay model and 3D phase boundary model are assigned to reduction of WO_3 → $WO_{2.9}$ followed by reduction of $WO_{2.9}$ → WO_2 respectively.

2. The apparent activation energy for reduction of 4CZ.9WO_3 (WO_3/$WO_{2.9}$ → WO_2) was calculated at 142 ± 3* kJ/mol, which is less than the value of 189 ± 4* kJ/mol obtained for reduction of unpromoted WO_3.

3. The rate controlling step of the oxidation reaction for 4CZ.9WO_3 was determined to be chemical reaction based.

4. The apparent activation energy for the oxidation of 4CZ.9WO_3 (WO_2 → $WO_{2.9}$/WO_3) was calculated as 109 ± 7^+ kJ/mol.

5. The reaction rate expression for oxidation was derived as:

$$r_{H_2} = [0.064 + (F \times 0.00038)] \cdot e^{(-108750/8.314 \times T)} \cdot [P_{H_2O}]^{0.75}$$

This is indicative of a high dependence of H_2O partial pressure upon reaction rate and some dependence upon flow rate. The reaction is primarily chemical reaction controlled however, the slight dependence upon flow rate indicates there also exists some degree of mass transfer control. This derived expression gives a good fit between theoretical and experimentally obtained reaction rates.

8.5 References

1. J. Bessières, A. Bessières, and J.J. Heizmann, 'Iron oxide reduction kinetics by hydrogen', *International Journal of Hydrogen Energy* **1980**, 5(6), 585-595
2. J.A. Peña, E. Lorente, E. Romero, and J. Herguido, 'Kinetic study of the redox process for storing hydrogen: Reduction stage', *Catalysis Today* **2006**, 116(3), 439-444
3. A. Bonalde, A. Henriquez, and M. Manrique, 'Kinetic analysis of the iron oxide reduction using hydrogen-carbon monoxide mixtures as reducing agent', *I.S.I.J. International* **2005**, 45(9), 1255-1260
4. M.V.C. Sastri, R.P. Viswanath, and B. Viswanathan, 'Studies on the reduction of iron oxide with hydrogen', *International Journal of Hydrogen Energy* **1982**, 7(12), 951-955
5. H.A. Ebrahim and E. Jamshidi, 'Kinetic study of zinc oxide reduction by methane', *Chemical Engineering Research & Design* **2001**, 79(A1), 62-70
6. H.A. Ebrahim and E. Jamshidi, 'Effect of mass transfer and bulk flow on the zinc oxide reduction by methane', *Industrial & Engineering Chemistry Research* **2002**, 41(11), 2630-2636
7. V. Galvita and K. Sundmacher, 'Redox behaviour and reduction mechanism of Fe_2O_3-$CeZrO_2$ as oxygen storage material', *Journal of Materials Science* **2007**, 42(22), 9300-9307
8. E. Lorente, J.A. Peña, and J. Herguido, 'Kinetic study of the redox process for separating and storing hydrogen: Oxidation stage and ageing of solid', *International Journal of Hydrogen Energy* **2008**, 33(2), 615-626
9. K.S. Go, S.R. Son, and S.D. Kim, 'Reaction kinetics of reduction and oxidation of metal oxides for hydrogen production', *International Journal of Hydrogen Energy* **2008**, 33(21), 5986-5995
10. P. Charvin, S. Abanades, G. Flamant, and F. Lemort, 'Two-step water splitting thermochemical cycle based on iron oxide redox pair for solar hydrogen production', *Energy* **2007**, 32(7), 1124-1133

11. M. Ishida, H. Jin, and T. Okamoto, 'A Fundamental Study of a New Kind of Medium Material for Chemical-Looping Combustion', *Energy & Fuels* **1996**, 10, 958-963

12. H.-J. Ryu, D.-H. Bae, K.-H. Han, S.-Y. Lee, G.-T. Jin, and J.-H. Choi, 'Oxidation and Reduction Characteristics of Oxygen Carrier Particles Reaction Kinetics by Unreacted Core Model', *Korean Journal of Chemical Engineering* **2001**, 18(6), 831-837

13. J.M. Kanervo and K. A.O.I., 'Kinetic Analysis of Temperature-Programmed Reduction: Behaviour of a CrO_x/Al_2O_3 Catalyst', *Journal of Physical Chemistry B* **2001**, 105, 9778-9784

14. O.J. Wimmers, 'Analytical expressions for temperature programmed reduction patterns using solid-state kinetics', *Thermochimica Acta* **1985**, 95(1), 67-72

15. H.E. Kissinger, 'Reaction Kinetics in Differential Thermal Analysis', *Analytical Chemistry* **1957** 29 (11), 1702-1706

16. P. Malet and A. Caballero, 'The Selection of Experimental Conditions in Temperature-programmed Reduction Experiments', *Journal of the Chemistry Society, Faraday Transactions I* **1988** 84(7), 2369-2375

17. O.J. Wimmers, P. Arnoldy, and J.A. Moulijn, 'Determination of the Reduction Mechanism by Temperature-Programmed Reduction: Application to Small Fe_2O_3 Particles', *Journal of Physical Chemistry* **1986**, 90, 1331-1337

18. O. Levenspiel, 'Chemical Reaction Engineering', 2nd ed. *John Wiley & Sons, Inc.*: New York, **1972**

19. K. Svoboda, G. Slowinski, J. Rogut, and D. Baxter, 'Thermodynamic possibilities and constraints for pure hydrogen production by iron based chemical looping process at lower temperatures', *Energy Conversion and Management* **2007**, 48(12), 3063-3073

CONCLUSIONS

9.1 Conclusions

Based on the Steam-Iron Process for clean hydrogen generation, a series of metal oxides were assessed and tested for their reactivity and potential hydrogen production capability under a range of conditions.

Thermodynamic feasibility studies were performed over a selection of metal oxides for their reactivity in both methane reduction and water re-oxidation to produce clean hydrogen. The systems comprising Fe_3O_4/FeO/Fe, WO_3/WO_2/W and SnO_2/SnO/Sn were identified as suitably active for further experimental analysis. Other metal oxides analysed were considered unsuitable for the Steam-Metal process due to low melting point and high cost (In_2O_3), low oxygen storage capacity (Nb_2O_5) and formation of metal carbide from carbon based reductants (MoO_2). To improve redox reactivity, prevent metal oxide deactivation and achieve stabilisation of the intermediate metal oxide phase of the selected systems, use of promoters was employed.

Addition of CeO_2 and CeO_2/ZrO_2 promoters to Fe_2O_3 improved redox reactivity compared to unpromoted Fe_2O_3, along with increasing surface area retention and thereby limiting metal oxide deactivation. Stabilisation of FeO during repeated redox of CeO_2/ZrO_2 promoted Fe_2O_3 was observed with use of H_2 as a reductant and H_2O as an oxidant. Deactivation of Fe_2O_3 was attributed primarily to carbon formation when using both CO and CH_4 as reductants. This resulted from complete reduction to form metallic Fe, over which methane decomposition and the Boudouard Reaction are catalysed.

Addition of CeO_2/ZrO_2 to SnO_2 retards sintering as well as improving reducibility. However, methane proved to be a poor reductant over unpromoted SnO_2. Addition of CeO_2/ZrO_2 shows slightly improved reducibility of surface oxygen species, but does not

catalyse further reduction of bulk SnO_2 oxygen species. It is clear that CeO_2/ZrO_2 promoted SnO_2 is not a good system for the Steam-Metal Process.

Addition of CeO_2/ZrO_2 increases stability of WO_3 with higher surface area retention observed over a number of cycles. Within this work a unique Ce_2O_3/ZrO_2 promoted WO_3 structure was found at a composition of 31mol% [CeO_2/ZrO_2] / 69 mol% WO_3. Using this compound, stabilised formation of WO_2 (31 mol% [Ce_2O_3/ZrO_2] / 69 mol% WO_2) is observed using methane as a reductant. In comparison, reduction of unpromoted WO_3 forms WC. Optimal operating conditions for this process were found with a concentration of 50% CH_4 in He/Ar at a flow rate of 60mL / min for reduction, and 47% H_2O saturation in He/Ar at a flow rate of 120 mL / min for oxidation. Both reduction and oxidation were performed at a temperature of 750ºC. Redox was repeated over 20 cycles, each time showing stoichiometric levels of clean hydrogen production.

A kinetic study of the 31 mol% [CeO_2/ZrO_2] / 69 mol% WO_3 shows $WO_3/WO_{2.9} \rightarrow WO_2$ reduction conforms to a 1D phase boundary / unimolecular decay model. This is defined as a shrinking core type model based on the chemical reaction process as the rate determining step. WO_3 also reduced via the same 1D phase boundary / unimolecular decay mechanism for reduction of $WO_3 \rightarrow WO_{2.9}$, following which $WO_{2.9} \rightarrow WO_2$ reduced via a 3D phase boundary mechanism. Both unpromoted and promoted WO_3 showed reduction behaviour consistent with the 3D phase boundary mechanism for the reduction of $WO_2 \rightarrow W$. The apparent activation energy for the reduction of 4CZ.9WO_3 ($WO_3/WO_{2.9} \rightarrow WO_2$) was calculated at 142 ± 3* kJ/mol, which is less than the value of 189 ± 4* kJ/mol obtained for reduction of unpromoted WO_3 ($WO_{2.9} \rightarrow WO_2$). The rate controlling step of the oxidation reaction of 31 mol% [CeO_2/ZrO_2] / 69 mol% WO_3 for $WO_2 \rightarrow WO_{2.9}/WO_3$ formation was also determined to be chemical reaction based. The apparent activation energy for oxidation was calculated as 109 ± 7 kJ/mol. The reaction rate expression for oxidation was derived as:

$$r_{H_2} = [0.064 + (F \times 0.00038)] \cdot e^{(-108750/8.314 \times T)} \cdot [P_{H_2O}]^{0.75}$$

This shows a high dependence of reaction rate upon H_2O partial pressure and some dependence upon flow rate due to minimal mass transfer limitations. The derived expression gives a good fit between theoretical and experimentally obtained reaction rates. The rate controlling mechanism of the overall redox process is determined to be based primarily on chemical reaction kinetics, with reaction rate directly proportional to temperature. Formation of WO_2 from methane reduction of $4CZ.9WO_3$ is temperature dependent, with reduction at 750ºC (1023K) shown to be the optimal temperature for operation of the overall process, giving compromise between high rate of re-oxidation and stabilised reduction of $4CZ.9WO_3$.

In summary, 31mol% [CeO_2/ZrO_2] / 69 mol% WO_3 exhibited stabilised reduction by methane, forming 31mol% [Ce_2O_3/ZrO_2] / 69 mol% WO_2. Re-oxidation by water yielded clean hydrogen, with no observed CO_x by products. Addition of CeO_2/ZrO_2 was observed to lower the activation energy of reduction, as compared to unpromoted WO_3. Repeated redox over 20 cycles showed minimal loss in hydrogen production capacity with good surface area retention.

From an industrial viewpoint, this process has a number of advantages over currently implemented hydrogen production technologies. There is currently no network available for hydrogen distribution and inherent risks involved with transporting hydrogen, both of which limit the widespread utilisation of hydrogen as an energy carrier. The Steam-Metal Process has significant potential to fill these gaps, with the ability to implement small to medium scale hydrogen production centres, creating the possibility for on-site and decentralised hydrogen production. The major limitation with use of iron oxide in this process from an industrial sense is its rapid deactivation due to sintering effects combined with carbon deposition from carbon based reductants. However, the advantages of using iron oxide have generated much interest in improving its functionality, with a wide range of literature seeking to address these issues through a variety of methods. The use of promoted tungsten oxide in this process has the possibility to eliminate such problems as

found with iron oxide, whilst generating a comparable amount of hydrogen ($WO_3 \leftrightarrow WO_2 \equiv Fe_3O_4 \leftrightarrow FeO$). A major advantage of using tungsten oxide is the lack of carbon produced during the methane reduction process, as compared to methane reduction of iron oxide based samples, allowing for clean hydrogen production upon re-oxidation and mitigating the need for further hydrogen purification. The high level of hydrogen production observed over numerous cycles despite decreasing surface area shows minimal deactivation of tungsten oxide. Implementation of a fluidized bed system may improve the performance of this process, particularly from an industrial sense, as is addressed in recommendations for future work below.

9.2 Recommendations

Use of iron oxide in the Steam-Metal Process is desirable, for its high oxygen storage capacity, relatively low temperature of reduction and re-oxidation, and the fact it is cheap and widely available. Recommendations for further investigation of iron oxide (1, 2 and 3 below) based on the results of this thesis include:

1. Optimisation of the ratio of CeO_2/ZrO_2 promoter addition to Fe_2O_3 to determine possible promoter addition concentration and/or ideal reaction conditions at which methane reduction forms stabilised FeO. Based upon experimental work with H_2 reduction of CeO_2/ZrO_2 promoted Fe_2O_3 (**Chapter 5.3.2**), it is possible to stabilise reduction of Fe_2O_3 to some extent. Upon further investigation, more stringent reaction conditions may be found to achieve this same stabilisation with methane reduction.

2. Introduction of precious metals such as Pt onto CeO_2/ZrO_2 promoted Fe_2O_3 to facilitate methane reduction without methane decomposition which forms carbon. Use of precious metals including Pt, Rh and Pd have shown to lower activation energy and accelerate redox reactions, along with facilitating syngas formation from methane in the reduction of metal oxides to mitigate carbon formation [1, 2].

3. More detailed analysis of optimal reaction conditions including flow rate, reaction temperature and reactant concentration for redox of CeO_2/ZrO_2 promoted Fe_2O_3. Optimisation of reaction conditions for the redox of CeO_2/ZrO_2 promoted WO_3 (**Chapter 7.4.1**) showed the possibility for improved reaction kinetics and maximisation of hydrogen production.

4. Study of SnO_2 for CH_4/H_2O redox using other more active promoters such as Cr and Fe. Addition of Cr and Fe to SnO_2 and sulfated SnO_2 show extensive reduction by methane [3-5]. By achieving deeper reduction of SnO_2 and promoted

SnO_2, increased hydrogen production is possible upon re-oxidation of reduced SnO_2 species.

5. Consideration of a circulating system such as a fluidized bed in order to investigate possible commercialisation of the WO_3 based system. The use of a fixed bed system as reported in this thesis has limitations associated with reaction gradients, especially regarding the exact nature of achieving stabilised partial reduction of the promoted WO_3 system. Fluidized bed reactors have a number of advantages over fixed bed reactors and are predominantly utilised in numerous industrial processes. Due to the nature of its operation allowing for constant mixing, the utilisation of a fluidized bed reactor gives uniform particle mixing, uniform temperature gradient and the ability to operate the reaction process continuously, which is particularly advantageous in a continuous redox type process [6].

9.3 References

1. K. Urasaki, N. Tanimoto, T. Hayashi, Y. Sekine, E. Kikuchi, M. Matsukata, 'Hydrogen production via steam–iron reaction using iron oxide modified with very small amounts of palladium and zirconia', *Applied Catalysis A: General*, **2005** 288, 143-148
2. K. Otsuka, S. Takenaka, 'Storage and Supply of Pure Hydrogen Mediated by the Redox of Iron Oxides', *Journal of the Japan Petroleum Institute*, **2004** 47(6), 377-386
3. X. Wang and Y.-C. Xie, 'CH_4 deep oxidation over active and thermally stable catalysts based on Sn-Cr composite oxide', *New Journal of Chemistry* **2001**, 25, 1621-1626
4. X. Wang and Y.-C. Xie, 'Total oxidation of CH_4 on Sn-Cr composite oxide catalysts', *Applied Catalysis B - Environmental* **2001**, 35, 85–94
5. X. Wang and Y.-C. Xie, 'Low-Temperature CH_4 Total Oxidation on Catalysts based on High Surface Area SnO_2', *Reaction Kinetics and Catalysis Letters* **2001**, 72(1), 115-123
6. P. Trambouze, J-P. Euzen, 'Chemical reactors: From Design to operation', (R. Bononno, Trans.), *Paris: Editions Technip* **2004**

APPENDIX I

Calculation of Gas Concentration Conversions

The following procedure was used to calculate the conversion of gas flow concentration as a function of the outgoing mass spectrometer ion current during all Steam-Iron/Metal Process testing.

To convert ion current signal into a gas percentage, a conversion factor was first established using a bypass gas flow. The ion current for the selected gas of interest (H_2, CH_4, CO, CO_2, H_2O) was measured at a known gas concentration. A second reference gas (Ar) was also monitored in the gas stream to ensure any fluctuations observed in the gas signal were a function of gas consumption or production rather than random fluctuations in gas flow. The ratio of the ion current of reactant gas against the ion current of reference gas was equated to a specific gas concentration:

$$\frac{Bypass \cdot Gas_{react}}{Bypass \cdot Gas_{ref}} \equiv x\%$$

Consequently this conversion factor was used to determine the change in the reactant gas with respect to the reference gas and obtain a value for changing gas concentration during the experiment:

$$\left[x\% / \left(\frac{Bypass \cdot Gas_{react}}{Bypass \cdot Gas_{ref}} \right) \right] \times \frac{Experimental \cdot Gas_{react}}{Experimental \cdot Gas_{ref}} = y\%$$

This gas concentration value can then be converted into moles by application of the following formula:

$$Moles \cdot gas = \frac{y\% \times flowrate \times (gas \cdot density)}{(gas \cdot molecular \cdot mass)}$$